

---

# Effects of profiles on microinstabilities in tokamaks

David Dickinson

---

Submitted in accordance with the requirements  
for the degree of Doctor of Philosophy

University of York  
Physics

September 2012



---

## Abstract

Turbulent transport of heat and particles significantly degrades the confinement in tokamaks. Whilst the confinement improves in larger devices, these are more expensive and the economic viability of future fusion power plants depends upon understanding turbulence so that operating scenarios can be optimised.

Gyrokinetic models are able to describe the plasma turbulence responsible for transport. The assumption that the equilibrium varies slowly relative to the radial width of the instability is often exploited to reduce the global gyrokinetic system to a local one. The relation between the global and local systems is a key topic in this thesis. It is shown that local solutions can only capture the true global behaviour when freedoms in the system are treated correctly. A procedure to reconstruct the global solution from the local one has been developed and successfully tested.

The spontaneous transition to a regime of high confinement, observed on many tokamaks, is associated with the suppression of turbulence in a narrow region near the plasma edge, known as the pedestal, and is accompanied by edge localised instabilities (ELMs) which can eject large amounts of energy in a short time, damaging the confinement vessel. Understanding the ELM and pedestal behaviour is crucial to predict the performance of future tokamaks, as well as offering insight into techniques to reduce the threat of damage due to ELMs. The application of gyrokinetics to study microinstabilities in the edge region of MAST in the time between two ELMs is presented as part of this thesis. This work finds kinetic ballooning modes to be unstable in the pedestal whilst microtearing modes are unstable in the shallow gradient region towards the core. The transition from MTMs to KBMs at the interface between the two regions has been studied and may play an important role in the pedestal evolution.



# Contents

Abstract	i
List of Figures	viii
List of Tables	xii
Acknowledgments	xv
Declaration	xvii
<b>1 Supplying the world's energy demands</b>	<b>1</b>
1.1 Global energy concerns . . . . .	1
1.2 Nuclear fusion as an energy source . . . . .	3
1.2.1 Heating requirements and energy gain . . . . .	6
1.3 Magnetic confinement fusion . . . . .	7
1.3.1 Conserved quantities . . . . .	8
1.3.2 Magnetic mirror confinement . . . . .	10
1.3.3 Tokamaks . . . . .	12
1.3.3.1 Particle drifts . . . . .	13
1.3.3.2 The need for a poloidal magnetic field . . . . .	14
<b>2 Understanding magnetic confinement</b>	<b>19</b>
2.1 Diffusive losses . . . . .	19
2.2 Classical estimates . . . . .	20
2.3 Neoclassical estimates . . . . .	21

2.4	Fluctuation driven transport . . . . .	23
2.4.1	A picture of fluctuation driven transport . . . . .	23
2.4.2	Diffusive estimates . . . . .	24
2.4.3	Transport calculations . . . . .	25
2.5	Turbulent fluctuations in experiment . . . . .	26
2.5.1	Fluctuation characteristics . . . . .	27
2.5.2	Transport barriers . . . . .	28
2.5.2.1	Internal transport barriers . . . . .	29
2.6	Empirical scaling laws . . . . .	30
2.7	One dimensional transport models . . . . .	32
2.8	Predictions for ITER . . . . .	35
<b>3</b>	<b>Theoretical study of fluctuations</b>	<b>37</b>
3.1	The need for theory . . . . .	37
3.2	Two fluid drift instabilities in shearless slab geometry . . . . .	38
3.2.1	The electron drift wave . . . . .	38
3.2.2	Ion temperature gradient mode . . . . .	41
3.2.2.1	The ITG dispersion relation . . . . .	42
3.2.3	Incorporating extra effects . . . . .	45
3.3	Kinetic plasma description . . . . .	45
3.3.1	The kinetic equation . . . . .	46
3.4	Gyrokinetics . . . . .	48
3.4.1	Linearised kinetic equation . . . . .	49
3.4.2	Coordinates . . . . .	49
3.4.3	Gyrokinetic orderings . . . . .	51
3.4.3.1	Ordering the linearised Vlasov equation . . . . .	51
3.4.3.2	The leading order equation . . . . .	53
3.4.3.3	The first order equation . . . . .	53
3.4.4	Nonlinear effects . . . . .	54

<b>4</b>	<b>Using the gyrokinetic equation</b>	<b>57</b>
4.1	Numerical simulations . . . . .	57
4.1.1	Numerical approaches . . . . .	57
4.1.1.1	Radially local vs. global . . . . .	58
4.2	Challenges for gyrokinetics . . . . .	59
4.3	Topics addressed in this thesis . . . . .	60
<b>5</b>	<b>On local approximations to global gyrokinetic theory</b>	<b>63</b>
5.1	An introduction to ballooning theory . . . . .	63
5.2	A gyrokinetic toroidal ITG model . . . . .	68
5.2.1	The global model . . . . .	69
5.2.1.1	Poloidal Fourier decomposition . . . . .	73
5.2.2	The local model . . . . .	74
5.3	Choosing the local model's free parameters to fit the global model . . . . .	77
5.3.1	The Fourier-Ballooning representation . . . . .	79
5.3.2	Relating the local and global mode frequencies . . . . .	80
5.3.2.1	Quadratic radial variation: Isolated modes . . . . .	81
5.3.2.2	Linear radial variation: General modes . . . . .	82
5.3.3	Predicting the global mode structure . . . . .	83
5.3.3.1	Isolated modes: Radial width and poloidal angle . . . . .	83
5.3.3.2	General modes: Radial width and poloidal angle . . . . .	84
5.4	Numerical solutions . . . . .	85
5.4.1	Numerical approach: Global model . . . . .	85
5.4.1.1	Updating the frequency . . . . .	88
5.4.2	Numerical approach: Local model . . . . .	88
5.4.3	The cylindrical limit . . . . .	90
5.4.4	Benchmarking: Global code . . . . .	91
5.4.5	Benchmarking: Local code . . . . .	92
5.4.6	Convergence testing . . . . .	92

5.5	Global modes: The effect of profiles . . . . .	93
5.5.1	Isolated modes . . . . .	94
5.5.2	General modes . . . . .	96
5.6	From local to global . . . . .	97
5.6.1	Quadratic profiles . . . . .	98
5.6.2	Linear profiles . . . . .	100
5.7	Discussion . . . . .	103
5.7.1	Sheared flows . . . . .	104
5.7.1.1	Isolated modes . . . . .	106
5.7.1.2	General modes . . . . .	108
5.7.2	Future work . . . . .	109
<b>6</b>	<b>Gyrokinetic stability of the MAST H-mode pedestal</b>	<b>113</b>
6.1	Predicting the pedestal's properties . . . . .	113
6.1.1	The peeling-ballooning ELM model . . . . .	114
6.1.2	The EPED model . . . . .	118
6.2	Testing an EPED-type model for the MAST pedestal . . . . .	124
6.2.1	Experimental observations . . . . .	125
6.2.2	MHD stability analysis . . . . .	127
6.3	A gyrokinetic study of the MAST pedestal region . . . . .	132
6.3.1	Microstability during the ELM cycle . . . . .	134
6.3.2	Exploring the pedestal expansion . . . . .	138
6.3.2.1	Surface $a$ . . . . .	139
6.3.2.2	Surface $b$ . . . . .	142
6.3.2.3	Surface $c$ . . . . .	144
6.4	Discussion . . . . .	145
6.4.1	Future work . . . . .	148

---

<b>7</b>	<b>Summary and discussion</b>	<b>151</b>
7.1	The effect of equilibrium variations . . . . .	152
7.2	Stability of the pedestal . . . . .	153
<b>A</b>	<b>Fluid equations from the kinetic equation</b>	<b>155</b>
	<b>Bibliography</b>	<b>157</b>



# List of Figures

1.1	Total energy usage by source, 1965-2010. . . . .	1
1.2	U.K. renewable energy usage, 1990-2009 . . . . .	2
1.3	Binding energy curve . . . . .	4
1.4	Reaction rates vs. temperature for a range of fusion reactions . . . . .	5
1.5	Motion of a charged particle in a magnetic field . . . . .	8
1.6	The Lorentz force in a spatially varying magnetic field . . . . .	10
1.7	Illustration of a magnetic mirror device . . . . .	11
1.8	Loss cone in velocity space . . . . .	11
1.9	Toroidal magnetic field from a straight conductor . . . . .	12
1.10	The process behind $\nabla B$ confinement losses . . . . .	14
1.11	The poloidal and toroidal fields . . . . .	15
1.12	A simple tokamak . . . . .	16
1.13	Nested flux surfaces . . . . .	17
1.14	Progress in achieved triple product. . . . .	18
2.1	Poloidal projection of trapped and passing orbits . . . . .	21
2.2	Diffusion coefficient as a function of collisionality . . . . .	23
2.3	Measured fluctuation amplitude and particle flux profiles. . . . .	27
2.4	Example L-mode, H-mode and ITB pressure profiles . . . . .	29
2.5	Comparison of measured $\tau_E$ and empirical predictions. . . . .	33
3.1	Simple picture of the drift wave . . . . .	39
3.2	Slab ITG stability boundary . . . . .	44

5.1	Resonant perturbation in slab . . . . .	64
5.2	Cartoon of mapping from infinite to periodic domain. . . . .	66
5.3	Isolated mode properties vs $n$ . . . . .	92
5.4	Complex mode frequency vs. coupling strength (isolated) . . . . .	95
5.5	Isolated mode radial and global structure . . . . .	95
5.6	Relative phase between Fourier modes for isolated mode . . . . .	96
5.7	Complex mode frequency vs. coupling strength (general) . . . . .	97
5.8	General mode radial and global structure . . . . .	97
5.9	Relative phase between Fourier modes for general mode . . . . .	98
5.10	Complex local frequency vs. $x$ and $k$ (isolated) . . . . .	98
5.11	Fourier mode phase compared to the local prediction. . . . .	99
5.12	Global mode structure calculated using local results (isolated) . . . . .	100
5.13	Complex local frequency vs. $x$ and $k$ (general) . . . . .	101
5.14	Fourier mode phase compared to the local prediction. . . . .	102
5.15	Global mode structure calculated using local results (general) . . . . .	102
5.16	Time dependence of local growth rate due to sheared flow. . . . .	105
5.17	Global growth rate and width vs. shearing rate (isolated profiles) . . . . .	107
5.18	Global growth rate and width vs. shearing rate (general profiles) . . . . .	108
6.1	Visible images of ELMs . . . . .	115
6.2	Cartoon of peeling-ballooning based ELM cycle . . . . .	117
6.3	Cartoon of pedestal prediction using two constraints . . . . .	121
6.4	Comparison of EPED1 prediction and observation. . . . .	122
6.5	Composite inter-ELM density and temperature profiles. . . . .	126
6.6	Composite inter-ELM pressure profiles. . . . .	127
6.7	Ideal ballooning stability through ELM cycle . . . . .	128
6.8	Finite- $n$ stability vs. $\alpha_{\max}$ . . . . .	129
6.9	PB stability boundary as a function of time. . . . .	130
6.10	MHD stability constraints as a function of time. . . . .	131

---

6.11 MHD stability constraints as a function of pedestal width. . . . .	132
6.12 Profile of ion $\rho_*$ in edge region. . . . .	133
6.13 Parity factor in edge region . . . . .	135
6.14 Example twisting and tearing parity eigenfunctions. . . . .	136
6.15 Growth rate vs. $\beta$ for twisting and tearing parity instabilities. . . . .	137
6.16 Growth rate as a function of $k_y \rho_i$ and $\psi_N$ . . . . .	138
6.17 Growth rate as a function of $k_y \rho_i$ and $t$ . . . . .	139
6.18 Cartoon indicating surfaces of interest . . . . .	140
6.19 Length scale scans about surface $a$ . . . . .	141
6.20 Pressure length scale scan about surface $a$ . . . . .	142
6.21 Length scale scans about surface $b$ . . . . .	143
6.22 Normalised pressure scan about surface $b$ . . . . .	143
6.23 Normalised pressure scan about surface $c$ . . . . .	144



# List of Tables

2.1	Empirical engineering scaling law coefficients . . . . .	32
2.2	Empirical physical scaling law coefficients . . . . .	32
2.3	ITER & JET machine parameters . . . . .	36
4.1	Gyrokinetic code characteristics . . . . .	58
5.1	Gamma function values . . . . .	72
5.2	Tridiagonal matrix representation of the global dispersion relation . .	86
5.3	Standard profile parameters . . . . .	94



# Acknowledgments

I am extremely grateful for the role my supervisors, Dr. Colin Roach and Prof. Howard Wilson, have played during my PhD. They have both offered invaluable support and guidance throughout my research, for which I'm very thankful. Their insight and scientific rigour have provided inspiration and offers a great target to aspire to. I would specifically like to thank them for the comments and encouragement they provided whilst writing this thesis.

I have had numerous interesting and useful encounters with many members of the field, of which there are too many to thank individually. Discussions with fellow PhD students have proven especially rewarding, both academically and socially. In particular I'd like to thank P. Buxton, A. Lampson and S. Myers from York for helping me adjust to life as a PhD student. The many conversations with P. Hill during my time at CCFE on physics, coding and external interests have been invaluable in improving my knowledge and understanding on a wide range of topics. I'd also like to thank J.W. Connor, R.J. Hastie, K. Imada, A. Kirk, R. Lake, S. Saarelma, R. Scannell, G. Szepesi and J.B. Taylor for useful discussions.

This work was made possible through funding provided jointly by CCFE and EPSRC under Industrial Case Voucher 08001013. The computationally intensive gyrokinetic simulations were enabled through access to the HPC-FF supercomputer at Jülich, the U.K. HECToR supercomputer through EPSRC Grant No. EP/H002081/1 and the HELIOS supercomputer system under the Broader Approach collaboration between Euratom and Japan.

*Finally, I would like to thank Becky and my family for all their support and understanding during my studies. Without them this work would not have been possible.*



# Declaration

The work presented in this thesis was performed at the University of York and Culham Centre for Fusion Energy under the joint supervision of Prof. H. R. Wilson and Dr. C. M. Roach. I declare that this work is my own except where indicated by appropriate citation and with the exceptions given below.

Components of the results given in chapter 5 have been presented at numerous conferences and appear in the following conference proceedings:

1. D. Dickinson, C. Roach, and H. Wilson, in 38<sup>th</sup> EPS Conference on Plasma Physics, edited by A. Becoulet, T. Hoang, and U. Stroth (European Physical Society, Strasbourg, 2011). [1]
2. H. Wilson, D. Dickinson, and C. Roach, in 39<sup>th</sup> EPS Conference on Plasma Physics, edited by S. Ratynskaya, L. Blomberg, and A. Fasoli (European Physical Society, Stockholm, 2012). [2]

The original algorithms underlying the numerical code used in section 5.4 were provided by H. R. Wilson.

Several of the results presented in chapter 6 are the product of a joint research project, the results of which have been published in the following articles:

1. D. Dickinson, S. Saarelma, R. Scannell, A. Kirk, C. Roach, and H. Wilson, Plasma Physics and Controlled Fusion 53, 115010 (2011). [3]
2. D. Dickinson, C. Roach, S. Saarelma, R. Scannell, A. Kirk, and H. Wilson, Physical Review Letters 108, 135002 (2012). [4]

In particular the experimental observations from MAST presented in section 6.2.1 have been obtained by R. Scannell and A. Kirk and the MHD equilibrium and stability calculations given in section 6.2.2 have been performed by S. Saarelma.



# Chapter 1

## Supplying the world's energy demands

### 1.1 Global energy concerns

The world's population increased by approximately 28% between 1990 and 2009, equivalent to 1.5 billion people [5]. When coupled to the rising wealth and industrialisation of nations such as India, China and Brazil the increasing demand on the finite energy resources available to the planet is enhancing the importance of widely available, affordable energy. Figure 1.1 shows the annual total energy usage (in units of million tonnes of oil equivalent) from different sources during the period 1965 to 2010, with the contribution from different energy sources illustrated by the shaded regions [6].

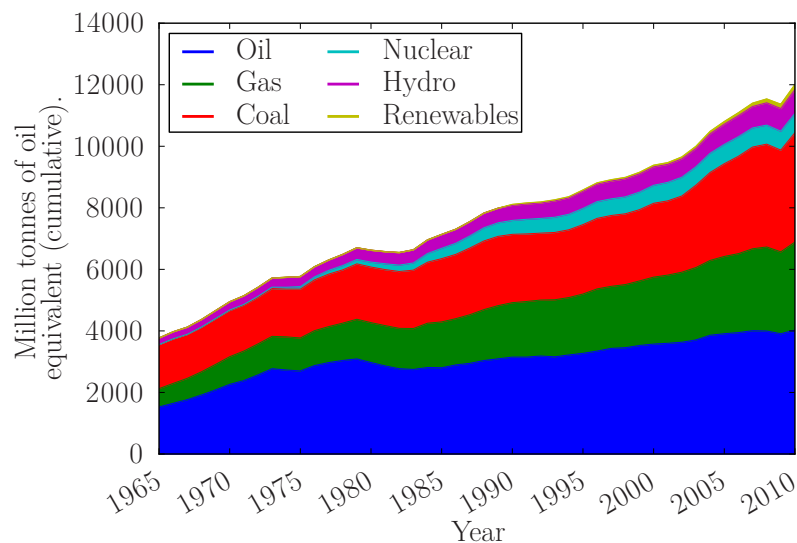


**Figure 1.1:** Annual total energy usage in the period between 1965 and 2010 measured in million tonnes of oil equivalent [6]. The contributions from different energy sources are shown by the shaded regions.

Over this period fossil fuels (oil, gas and coal) have dominated usage, and energy consumption has increased linearly such that net consumption has roughly tripled. Whilst consumption from alternative sources (nuclear, hydro and renewables) has increased over this period, the increased demand has been mostly met by higher fossil fuel usage. Recent estimates of oil, coal and gas depletion times (based on predicted fossil fuel demand, production and discovery obtained from British Petroleum and the U.S. Energy Information Administration) predict that oil supplies will be fully depleted by around 2043, coal will last until around 2115 and gas is somewhere in between [7]. This highlights the importance of the development and deployment of alternative energy sources and motivates research into enhancing existing technologies as well as developing new ones. Renewable sources such as wind, solar and tidal offer the potential for a plentiful supply of low carbon energy but can suffer from intermittent generation and geographical restrictions. Such sources have increased in popularity in recent years due in part to government subsidies, the increasing cost of fossil fuels and improvements in efficiency driven by research. Figure 1.2 shows the increase in U.K. renewable energy usage between 1990 and 2009 as a percentage of total energy consumption. This increase has been mostly due to increases in landfill gas and wind energy [8].

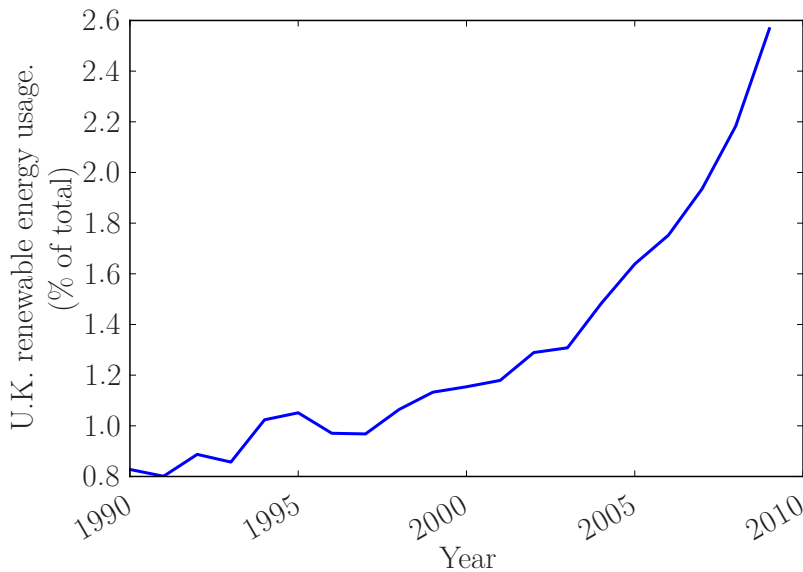


**Figure 1.2:** Renewable energy usage in the U.K. between 1990 and 2009 as a percentage of total energy consumption [9].

Despite the improving efficiency and reducing cost, renewable energy sources remain strongly dependent on local geographic conditions and hence are limited in scope. Research being carried out into advanced batteries, energy stores (such as generating hydrogen) and long-distance electricity transmission hope to address some of this limitation; ideally an alternative energy source which is globally abundant and transportable is desired. This can be filled in some part by nuclear fission reactors, where although the fuel can have high transportation and production costs and the

known reserves are thought to be sufficient for only a few hundred years<sup>1</sup> [10], the low carbon and high energy density characteristics of fission energy make it an important consideration. With advanced fast fission and breeder reactors, fuel efficiency increases significantly (by approximately 1-2 orders of magnitude) and existing fuel reserves can offer around 30,000 years of energy based on current usage trends [11]. The problems of long term spent fuel usage, though reduced by the introduction of advanced reactors, along with the negative public opinion associated with fission energy have limited its expansion. As fossil fuels become more expensive fission is likely to play an increasing role in meeting energy demands despite current views.

## 1.2 Nuclear fusion as an energy source

It is clear that no current technology offers the sole route to global energy security for extended periods of time; a complimentary approach is required where a range of sources are used as available. This still leads to issues whereby renewable sources may not be practical or efficient for a particular region and access to fission fuels is restricted due to safety, security and storage concerns. An alternative clean fuel based energy source which does not have the safety and security risks associated with fission is highly desirable. Fusion is an alternative nuclear process to fission which releases some of the binding energy stored in nuclei. In fission this energy is released when heavy nuclei are split whereas in fusion this energy comes when joining light nuclei. The average binding energy per nucleon is shown as a function of the number of nucleons in the nucleus for the most common isotopes in figure 1.3. It is important to note that due to convention an increase in the binding energy per nucleon corresponds to lower stored energy in the nucleus and hence any nuclear reaction which acts to increase the total binding energy is exothermic. Changing the number of nucleons in a nucleus can alter the average binding energy, reducing the system to a lower energy state. For heavy nuclei this can be achieved when a large nucleus becomes deformed, due to neutron capture for example, weakening the net effect of the strong nuclear force and hence allowing a group of nucleons to escape, thereby splitting the original nucleus. If two light nuclei become close enough to interact via the strong force they may fuse together resulting in a heavier nucleus, releasing energy in the process.

Whilst fission occurs naturally on earth, fusion is rare. This is due to the Coulomb repulsion between nuclei which acts as a barrier to spontaneous fusion; the nuclei must have enough energy to approach sufficiently close for the strong force to take effect. For this reason fusion is easiest to achieve between isotopes of hydrogen. This

---

<sup>1</sup>It is important to note that estimates of the lifetime of known reserves depend strongly on the specific assumptions made such as the likely impact of new extraction technologies for example.

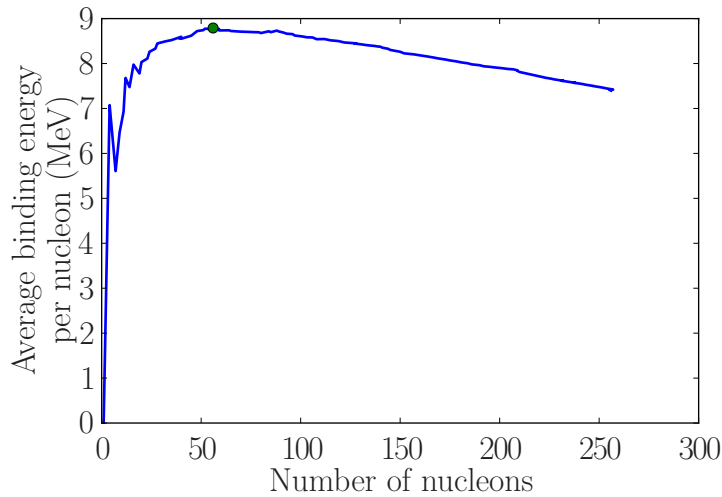
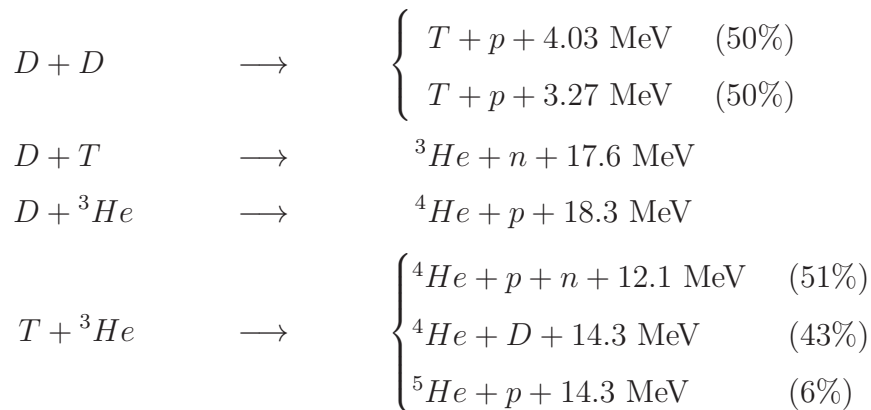


**Figure 1.3:** The average binding energy per nucleon (MeV) against number of nucleons in nucleus for the most abundant isotopes. The most stable nucleus, iron, is shown by the green point.

barrier can be estimated by calculating the potential energy stored in the electric field when two protons are brought close enough for the strong force to take over. Taking this distance as the classical radius of hydrogen,  $r_0 = 1.2$  fm, then using

$$U = \frac{qQ}{4\pi\epsilon_0 r} \quad (1.1)$$

with  $q = Q = e$ , the potential energy can be estimated to be around 0.6 MeV. For singly charged nuclei with energy of 0.3 MeV fusion can occur spontaneously. Such energies are easily obtainable using small particle accelerators (and have been since the early 1930s) allowing individual fusion events to be initiated in the lab. To obtain a reasonable reaction rate however, it is necessary to have a large number of fuel nuclei with this energy. An energy of 0.3 MeV corresponds to a temperature of around  $3 \times 10^9$  K. After taking into account quantum tunnelling through the Coulomb barrier, it can be shown that fuel held at  $\sim 10^8$  K gives a reasonable fusion reaction rate. Several fusion reactions which can be considered are given below (if multiple outcomes exist the probability of each branch is shown in brackets) [12].



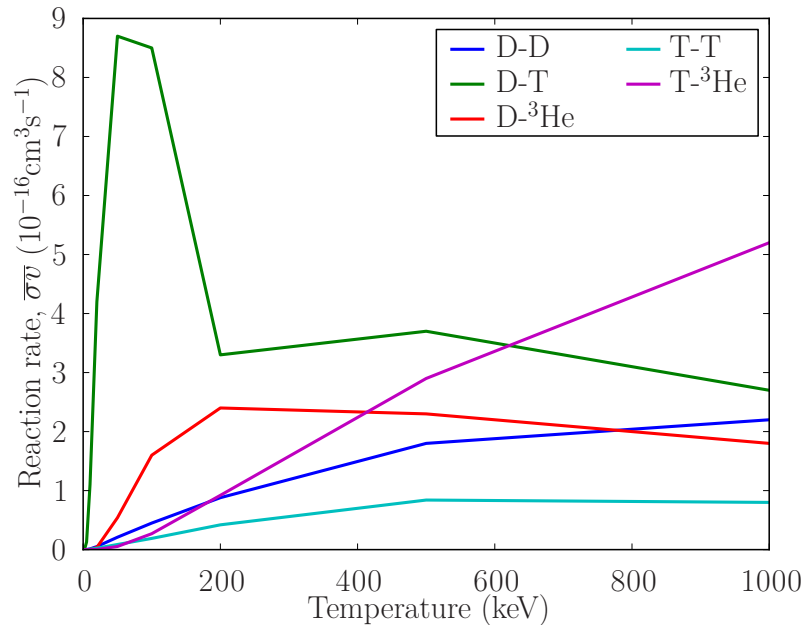
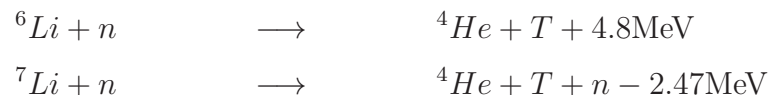


**Figure 1.4:** The reaction rate averaged over a Maxwellian energy distribution,  $\bar{\sigma v}$ , as a function of temperature for a range of possible fusion reactions involving deuterium, tritium and helium-3. Data obtained from [12].

Figure 1.4 shows the reaction rates averaged over a Maxwellian velocity distribution,  $\bar{\sigma v}$ , as a function of temperature for these fusion reactions [12]. It can be seen that the deuterium-tritium, (D-T), reaction has the highest reaction rate in the temperature range considered and also that this peak occurs at a relatively low temperature ( $\sim 100$  keV). This reaction also releases the second largest amount of energy (17.6 MeV) of the reactions considered. These two properties make this reaction appealing for commercial energy production as for a given reaction rate the output power will be maximised. One potential set back is that the high energy neutrons ( $\sim 14.1$  MeV) can lead to the activation of materials near the reacting fuel and indeed some research has been made into alternative aneutronic fusion reactions [13, 14]. Such approaches are currently not being pursued on a large scale due in part to the requirement for much larger heating and the rarity of the required fuels (e.g.  $^3\text{He}$ ). In contrast deuterium, a stable isotope of hydrogen, is in plentiful supply on earth with around 1 deuterium atom for every 6500 hydrogen atoms in Vienna standard mean ocean water [15]. Tritium is unstable and decays with a half life of around 12.3 years [16] so is not readily available in nature; Tritium is produced as a by-product in CANDU fission reactors, though at a low rate [17]. It can however, also be produced through neutron activation of lithium in the following reactions:



As the D-T fusion reaction produces energetic neutrons it is feasible to use these to

produce tritium from lithium, allowing a continual replenishment of tritium. Lithium is relatively abundant with 60 parts per million (ppm) by weight in the earth's crust and 0.17 ppm in sea water [18]. Estimates for the amount of economically available  ${}^6\text{Li}$  predict enough to provide energy for the order of 20,000 years at current energy consumption levels [10]. In this time period it can be anticipated that with increased experience and research, alternative fusion reactions may become viable; in particular if D-D is achievable the worlds oceans contain enough deuterium for around  $10^9$  years of energy at current consumption rates [10].

### 1.2.1 Heating requirements and energy gain

At temperatures of relevance for fusion, D and T will be fully ionised<sup>2</sup> forming a plasma. The D-T reaction generates 17.6 MeV which is shared between the  ${}^4\text{He}$ , or  $\alpha$  particle, (3.5 MeV) and neutron (14.1 MeV) produced in the reaction. Whilst the uncharged neutrons will not strongly interact with the plasma, the charged  $\alpha$  particle will give up some of its energy to the fuel ions. This provides a heating power per unit volume,  $P_\alpha$ , which depends on the fuel density and reaction rates, defined as

$$P_\alpha = \frac{n^2}{4} \bar{\sigma} v E_\alpha \quad (1.2)$$

where  $E_\alpha$  is the energy of the  $\alpha$  particle and  $n$  is the fuel number density. To maintain the fuel's stored energy the total heating power must balance any losses. The loss power is simply defined as the ratio of the stored energy per unit volume,  $W = 3nT$ , to some characteristic energy confinement time,  $\tau_E$ . This leads to an expression for power balance:

$$P_H + \frac{n^2}{4} \bar{\sigma} v E_\alpha = \frac{3nT}{\tau_E} \quad (1.3)$$

where  $P_H$  is the externally supplied heating power per unit volume. For suitable conditions it is possible to reduce the external heating power to 0 whilst maintaining power balance, a state known as ignition. A simple condition for reaching ignition can be derived from eqn. 1.3:

$$n\tau_E \geq \frac{12}{E_\alpha} \frac{T}{\bar{\sigma} v} \quad (1.4)$$

The reaction rate is solely a function of  $T$  and in the region of interest is reasonably approximated by  $\bar{\sigma} v = 1.1 \times 10^{-24} T^2 \text{ m}^{-3} \text{ keVs}$  (with  $T$  in keV). Substituting this into eqn. 1.4 and rearranging leads to a condition on the triple product  $nT\tau_E$ :

$$nT\tau_E \gtrsim 3 \times 10^{21} \text{ keVsm}^{-3} \quad (1.5)$$

---

<sup>2</sup>The ionisation energy of D and T is similar to that of H (13.6 eV). This is well below the thermal energy which is of the order of keV.

This is similar to the criterion developed by Lawson [19] though in that case the direct  $\alpha$  heating was neglected. Instead a reactor efficiency factor was introduced for producing the external heating from the generated fusion energy<sup>3</sup>. A figure of merit,  $Q$ , for the approach to ignition is often referenced and is simply defined as  $Q = P_{fus}/P_H$ , where  $P_{fus}$  is the fusion power.  $Q = 1$  is known as break-even, where the total fusion power matches the applied heating power, whilst ignition corresponds to  $Q = \infty$ .

Most research into fusion as an energy source is focused on controlling the parameters  $n$ ,  $T$  and  $\tau_E$ . At such high temperatures a major concern is how to confine a sufficiently dense and hot fuel for long enough, and many different confinement options have been considered. Most approaches can be split into two main groups; inertial or magnetic confinement. In inertial confinement the fuel is compressed and heated rapidly in an intense burst: the confinement time is low, but density and temperature are high. Magnetic confinement is a steadier approach where  $\tau_E$  is much larger and exploits the fact that at the temperatures of relevance for fusion the fuel will be fully ionised to control the resulting plasma with EM fields. The approach studied in this thesis is that of magnetic confinement.

### 1.3 Magnetic confinement fusion

The ionised fuel, or plasma<sup>4</sup>, consists of a large number of charged particles which must obey the Lorentz force law:

$$m\dot{\underline{v}} = \underline{F} = q(\underline{E} + \underline{v} \times \underline{B}) \quad (1.6)$$

where  $m$  and  $q$  are the particle's mass and charge,  $\underline{B}$  is the magnetic field,  $\underline{E}$  is the electric field and dot notation is used to denote time derivatives. Considering the case with  $\underline{E} = 0$  and  $\underline{B} = B\hat{e}_z$ , the three components of eqn. 1.6 are

$$\dot{v}_x = \omega_c v_y \quad (1.7a)$$

$$\dot{v}_y = -\omega_c v_x \quad (1.7b)$$

$$\dot{v}_z = 0 \quad (1.7c)$$

where  $\omega_c = qB/m$  is known as the gyrofrequency<sup>5</sup>. The equations in eqn. 1.7a-eqn. 1.7c describe circular motion in the  $x$ - $y$  plane about a central point known

<sup>3</sup>This efficiency was taken to be 30%, which is comparable with the 20% of fusion energy used directly through  $\alpha$  heating.

<sup>4</sup>The precise definition of a plasma is in fact stricter than simply a collection of ionised particles see for example Ref [20].

<sup>5</sup>Alternatively known as the cyclotron frequency.

as the gyrocentre, with angular frequency  $\omega_c$ . Such an effect on the perpendicular motion essentially confines the particle in two dimensions; this forms the basis of all magnetic confinement schemes. The radius of the particle's orbit,  $\rho_L$  is known as either the Larmor radius or gyroradius, and is

$$\rho_L = \frac{mv_{\perp}}{qB} = \frac{v_{\perp}}{\omega_c} \quad (1.8)$$

where  $v_{\perp}$  is the particle's perpendicular velocity. In this example the motion parallel to the field line is unaffected by the magnetic field.

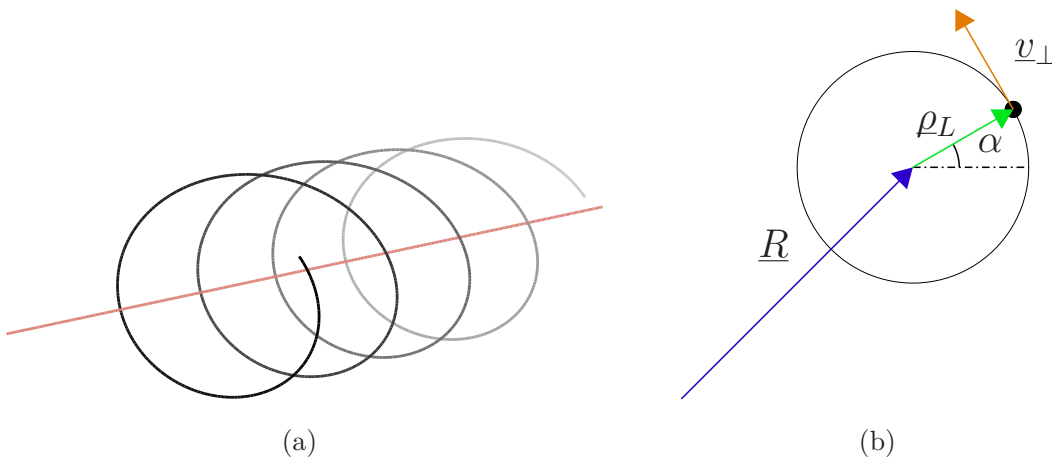


**Figure 1.5:** The motion of a charged particle in the presence of a magnetic field determined from the Lorentz force law eqn. 1.6. Figure 1.5(a) shows the motion of a charged particle (black line) in the presence of a magnetic field line (red line). The position of a charged particle can be described in terms of the position of the “guiding centre”,  $\underline{R}$ , and the directed Larmor radius  $\rho_L$  as shown in figure 1.5(b). The position of the particle around the gyroorbit can also be described by the gyrophase angle,  $\alpha$ .

### 1.3.1 Conserved quantities

According to Noether's theorem [21] physical systems<sup>6</sup> with symmetries leading to periodic motion will contain conserved quantities. Taking the dot product of eqn. 1.6 with  $\underline{v}$  for the case with  $\underline{E} = 0$  and using Newton's 2nd law one finds that  $m\underline{v}^2/2 \equiv \varepsilon$  is a conserved quantity<sup>7</sup>:

$$\underline{v} \cdot \underline{F} = m\underline{v} \cdot \dot{\underline{v}} = q\underline{v} \cdot (\underline{v} \times \underline{B}) \equiv 0 \quad (1.9)$$

<sup>6</sup>The theorem is only strictly applicable to certain systems (those described by a Lagrangian or Hamiltonian).

<sup>7</sup>If the electric field is retained then using  $\underline{E} = -\nabla\phi$  and  $\underline{v} \cdot \nabla = d/dt$  it is easy to show that it is the total particle energy,  $mv^2/2 + q\phi$ , which is conserved.

The gyromotion of a particle with charge,  $q$ , in a magnetic field leads to a ring current,  $I$ :

$$I = \frac{qv_{\perp}}{2\pi\rho_L} \quad (1.10)$$

The magnetic moment of such a current loop is given by  $\mu = I\underline{S}$ , where  $\underline{S}$  is the vector area. As such the magnetic moment of a charged particle in a magnetic field is given by

$$\underline{\mu} = -\frac{mv_{\perp}^2}{2B}\underline{b} \quad (1.11)$$

with  $\underline{b} = \underline{B}/B$ .

Taking the dot product of eqn. 1.6 with  $\underline{v}_{\perp}$  gives

$$m\frac{dv_{\perp}^2}{dt} = q\underline{v}_{\perp} \cdot \underline{E} = q\underline{E} \cdot \frac{d\underline{l}}{dt} \quad (1.12)$$

where  $\underline{l}$  is the position around the gyroorbit,  $\underline{l} = \rho_L(\hat{\underline{e}}_x \cos \alpha + \hat{\underline{e}}_y \sin \alpha)$ , with  $\alpha$  known as the gyrophase and  $\underline{E}$  is the electric field induced by variations in the magnetic field as the particle gyrates. Integrating eqn. 1.12 over one gyroperiod (i.e. from  $t = 0 \rightarrow 2\pi/\omega_c$ ) gives the change in the perpendicular kinetic energy,  $\Delta\varepsilon_{\perp}$ :

$$\Delta\varepsilon_{\perp} = q \int \underline{E} \cdot d\underline{l} \quad (1.13)$$

Treating  $\underline{E}$  to be slowly varying (spatially and temporally) the integral in eqn. 1.13 can be treated as closed and as such can be rewritten using Stokes' theorem and the Maxwell-Faraday relation to give

$$\Delta\varepsilon_{\perp} \approx q \oint_C \underline{E} \cdot d\underline{l} = q \oint_S \nabla \times \underline{E} \cdot d\underline{S} = -q \oint_S \dot{\underline{B}} \cdot d\underline{S} \quad (1.14)$$

Taking  $\dot{\underline{B}} = \Delta B \omega_c / 2\pi$ , with  $\Delta B$  the change in  $B$  in one gyroperiod, to be constant over the surface of integration (which will be increasingly valid for small  $\rho_L$ ), eqn. 1.14 leads to

$$\Delta\varepsilon_{\perp} = \mu \Delta B \quad (1.15)$$

As  $\varepsilon_{\perp} = \mu B$  the LHS of eqn. 1.15 can be expanded as  $\Delta\varepsilon_{\perp} = \mu \Delta B + B \Delta \mu$  and hence  $\Delta \mu = 0$ , implying  $\mu$  is conserved. It is important to note that this result only holds for fields which do not vary at all on gyromotion scales. In practice this means that the expression for  $\mu$  used here is only conserved to the lowest order in  $\rho_L/L$ , where  $L$  is the spatial scale of field variations<sup>8</sup>. It is possible to construct a magnetic moment which is conserved to higher orders, see for example Ref [22].

---

<sup>8</sup>Temporal variations are also important and as such  $\mu$  is also only conserved to order  $\omega/\omega_c$ , where  $\omega$  is the characteristic frequency of field variations.

### 1.3.2 Magnetic mirror confinement

As a consequence of the conservation of  $\mu$  it is clear that as the magnetic field strength increases the particle's perpendicular velocity must also increase. The conservation of energy then implies that the parallel velocity must decrease. For a sufficiently large increase in field the parallel velocity is reduced to zero.

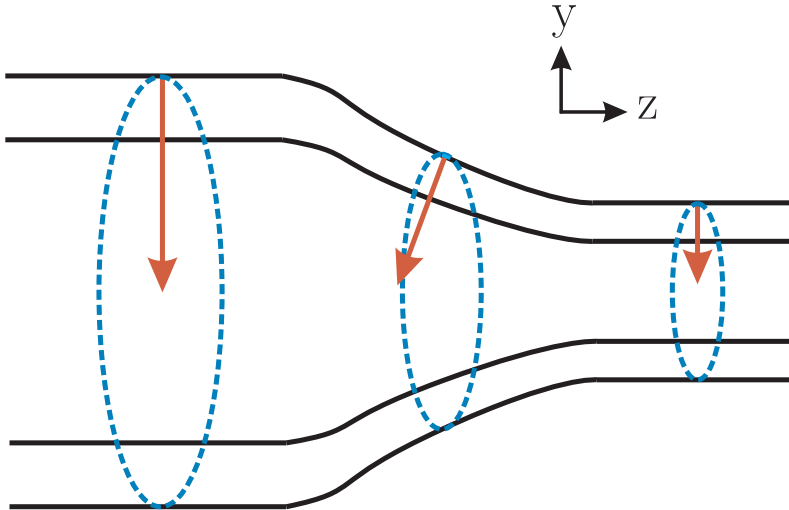


**Figure 1.6:** The direction of the Lorentz force (red arrows) at different positions in a spatially varying magnetic field (black lines). It can be shown that the flux through the surface defined by the particle's gyromotion (blue lines) is conserved as a consequence of the conservation of  $\mu$ .

Figure 1.6 shows the Lorentz force on a charged particle moving in a spatially varying magnetic field. A magnetic field predominantly in the  $\hat{e}_z$  direction with a strength dependent on  $z$ , must in fact also have a component perpendicular to  $\hat{e}_z$  in order to satisfy  $\nabla \cdot \underline{B} = 0$ . As the Lorentz force is directed perpendicular to the magnetic field this implies that in the region of increasing field strength the Lorentz force has a component in the  $-ve z$  direction. A particle with a low initial parallel velocity can be reflected by this force. Particles with higher initial parallel velocity may traverse the region of increasing field strength, though will be decelerated in the parallel direction. This physics is the basis for a simple magnetic confinement scheme known as the magnetic mirror. Such a scheme incorporates a magnetic field which has a minimum in its strength. Consider two Helmholtz coils separated by some distance along a common axis, such that the magnetic field strength along this axis has a minimum between the coils as shown in figure 1.7. Charged particles in this central region can be trapped due to the reflective effect of each of these coils restricting motion along the common axis.

The quantity,  $\lambda_t$ , gives the ratio of the parallel and perpendicular velocity components for the particle at the position of the minimum field strength,  $B_{min}$ . It is defined as  $\lambda_t = \cot(\theta)$  where  $\theta$  is the angle between  $\underline{v}$  and  $\underline{B}$ , known as the pitch angle, lead-

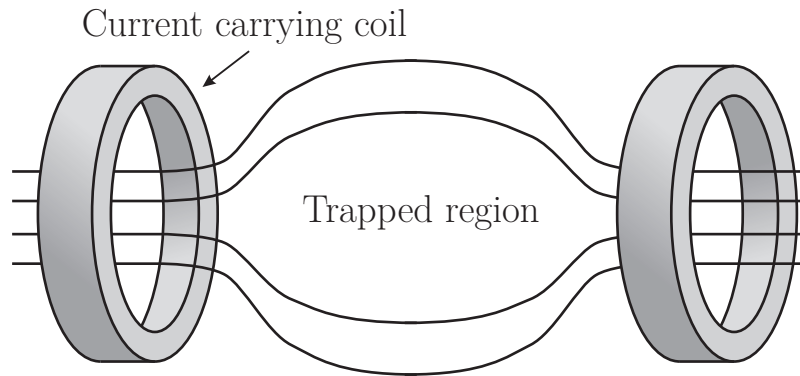


**Figure 1.7:** A simple cartoon of a magnetic mirror confinement device. Current is sent through two coils to generate a magnetic field. The strength is largest in the centre of each coil resulting in a well in between the coils where particles can be trapped.

ing to  $\lambda_t$  being labelled the pitch angle variable. Using the conserved quantities,  $\varepsilon$  and  $\mu$ , it is simple to derive the condition for particles to be trapped. Particles with  $\lambda_t$  satisfying

$$\lambda_t = \frac{v_{\parallel 0}}{v_{\perp 0}} \leq \sqrt{\frac{B_{max}}{B_{min}} - 1} \quad (1.16)$$

will be trapped, all other particles can be considered untrapped and will immediately leave the device. This leads to the idea of a loss cone in velocity space illustrated in figure 1.8, whereby particles which enter the loss region will be immediately lost from the device.

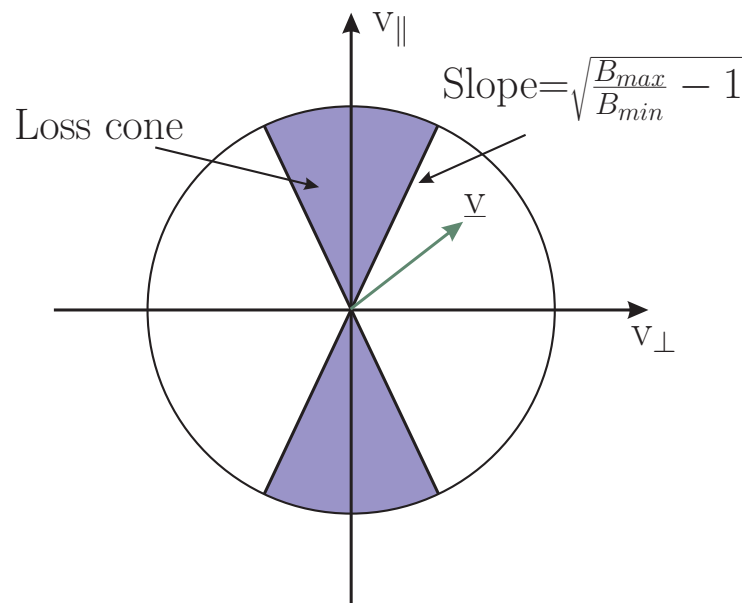


**Figure 1.8:** Diagram showing the trapped and untrapped regions of velocity space with the boundary set by the lines with gradient  $\pm\sqrt{\frac{B_{max}}{B_{min}} - 1}$ . Particles in the shaded region, known as the loss cone, are not trapped and will be lost from the magnetic mirror machine.

Collisions between the trapped particles will scatter particles in velocity space such that the distribution relaxes to a Maxwellian. As such trapped particles will be

scattered into the loss cone and will then be lost<sup>9</sup>. The result is that all particles will eventually be lost from any magnetic mirror device provided the loss cone has non-zero area (i.e.  $B_{max} \neq \infty$ ). This proves to be a challenge for the use of magnetic mirror devices as a confinement system for use in a fusion reactor. The focus has generally moved away from mirror confinement with developments in alternative magnetic confinement schemes, the most popular of which will now be discussed.

### 1.3.3 Tokamaks

Whilst charged particles in a magnetic field are confined in the two directions perpendicular to the field line they are free to move in the parallel direction. Magnetic mirror devices attempt to restrict this motion using a field with a strength that varies along the field line. An alternative magnetic confinement system attempts to overcome the “end-losses” of traditional mirror machines by using closed field lines such that whilst the particles are free to move along the field line they cannot leave a finite volume. This basic design principle led to the development of the main magnetic confinement device used currently, known as the tokamak. Starting from a simple toroidal magnetic field such as that produced by the current in an infinite straight conductor, as shown in figure 1.9, the essential ingredients for magnetic confinement of a tokamak plasma will now be discussed.

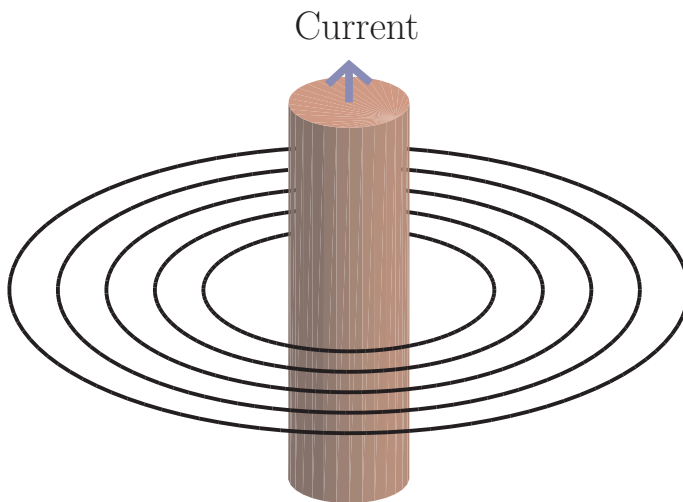


**Figure 1.9:** Diagram showing the toroidal magnetic field (black) produced by a straight current (blue). The field strength drops off as  $B \sim 1/R$ , resulting in a radially directed gradient.

<sup>9</sup>In fact  $\mu$  is not exactly conserved for  $\rho_L \neq 0$ , and particles can enter the loss cone without the need for collisions.

### 1.3.3.1 Particle drifts

Now that the magnetic field is curved additional factors become important in determining the particle's true motion and it will no longer be given solely by simple gyromotion as shown in figure 1.5. The simple circular magnetic field illustrated in figure 1.9 for example will necessarily have a gradient in field strength directed towards the centre of the circle. Treating the particle as a magnetic dipole, there is an additional force due to the interaction with the magnetic moment and the field of the form  $\underline{F} = -\nabla(\underline{\mu} \cdot \underline{B})$ . Furthermore as  $\underline{B}$  is curved the frame following the particle motion along  $\underline{B}$  is not an inertial frame, and thus in this frame the particle experiences a centrifugal force. This force is given by  $-mv_{\parallel}^2 \underline{R}_c / R_c^2 = -mv_{\parallel}^2 (\underline{b} \cdot \nabla) \underline{b}$ , where  $\underline{R}_c$  is the radius of curvature. The resulting force equation including these two geometrical terms is then

$$m\dot{\underline{v}} = q\underline{E} + q(\underline{v} \times \underline{B}) - \nabla(\underline{\mu} \cdot \underline{B}) - mv_{\parallel}^2 \underline{b} \cdot \nabla \underline{b} \quad (1.17)$$

Assuming static fields and using the conservation of  $\mu$  the time derivative of eqn. 1.17 is

$$\frac{d^2 \underline{v}}{dt^2} = \left[ \frac{q^2}{m^2} (\underline{v} \times \underline{B}) + \frac{q^2}{m^2} \underline{E} - \frac{q\mu}{m^2} \nabla B - \frac{qv_{\parallel}^2}{m} \underline{b} \cdot \nabla \underline{b} \right] \times \underline{B} \quad (1.18)$$

The 1<sup>st</sup> term on the RHS of eqn. 1.18 simply gives the gyromotion as in the case with a homogeneous magnetic field. Taking the perpendicular component of eqn. 1.18 yields

$$\frac{d^2 \underline{v}_{\perp}}{dt^2} = -\omega_c^2 \left( \underline{v}_{\perp} - \frac{\underline{E} \times \underline{B}}{B^2} + \frac{\mu}{qB^2} \nabla B \times \underline{B} + \frac{mv_{\parallel}^2}{qB} [(\underline{b} \cdot \nabla) \underline{b}] \times \underline{b} \right) \quad (1.19)$$

Noting that the 2<sup>nd</sup>, 3<sup>rd</sup> and 4<sup>th</sup> terms on the RHS of eqn. 1.19 are independent of time (under the static field assumption and noting that  $|v_{\perp}|$  and  $v_{\parallel}$  are independent of time) it is convenient to make the substitution  $\underline{v}_{\perp} = \underline{v}_g + \underline{c}$  where  $\underline{c} = \underline{v}_{E \times B} + \underline{v}_{\nabla B} + \underline{v}_{curv}$  represents the three constant terms, with  $\underline{v}_{E \times B}$ ,  $\underline{v}_{\nabla B}$  and  $\underline{v}_{curv}$  defined by

$$\underline{v}_{E \times B} = \frac{\underline{E} \times \underline{b}}{B} \quad (1.20)$$

$$\underline{v}_{\nabla B} = \frac{\mu}{\omega_c m} \underline{b} \times \nabla B \quad (1.21)$$

$$\underline{v}_{curv} = \frac{v_{\parallel}^2}{\omega_c} \underline{b} \times [(\underline{b} \cdot \nabla) \underline{b}] = \frac{v_{\parallel}^2}{\omega_c} \underline{b} \times \nabla b \quad (1.22)$$

Under this substitution eqn. 1.19 reduces to

$$\ddot{\underline{v}}_g = -\omega_c^2 \underline{v}_g \quad (1.23)$$

which has the solution

$$\underline{v}_\perp = \underline{v}_g \exp(i\omega_c t) + \underline{v}_{E \times B} + \underline{v}_{\nabla B} + \underline{v}_{curv} \quad (1.24)$$

The 1<sup>st</sup> term on the RHS of eqn. 1.24 simply gives the gyromotion around the field line whereas the 2<sup>nd</sup>, 3<sup>rd</sup> and 4<sup>th</sup> terms give the drift of the gyrocentre relative to the field line.

### 1.3.3.2 The need for a poloidal magnetic field

The drift velocities due to the magnetic geometry,  $\underline{v}_{\nabla B}$  and  $\underline{v}_{curv}$ , for the simple toroidal field case shown in figure 1.9 are in the vertical direction as both  $\nabla B$  and  $R_c$  are in the radial direction. The sign depends upon the charge of the particle involved and hence electrons and ions drift in opposite directions. This generates a vertical electric field which then results in a non-zero  $\underline{v}_{E \times B}$  in the radial direction. Whilst the geometrical drifts give a vertical motion, the resulting charge separation driven drift is in the radial direction, as illustrated in figure 1.10. This radial drift is charge independent and will cause all confined particles to leave the confinement device for any finite sized machine.

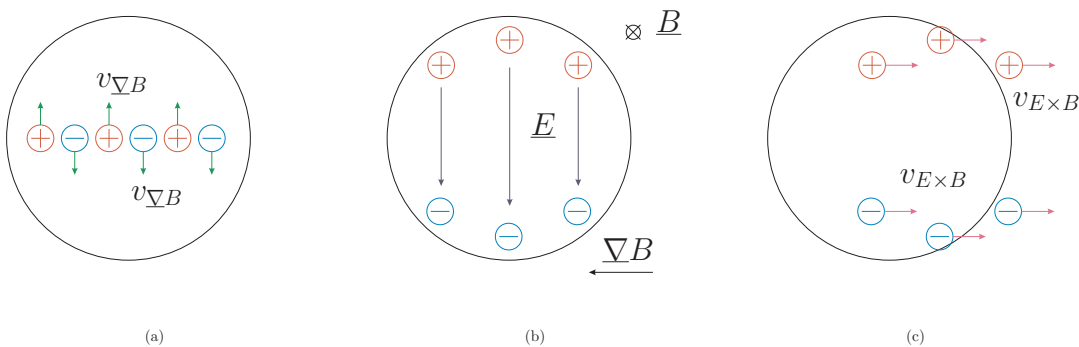


**Figure 1.10:** Step by step illustration of losses due to the  $\nabla B$  (or equivalently curvature) drift. The  $\nabla B$  drift causes particles of opposite charge to drift in opposite directions as in figure 1.10(a). This leads to an electric field as given in figure 1.10(b), resulting in a radial drift shown in figure 1.10(c).

To overcome this problem a technique to cancel out this vertical drift is required. In practice this can be achieved by incorporating an additional magnetic field which acts to move particles from one vertical limit to the other. Such a magnetic field is shown in figure 1.11 and is in the poloidal direction.

The combination of toroidal and poloidal magnetic fields results in a helical field which connects the upper and lower regions. As the charged particles are free to flow parallel to the field line this connection essentially short circuits the upper and lower regions, preventing an electric field building up and hence avoiding the associated

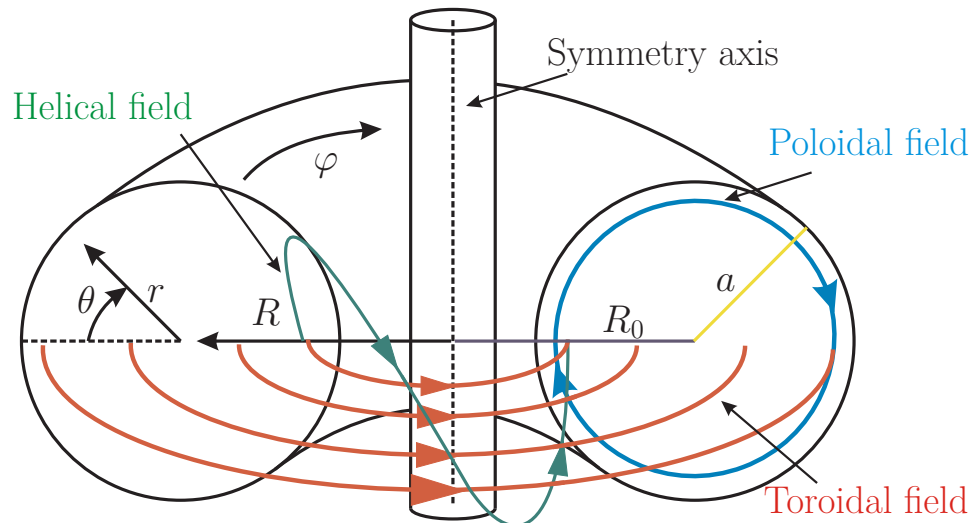


**Figure 1.11:** Poloidal (blue) and toroidal (red) magnetic fields. The resultant helical (green) field allows particles which have drifted to one vertical limit to move to the other through their parallel motion, thereby cancelling out the electric field and removing the radial  $\underline{E} \times \underline{B}$  drift. The minor and major radii,  $a$  and  $R_0$ , are shown in yellow and purple respectively.

radial  $\underline{E} \times \underline{B}$  drift. In tokamaks this poloidal field is generated by currents flowing within the plasma in the toroidal direction<sup>10</sup>. These currents are driven by an induced toroidal voltage produced by changing the current through a solenoid aligned with the symmetry axis at the centre of the torus. The available solenoid current and flux swing limits the duration over which the poloidal field can be sustained and hence the duration of confinement. Advanced tokamak designs often incorporate a large fraction of self-generated currents and alternative current drives which can provide sufficient poloidal field without relying on external induction and indeed such current sources are crucial in conceptual designs for future steady state reactors [23]. A simple schematic of a tokamak is shown in figure 1.12 which illustrates the various fields and their sources.

The pitch of the helical magnetic field depends upon the relative strength of the poloidal and toroidal magnetic fields,  $B_\theta$  and  $B_\phi$ . Typically in standard tokamaks  $B_\phi$  is much larger than  $B_\theta$  (by around an order of magnitude [25]) although in a class of tokamak designs known as spherical tokamaks (STs),  $B_\theta$  and  $B_\phi$  are comparable. It is useful to define the inverse aspect ratio  $\epsilon = a/R_0$ , where  $a$  is the distance from the centre of the plasma to the edge and  $R_0$  is the distance from the symmetry axis to the centre of the plasma, known as the magnetic axis, as illustrated in figure 1.11. STs have  $\epsilon \sim 1$  whereas in “standard” tokamaks  $\epsilon < 1$  (typically referred to as large aspect ratio devices). A parameter known as the safety factor, denoted  $q$ , gives a

<sup>10</sup>An alternative toroidal MCF scheme known as a stellarator uses precisely shaped magnetic coils to create the helical field directly, but these will not be discussed here.

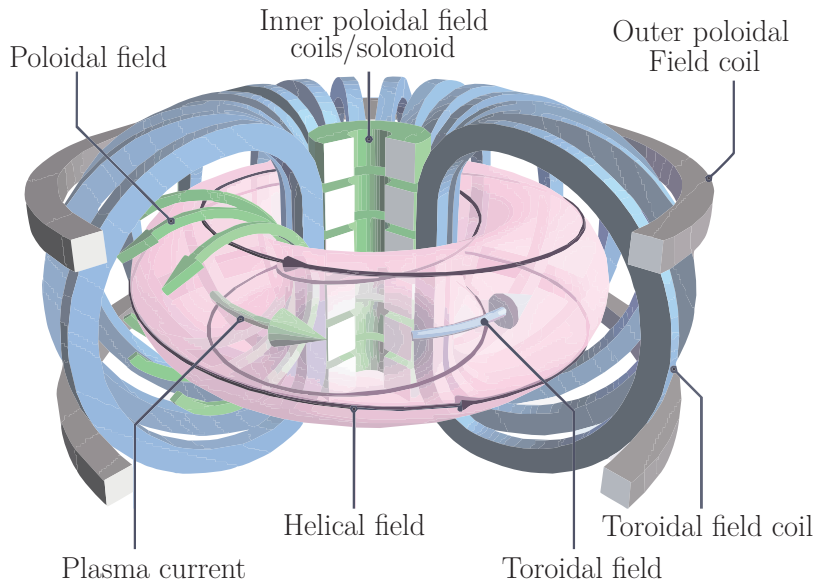


**Figure 1.12:** A simple tokamak layout including a central solenoid to drive toroidal current giving a poloidal field and current carrying coils used to produce the toroidal field. Reproduced with permission from Ref [24]

measure of the twist or pitch of the field line and is defined:

$$q(r) = \frac{1}{2\pi} \oint \frac{r}{R} \frac{B_\varphi}{B_\theta} d\theta \quad (1.25)$$

with the minor radius  $r$  and major radius  $R$  as defined in figure 1.11. The safety factor can be thought of as the number of toroidal traversals along the field line required to travel  $2\pi$  in  $\theta$ . Considering the magnetic field coils to be toroidally symmetric<sup>11</sup> it is clear that a field line starting at a specified location in the poloidal cross section,  $r$ - $\theta$ , will have the same value of  $q$  no matter the initial toroidal angle and hence these field lines define surfaces of constant  $q$ . Due to the typical magnetic field structure in a tokamak the toroidally symmetric surfaces of constant  $q$  are nested and centred on the magnetic axis, as shown in figure 1.13. Special surfaces exist, known as rational surfaces, where after an integer number of toroidal rotations,  $m$ , the field line joins with itself having undergone an integer number of poloidal rotations,  $n$ <sup>12</sup>.

These surfaces in which the field lines lie can be labelled by a quantity  $\psi$  where  $\underline{B} \cdot \underline{\nabla} \psi = 0$  such that  $\psi$  is constant on a given surface. A common label is the poloidal

<sup>11</sup>This is commonly referred to as axisymmetry. In practice the finite number of magnetic coils used to produce the field leads to some degree of asymmetry.

<sup>12</sup>Elsewhere the flux surfaces are referred to as irrational and here one may consider a single field line to cover the entire surface. Clearly there are an infinite number of potential rational surfaces however the term rational surface typically refers to low order rational numbers. A rough cut-off criteria could be that if the length of the field line before it joins back onto itself is larger than the parallel coherence length then the surface is considered irrational.

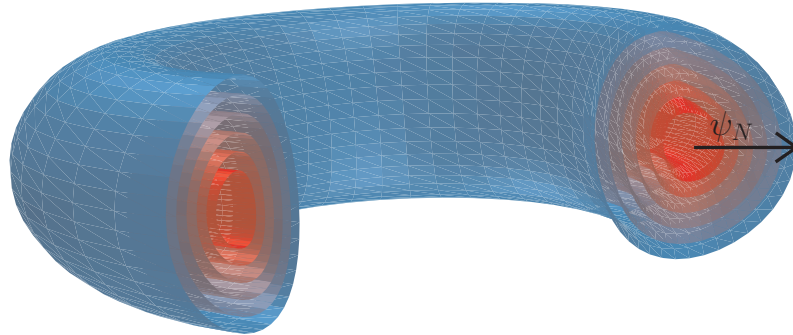


**Figure 1.13:** Illustration of the nested flux surface structure found in tokamaks. They can be labelled by the normalised flux,  $\psi_N$ .

flux,  $\psi$ , which can be calculated by integrating  $B_\theta$  over one of these surfaces:

$$\psi = \int_S B_\theta dS \quad (1.26)$$

As such these nested surfaces are referred to as flux surfaces<sup>13</sup>.

Particles are relatively free to flow rapidly along field lines and as such any local density or temperature perturbation can be rapidly equilibrated. This leads to the idea that certain parameters will remain roughly constant along a field line. Such quantities are often referred to as flux functions as they are expected to be (roughly) constant over the whole flux surface in which the field line lies. Various other processes can prevent such quantities being true flux functions<sup>14</sup> but it is often a useful 0<sup>th</sup> order approximation. For a typical current generation tokamak the Larmor radius for protons can be of the order of 5 mm, which is much smaller than the minor radius of the plasma,  $a \sim 1$  m. As such it is reasonable to consider the particles to lie on the flux surface to the lowest order. In practice, however, various physical processes can lead to significant excursions from the flux surface, which can significantly degrade the confinement efficiency. This confinement efficiency is of key importance to the viability and success of commercial fusion reactors, as discussed previously. The progress made in the study of magnetic confinement fusion can be characterised somewhat by the improvement in the triple product achieved over the years. The diagram in figure 1.14, reproduced from Ref [26], illustrates the vast advances made towards reactor relevant conditions, due in large part to the efforts devoted to the

<sup>13</sup>The flux is often normalised to the value on the last closed flux surface (LCFS),  $\psi_N = \psi/\psi_{LCFS}$ .

<sup>14</sup>One example is that a strong toroidal rotation of the plasma can lead to a higher density on the side of the flux surface at largest major radius.



# Chapter 2

## Understanding magnetic confinement

### 2.1 Diffusive losses

The Lawson criterion given in eqn. 1.5 highlights the need for optimising the product of density, temperature and energy confinement time, in order to achieve a net energy gain. It was shown in figure 1.4 that the fusion reaction rate peaks at a certain optimal temperature. Further to this, various operational density limits have been observed [27–29] which place an upper (and a lower<sup>1</sup>) limit on the achievable densities in a tokamak plasma. As the maximum density and optimal temperature are essentially fixed, improving the energy confinement time provides the main route to increasing the triple product. For this reason it is useful to understand what controls  $\tau_E$  and to be able to predict its value. The study of confinement forms a large part of current day research into tokamaks and fusion plasma physics.

The energy confinement time,  $\tau_E$ , can be given the simple definition of the ratio of stored energy to power loss. Hence in a toroidal confinement device  $\tau_E$  is set by the radial flux of heat and particles, i.e. transport across flux surfaces. The simplest picture is to consider this flux as a 1D diffusive process caused by particle collisions, and described by Fick’s 2nd law [31] (in the absence of sources):

$$\frac{\partial A}{\partial t} = D \frac{\partial^2 A}{\partial x^2} \quad (2.1)$$

where  $A$  is the diffusing quantity, such as  $n$  or  $T$ , and  $D$  is the diffusion coefficient<sup>2</sup>

---

<sup>1</sup>Low density plasmas are particularly susceptible to instabilities known as locked modes which severely limit operation [30].

given by

$$D = \frac{\Delta x^2}{\Delta t} \quad (2.2)$$

with  $\Delta x$  the radial step size and  $\Delta t$  the decorrelation time (such as the time between collisions). In such a 1D system eqn. 2.1 is satisfied by

$$A(x, t) = \frac{1}{\sqrt{4\pi Dt}} \exp\left(-\frac{x^2}{4Dt}\right) \quad (2.3)$$

This was used by Einstein when considering Brownian particles to show [32] that in 1D the averaged distance travelled by such a particle after time  $t$  is given by

$$\langle x^2 \rangle = 2Dt \quad (2.4)$$

## 2.2 Classical estimates

In 1946 a patent for a toroidal fusion reactor<sup>3</sup> was submitted by two members of Imperial College, Thomson and Blackman [33]. In this patent the minor radius is given as being 30 cm and the resulting  $\tau_E$  is estimated at 65 s. With an estimated density of  $\sim 3.5 \times 10^{20} \text{ m}^{-3}$  and ion temperature of 400 keV [34] it was predicted that the fusion power would be around 9 MW for an input heating power of only 2 MW giving  $Q \sim 4.5$ . Considering this was based upon the D-D fusion reaction it's clear that if such figures could indeed have been achieved then commercial fusion production should not be a significant challenge. Such high confinement times were not however achievable in this device, with the overestimate due to the choice of step size and decorrelation time used in the calculation of  $D$  and the subsequent evaluation of eqn. 2.3. Thomson and Blackman chose the step size for species  $j$  to be the particles gyroradius,  $\rho_{L,j}$ , and the time step to be given by the collision time,  $1/\nu_j$ , leading to what is referred to as classical diffusion. Limiting the calculation of the diffusion coefficient to the lower electron value due to ambipolarity<sup>4</sup> [35] and substituting expressions for  $\rho_{L,e}$  and  $\nu_e$  one finds the expression for the classical diffusion coefficient,  $D_c$ , to be:

$$D_c = \frac{\rho_L^2}{\nu} = \frac{ne^2}{8B^2\pi\epsilon_0^2} \sqrt{\frac{m_e}{T_e}} \ln \Lambda \quad (2.5)$$

<sup>2</sup>Throughout the literature and in this document, the symbol  $D$  is taken to refer to particle diffusion whereas  $\chi$  is used for thermal diffusivities.

<sup>3</sup>This device was not in fact a tokamak but a class of device known as a “z-pinch”.

<sup>4</sup>If ions and electrons diffused at different rates an electric field would be created, retarding the faster motion.

Substituting the parameters specified in the original patent<sup>5</sup> into eqn. 2.5 and assuming a typical value of the Coloumb logarithm,  $\ln \Lambda$ , of 15 one finds  $D_c \sim 6.9 \times 10^{-4} \text{ m}^2 \text{ s}^{-1}$ . Using this value with eqn. 2.4 it can be seen that the mean time taken for a particle to travel 0.3 m is  $\sim 65 \text{ s}$ , in agreement with the patent. In practice a confinement time several orders lower than this prediction was achieved, indicating that the physics model used in making this prediction is incomplete.

## 2.3 Neoclassical estimates

In chapter 1 it was seen that the toroidal geometry of the magnetic field resulted in additional terms in the Lorentz equation, leading to a drift of the gyrocentre. The magnetic geometry of a tokamak also modifies the particle orbits, affecting the calculation of the diffusion coefficient. Taking these effects into account gives the neoclassical diffusion coefficient,  $D_n$ . In a tokamak the magnetic field strength is (approximately) inversely proportional to the major radius,  $R$ . This results in trapping of some particles due to the magnetic mirror effect as they move along a helical field line; other particles have sufficient parallel motion to avoid being reflected and are called passing particles. Trapped particles will bounce back and forth along magnetic field lines between the two poloidal angles where  $B(\theta) = B_{crit}$  whilst passing particles move through all poloidal angles. The  $\nabla B$  and curvature drifts cause the gyrocentre to drift continuously vertically; the effect of this is to shift the gyrocentre relative to the flux surface. The poloidal projection of such orbits are shown in figure 2.1 for passing<sup>6</sup> and trapped particles.

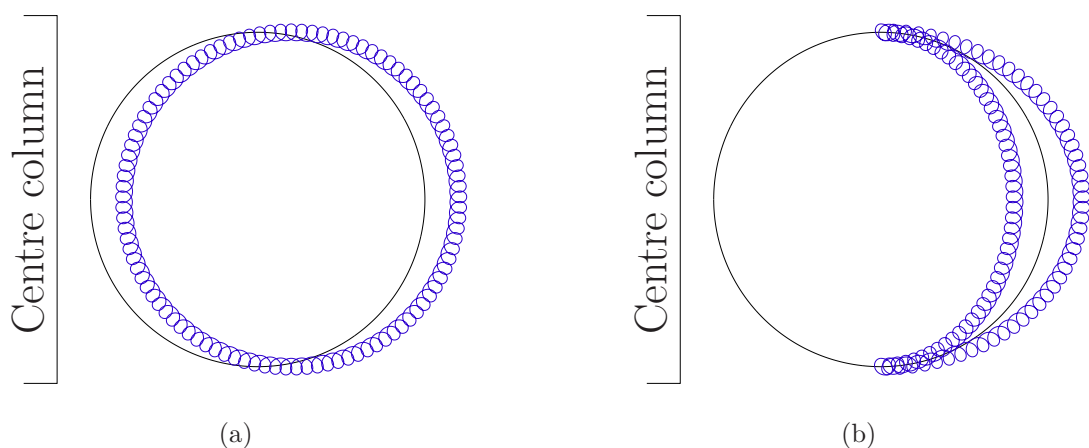


**Figure 2.1:** Poloidal projection of passing [2.1(a)] and trapped [2.1(b)] particle orbits (blue). Drifts due to the magnetic geometry shift orbits from the flux surface (black).

<sup>5</sup>The actual parameters used are  $n_e = 3.5 \times 10^{20} \text{ m}^{-3}$ ,  $B = 1 \text{ T}$  and  $T_e = 55 \text{ keV}$ .

<sup>6</sup>The direction of the shift for passed particles can be either towards or away from the centre column dependent upon whether the particles are travelling in the positive or negative toroidal direction, corresponding to co and counter passing particle orbits respectively.

The trapped particle orbits are often referred to as banana orbits due to their shape. Given the time between bounces, it is possible to estimate the width of these orbits, and hence the radial excursion. A barely trapped particle, when  $B_{crit} = B(\pi)$ , travels a distance  $2\pi qR$  between bounce points and hence the time taken for half a banana orbit is approximated by

$$t_b \approx \frac{2\pi qR}{v_{th}\sqrt{\epsilon}} \quad (2.6)$$

assuming a parallel velocity  $v_{\parallel} \approx v_{th}\sqrt{\epsilon}$ , where  $v_{th}$  is the thermal velocity,  $\sqrt{2T/m}$ . The drift velocity due to geometrical factors can be approximated by

$$v_D \approx \frac{mv^2}{eBR} \quad (2.7)$$

and the width of the banana orbit,  $w_b$ , is given by [25]

$$w_b = t_b v_D \approx \frac{q\rho_L}{\sqrt{\epsilon}} \quad (2.8)$$

Using the approximation  $q \approx \epsilon B/B_{\theta}$  (suitable at large aspect ratio) it is possible to write  $w_b \approx \sqrt{\epsilon}\rho_{\theta}$  where  $\rho_{\theta}$  is known as the poloidal Larmor radius. The banana width will typically be much larger than the Larmor radius (as  $q/\sqrt{\epsilon} > 1$ ), giving a significant increase in the estimate of the diffusion coefficient. Collisions cause trapped particles to diffuse through velocity space, resulting in detrapping after diffusing an angle in velocity space  $\sim \sqrt{\epsilon}$ . Hence the relevant collision frequency will be modified, giving an effective collision frequency  $\nu_{\text{eff}} = \nu/\epsilon$ . Combining these step sizes and multiplying by  $\sqrt{\epsilon}$  to account for the fraction of particles that are trapped, the neoclassical diffusion coefficient can be found. This estimate is given by

$$D_n \approx \sqrt{\epsilon} \left( \frac{(q\rho_L)}{\sqrt{\epsilon}} \right)^2 \frac{\nu}{\epsilon} = \frac{q^2}{\epsilon^{3/2}} D_c \quad (2.9)$$

and is larger than the classical value by a factor  $q^2/\epsilon^{3/2}$ .

For the neoclassical argument presented here to be valid, the collisionality must be low enough such that a trapped particle can undergo at least one banana orbit before colliding (so roughly  $\nu < 1/t_b$ ). This regime of low collisionality is known as the banana regime; for high collisionality, known as the Pfirsch-Schlüter regime, the diffusion coefficient is yet larger. In between high and low collisionality the plasma is said to be in the plateau regime and the diffusion coefficient is insensitive to the collisionality [36]. Figure 2.2 shows a cartoon of the classical and neoclassical diffusion coefficients as a function of collisionality, highlighting the three main regimes.

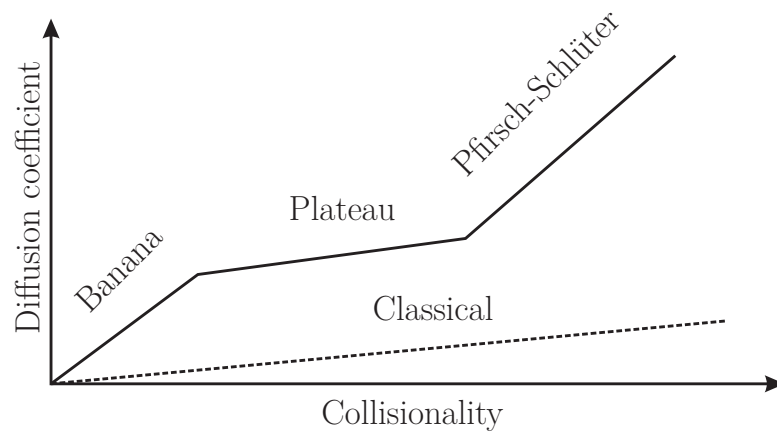


**Figure 2.2:** A cartoon of the neoclassical diffusion coefficient as a function of collisionality (solid line). Three distinct regimes can be identified at low, medium and high collisionality known as banana, plateau and Pfirsch-Schlüter respectively. The classical value is also shown (dashed line).

## 2.4 Fluctuation driven transport

Confinement time predictions made using neoclassical estimates of the diffusion coefficient are an improvement on classical values but are still typically much higher than experimentally observed levels<sup>7</sup>. This additional observed transport is often referred to in the literature as anomalous and its existence has provided a significant challenge to the production of economic fusion energy. It is thought that this anomalous transport is due to fluctuations in the plasma parameters and the EM fields caused by turbulence [37], leading to the preferred name turbulent transport. This turbulence is thought to be due to the nonlinear interaction of small scale instabilities, known as microinstabilities, which are driven by gradients in the equilibrium plasma parameters. Experimental measurements and theoretical studies suggest that a class of microinstabilities known as drift modes are of particular importance.

### 2.4.1 A picture of fluctuation driven transport

Fluctuations in the EM fields modify the Lorentz equation and perturb the particle motion. Any perturbation of the velocity perpendicular to the equilibrium flux surface can result in a radial excursion and hence lead to a flow of energy and particles across the surface.

Consider the case of a cuboid slab of plasma, periodic in the  $\hat{e}_y$  and  $\hat{e}_z$  directions, with an equilibrium magnetic field  $\underline{B} = B\hat{e}_z$  and no electric field. Connection with toroidal geometry can be made using the mapping,  $(x, y, z) \rightarrow (\psi_N, \theta, \varphi)$ , and as

<sup>7</sup>Up to two orders of magnitude for electrons! Despite this, in certain regimes observed ion transport can occasionally be in good agreement with neoclassical predictions.

such it is the transport of particles in the  $\hat{e}_x$  direction that is of most interest. Introducing a perturbation to the electric field,  $\underline{E}_1 = -\nabla\phi_1$ , results in an  $\underline{E} \times \underline{B}$  motion perpendicular to the equilibrium field lines. The component of this velocity in the  $\hat{e}_x$  direction gives a flow of particles across the  $y$ - $z$  plane and is given by

$$v_{1x}^{E \times B} = \frac{E_{1y}}{B} = \frac{(-\nabla\phi_1)_y}{B} \quad (2.10)$$

Introducing a magnetic perturbation perpendicular to the equilibrium field line leads to a perturbed field line which no longer lies purely in the  $\hat{e}_z$  direction and can cross the  $y$ - $z$  plane if  $B_{1x} \neq 0$ . Particle motion along the perturbed field line can then have a component in the direction perpendicular to the equilibrium surface, with the component in the  $\hat{e}_x$  direction given by

$$v_{1x}^{mag} = v_{\parallel} \frac{B_{1x}}{B} = v_{\parallel} \frac{(\nabla \times \underline{A}_1)_x}{B} \quad (2.11)$$

Whilst the net velocity perpendicular to the  $y$ - $z$  plane is given by the sum  $v_{1x}^{E \times B} + v_{1x}^{mag}$ , it is important to note that the amplitude of  $\phi_1$  and  $\underline{A}_1$  will vary with time and space and as such this perpendicular velocity is not constant. Indeed the existence of a perturbation will provoke a response from the particles, which will affect this initial perturbation. This can be seen as a consequence of the ease of motion along field lines; a local electrostatic potential perturbation corresponding to a local ion density perturbation will rapidly draw in electrons from along the field line, for example. Fluctuations have a wave like character and it is useful to use a Fourier representation for a fluctuating quantity  $f_1$ :

$$f_1 = \sum_k f_k \exp(i[\underline{k} \cdot \underline{r}] - i\Omega_k t) \quad (2.12)$$

where each Fourier component has a unique wavenumber,  $\underline{k}$ , an associated complex frequency,  $\Omega_k = \omega_k + i\gamma_k$  and amplitude  $f_k$ . Considering the case where one Fourier component is dominant, the perpendicular velocity,  $v_{1x}$ , is:

$$v_{1x} = \frac{k_y}{B} (\phi_1 + v_{\parallel} A_{1\parallel}) \quad (2.13)$$

## 2.4.2 Diffusive estimates

A characteristic length scale for such perturbations is  $1/k_y$  whilst the characteristic time scale is  $1/\omega_k$ . These characteristic scales can be used to give a simple estimate for the diffusion coefficient as for the classical and neoclassical cases, i.e.  $D_t \sim \omega_k/k_y^2$ .

The most important microinstabilities are believed to belong to a class known as drift modes<sup>8</sup>. These modes have a characteristic frequency known as the electron diamagnetic frequency<sup>9</sup>,  $\omega_{*e}^n$ , defined for this system as

$$\omega_{*e}^n = -\frac{k_y T_e}{e B L_n} \quad (2.14)$$

where  $1/L_n = (1/n)(dn/dx)$ . The most important microinstabilities are generally considered to have wavelengths on the order of either  $\rho_{Li}$  or  $\rho_{Le}$ , such that  $k_y \rho_L \sim 1$  (these are said to be ion scale and electron scale respectively). Using this along with eqn. 2.14 an estimate for the diffusion coefficient, known as the gyroBohm value, can be made:

$$D_t = D_{gB} \approx \omega_{*e}^n / k_y^2 \approx \rho_L^2 \frac{v_{th}^2}{\rho_L \omega_c L_n} \approx \rho_* \rho_L^2 \omega_c \quad (2.15)$$

with  $\rho_* = \rho_L / L_n$ . More generally  $L_n$  can be replaced with some generic equilibrium length scale,  $L_{eq}$ , such as the minor radius,  $a$ . In the nonlinear phase different modes can couple together to form extended coherent structures with characteristic length scales that can exceed that suggested by the relation  $k_y \rho_L \sim 1$ . If the previous analysis is repeated using a characteristic length scale  $\sim L_{eq}$  then the Bohm diffusion coefficient,  $D_B = \rho_L^2 \omega_c = D_{gB} / \rho_*$ , is found.

Two machines operating with identical  $\rho_L$  and  $\omega_c$  but different minor radius will have the same value of  $D_B$  but different values of  $D_{gB}$ . The question as to whether  $D$  scales like Bohm or gyroBohm estimates is immensely important to the success of future fusion power plants, as on next step devices one of the largest extrapolations is in the parameter  $\rho_*$ .

### 2.4.3 Transport calculations

A fluid model expression for the flux of particles due to turbulent fluctuations,  $\underline{\Gamma} = n\underline{v}$ , can be obtained from the continuity equation:

$$\dot{n} + \underline{\nabla} \cdot \underline{\Gamma} = S \quad (2.16)$$

where  $S$  represents the net particle source/sink. The density and velocity can be linearised by expanding as sums of a time averaged component and a fluctuating piece (the long time average of which is zero), i.e.  $n = n_0 + n_1$  and  $v_x = 0 + v_{1x}$  (i.e. no equilibrium flows). Under this substitution the particle flux in the  $\hat{e}_x$  direction becomes  $\Gamma_x = n_0 v_{1x} + n_1 v_{1x}$ , which can be time averaged to give  $\langle \Gamma_x \rangle_t = \langle n_1 v_{1x} \rangle_t$

<sup>8</sup>These modes will be discussed in more detail in chapter 3.

<sup>9</sup>Frequencies with the same sign as  $\omega_{*e}^n$  are said to be in the electron direction whilst those with opposite sign are in the ion direction.

where the operator  $\langle \dots \rangle_t$  is defined as

$$\langle f \rangle_t = \frac{1}{\tau} \int_0^\tau f dt \quad (2.17)$$

with  $\tau$  some time significantly larger than the characteristic time of the fluctuations. The average flux per unit area can then be calculated by averaging over the  $y$ - $z$  plane and the resulting expression is

$$\langle \Gamma_x \rangle_{t,S} = \langle n_1 v_{1x} \rangle_{t,S} = \frac{1}{S} \int_S \left\langle \frac{n_1 E_{1y}}{B} \right\rangle_t dS + \frac{1}{S} \int_S \left\langle \frac{n_1 v_{\parallel} B_{1x}}{B} \right\rangle_t dS \quad (2.18)$$

In the case where the density and potential fluctuations are in phase,  $\langle \Gamma_x \rangle_{t,S}$  will be exactly 0. Knowledge of the phase relationship between these quantities is therefore essential for quantitative estimates of  $\langle \Gamma \rangle_{t,S}$ . Whilst measurements of fluctuation amplitudes have been possible in experiment for some time (as discussed in the next section) the task of precisely measuring phase relations is challenging and not routinely feasible. Despite this, experimental measurements are important in helping to characterise the fluctuations, providing useful information for testing theories and developing predictive models.

## 2.5 Turbulent fluctuations in experiment

Small scale fluctuations have been studied throughout the history of experimental tokamak research and a range of diagnostic techniques have been developed. Fluctuations near the edge of the plasma can be measured directly using probes, e.g. Langmuir probes can provide data on  $\phi_1$ ,  $n_{1e}$  and  $T_{1e}$  in the outer regions of plasma [38, 39]. Magnetic fluctuations near the edge can be measured using magnetic pickup coils known as Mirnov coils. To obtain fluctuation measurements deeper into the plasma, probes can no longer be used, due to both the damage to the probe by the hot plasma and the impurities introduced into the plasma. Techniques using EM radiation, both active and passive, offer the potential to obtain information across the entire plasma without interacting significantly with it. A range of techniques are used on current tokamaks which can provide spatially and temporally resolved measurements of temperature and density fluctuations. These include<sup>10</sup> microwave scattering [40], beam emission spectroscopy (BES) [41, 42] and electron cyclotron emission (ECE) [43, 44].

---

<sup>10</sup>Interested readers are directed to an early overview of various techniques included in Ref [45] and some results obtained in Ref [46]. For a more detailed discussion see Ref [47]

### 2.5.1 Fluctuation characteristics

Measurements made using Langmuir probes have allowed correlations between  $n_1$  and  $\phi_1$  [48–50]. Such measurements can be used to calculate the electrostatic fluctuation induced transport following an approach similar to that in section 2.4.3. Such measurements are challenging and limited to the very edge of the plasma but do suggest fluctuation induced transport is significant. More commonly, fluctuation diagnostics yield fluctuation amplitude as a function of position, which can be compared with the local transport properties inferred from other sources. The normalised fluctuations  $q\phi_1/T$ ,  $n_1/n$  and  $T_1/T$  are typically seen to vary from  $\mathcal{O}(1\%)$  in the core to  $\mathcal{O}(80\%)$  nearer the edge [51]. The normalised magnetic field fluctuations are typically observed to be  $\mathcal{O}(0.01\%)$ , although as  $v_{\parallel}$  can be large the radial transport due to magnetic perturbations can still be significant. By operating over a range of parameters the correlation between the fluctuation amplitude behaviour and that of the local transport can be probed. Figure 2.3(a) shows measurements of normalised fluctuation amplitudes from the TEXT tokamak [52] as a function of radius. This can be compared with figure 2.3(b) which shows the calculated particle fluxes as a function of radius. It can be seen that both the particle flux and  $\phi_1$  peak at the same radial position and drop off at a similar rate.

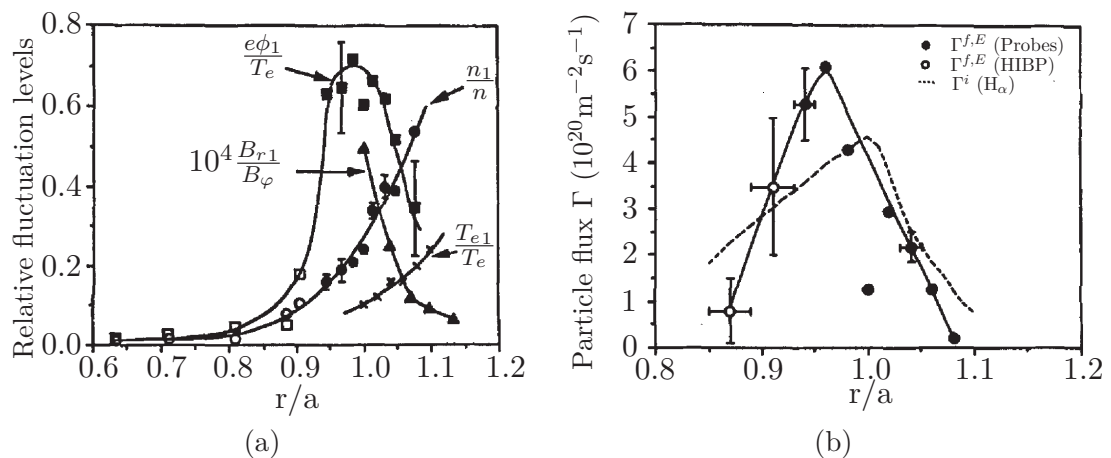


**Figure 2.3:** Radial profiles of normalised fluctuation amplitudes [figure 2.3(a)] and particle flux [figure 2.3(b)] measured on the TEXT tokamak [52]. The electrostatic particle flux measured by Langmuir probes (solid points) and a heavy ion beam probe (open points) is seen to peak at the same position as the normalised potential fluctuations. Reprinted with permission from Ref [45]. Copyright 1990, American Institute of Physics.

Diagnostics using EM radiation often make measurements that resolve separate Fourier components (individual wavevectors,  $\underline{k}$ ) which allows the amplitude spectra to be determined over some range. Such studies have been performed on a range of large aspect ratio tokamaks [46] using a variety of techniques. The general observations from these studies is that the measured amplitude spectra tends to peak

for  $0.2 \leq k_{\theta} \rho_s \leq 0.6$  (where  $\rho_s = v_{th}/\omega_{ci}$ ), which is consistent with ion scale drift wave instabilities. The frequency spectrum can generally also be obtained for a given wavevector. Measurements show that the observed amplitude frequency spectra peak at frequencies of about  $\omega_{*e}^n$  ( $\sim 100$  kHz) [40]. The width of the observed frequency spectrum is typically of the same order as the frequency with peak amplitude, meaning the fluctuations are often referred to as broadband [53]. This has been used as evidence for the nonlinear nature of the turbulence causing these fluctuations<sup>11</sup> [54].

## 2.5.2 Transport barriers

Experiments in the early 80s on the ASDEX tokamak [55] found plasmas with large core density and temperature [56]. This regime of operation, known as H-mode, was an unexpected consequence of operating with higher levels of auxiliary heating<sup>12</sup>. Pressure profiles in H-mode exhibit a steep pressure gradient near the edge of the plasma, known as the pedestal, whilst the gradient in the core region remains similar to that seen in the standard mode of operation, known as L-mode. A comparison of typical H-mode and L-mode pressure profiles is shown for the spherical tokamak MAST [57] in figure 2.4. This local steepening is a sign that the transport near the edge has been reduced, forming an edge transport barrier (ETB).

The amplitude of the edge density fluctuations decrease by around 50% after the transition to H-mode [59, 60]. In addition, the light radiated from the edge due to electron-neutral interactions, known as  $D_{\alpha}$  light, undergoes a significant reduction at the transition from L-mode to H-mode. This is further evidence to suggest that the particle transport has been severely reduced in H-mode as it implies a reduction in electron density outside the outer flux surface. Access to H-mode is available on most major tokamaks<sup>13</sup> and experimental recipes for obtaining H-mode are fairly well developed. The transition from L-mode to H-mode has been associated with a threshold power input,  $P_{LH}$ , and using existing results it is possible to predict the threshold power based on an empirical scaling. Despite this, the precise cause of the transition remains unclear and is a topic of current research with many different proposed explanations [62]. Many theories identify sheared plasma flows as playing a part in suppressing fluctuations near the edge. This is somewhat consistent with the observation of the development of a sheared radial electric field near the pedestal<sup>14</sup>

<sup>11</sup>Linear drift modes have a well defined frequency related to the poloidal wavenumber. A system resulting from the superposition of several drift modes would be expected to exhibit a frequency spectrum involving narrow peaks representative of a linear sum of spectra corresponding to different poloidal wavenumbers. This picture of linear superposition is not consistent with the data shown in Ref [54] which shows the frequency spectra at fixed wavenumber to be broad.

<sup>12</sup>This refers to heating applied in addition to “natural” Ohmic heating.

<sup>13</sup>High confinement modes can also be found in stellarators [61].

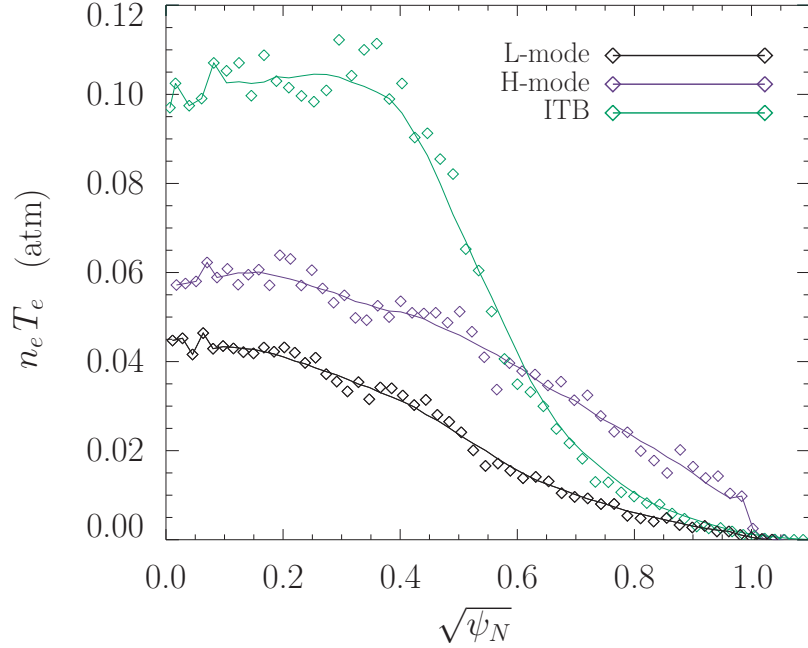


**Figure 2.4:** Experimentally measured pressure profiles from the spherical tokamak MAST. Data for L-mode (black) is from shot 24763 [3] at 0.1787s, data from H-mode (blue) is from the same shot but at 0.2533s whilst the ITB data (green) is from shot 24600 at time 0.2707s [58]. The H-mode and L-mode comparison shows the significant increase in stored plasma energy achieved in H-mode.

which is associated with a sheared  $\underline{E} \times \underline{B}$  flow.

The steepening of the edge pressure gradient leads to a much larger stored energy and  $\tau_E$  is seen to increase by approximately a factor 2 relative to L-mode. The lower transport and higher stored energy in H-mode make it an appealing operational regime; unfortunately it does not come without cost. Periodic magnetohydrodynamic (MHD) instabilities are commonly observed near the edge of H-mode plasmas [63, 64]. These edge localised modes, or ELMs, are observed as filamentary structures which expand radially outwards [65], leading to a rapid loss of particles and energy. The energy lost in an ELM can account for  $\sim 5 - 20\%$  of the energy stored in the pedestal [66] and will be deposited on the machine walls, which can result in large, localised transient heat loads and thereby limit the operational lifetime of plasma facing components (PFCs). A more detailed discussion of ELM behaviour will be provided in chapter 6.

### 2.5.2.1 Internal transport barriers

More recently, regions of suppressed transport have been observed in the core region, indicating the formation of internal transport barriers (ITBs) and resulting in steep

<sup>14</sup>Separating cause from effect can be challenging experimentally, creating difficulty in making conclusive statements about the cause of the fluctuation suppression.

pressure gradient regions in the core [67–69] as shown in figure 2.4. The formation of ITBs is thought to have some similarity to that of ETBs, for example sheared flows are thought to be important for ITB formation [58]. Differences are however apparent; the role of neutral particles is often considered to be important in ETBs but will be less relevant for ITBs. The development of ITBs appears to be strongly dependent on the  $q$  profile and the associated magnetic shear,  $\hat{s} = (r/q)(dq/dr)$ , whilst this appears to be less relevant for ETBs. These ITBs can offer similar increases to the confinement time as ETBs and provide other potential benefits such as enhanced self generated currents associated with the resulting steep pressure gradient<sup>15</sup>. Like ETBs, ITBs are associated with instabilities which lead to the (partial) collapse of the barrier [70]. These instabilities can in themselves be less damaging than ELMs, though often the large pressure gradients associated with these internal barriers can destabilise MHD modes which trigger a plasma disruption leading to the rapid deposition of the plasma stored energy on the vessel walls [71]. These disruptions can be significantly more damaging than single ELMs and as such pose a great threat to large tokamaks which operate with high plasma stored energy. By careful current drive and heating control it has been possible to develop scenarios which avoid the MHD activity which leads to these disruptions, and relatively stable ITBs have been demonstrated on the JET tokamak which survive for several energy confinement times [72, 73]. Scenarios combining an ITB with a H-mode pedestal offer the potential for improved performance and there has been some evidence to suggest that these double barrier scenarios can in some cases offer improved stability [74, 75]. A large amount of experimental and modelling focus is given to developing various advanced operating regimes suitable for next generation tokamaks. These advanced scenarios can be broadly split into two main categories [76]; so called “steady-state” which utilise reversed shear profiles to trigger ITBs thereby providing a large non-inductive current drive and “hybrid” scenarios which have a flat shear profile in the core allowing operation at lower plasma current<sup>16</sup> (thereby extending the maximum duration of inductively driven pulses) [77].

## 2.6 Empirical scaling laws

Whilst the measurement of fluctuation amplitudes is a useful indicator to what’s happening in a given experiment, it is useful to be able to compare and quantify the performance of different tokamaks and individual discharges. As such it is useful

<sup>15</sup>These currents are often referred to as bootstrap currents and form an important role in designs for steady state operation where non-inductive currents are essential [23].

<sup>16</sup>Whilst the absence of the non-inductively driven current due to an ITB may seem like a major downside to the hybrid scenario it poses much less of a control challenge. In addition these hybrid scenarios can avoid limits imposed by certain large scale instabilities, such as tearing modes, allowing high performance operation.

to be able to make consistent measurements and predictions across machines of a parameter indicative of performance, such as the global energy confinement time,  $\tau_E$ . This can be determined indirectly through measurement of the total plasma stored energy,  $W$ , and the applied heating power,  $P_H$ , and then applying energy balance [78]:

$$\dot{W} = P_H - \frac{W}{\tau_E} \quad (2.19)$$

The stored energy is a relatively simple measurement [79] allowing the global energy confinement to be calculated and compared across a large range of tokamaks. This provides a large database with which to study any dependencies  $\tau_E$  may have on various operating and machine parameters. Such studies have allowed the development of empirical scaling laws such that  $\tau_E$  can be estimated for a tokamak operating with a given set of dimensionless parameters. This can provide predictions of the basic confinement properties of discharges yet to be performed.

The most commonly used empirical scalings [25, 80] take the general form:

$$\tau_E = CI^{\alpha_I} B^{\alpha_B} P^{\alpha_P} n^{\alpha_n} A^{\alpha_A} R^{\alpha_R} \epsilon^{\alpha_\epsilon} \kappa^{\alpha_\kappa} \quad (2.20)$$

where  $C$  is a constant,  $\alpha_x$  are the fitted coefficients,  $I$  is the plasma current in MA,  $P$  is the applied heating power in MW,  $B$  is the toroidal magnetic field,  $n$  is the density in units of  $10^{19}\text{m}^{-3}$ ,  $A$  is the average atomic mass,  $R$  is the major radius,  $\epsilon$  is the inverse aspect ratio and  $\kappa$  is known as the elongation (a measure of the plasma's cross-sectional shape). These are known as engineering parameters, an alternative representation is also used and is given in terms of physical parameters:

$$\tau_E \propto \tau_B \rho_*^{\alpha_{\rho_*}} \nu_*^{\alpha_{\nu_*}} \beta^{\alpha_\beta} A^{\alpha_A} q_c^{\alpha_{q_c}} \epsilon^{\alpha_\epsilon} \kappa^{\alpha_\kappa} \quad (2.21)$$

Here  $\tau_B = ea^2B/T$  is known as the Bohm time,  $\nu_*$  is the normalised collisionality,  $\beta \sim n_e(T_e + T_i)/B^2$  is the normalised plasma pressure, and  $q_c \sim \epsilon^2 RB/\mu_0 I$  is known as the cylindrical safety factor.

As different modes of operation behave somewhat differently, separate coefficients are found for Ohmic, L-mode and H-mode discharges, resulting in several scalings. The data in table 2.1 shows the fitted engineering coefficients for Ohmic operation [25], the commonly used coefficients for L-mode plasmas [81] and two scalings for H-mode depending on whether ELMs are present or not (IPB98(y,2) and ELM free respectively).

Representing the H-mode and L-mode data in terms of physical values leads to the coefficients given in table 2.2. It is clear from these physical coefficients that  $\tau_E$  for L-mode plasmas is roughly independent of  $\rho_*$  whereas for H-mode it is approximately inversely proportional. These findings are consistent with previous observations of

Name	$C$	$\alpha_I$	$\alpha_B$	$\alpha_P$	$\alpha_n$	$\alpha_A$	$\alpha_R$	$\alpha_\epsilon$	$\alpha_\kappa$
Ohmic	0.35	-1.0	1.0	0.0	1.0	0.0	4.0	3.0	1.0
L-mode	0.023	0.96	0.03	-0.73	0.4	0.2	1.83	-0.06	0.64
IPB98(y,2)	0.056	0.93	0.15	-0.69	0.41	0.19	1.97	0.58	0.78
ELM free	0.0314	0.94	0.27	-0.68	0.34	0.43	1.98	0.1	0.68

**Table 2.1:** Coefficients for use in  $\tau_E$  empirical scaling laws of the form given in eqn. 2.20 (engineering) for Ohmic, L-mode and H-mode plasmas (IPB98(y,2) and ELM free).

Bohm type scaling in L-mode [82] but suggests gyroBohm scaling for H-mode. This highlights the importance of H-mode operation for future larger tokamaks to exploit the expected gyroBohm scaling.

Name	$\alpha_{\rho_*}$	$\alpha_{\nu_*}$	$\alpha_\beta$	$\alpha_A$	$\alpha_{q_c}$	$\alpha_\epsilon$	$\alpha_\kappa$
L-mode	0.15	0.19	-1.41	0.67	-3.47	-0.09	3.22
IPB98(y,2)	-0.7	-0.01	-0.9	0.96	-3.0	0.73	2.3
ELM free	-0.89	-0.13	-0.92	1.78	-2.77	-1.17	2.9

**Table 2.2:** Coefficients for use in  $\tau_E$  empirical scaling laws of the form given in eqn. 2.21 (physical) for L-mode and H-mode plasmas (IPB98(y,2) and ELM free).

The difference in coefficients for L-mode and H-mode highlight the weakness of such an empirical scaling approach: reliable predictions can only be expected when remaining within the sampled parameter regimes. Despite this, extrapolation using these empirical laws should be reasonable provided there are no significant changes to the plasma's behaviour. Figure 2.5 shows a comparison of experimental measurements of  $\tau_E$  and scaling law predictions for a large range of tokamaks; the agreement is fairly good. A prediction for the next generation tokamak ITER, (discussed in more detail in section 2.8) made using this scaling is also shown in this figure. The difference in dimensionless parameters between current devices and ITER is significant and as a result such empirical scalings should only hold a limited weight. By pushing existing tokamaks into new parameter regimes the scope of these empirical scalings can be improved and statistical significance enhanced.

## 2.7 One dimensional transport models

Predictions of  $\tau_E$  can be used to estimate the fusion power that will be achieved, which is of course a crucial parameter for future fusion reactors. Such an approach however, neglects the radial profiles of the temperature and density which will result in a spatially varying fusion reaction rate. An alternative is to take some simple parameterisation for these profiles, the parameters for which can then be fitted to an experimental database, giving an empirical estimate of the profiles. The ideal

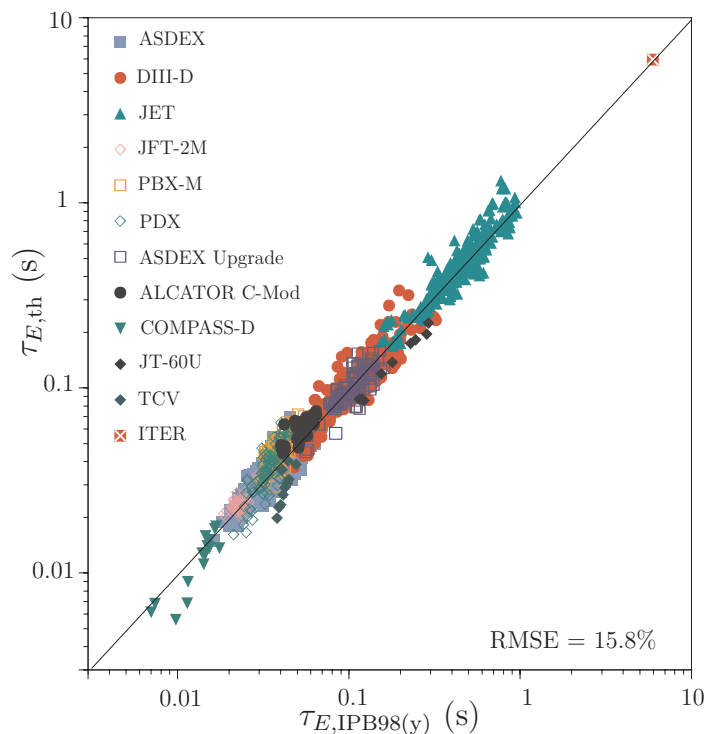


**Figure 2.5:** Comparison of empirical predictions of  $\tau_E$  in H-mode using the IPB98(y) scaling compared to measurements across a large range of tokamaks. Reproduced with permission from Ref [80].

approach however, is to be able to determine the profiles from first principles without relying on experimental fitting.

A common technique currently used to predict profiles, known as one dimensional transport modelling, typically predicts temperature and density profiles given specified sources and sinks, allowing various parameters, including the fusion power, to be predicted. To do this requires a way to estimate or calculate the transport levels across the plasma and here 1D transport models can be categorised into two main groups. The first of these are “semi-empirical” models which often involve using diffusivity profiles with magnitudes informed by experiment. These approaches suffer the same restrictions as empirical scaling laws as they rely on fitting and trends based on experimental observations and hence are somewhat restricted to the sampled parameter ranges. The second class of models are known as “physics-based” and use theoretically based models for estimating the transport levels expected. Clearly physics-based models offer more scope for extrapolation, provided the physics model is suitably complete. Indeed, sufficiently complete models should be able to extend to entirely new regimes of operation. It should be noted however, that these physics-based models can still contain fitting parameters which will affect the results; these parameters may or may not be determined from experiment<sup>17</sup>.

<sup>17</sup>A simple example of this can be demonstrated by recalling eqn. 2.18 and assuming a linear fluid simulation is performed to determine the phase between the perturbations. It is still necessary to define the amplitude of these perturbations in order to calculate the flux. This information could be provided either by experimental observations or a more complete nonlinear theory.

These physics-based models can automatically contain some effects whilst others, such as transport barriers, may need to be imposed as in the semi-empirical case. Such missing elements can be incorporated into these models as understanding and theory improves, reducing the required inputs and hence increasing the confidence in the predictions made.

As the transition to H-mode and subsequent edge transport behaviour is not well understood these transport models do not usually treat the pedestal region and instead take the temperature and density at the top of the pedestal as a boundary condition. The prediction of these models can be sensitive to this pedestal height, making predictive models for the pedestal an important area of research, which will be discussed in more detail later.

In Ref [80] a number of different one dimensional transport models are discussed and compared for a common database of discharges across a range of tokamaks. The physics-based models considered in this reference can be split into two main categories; those based on models for various different instabilities and those taking a “gyrofluid” approach. The multi-mode-model (MMM) is a widely used model which describes several different instabilities thought to be relevant for tokamak anomalous transport. The gyrofluid models involve a system of equations derived by taking moments of a kinetic description of the plasma, suitable for strongly magnetised plasmas, known as gyrokinetics (discussed in chapter 3). The resulting system of equations can then be solved numerically to determine the fluxes of the various quantities of interest. These gyrofluid models should be capable of describing a large range of operating regimes and automatically incorporating a number of relevant effects. Despite this these gyrofluid models approximate the full gyrokinetic system, specifically velocity dependent effects, using fluid closures and as such cannot be considered complete.

As computational power has increased it has become possible to treat more complex models numerically. Indeed, solutions of the nonlinear gyrokinetic equation can be obtained routinely (albeit at relatively large computational expense). This has allowed comparisons of gyrofluid model predictions with those obtained from gyrokinetic solutions [83–85]. This allows gyrofluid models to be tuned against these gyrokinetic results, providing the opportunity to construct gyrofluid models entirely independent of experiment<sup>18</sup>. Recent computational advances have allowed the development of transport models based upon full gyrokinetic simulations which would have previously been unfeasible. The frameworks TRINITY [86] and TGYRO [87] have been developed to allow one dimensional transport analysis given local fluxes on a range of surfaces. These fluxes can be calculated from a range of sources including

---

<sup>18</sup>This in turn allows gyrofluid models to be compared to experiment without biasing the comparison through experimental tuning.

gyrofluid and gyrokinetic simulations. Such an approach offers a route to predictive transport studies leveraging the full physics model contained in gyrokinetics. Even with the computational power currently available such an approach is not practical for routine analysis and gyrofluid models, such as TGLF [84], provide a useful, fast, model which can be used to perform inter-experiment analysis. It is important to note that such models typically require information on the nonlinear saturated amplitude of the fluctuations; in the case of TGLF this information is derived from a fit to a database of nonlinear gyrokinetic simulations and hence its applicability outside the regimes covered by these simulations are not well known.

The field of gyrokinetics is clearly of large importance to the predictions made by a number of one dimensional transport models and offers a direct method to obtain nonlinearly saturated fluctuation amplitudes and the associated fluxes, albeit at large computational expense. As such it is important to consider how well gyrokinetics represents the physical system of interest. The study and refinement of gyrokinetics is a topic of great interest for tokamak research.

## 2.8 Predictions for ITER

In 1997 the Joint European Torus (JET) tokamak achieved a record fusion power of 16.1MW, corresponding to a  $Q$  of 0.62 [88]. Whilst the development of advanced operating scenarios incorporating transport barriers has provided significant improvements to the obtainable confinement times over the past few decades, achieving significantly higher  $P_{fus}$  and  $Q$  is out of the reach of current generation tokamaks. This limits the ability to study reactor relevant issues, including the demonstration of significant net energy production. The need for a next generation tokamak to address these issues was identified by the international fusion community and led to an agreement, finalised in 2006<sup>19</sup>, for the joint design and construction of such a machine. This tokamak, known as ITER, is a joint collaboration between the European Union, India, the Russian Federation, Japan, the People's republic of China, South Korea and the USA, and is currently under construction in Cadarache, France. Several of the key machine parameters for the final ITER design [89] are given in table 2.3, and are compared with JET, currently the largest tokamak.

The main aims of ITER are [90]:

- To demonstrate large  $Q$  operation ( $Q = 10$  is the desired target).
- Achieve high performance, long time scale discharges ( $\sim 1000$  s) through external current drive.

---

<sup>19</sup>The original discussions first took place in 1985, involving a subset of the current participants.

Name	ITER	JET
Major radius	6.2 m	2.96 m
Minor radius	2.0 m	0.93 m
Plasma volume	$\sim 837 \text{ m}^3$	$\sim 85 \text{ m}^3$
Plasma current	15 MA	6 MA
Toroidal field	5.3 T	4.0 T

**Table 2.3:** A summary of the key machine parameters for ITER and JET.

- Investigate and develop techniques for tritium breeding.
- Demonstrate and refine technologies required for future reactors such as remote handling capabilities.

A large portion of theoretical and experimental work in the past two decades has been targeted towards optimising the ITER design and making predictions for the expected performance properties. Clearly to obtain  $Q = 10$  will require significant improvements to the  $\tau_E$  achieved on current generation machines.

It can be seen from figure 2.5 that the ELMy H-mode empirical scaling predicts a confinement time of 5 – 6 s for ITER. If ITER were to operate in L-mode the confinement time is predicted to be about 2 s which is not sufficient to achieve  $Q = 10$ . It is important to note that these empirical scalings involve extrapolating a large distance beyond the currently achievable parameter range and as such should be accompanied by large uncertainties.

Recent predictions for the obtainable fusion power in the ITER H-mode made using the gyrofluid code GLF23 suggest an achievable fusion power of around 400 MW for a pedestal temperature  $\sim 4$  keV [91]. Such performance corresponds to  $Q \sim 8-12$ , suggesting ITER should achieve near its target using the H-mode baseline scenario. An earlier comparison between GLF23 and other transport models [92] shows reasonable agreement between the models although the discrepancies can still be significant. The predictions of such transport models can be very sensitive to the physics models included and other assumptions made. By investigating the underlying mechanisms driving the transport the most important elements in transport models can be identified.

# Chapter 3

## Theoretical study of fluctuations

### 3.1 The need for theory

The previous chapter introduced the concept of fluctuation driven transport and highlighted its importance in achieving high fusion power and  $Q$ , making it a highly significant topic for ITER and future reactors. Whilst various empirical methods such as scaling laws allow predictions to be made for the confinement properties of ITER, such extrapolations may not correctly represent all the relevant physics due to the limited parameter regime sampled in current experiments. By developing a theoretical model that is able to approximate the most relevant physics, it should be possible not only to produce predictions with much higher confidence but also to gain insight into the most important underlying processes. Such physical insight can be invaluable in interpreting experimental observations and can be used to direct experiments towards optimal operation.

The expected level of agreement between theoretical predictions and experimental observations depends upon how well the relevant physics has been captured by the theoretical model. Iteration from simple models to more complex ones allows more detailed comparisons between theory and experiment. Analytical theory usually requires approximations which may or may not be valid in the regimes of interest. With the rapid increase in computational power it has become possible to exploit more complete descriptions of the system and over the decades it has become more feasible to attempt direct numerical solution using more sophisticated models, helping to reduce the number of approximations required.

It has already been mentioned that drift wave microinstabilities are thought to be responsible for the observed fluctuations, and they have been the focus of a range of studies. This chapter will introduce the theoretical framework, known as gyrokinetics, widely used in the study of microinstabilities. First, however, a simpler fluid

drift wave model will be discussed to illustrate some of the underlying physics of drift modes.

## 3.2 Two fluid drift instabilities in shearless slab geometry

Due to the large difference in mass between ions and electrons their thermal velocity differs by a factor  $\sim 60$  (for Deuterium plasmas) and the ions have a much larger inertia. The two species' parallel motion is different and it is often important to use models which treat ions and electrons separately. One approach is known as the two fluid model, whereby the ions and electrons are treated as two separate fluids which interact through EM fields. Each is then described by a set of fluid equations such as the continuity and momentum (or force-balance) equations:

$$\dot{n}_s + \underline{\nabla} \cdot (n_s \underline{v}_s) = 0 \quad (3.1)$$

$$m_s n_s (\dot{\underline{v}}_s + (\underline{v}_s \cdot \underline{\nabla}) \underline{v}_s) = -\underline{\nabla} \cdot \underline{P}_s + n_s \underline{F}_s + \underline{C} \quad (3.2)$$

Here the subscript  $s$  is a species label,  $n$  is the density,  $\underline{P}$  is the pressure tensor<sup>1</sup>,  $\underline{F}$  is the Lorentz force and  $\underline{C}$  is the rate of change of momentum due to collisions. These fluid equations can be derived rigorously from a full kinetic model (discussed in the next section, see appendix A for more details). Approximations are required to obtain a closed set of equations.

Such models can be of varying complexity depending on the physics of interest and indeed the electron drift wave, from which drift instabilities develop, can be described by a fairly simple form.

### 3.2.1 The electron drift wave

There are a range of drift instabilities that can develop in a tokamak plasma related to a specific wave known as the electron drift wave. These drift waves are contained in simple two fluid models using a slab geometry such as that introduced in section 2.4.1 with a uniform magnetic field in the  $\hat{e}_z$  direction.

Consider such a slab with uniform electron temperature, cold ions ( $T_i \sim 0$ ), no equilibrium flows and an equilibrium density gradient in the  $\hat{e}_x$  direction. If an ion density perturbation,  $n_{i1} \sim \exp(i[k_y y + k_z z - \Omega t])$  (with wavevector,  $\underline{k} = k_y \hat{e}_y + k_z \hat{e}_z$ , and complex frequency,  $\Omega = \omega + i\gamma$ ), is introduced a small charge imbalance

<sup>1</sup>This reduces to the standard scalar pressure for an isotropic system.

will exist and an electric field will be generated in both the  $\hat{e}_y$  and  $\hat{e}_z$  directions. This situation is illustrated in figure 3.1 which shows that after the perturbation is introduced the contours of constant  $n_i$  no longer lie purely in the  $y$ - $z$  plane. The electric field which is generated will result in an  $\underline{E} \times \underline{B}$  motion in the  $\hat{e}_x$  direction which acts to increase the density in rarefied regions and decrease it in compressed regions. This sets up an oscillation which is the electron drift wave.

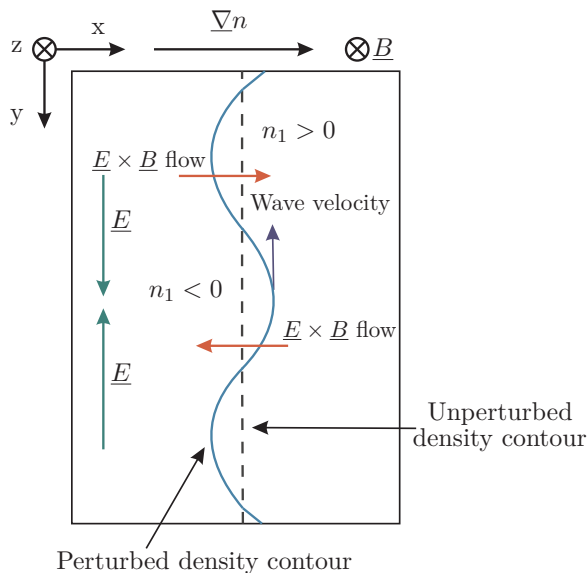


**Figure 3.1:** A simple cartoon of the slab electron drift wave. A perturbation to the equilibrium density (shown by the blue contour) results in an electric field (shown by the green lines) perpendicular to the magnetic field and the density gradient. The resulting  $\underline{E} \times \underline{B}$  motion causes the perturbation to propagate in the  $y$  direction but does not alter its amplitude in this simple case.

To describe this mathematically the two fluid approach can be applied with suitable assumptions. Electrons are assumed to respond rapidly along the field line relative to the modes' characteristic time<sup>2</sup>, i.e.  $k_z v_{the} \gg \Omega$ , whilst, due to the disparate masses, the ions are assumed to be stationary. The electron parallel force balance neglecting electron inertia, assuming a scalar pressure and in the absence of collisions, is obtained from eqn. 3.2 to give:

$$n_e q_e E_z - (\nabla P_e)_z = 0 \quad (3.3)$$

Substituting  $n_e = n_0 + n_{e1}$  into eqn. 3.3 and linearising, assuming no equilibrium temperature gradient, leads to an expression for the perturbed electron density,  $n_{e1}$ :

$$n_{e1} = -n_0 \frac{q_e \phi_1}{T_e} \quad (3.4)$$

This is typically referred to as the adiabatic or Boltzmann response and is a com-

<sup>2</sup>The use of this ordering prohibits taking  $k_z = 0$  at any point but it will still be possible to consider the limit  $k_z \rightarrow 0$ .

mon approximation valid when  $k_z v_{the} \gg \Omega$ . Assuming cold ions (such that the ion pressure is negligible) and linearising the ion momentum equation leads to

$$-im_i \Omega \underline{v}_1 = q_i (\underline{v}_1 \times \underline{B} - \underline{\nabla} \phi_1) \quad (3.5)$$

where  $\underline{v}_1 = \underline{v}_{i1}$ . Using a suitable vector relation<sup>3</sup> this can be solved for  $\underline{v}_1$  to give

$$\underline{v}_1 = \frac{1}{1-x^2} \left( \frac{x}{B} \right) \left[ -i \underline{\nabla} \phi_1 + x \frac{\underline{\nabla} \phi_1 \times \underline{B}}{B} + ix^2 (\underline{b} \cdot \underline{\nabla} \phi_1) \underline{b} \right] \quad (3.6)$$

with  $x = \omega_c / \Omega$ . The ion cyclotron frequency,  $\omega_c$ , is  $\mathcal{O}(100\text{MHz})$  which is large relative to that of the observed fluctuations and hence we make the assumption that  $\Omega \ll \omega_c$  and hence  $1/x \ll 1$ . This allows eqn. 3.6 to be simplified to

$$\underline{v}_1 \approx -\frac{\underline{\nabla} \phi_1 \times \underline{B}}{B^2} + i \frac{1}{xB} \underline{\nabla}_\perp \phi_1 - i \frac{x}{B} \underline{\nabla}_\parallel \phi_1 \quad (3.7)$$

where the first term is simply the  $\underline{E} \times \underline{B}$  velocity and the other terms can be associated with the polarisation drift. The linearised ion continuity equation, using  $\underline{v}_0 = 0$ , is

$$i\Omega n_{i1} = n_0 \underline{\nabla} \cdot \underline{v}_1 + \underline{v}_1 \cdot \underline{\nabla} n_0 \quad (3.8)$$

By substituting eqn. 3.7 into eqn. 3.8 and noting that the parallel and perpendicular gradients of  $\phi_1$  are perpendicular to  $\underline{\nabla} n_0$  and that the divergence of the  $\underline{E} \times \underline{B}$  flow is zero for uniform  $\underline{B}$ , one finds

$$\frac{n_{i1}}{n_0} = \frac{1}{\omega_c B} \Delta_\perp \phi_1 - \frac{q_i}{\Omega^2 m_i} \Delta_\parallel \phi_1 - i \frac{1}{\Omega n_0 B^2} (\underline{\nabla} n_0 \times \underline{B}) \cdot \underline{\nabla} \phi_1 \quad (3.9)$$

where  $\Delta_\parallel = \underline{\nabla} \cdot \underline{\nabla}_\parallel$  and  $\Delta_\perp = \underline{\nabla} \cdot \underline{\nabla}_\perp$ . Now applying quasi-neutrality, i.e. enforcing  $n_{i1} = n_{e1}$ , the perturbed densities can be eliminated. After taking advantage of the plane-wave form for  $\phi_1$  to evaluate the gradient terms, the dispersion relation is found:

$$(1 + k_y^2 \rho_s^2) \Omega^2 - \Omega \omega_{*e}^n - \omega_s^2 = 0 \quad (3.10)$$

Here  $\omega_s = k_z c_s$  is the sound frequency,  $c_s = \sqrt{T_e / m_i}$  is the sound speed,  $\rho_s = c_s / \omega_{ci}$  and  $\underline{v}_{*e}$  and  $\omega_{*e}^n$  are the electron diamagnetic velocity and frequency respectively:

$$\underline{v}_{*e} = \frac{T_e}{q_e B^2 n_0} \underline{\nabla} n_0 \times \underline{B} \quad (3.11)$$

$$\omega_{*e}^n = \underline{v}_{*e} \cdot \underline{k} = -\frac{k_y T_e}{e B L_n} \quad (3.12)$$

<sup>3</sup>It is possible to show  $\underline{x} = \underline{a} + \underline{x} \times \underline{b} \Rightarrow \underline{x} = (\underline{a} + \underline{a} \times \underline{b} + [\underline{a} \cdot \underline{b}] \underline{b}) / (1 + b^2)$

The two solutions of the quadratic equation in eqn. 3.10 are:

$$\Omega = \frac{\omega_{*e}^n \pm \sqrt{\omega_{*e}^{n2} + 4(1 + k_y^2 \rho_s^2) \omega_s^2}}{2(1 + k_y^2 \rho_s^2)} \quad (3.13)$$

Different waves can be identified in various situations, for example in the case without an equilibrium density gradient and  $k_y \rho_s \ll 1$  the solution reduces to  $\Omega = \omega = \pm k_z c_s$  which is simply the relation for an ion sound wave (note  $\gamma = 0$  so there is no growth or decay of the wave). In the more relevant case where there is an equilibrium density gradient and  $k_z c_s \ll \omega_{*e}^n$ , the result  $\Omega \approx \omega_{*e}^n$  can be obtained, which describes the electron drift wave.

In the model described the mode frequency,  $\Omega$ , is purely real and hence these waves neither grow nor decay. This is a consequence of the density and potential perturbations being exactly in phase. By breaking this phase relation  $\Omega$  can develop an imaginary component and the wave becomes unstable (or stable). There are a variety of processes, such as collisions [93], which can introduce a phase shift, leading to a range of different instabilities which can develop from the electron drift wave. One example is that in the derivation of the electron response, the effect of collisions and non-isotropic pressure were neglected. Including these dissipative effects the electron response can gain a non-adiabatic component which results in a phase shift<sup>4</sup>.

The introduction of other equilibrium gradients can also destabilise the drift wave. The resulting instabilities are often referred to as reactive in order to distinguish them from the dissipative instabilities. One such instability which results from the presence of ion temperature gradients will now be discussed in the two fluid picture.

### 3.2.2 Ion temperature gradient mode

The instability driven by the ion temperature gradient, known as the ITG mode, is widely understood to limit performance in the core of large aspect ratio tokamaks [94, 95], and the impact of ITG driven fluctuations forms the basis for a number of 1D transport models<sup>5</sup>. The basic physics required to describe some of the main features of ITG modes are included in the simple two fluid model of section section 3.2 which can also be used to derive the slab ITG dispersion relation, providing some insight into the mode.

<sup>4</sup>This can be considered as introducing a friction which prevents the electrons from responding instantaneously.

<sup>5</sup>ITG based models often also include the trapped electron mode (TEM) which is also thought to play a significant role in core transport.

### 3.2.2.1 The ITG dispersion relation

As in the electron drift wave case, we assume  $k_z v_{the} \gg \Omega$  and electrons are again taken to be adiabatic such that their response is given by eqn. 3.4. To obtain the ITG mode it is important to set  $\nabla T_i \neq 0$ . The ITG mode does not require a density gradient but this shall be retained here to highlight its effects. It is necessary to allow significant ion temperatures such that  $P_i \neq 0$  and hence it is necessary to describe ion pressure fluctuations. An adiabatic equation of state,

$$\frac{d}{dt} (P n^{-\kappa}) = 0 \quad (3.14)$$

is assumed, with  $\kappa$  the ratio of specific heats (typically 5/2). Using the ion continuity equation to eliminate the density from eqn. 3.14 leads to the ion pressure equation:

$$\dot{P}_i + \underline{v}_i \cdot \nabla P_i + \kappa P_i \nabla \cdot \underline{v}_i = 0 \quad (3.15)$$

In addition, the pressure gradient term in the ion momentum equation must be retained. Following Ref [95] the perpendicular ion velocity is assumed to be solely the perturbed  $\underline{E} \times \underline{B}$  velocity. If instead the linearised ion momentum equation is solved following the same approach as in section 3.2.1 in the absence of collisions and assuming a scalar pressure then eqn. 3.7 is reproduced with an additional diamagnetic term due to the pressure gradient. In a more rigorous approach it is found that components of the pressure tensor can in fact cancel the diamagnetic component of the velocity<sup>6</sup> (in the case of uniform  $\underline{B}$ ) [22, 96]. Hence if the polarisation drift is assumed to be negligible<sup>7</sup> then it can be seen that this approach leaves only the  $\underline{E} \times \underline{B}$  component as significant. By taking the dot product of the ion momentum equation with  $\underline{b}$  an expression for the parallel velocity can be found:

$$\underline{v}_{1\parallel} = -i \frac{1}{m_i \Omega} \left( q_i \nabla_{\parallel} \phi_1 + \frac{\nabla_{\parallel} P_1}{n_o} \right) \quad (3.16)$$

Noting that only the divergence of  $\underline{v}_{1\parallel}$  enters the continuity equations it is useful to calculate this now. The resulting expression can be simplified by making the substitution  $\nabla \cdot \nabla_{\parallel} = \Delta_{\parallel} = -k_z^2$ :

$$\nabla_{\parallel} \cdot \underline{v}_{1\parallel} = i \frac{k_z^2 c_s^2}{\Omega T_e} \left( q_i \phi_1 + \frac{P_1}{n_o} \right) = \frac{i \omega_s^2}{\Omega T_e} \left( q_i \phi_1 + \frac{P_1}{n_o} \right) \quad (3.17)$$

<sup>6</sup>In the literature this is referred to as ‘‘gyroviscous cancellation’’. A simple physical justification can be given in so far as the perpendicular velocity enters the continuity equations solely to convect heat and particles. As the diamagnetic drift is a fluid drift it cannot result in this convection

<sup>7</sup>These polarisation terms were retained in the electron drift wave dispersion derivation and contributed the  $k_y^2 \rho_s^2$  terms. The case considered here can be considered the same in the limit of  $k_y^2 \rho_s^2 \rightarrow 0$ .

The perpendicular velocity only enters through terms of the form  $\underline{v}_{1\perp} \cdot \underline{\nabla}f_0$ , where  $\underline{\nabla}f_0$  is an equilibrium gradient in the radial direction. Such terms take the form

$$\underline{v}_{1\perp} \cdot \underline{\nabla}f_0 = \frac{\underline{\nabla}f_0 \times \underline{b}}{B} \cdot \underline{\nabla}\phi_1 \quad (3.18)$$

Making the substitution  $(\underline{\nabla}f_0 \times \underline{b}) \cdot \underline{\nabla} \rightarrow -ik_y f_0 / L_f$  this simplifies to

$$\underline{v}_{1\perp} \cdot \underline{\nabla}f_0 = -i \frac{k_y f_0}{BL_f} \phi_1 \quad (3.19)$$

Now these velocity relations can be substituted into the linearised ion continuity equation, leading to

$$-i\Omega n_1 - i \frac{k_y n_0}{BL_n} \phi_1 + i \frac{\omega_s^2 n_0}{\Omega T_e} \left( q_i \phi_1 + \frac{P_1}{n_0} \right) = 0 \quad (3.20)$$

Using the Boltzmann relation given in eqn. 3.4,  $n_1$  can be eliminated allowing eqn. 3.20 to be written:

$$- \Omega \frac{n_0 q_i}{T_e} \phi_1 + \omega_{*e}^n \frac{n_0 q_i}{T_e} \phi_1 + \frac{\omega_s^2 n_0}{\Omega T_e} \left( q_i \phi_1 + \frac{P_1}{n_0} \right) = 0 \quad (3.21)$$

Gathering terms relating to the two different fluctuations provides an expression for  $P_1$  in terms of  $\phi_1$ :

$$\left[ \Omega^2 - \omega_{*e}^n \Omega - \omega_s^2 \right] n_0 q_i \phi_1 = \omega_s^2 P_1 \quad (3.22)$$

Following an identical procedure for the ion pressure equation, eqn. 3.15, gives:

$$\left[ \Omega^2 - \frac{\kappa \omega_s^2}{\tau} \right] P_1 = \left[ \frac{\kappa \omega_s^2}{\tau} - \Omega \omega_*^P \right] n_0 q_i \phi_1 \quad (3.23)$$

Here the temperature ratio  $\tau = T_e / T_i$  has been introduced along with the pressure diamagnetic frequency  $\omega_*^P$ :

$$\omega_*^P = \frac{k_y T_i}{q_i B L_P} \quad (3.24)$$

Substituting eqn. 3.22 into eqn. 3.23 then yields the dispersion relation:

$$\Omega^3 - \Omega^2 \omega_{*e}^n - \Omega \omega_s^2 \left( 1 + \frac{\kappa}{\tau} \right) + \omega_s^2 \left( \omega_*^P + \frac{\kappa}{\tau} \omega_{*e}^n \right) = 0 \quad (3.25)$$

This is a cubic equation which can provide a root with a positive imaginary component, implying an unstable wave solution. It is perhaps more natural to express this relation in terms of  $\omega_{*e}^n$  and  $\omega_{*i}^T$ , where  $\omega_{*i}^T$  is the ion temperature diamagnetic frequency

$$\omega_{*i}^T = \frac{k_y T_i}{q_i B L_T} \quad (3.26)$$

as this allows the effects of temperature and density gradients to be isolated. Noting that  $\omega_*^P = \omega_{*i}^T - \omega_{*e}^n/\tau$  the dispersion relation can be written:

$$\Omega^3 - \Omega^2 \omega_{*e}^n - \Omega \omega_s^2 \left(1 + \frac{\kappa}{\tau}\right) + \omega_s^2 \left(\omega_{*i}^T + \left(\frac{\kappa - 1}{\tau}\right) \omega_{*e}^n\right) = 0 \quad (3.27)$$

In the limit of cold ions  $1/\tau \rightarrow 0$  and  $\nabla T_i = 0$ , eqn. 3.27 reduces to the electron drift wave dispersion relation, eqn. 3.10, seen previously (assuming  $k_y^2 \rho_s^2 = 0$ ). Further it can be noted that in the absence of a density gradient eqn. 3.25 reduces exactly to equation 9 of Ref [95]. It is useful to note that a cubic  $a + bx + cx^2 + dx^3 = 0$ ,  $a, b, c, d \in \mathbb{R}$ , has complex roots *iff*  $\Delta < 0$  with  $\Delta = 18abcd - 4c^3a + c^2b^2 - 4db^3 - 27d^2a^2$ . Hence, taking  $\kappa = 1$ ,  $\tau = 1$  and  $\omega_{*e}^n = 0$  for simplicity, this yields the condition for ITG instability of  $\omega_{*i}^T > 1.089\omega_s$ , which is approximately described by

$$\frac{c_s}{\omega_c L_T} > \frac{k_z}{k_y} \quad (3.28)$$

Retaining the density gradient modifies this relation and provides a stabilising influence. This is highlighted in figure 3.2 which shows the instability boundary as a function of  $\omega_{*e}^n/\omega_s$  and  $\omega_{*i}^T/\omega_s$ . It can be seen that even in the absence of a density gradient it is possible to support a small temperature gradient without instability and only by exceeding some critical gradient will the mode be unstable. This concept of critical gradients is important in 1D transport models as it can lead to the idea of a ‘‘stiff profile’’ where the onset of turbulence at the critical gradient pins the profile.

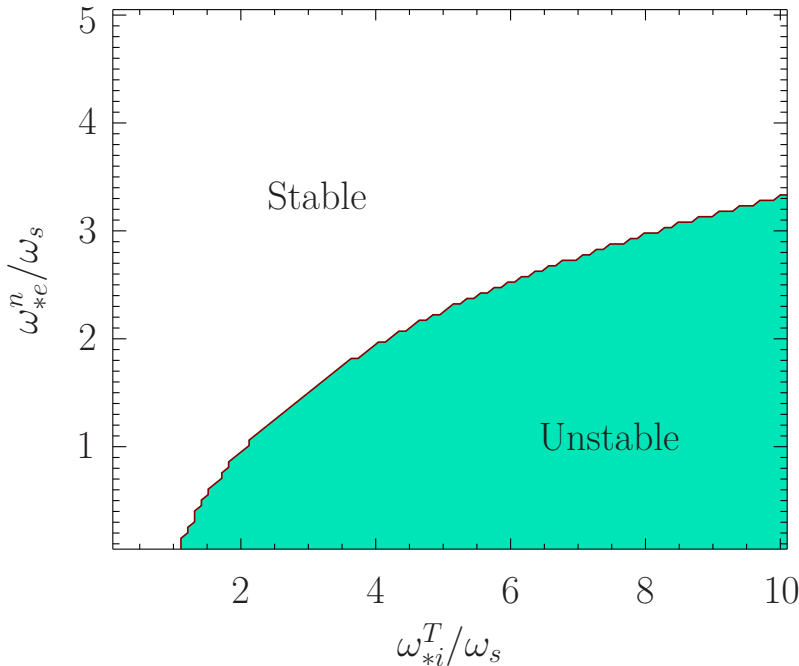


**Figure 3.2:** The shaded region shows the unstable region for the two fluid slab ITG mode as a function of  $\omega_{*e}^n/\omega_s$  and  $\omega_{*i}^T/\omega_s$  under the assumptions  $\kappa = 1$  and  $\tau = 1$ .

### 3.2.3 Incorporating extra effects

It has been seen that slab two fluid calculations can lead to dispersion relations describing various waves and instabilities of relevance to the study of anomalous transport and can provide some basic insight into these modes. The slab geometry used here only bears a passing resemblance to the full toroidal system of tokamaks and important effects have been neglected or simplified when looking at this “shearless slab”. For example the pitch of the magnetic field in a tokamak varies with radius, i.e. the field is sheared, which can provide an important stabilising influence to such drift modes [97]. The fact that  $B$  is not uniform in toroidal systems such as tokamaks also provides important modifications to the system which can significantly alter the behaviour.

It has already been discussed that there are a large range of factors which can drive drift waves; to describe a general system where any of these factors can be active it is important to include all such effects in the model. Moreover for calculations of turbulent transport it is necessary to retain the saturation mechanisms contained in nonlinear terms: i.e. linear theory is helpful but insufficient. Including these factors rapidly increases the complexity of two fluid models. Whilst such models provide physical insight, it is useful to consider alternative approaches. By returning to a kinetic theory (from which the two fluid approach is derived) it is possible to obtain a more complete description of the plasma fluctuations.

## 3.3 Kinetic plasma description

Earlier in section 1.3.3 it was seen that a single charged particle’s motion can be described by the Lorentz equation provided the EM fields have been specified. The EM fields which are used in the Lorentz equation consist of both externally prescribed fields and those generated by the charged particles themselves. Hence to evolve the particle motion it is necessary to know both the charge density,  $\rho_c(\underline{x}, t)$ , and current density,  $\underline{J}(\underline{x}, t)$ , over the whole system in space,  $\underline{x}$ , and time. This information is available if the position and velocity of all the charged particles are known at the initial time,  $t = t_0$ . The ideas behind solving such a system to obtain the position of all particles at some later time,  $t = t_f$ , lend themselves to a numerical analogy. Considering time to be a discrete quantity with spacing  $\Delta t$ , at an initial time  $t_0$  the position and velocity of all particles are considered known and Maxwell’s equations can be used to solve for the EM fields. These fields can then be used with the Lorentz equation to advance the position and velocity of particles to the next point in time,  $t = t_0 + \Delta t$ . This process could then be repeated until the desired time had been reached.

Given that plasma in tokamaks can have a density of the order  $10^{20} \text{ m}^{-3}$  and volume approaching  $100 \text{ m}^3$  (a factor 10 higher for ITER) the solution of each particle's equation of motion is not practical<sup>8</sup>. Rather than talking about the position and velocity of  $N$  particles the system can be described by a distribution function for each species,  $f_s(\underline{x}, \underline{v}, t)$ , which details the number density of species  $s$  at a given point in the 6D “phase-space”<sup>9</sup>,  $(\underline{x}, \underline{v})$ , such that  $\int f_s d\underline{x} d\underline{v} = N$ . By formulating the evolution of  $f_s$  it is possible to repeat the same sort of iterative process as with the single particle picture in order to describe the system at a later time. This evolution is described by the kinetic equation which will now be discussed.

### 3.3.1 The kinetic equation

It is convenient to introduce the generic phase-space coordinates,  $z_i$ , with index  $i \in \{1, 2, 3, 4, 5, 6\}$  representing  $(\underline{x}, \underline{v})$  and hence a position in phase-space is represented by the single vector,  $\underline{z}$ . Suppose the system of interest is composed of a single particle such that  $f_s(\underline{z}, t) = \delta[\underline{z} - \underline{z}_j(t)]$ , with  $\delta$  the Dirac delta function and  $\underline{z}_j(t)$  the particle's instantaneous phase-space position. Clearly the change in  $f_s$  along the particle trajectory through phase-space is zero, leading to

$$\frac{\partial f_s}{\partial t} + \frac{dz_i}{dt} \frac{\partial f_s}{\partial z_i} = 0 \quad (3.29)$$

where the Einstein summation convention is assumed. This equation<sup>10</sup> can be identified as a continuity equation for  $f_s$  in the 6D phase-space in the absence of sources and sinks (provided by nuclear and atomic processes). In the case with  $N$  particles of species  $s$ ,  $f_s$  is in fact a sum over these single particle distribution functions but eqn. 3.29 still holds.

The terms  $\partial z_i / \partial t, i \in \{1, 2, 3\}$  can be identified as a velocity,  $\underline{v}$ , whilst  $\partial z_i / \partial t, i \in \{4, 5, 6\}$  describes the acceleration,  $\underline{a}$ , i.e. the force on the particle per unit mass<sup>11</sup>. In this case the force is just the Lorentz force and depends upon the EM fields, which in turn depend upon  $\rho_c$  and  $\underline{J}$ . These two quantities can be expressed in terms of the species distribution functions using:

$$\rho_c(\underline{z}, t) = \sum_s q_s \int f_s d\underline{v} \quad (3.30)$$

<sup>8</sup>A simple estimate, assuming each equation of motion can be solved in one computational cycle, suggests that the time taken to solve for  $10^{22}$  particles is  $\sim 1$  year when running on  $10^5$  3 GHz processors.

<sup>9</sup>In fact  $f_s$  represents the probability of finding a particle of species  $s$  in the “phase-space” volume element,  $d\underline{x} d\underline{v}$ .

<sup>10</sup>Often referred to as the Klimontovich-Dupree equation.

<sup>11</sup>It can be noted that until the force is specified eqn. 3.29 is a general form valid for a range of cases including neutral fluids.

$$\underline{J}(\underline{z}, t) = \sum_s q_s \int f_s \underline{v} d\underline{v} \quad (3.31)$$

Hence eqn. 3.29 along with Maxwell's equations form a closed system of equations.

The distribution described here is essentially a set of delta functions, each representing a single particle. As such, nothing appears to have been gained over individual particle tracking other than a simplified notation and dependence on  $(\underline{x}, \underline{v})$  rather than  $\{\underline{x}_i, \underline{v}_i\}$ . Progress can be made by noting that the interest lies with the macrostate rather than the microstate. Thus rather than considering the microstate defined by  $f_s$  it is appropriate to consider the ensemble average,  $\langle f_s \rangle$ . This ensemble average acts to smooth out the point like nature of  $f_s$  resulting in a smoothly varying distribution function as well as EM fields. The ensemble average is loosely defined as:

$$\langle f_s \rangle = \frac{1}{\Delta z} \int_{\Delta z} f_s d\underline{z} \quad (3.32)$$

where  $\Delta z$  represents a small phase-space volume containing a statistically significant number of particles. Ensemble averaging eqn. 3.29 leads to

$$\frac{\partial \langle f_s \rangle}{\partial t} + \underline{v} \cdot \frac{\partial \langle f_s \rangle}{\partial \underline{x}} + \left\langle \underline{a} \cdot \frac{\partial f_s}{\partial \underline{v}} \right\rangle = 0 \quad (3.33)$$

The last term on the LHS of eqn. 3.33 can be written

$$\left\langle \underline{a} \cdot \frac{\partial f_s}{\partial \underline{v}} \right\rangle = \langle \underline{a} \rangle \cdot \frac{\partial \langle f_s \rangle}{\partial \underline{v}} - C(\langle f_s \rangle) \quad (3.34)$$

where  $C(\langle f_s \rangle)$ , known as the collision operator, accounts for individual particle interactions, or collisions, which prevent  $\underline{a}$  and  $f_s$  from being statistically independent. Utilising eqn. 3.34, dropping the ensemble average notation,  $\langle \dots \rangle$  (as will be the case for the rest of this thesis) and substituting in for  $\underline{a}$  from the Lorentz equation, makes it possible to write eqn. 3.33 as

$$\frac{\partial f_s}{\partial t} + \underline{v} \cdot \frac{\partial f_s}{\partial \underline{x}} + \frac{q_s}{m_s} [\underline{E} + \underline{v} \times \underline{B}] \cdot \frac{\partial f_s}{\partial \underline{v}} = C(f_s) \quad (3.35)$$

In the absence of collisions eqn. 3.35 is known as the Vlasov equation. When including collisions the equation is generally named after the choice of collision operator used, a common choice being the Fokker-Planck operator<sup>12</sup>.

---

<sup>12</sup>The specific form of the collision operator will not be discussed in this thesis.

## 3.4 Gyrokinetics

The Vlasov equation, eqn. 3.35, describes the evolution of the system, but it still amounts to a 6D problem involving a large range of spatial and temporal scales, much like the particle tracking approach. It is however a useful starting point for a range of more tractable approaches such as the fluid description used earlier<sup>13</sup>.

Under certain approximations it is possible to simplify the kinetic equation to leave the gyrokinetic equation, which is simpler to solve.

The main idea behind gyrokinetics exploits the separation of time scales between that of the rapid gyromotion and the relatively slow drift wave motion. Under this assumption it is possible to average over the rapid gyromotion without losing the physics relevant to the processes of interest. This averaging can be applied to the kinetic equation, reducing the dimensionality of the problem to 5D, resulting in an equation for the evolution of the gyroaveraged distribution function. This averaged distribution function can now be considered as describing the distribution of charged rings, rather than particles.

Since the first gyrokinetic derivations [98, 99] several different approaches have been developed to obtain the gyroaveraged kinetic equation (or gyrokinetic equation, GKE). These derivations usually contain three main sections;

- Physically motivated ordering assumptions, known as the gyrokinetic orderings, which take advantage of the relevant physics and allows a separation of the kinetic equation into a set of ordered equations.
- Choose coordinates to isolate the rapid gyromotion from the slower drift motions.
- Separation of the ordered equations, employing gyroaveraging where necessary to remove the rapid motion from the problem.

A brief outline of some of these key steps, highlighting important points and ideas, will be covered here. More complete and rigorous derivations have been covered in detail in a wide range of publications<sup>14</sup> which will not be replicated here, in particular a large amount of algebra is neglected in section 3.4.3.2 and section 3.4.3.3.

Focus will be given to the linear gyrokinetic equation, which is sufficient for stability calculations. For the calculation of particle and heat fluxes both the phase and amplitude of the fluctuations are important; nonlinear interactions are required to saturate the fluctuation amplitudes and the nonlinear GKE is discussed briefly in section 3.4.4.

<sup>13</sup>For details on the fluid derivation from the Vlasov equation see appendix A.

<sup>14</sup>The discussion presented here roughly follows that of [22], [100], [101] and [102].

### 3.4.1 Linearised kinetic equation

It is convenient to represent the species distribution function,  $f_s$ , as a sum of ordered terms such as

$$f_s = f_{s0} + \epsilon f_{s1} + \mathcal{O}(\epsilon^2) \quad (3.36)$$

with  $\epsilon \ll 1$ . Here the lowest ( $0^{\text{th}}$ ) order term is considered to represent the equilibrium value whilst the  $1^{\text{st}}$  order term is a linear perturbation to this; in linear theory, as considered here, all higher order terms are dropped. The same process can be applied to the electromagnetic fields (and the associated potentials), such that a quantity  $S$  is represented by  $S = S_0 + \epsilon S_1$ . Applying such an expansion to the Vlasov equation<sup>15</sup> allows the  $0^{\text{th}}$  and  $1^{\text{st}}$  order terms to be separated producing two ordered equations:

$$\underline{v} \cdot \underline{\nabla} f_0 + \frac{q}{m} \chi_0 \cdot \underline{\nabla}_v f_0 = 0 \quad (3.37)$$

$$\frac{\partial f_1}{\partial t} + \underline{v} \cdot \underline{\nabla} f_1 + \frac{q}{m} \chi_0 \cdot \underline{\nabla}_v f_1 + \frac{q}{m} \chi_1 \cdot \underline{\nabla}_v f_0 = 0 \quad (3.38)$$

where the species subscript has been dropped and  $\chi$  is defined:

$$\chi = \underline{E} + \underline{v} \times \underline{B} = -\underline{\nabla} \phi - \frac{\partial \underline{A}}{\partial t} + \underline{v} \times \underline{B} \quad (3.39)$$

It will be assumed that all equilibrium quantities are static, i.e.  $\partial f_0 / \partial t = 0$  etc., somewhat simplifying the leading order equation. The  $1^{\text{st}}$  order equation, eqn. 3.38, is the Vlasov equation linearised with respect to perturbations. To proceed further it is useful to consider the phase-space coordinates used.

### 3.4.2 Coordinates

Whilst the linearised Vlasov equation given in eqn. 3.38 is expressed in terms of  $\underline{x}$  and  $\underline{v}$ , it is useful to consider alternative coordinates which exploit properties of the system. To aid the gyroaverage procedure it is useful to consider a set of velocity coordinates which makes the gyromotion explicit. A simple coordinate set satisfying this is  $(v_\perp, \alpha, v_\parallel)$  where  $\alpha$  is the gyrophase (defined in figure 1.5). The vector velocity can then be defined as  $\underline{v} = \underline{v}_\perp + v_\parallel \underline{b}$  with  $\underline{v}_\perp$  defined as

$$\underline{v}_\perp = v_\perp [\hat{e}_1 \cos(\alpha) - \hat{e}_2 \sin(\alpha)] \quad (3.40)$$

where  $\hat{e}_1$  and  $\hat{e}_2$  complete the right handed coordinate set  $(\hat{e}_1, \hat{e}_2, \underline{b})$ .

An alternative choice of velocity space coordinates is  $(\mu, \kappa, \alpha)$  with  $\mu = v_\perp^2 / 2B$  the

---

<sup>15</sup>Collisions will be dropped throughout this outline derivation for simplicity. They can be incorporated into the final equation by reintroducing a generic, undefined collision operator.

magnetic moment per unit mass and  $\kappa = v^2/2$  the particle kinetic energy per unit mass. The set  $(\mu, \kappa, \alpha)$  cannot actually fully define a position in terms of  $\underline{v}_{\parallel}$  and  $\underline{v}_{\perp}$  due to the ambiguity introduced by using the  $\kappa$  coordinate which involves  $v^2$ . It is therefore necessary to introduce an additional binary coordinate,  $\sigma = v_{\parallel}/|v_{\parallel}|$ , which defines the direction of the parallel velocity. It is necessary to express  $\underline{\nabla}_v$  in the adopted coordinate system using

$$\underline{\nabla}_v = (\underline{\nabla}_v u_j) \frac{\partial}{\partial u_j} \quad (3.41)$$

to yield:

$$\underline{\nabla}_v h = \left[ v \frac{\partial}{\partial \kappa} + \frac{v_{\perp}}{B} \frac{\partial}{\partial \mu} + \frac{v_{\perp} \times \underline{b}}{v_{\perp}^2} \frac{\partial}{\partial \alpha} \right] h \quad (3.42)$$

This expression for  $\underline{\nabla}_v$  allows the linearised kinetic equation, eqn. 3.38, to be written as:

$$\begin{aligned} & \left[ \frac{\partial}{\partial t} + \underline{v} \cdot \underline{\nabla} + \omega_c \frac{\partial}{\partial \alpha} \right] f_1 = \\ & - \frac{q}{m} \left[ \underline{E}_1 \cdot \left( v \frac{\partial}{\partial \kappa} + \frac{v_{\perp}}{B} \frac{\partial}{\partial \mu} + \frac{v_{\perp} \times \underline{b}}{v_{\perp}^2} \frac{\partial}{\partial \alpha} \right) \right. \\ & \left. + \frac{(\underline{v}_{\parallel} \times \underline{B}_1) \cdot \underline{v}_{\perp}}{B} \frac{\partial}{\partial \mu} + \left( B_{1\parallel} - \frac{v_{\parallel}}{v_{\perp}} \cos(\alpha) B_{1\perp} \right) \frac{\partial}{\partial \alpha} \right] f_0 \end{aligned} \quad (3.43)$$

Some derivations of the GKE transform from the particle position spatial coordinate to a system based on the guiding centres. Whilst this approach is not explicitly applied here it is briefly introduced to complete the discussion<sup>16</sup>. Recalling figure 1.5 the gyrocentre position,  $\underline{X}$ , can be related back to the particle's position,  $\underline{x}$ , using

$$\underline{X} = \underline{x} - \rho_L \quad (3.44)$$

with the directed Larmor radius,  $\rho_L$ , given by

$$\rho_L = \rho_L(\underline{X}, \underline{v}) [\hat{\underline{e}}_1 \sin(\alpha) + \hat{\underline{e}}_2 \cos(\alpha)] = \frac{\underline{b} \times \underline{v}_{\perp}}{\omega_c} \quad (3.45)$$

In gyrokinetics perturbations with wavelengths the same size as  $\rho_L$  are allowed and effects from variations in the EM fields around the Larmor orbit are retained. As such  $\rho_L$  can change with  $\underline{x}$  and not just  $\underline{X}$ , introducing further complication as discussed in Ref [22].

<sup>16</sup>For a demonstration of the gyrokinetic equation derivation using these ‘‘guiding centre’’ coordinates see Ref [100].

### 3.4.3 Gyrokinetic orderings

To make further progress with the derivation of the GKE it is now useful to make assumptions about the system, specifically the relative order of different terms. These gyrokinetic orderings are physically motivated and take advantage of properties of the system, providing a complementary set to those introduced in section 3.4.1. The orderings are summarised as

$$\frac{\Omega}{\omega_c} \approx \frac{\rho_L}{L} \approx \frac{k_{\parallel}}{k_{\perp}} \approx \frac{L_{\perp}}{L_{\parallel}} \sim \delta \ll 1 \quad (3.46)$$

where  $\delta$  is a small number and  $L$ ,  $L_{\parallel}$  and  $L_{\perp}$  all represent some characteristic length scale. It can be noted that in the linear case it is assumed that  $\epsilon \ll \delta$ .

The first of these orderings is simply stating that the gyromotion is rapid relative to the mode frequency, which is consistent with drift waves, and provides temporal scale separation. The second ordering provides a separation of spatial scales suggesting equilibrium changes across one Larmor radius are small<sup>17</sup>. The final two orderings deal with anisotropy of the system rather than scale separations. The parallel wavelength is assumed to be large due to the rapid parallel motion whereas perpendicular motion is reduced, this is summarised by the ordering  $k_{\parallel} \ll k_{\perp}$ . Finally it is assumed that perturbed quantities vary on the length scale of  $\sim \rho_L$  in the perpendicular direction and  $\sim L$  in the parallel direction due to the ease of motion along the field line<sup>18</sup>. As such  $\nabla_{\perp} \sim 1/L_{\perp} \sim 1/\rho_L$  and  $\nabla_{\parallel} \sim 1/L_{\parallel} \sim 1/L$  and hence  $\nabla_{\parallel} h_1 \ll \nabla_{\perp} h_1$ .

An eikonal representation for the perturbed quantities can be used:

$$h_1 = h_{1A}(\underline{x}, \underline{v}) \exp(i\underline{k} \cdot \underline{x} - i\Omega t) \quad (3.47)$$

with the amplitude,  $h_{1A}$ , containing long length scale variation and the exponential containing short scales. Using this representation it can be shown that  $\nabla_{\parallel} \sim k_{\parallel}$  and  $\nabla_{\perp} \sim k_{\perp}$  which shows that these final two orderings are consistent with such an eikonal representation.

#### 3.4.3.1 Ordering the linearised Vlasov equation

It is possible to separate eqn. 3.43 into a set of ordered equations and due to the anisotropy of the spatial variation it is necessary to split the spatial gradient operator into short and long length scale components. For perturbed quantities these length scales can be matched with the perpendicular and parallel directions respectively but

<sup>17</sup>This ordering in fact follows from  $\Omega/\omega_c \ll 1$  for drift modes with  $\Omega \sim \omega_{*e}^n$  and  $k_y \rho_L \sim 1$ .

<sup>18</sup>Equilibrium quantities are assumed to vary only on long length scales such that  $\nabla h_0 \sim h_0/L$ .

for equilibrium parameters the long length scale is in all directions. As equilibrium gradients are not included in eqn. 3.43 this distinction is not important here and  $\underline{\nabla}_\perp$  and  $\underline{\nabla}_\parallel$  will be used to represent the short and long length scale gradients respectively. Applying the gyrokinetic orderings to the LHS of eqn. 3.43 allows it to be written as:

$$\left[ \frac{\partial}{\partial t} + \underline{v} \cdot \underline{\nabla} + \omega_c \frac{\partial}{\partial \alpha} \right] f_1 = (\mathcal{L}^1 + \mathcal{L}^\delta) f_1 \quad (3.48)$$

where the two ordered operators,  $\mathcal{L}^1$  and  $\mathcal{L}^\delta$  are defined as:

$$\mathcal{L}^1 = \omega_c \frac{\partial}{\partial \alpha} + \underline{v}_\perp \cdot \underline{\nabla}_\perp \quad (3.49)$$

$$\mathcal{L}^\delta = \frac{\partial}{\partial t} + \underline{v} \cdot \underline{\nabla}_\parallel \quad (3.50)$$

and the superscript indicates the order of the terms in  $\delta$ .

To order the RHS of eqn. 3.43 it is necessary to consider the order in  $\delta$  of the perturbed fields when expressed in terms of the EM potentials. Assuming  $\underline{B}_1 = \underline{B}_1^1 + \underline{B}_1^\delta$  and  $\underline{E}_1 = \underline{E}_1^1 + \underline{E}_1^\delta$  the RHS of eqn. 3.43 becomes:

$$\begin{aligned} -\frac{q}{m} \left[ \underline{E}_1 \cdot \left( \underline{v} \frac{\partial}{\partial \kappa} + \frac{\underline{v}_\perp}{B} \frac{\partial}{\partial \mu} + \frac{\underline{v}_\perp \times \underline{b}}{v_\perp^2} \frac{\partial}{\partial \alpha} \right) + \frac{(\underline{v}_\parallel \times \underline{B}_1) \cdot \underline{v}_\perp}{B} \frac{\partial}{\partial \mu} \right. \\ \left. + \left( B_{\parallel 1} - \frac{v_\parallel}{v_\perp} \cos(\alpha) B_{\perp 1} \right) \frac{\partial}{\partial \alpha} \right] f_0 = (\mathcal{M}^1 + \mathcal{M}^\delta) f_0 \end{aligned} \quad (3.51)$$

with  $\mathcal{M}^1$  and  $\mathcal{M}^\delta$  defined as:

$$\mathcal{M}^1 = \frac{q}{m} \left[ \underline{v}_\perp \cdot \underline{\nabla}_\perp \phi_1 \left( \frac{\partial}{\partial \kappa} + \frac{1}{B} \frac{\partial}{\partial \mu} \right) - \frac{v_\parallel \underline{v}_\perp \cdot \underline{\nabla}_\perp A_{1\parallel}}{B} \frac{\partial}{\partial \mu} \right] \quad (3.52)$$

$$\begin{aligned} \mathcal{M}^\delta = -\frac{q}{m} \left[ \underline{E}_1^\delta \cdot \left( \underline{v} \frac{\partial}{\partial \kappa} + \frac{\underline{v}_\perp}{B} \frac{\partial}{\partial \mu} \right) + \underline{E}_1^1 \cdot \frac{\underline{v}_\perp \times \underline{b}}{v_\perp^2} \frac{\partial}{\partial \alpha} \right. \\ \left. + \frac{\underline{v}_\perp \cdot (\underline{v}_\parallel \times \underline{B}_1^\delta)}{B} \frac{\partial}{\partial \mu} + \left( B_{\parallel 1}^1 - \frac{v_\parallel}{v_\perp} \cos(\alpha) B_{\perp 1}^1 \right) \frac{\partial}{\partial \alpha} \right] \end{aligned} \quad (3.53)$$

Finally it is helpful to represent both the equilibrium and perturbed distribution functions as a sum of parts ordered in  $\delta$ , such that eqn. 3.43 can be written as:

$$(\mathcal{L}^1 + \mathcal{L}^\delta) [f_1^1 + f_1^\delta + \mathcal{O}(\delta^2)] = (\mathcal{M}^1 + \mathcal{M}^\delta) [f_0^1 + f_0^\delta + \mathcal{O}(\delta^2)] \quad (3.54)$$

### 3.4.3.2 The leading order equation

Taking the leading order terms in eqn. 3.54 gives the equation  $\mathcal{L}^1 f_1^1 = \mathcal{M}^1 f_0^1$ , which using eqn. 3.50 and eqn. 3.52 leads to

$$\left( \omega_c \frac{\partial}{\partial \alpha} + \underline{v}_\perp \cdot \nabla_\perp \right) f_1^1 = \frac{q}{m} \left[ \underline{v}_\perp \cdot \nabla_\perp \phi_1 \left( \frac{\partial}{\partial \kappa} + \frac{1}{B} \frac{\partial}{\partial \mu} \right) - \frac{v_\parallel \underline{v}_\perp \cdot \nabla_\perp A_{1\parallel}}{B} \frac{\partial}{\partial \mu} \right] f_0^1 \quad (3.55)$$

Splitting  $f_1^1$  into gyrophase independent and gyrophase dependent parts provides a solution for  $f_1^1$ , given in eqn. 3.56, in terms of the EM potentials,  $f_0^1$  and a gyrophase independent function  $g$ , often referred to as the non-adiabatic component of the perturbed distribution function.

$$f_1^1 = \frac{q}{m} \left[ \phi_1 \left( \frac{\partial}{\partial \kappa} + \frac{1}{B} \frac{\partial}{\partial \mu} \right) - \frac{v_\parallel A_{1\parallel}}{B} \frac{\partial}{\partial \mu} \right] f_0^1 + g(\underline{x}, v_\parallel, v_\perp) \exp(-i\mathbf{k} \cdot \underline{\rho}_i) \quad (3.56)$$

### 3.4.3.3 The first order equation

The first order terms in eqn. 3.54 give:

$$\mathcal{L}^1 f_1^\delta + \mathcal{L}^\delta f_1^1 = \mathcal{M}^1 f_0^\delta + \mathcal{M}^\delta f_0^1 \quad (3.57)$$

After a small amount of manipulation this can be written as:

$$\frac{\partial}{\partial \alpha} \left[ f_1^\delta \exp(i\mathbf{k} \cdot \underline{\rho}_i) \right] + \frac{\exp(i\mathbf{k} \cdot \underline{\rho}_i)}{\omega_c} \mathcal{L}^\delta f_1^1 = \frac{\exp(i\mathbf{k} \cdot \underline{\rho}_i)}{\omega_c} (\mathcal{M}^1 f_0^\delta + \mathcal{M}^\delta f_0^1) \quad (3.58)$$

This provides an equation for  $f_1^\delta$  in terms of  $f_1^1$  and  $f_0$ , however by averaging eqn. 3.58 over the gyrophase the first term can be eliminated leaving an equation for  $g$  in terms of  $f_0$ . The gyroaverage is represented by  $\langle \dots \rangle$  and is defined as:

$$\langle h \rangle = \frac{1}{2\pi} \int_0^{2\pi} h \, d\alpha \quad (3.59)$$

Hence the gyroaveraged version of eqn. 3.58 is given by:

$$\left\langle \exp(i\mathbf{k} \cdot \underline{\rho}_i) \mathcal{L}^\delta f_1^1 \right\rangle = \left\langle \exp(i\mathbf{k} \cdot \underline{\rho}_i) (\mathcal{M}^1 f_0^\delta + \mathcal{M}^\delta f_0^1) \right\rangle \quad (3.60)$$

Proceeding with a significant amount of algebra and making the assumption that  $f_0^1$  is independent of  $\mu$  allows eqn. 3.60 to be written as

$$\left[ \frac{\partial}{\partial t} + (v_{\parallel} \underline{b} + \underline{v}_D) \cdot \nabla \right] g = - \left[ \frac{\nabla f_0^1}{B} \cdot \underline{b} \times \nabla_{\perp} + \frac{q}{m} \frac{\partial f_0^1}{\partial \kappa} \frac{\partial}{\partial t} \right] \left[ (\phi_1 - v_{\parallel} A_{1\parallel}) J_0(k\rho_L) + \frac{v_{\perp}}{k} B_{1\parallel} J_1(k\rho_L) \right] \quad (3.61)$$

which is the linear electromagnetic gyrokinetic equation. This is in agreement with equation 56 of Ref [103] in the absence of equilibrium flows and nonlinearities<sup>19</sup>.

Here  $\underline{v}_D$  contains the magnetic drifts and  $J_0(k\rho_L)$  and  $J_1(k\rho_L)$  are the 0<sup>th</sup> and 1<sup>st</sup> order Bessel functions respectively. The Bessel functions arise from the gyroaveraging operation and are defined as:

$$J_0(z) = \frac{1}{2\pi} \int_0^{2\pi} \exp(iz \cos \alpha) d\alpha \quad (3.62)$$

$$J_1(z) = -\frac{i}{2\pi} \int_0^{2\pi} \exp(iz \cos \alpha) \exp(i \cos \alpha) d\alpha \quad (3.63)$$

### 3.4.4 Nonlinear effects

The linearisation performed in section 3.4.1 is only valid for infinitesimal fluctuations and hence the linear GKE, eqn. 3.61, is only valid for small fluctuations. However, if an unstable solution exists then its amplitude will grow with time and hence after a certain amount of time the linearisation breaks down and the equation is no longer valid. To overcome this it is necessary to adopt a modified ordering for the fluctuations, which can be summarised by setting  $\epsilon = \delta$  such that

$$\frac{\Omega}{\omega_c} \approx \frac{\rho_L}{L} \approx \frac{k_{\parallel}}{k_{\perp}} \approx \frac{L_{\perp}}{L_{\parallel}} \approx \frac{f_1}{f_0} \approx \frac{q\phi_1}{T} \approx \frac{B_1}{B_0} \sim \delta \ll 1 \quad (3.64)$$

where the fluctuation terms,  $f_1$  etc., represent the total fluctuation rather than simply the linear piece used in the linear case. Repeating the procedure used to derive the linear GKE it is then possible to obtain the nonlinear EM GKE:

$$\left[ \frac{\partial}{\partial t} + (v_{\parallel} \underline{b} + \underline{v}_D) \cdot \nabla \right] g = - \left[ \frac{\nabla f_0^1}{B} \cdot \underline{b} \times \nabla_{\perp} + \frac{q}{m} \frac{\partial f_0^1}{\partial \kappa} \frac{\partial}{\partial t} + R_{ni} \right] \left[ (\phi_1 - v_{\parallel} A_{1\parallel}) J_0(k\rho_L) + \frac{v_{\perp}}{k} B_{1\parallel} J_1(k\rho_L) \right] \quad (3.65)$$

<sup>19</sup>This comparison simply involves setting the equilibrium flows to 0, i.e.  $\underline{V} = 0$ , and neglecting the final term on the RHS of equation 56 of Ref [103] which represents the nonlinearity.

where  $R_{ni}$  contains the gyroaveraged nonlinear interactions and is given by

$$R_{ni} = \frac{\nabla g}{B} \cdot \underline{b} \times \nabla_{\perp} \quad (3.66)$$

The nonlinear interactions can complicate solution of the GKE but provide effects important for quantitative calculations. For example, the fluctuation amplitude will saturate, allowing the quantitative calculation of heat and particle fluxes.



# Chapter 4

## Using the gyrokinetic equation

### 4.1 Numerical simulations

The electromagnetic gyrokinetic equation, such as that given in eqn. 3.65, describes the evolution of the non-adiabatic component of the perturbed distribution function,  $g$ , for a given system. Solutions of the GKE and the related gyrokinetic Maxwell's equations provide details of the fluctuating plasma parameters, such as density, and EM fields, giving insight into the processes driving transport. Analytical solution of the linear GKE is possible only under certain limits; analytic theory typically neglects important physics and is generally only applicable to simplified geometries. Such solutions can prove to be useful for exploring some of the underlying instability characteristics, but to study the full physical system it is necessary to adopt a numerical approach.

As computational power has increased over the years it has become possible to develop codes using increasingly complete gyrokinetic models, representing more realistic scenarios. Advanced algorithms and numerical schemes taking advantage of the properties of tokamaks have led to further reductions in computational cost and a large number of gyrokinetic simulation codes currently exist which can routinely solve the full linear and nonlinear GKE. Such advances and improvements in understanding and computational capabilities have led to the ability to study experimental discharges using gyrokinetic codes, providing insight into the physical processes driving the observed transport.

#### 4.1.1 Numerical approaches

There are several possible approaches that can be taken to numerically solve the GKE, which is reflected in the large number of gyrokinetic codes currently in exist-

ence. Such a range is useful as it provides means to independently benchmark the results from different codes in order to provide confidence in the conclusions drawn. Gyrokinetic codes can be classified on a variety of characteristics including the numerical scheme used and the physics contained. A few of the key characteristics are given in table 4.1 along with typical options, for a more complete discussion of the different approaches adopted in gyrokinetic codes the reader is referred to Ref [104].

Characteristic		
Fields	Electrostatic	Electromagnetic
GKE	Linear	Nonlinear
Electron model	Adiabatic	Gyrokinetic
Numerical approach	Eulerian	Lagrangian
Spatial domain	Local	Global

**Table 4.1:** A summary of important characteristics for gyrokinetic codes.

The first two characteristics simply describe the specific gyrokinetic system being solved whilst the third denotes whether the electrons are assumed to be adiabatic or if the electron GKE is used (often referred to as kinetic electrons)<sup>1</sup>. The numerical approach taken can be split into two main approaches: Eulerian (or continuum) codes which solve the equations on a fixed grid or hybrid-Lagrangian codes, known as particle in cell (PIC) codes, which adopt a marker tracking (or moving grid) type approach combined with fixed grids for the field calculations<sup>2</sup>. These approaches have significantly different numerical properties making them useful for independent benchmarking. The final characteristic discussed here refers to the simulations spatial domain, specifically how the poloidal and radial directions are treated. The treatment of the radial domain is an important topic in this thesis.

#### 4.1.1.1 Radially local vs. global

If the radial length scale of equilibrium profile variations,  $L_{eq}$ , is much larger than the characteristic radial size of drift instabilities,  $\sim \mathcal{O}(\rho_i)$ , then it is possible to apply a simplification to the GKE known as the local approximation. In this approximation<sup>3</sup> it is assumed that the equilibrium parameters are constant over the radial extent of the instability (whilst retaining non-zero gradients), introducing a degeneracy in the radial direction. It is then possible to transform the underlying equations to

<sup>1</sup>It should be noted that electromagnetic codes can include the electrostatic limit, nonlinear codes can be run as linear codes and codes with kinetic electrons can also use adiabatic electrons.

<sup>2</sup>In fact there is a third numerical approach, known as semi-Lagrangian, in which, rather than tracking the trajectory of specific particles as time advances as done in Lagrangian codes, at each time step the origin of particles on a fixed grid is calculated by finding their reverse trajectories. The particles properties can then be calculated through interpolation from the fixed grids onto the particles starting position. This approach is used in the gyrokinetic code GYSELA [105].

<sup>3</sup>This approximation and its application will be discussed in greater detail in chapter 5.

remove the radial dimension from the problem. This process yields the local GKE which is solved on a single flux surface, resulting in reduced computational demands compared to the global solution.

Gyrokinetic codes which do not use this approximation are known as global codes and retain the effects of radial profile variations. Global codes are therefore capable of simulations involving large radial domains covering many flux surfaces. This increased simulation domain significantly increases the computational cost of these global codes, but with the advent of large scale supercomputers their use has become more routinely feasible. Taking  $L_{eq}$  to represent the equilibrium variation and  $\rho_L$  to represent the mode size then the limit  $\rho_* \rightarrow 0$  represents the regime in which the local approximation is strictly valid. For large tokamaks, such as JET and ITER,  $\rho_*$  is indeed small in the core whilst near the edge and in other tokamaks, such as MAST,  $\rho_*$  can be larger and the local approximation will become less valid. Comparisons between global and local codes typically agree in the limit  $\rho_* \rightarrow 0$  [106, 107]. A more detailed study of the relationship between local and global representations and their solutions is the topic of chapter 5.

## 4.2 Challenges for gyrokinetics

There has been large progress made in the study of fluctuations over the past few decades, aided by increasing computational performance and diagnostic capabilities. It is now possible to provide quantitative predictions of transport properties in a range of experimental situations, and varying levels of agreement are found between predictions and experiment depending on the scenario studied [108, 109]. Despite this, the theoretical study of fluctuation driven transport is far from complete and there remain unresolved challenges which must be addressed.

The cyclical formation and collapse of edge transport barriers observed when operating in H-mode limits the obtainable barrier width and height, thereby limiting the maximum plasma performance achieved during H-mode. To make predictions of the performance of ITER it is important to understand this cycle. A model based on MHD stability constraints, known as EPED [110], has proved successful in predicting the barrier properties immediately prior to the collapse. The potential damage resulting from the energy and particles ejected during the barrier collapse, or ELM, is a key concern for ITER and techniques to reduce, or mitigate, the impact of these ELMs or remove them entirely are being investigated [111, 112]. The evolution of the edge barrier between two natural ELMs is dependent on the transport in the edge region due to microinstabilities. By understanding this evolution in terms of the microinstability behaviour, insight may be gained into the mechanisms behind

the current ELM mitigation techniques, which are currently not fully understood. Unfortunately as the normalised fluctuation amplitudes approach 1 near the edge, the gyrokinetic orderings used in chapter 3 break down. It is necessary to adopt a new approach. Similar issues are of relevance to gyrokinetics inside transport barriers where the local value of  $\rho_*$  (determined by  $\rho_L/L_n$  for example) is relatively large and global effects can become significant. An area of significant research focus is the development of a gyrokinetic formulation and codes suitable for edge regions and transport barriers. There has been significant progress in this area [113–115] and prototype codes have been developed to start to test possible numerical implementations [116–118]. There is however, still a long way to go before physically relevant edge gyrokinetic simulations are routinely feasible. A study of the microstability evolution in the edge region during an ELM cycle for the spherical tokamak MAST is presented in chapter 6. Whilst the formulation of gyrokinetics used here is not one developed for the edge region (and therefore the accuracy of the results is limited) this study can be viewed as a first step towards a complete treatment and can provide some preliminary insight into the physics involved.

The L-H transition and the formation of internal transport barriers are thought to be related to the suppression of turbulent fluctuations but it has not been possible to show the spontaneous formation of transport barriers in current codes. As mentioned previously, this suppression is often postulated to be due to sheared flows which can be large in current generation tokamaks with neutral beam heating. ITER will have neutral beam heating but the resulting rotation is expected to be relatively low (with a Mach number  $M = v_\varphi/v_{th_i} \approx 0.05$ ) [91, 119] and hence sheared flow suppression may be a weak process. It is however possible to get self generated spontaneous rotation in the plasma due to momentum transport processes [120] and the calculation of such momentum transport is currently being integrated into a number of gyrokinetic codes [121–123]. Momentum transport can be enhanced by various symmetry breaking processes [124] and it will be shown in chapter 5 that profile variations can contribute to this symmetry breaking.

### 4.3 Topics addressed in this thesis

A comparison between local and global models for a reduced linear gyrokinetic ITG model is presented in chapter 5 in order to explore the relation between these representations. Earlier work on this model [125] finds two classes of solution depending upon the profiles present. This finding is explored numerically in order to test the behaviour of these two classes of mode against the predictions implicit in earlier work [125, 126]. Typically, local codes are currently only capable of treating the less general of these two classes. The possibility of incorporating these profile effects into

existing local codes, such that they can treat both classes of mode, is explored. This would offer a means to leverage existing well developed local codes to perform studies including profile effects, allowing estimates of the resulting symmetry breaking for example.

Whilst the physics of transport barrier formation and evolution remain elusive, predictive models for the H-mode pedestal behaviour are of key importance to predictions of tokamak performance. The EPED predictive model has been tested against a number of large aspect ratio tokamaks and generally shows good agreement with experiment in these cases [127]. This model is based upon a combination of MHD and gyrokinetic instabilities and will be discussed in more detail in chapter 6. In practice the gyrokinetic stability is not usually calculated due to the difficulties of operating near the edge, and simpler models are used instead. To address how well these simple models represent the gyrokinetic stability, and to investigate the applicability of the EPED model to STs, a gyrokinetic study of the H-mode pedestal region on MAST has been performed. In particular the linear gyrokinetic stability has been probed using the local gyrokinetic code GS2<sup>4</sup> [128] at several times between two ELMs such that the effect of the evolution of the pressure profile on the microinstabilities can be investigated. Whilst the gyrokinetic model in GS2 is not derived for use in the edge, the use of such a tool provides a step towards a rigorous gyrokinetic treatment of the pedestal. An interesting transition between two classes of instability is observed at the interface between the shallow and steep gradient regions, and may be of importance for the pedestal evolution.

---

<sup>4</sup>A detailed overview of GS2 is available in Ref [129].



# Chapter 5

## On local approximations to global gyrokinetic theory

### 5.1 An introduction to ballooning theory

Linear potential perturbations in an axisymmetric system, such as  $\phi = \phi(r, \theta, \varphi)$ , can be Fourier decomposed in the toroidal direction to obtain,  $\phi = \phi(r, \theta) \exp(in\varphi)$ , where  $n$  is the toroidal mode number. In cylindrical and plane slab geometries it is also possible to decouple poloidal harmonics by decomposing poloidally such that  $\phi = \phi(r) \exp(i[n\varphi + m\theta])$ , with  $m$  the poloidal mode number<sup>1</sup>. The mode will be strongly resonant at the rational (or resonant) surface where  $q = m/n$  and the perturbation is exactly aligned with the magnetic field lines. This results in constant amplitude along the closed field lines as illustrated in figure 5.1.

In such systems these Fourier modes are entirely independent and depend only upon the conditions near the relevant resonant location. These modes are damped by a small amount of magnetic shear [97, 130] and so would not initially be expected in experimentally relevant situations. In more realistic geometry, where the magnetic field varies around a flux surface, modes with different  $m$  can couple together in such a way as to minimise this shear damping [131], thereby resulting in unstable modes which stretch across multiple rational surfaces. The behaviour of these coupled systems is somewhat more complex than the simple uncoupled behaviour, being both two dimensional and radially extended. However, provided the radial extent of the mode is small relative to that of equilibrium variations it is possible to exploit the resulting scale separation to simplify the problem, making its solution more feasible, and this is the subject of this chapter.

---

<sup>1</sup>In a plane slab geometry,  $\{x, y, z\}$ , the poloidal,  $\theta$ , and toroidal,  $\varphi$ , directions become the two periodic, perpendicular directions  $\{y, z\}$ , whilst in cylindrical geometry,  $\{r, \theta, z\}$ , the toroidal direction is mapped to  $z$ .

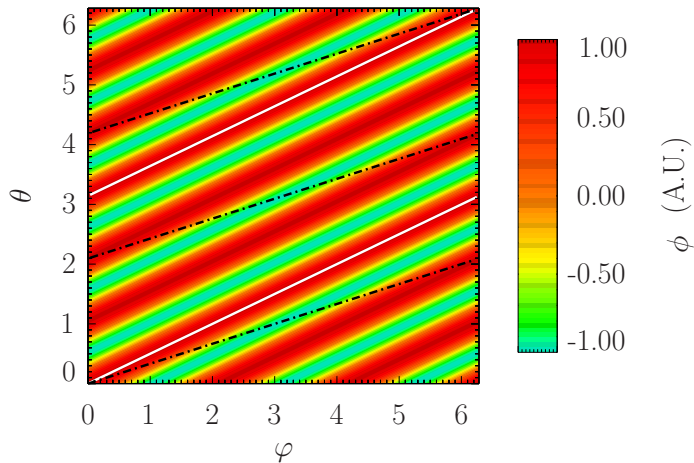


**Figure 5.1:** The perturbed potential in slab geometry for a mode with poloidal mode number,  $m = 6$ , and toroidal mode number,  $n = 3$ . A magnetic field line with  $q = m/n = 2$  is shown by the solid white line and is aligned with the perturbation such that the perturbation amplitude is constant along the field line. A magnetic field line with  $q = 3$  is shown by the dashed black line; this field line is not aligned with the perturbation and as such effectively short circuits the perturbation.

When there is strong separation between equilibrium and Larmor orbit length scales the ordering  $\rho_* \ll 1$  is satisfied and can be exploited to simplify the system. The applicability of radial scale separation is not restricted to the separation between equilibrium and Larmor orbit length scales; indeed the first demonstration of the local approach was for an MHD model [132] where strong separation between the rational surface spacing and the length scale associated with equilibrium variations was required. This separation is characterised by the ordering  $\Delta/L \ll 1$ , where  $\Delta = 1/nq'$  is the distance between neighbouring rational surfaces<sup>2</sup> and  $q'$  is the radial gradient of the safety factor,  $q$ . Hence, assuming  $q' \sim \mathcal{O}(1)$ , in the limit  $n \rightarrow \infty$  there is a separation of radial scales, which suggests a simplification can be made by adopting an Eikonal representation for the perturbation of the form:

$$\phi(r, \theta, \varphi) = A(r, \theta) \exp \left[ in \left( \varphi - \int^\theta q^* d\theta \right) \right] \quad (5.1)$$

where  $A$  is a slowly varying amplitude envelope and  $q_* = rB_\varphi/B_\theta R$  is the local safety factor such that  $q = (2\pi)^{-1} \oint q_* d\theta$ . The phase,  $n \left( \varphi - \int^\theta q^* d\theta \right)$ , is constant along a field line but in the limit  $n \rightarrow \infty$  varies rapidly across flux surfaces, representing the important characteristic  $k_{\parallel} \ll k_{\perp}$ . For the rest of this chapter the toroidal behaviour will be described solely by the toroidal mode number,  $n$ , and no explicit dependence on  $\varphi$  will be seen but can be recovered by multiplying by  $\exp(in\varphi)$ .

<sup>2</sup>Noting that  $nq = m = k_\theta r$  and  $\hat{s} = (r/q)(dq/dr)$  it can be seen that  $nq' \equiv k_\theta \hat{s}$  and hence for  $k_\theta \sim 1/\rho_L$  and  $\hat{s} \sim \mathcal{O}(1)$  the parameter  $\Delta = 1/nq' = 1/k_\theta \hat{s}$  is approximately equivalent to  $\rho_L$  and hence in this regime the scale separation ordering based on rational surface separation is equivalent to the  $\rho_*$  ordering used earlier.

The requirement for periodicity in  $\theta$  of eqn. 5.1 is given by:

$$A(r, \theta + 2\pi) - A(r, \theta) \exp(in2\pi q) = 0 \quad (5.2)$$

Taking the radial derivative of this leads to

$$A'(r, \theta + 2\pi) - A'(r, \theta) \exp(in2\pi q) = in2\pi q' A(r, \theta) \quad (5.3)$$

For the eikonal approach to be valid it is required that  $A$  varies slowly, specifically that  $A'/A \ll nq'$ . This means that eqn. 5.3 can only be satisfied at all locations if  $nq' \ll 1$  everywhere. As  $n$  is large this condition highlights that the eikonal representation, eqn. 5.1, is only valid for infinitesimal  $q'$  and hence, for the realistic case of sheared magnetic fields, is not applicable [133].

In order to take advantage of the spatial scale separation through the use of an eikonal form it is necessary to find a representation for  $\phi(r, \theta)$  which avoids the problem of the periodicity constraint. One technique is to map the problem from the finite  $\theta$  domain, periodic between  $-\pi$  and  $\pi$ , to the infinite domain,  $\eta$ , often referred to as the ballooning coordinate. This takes advantage of the fact that any periodic function,  $f(\theta)$ , can be represented by another function on the infinite domain,  $\hat{f}(\eta)$  through the relation:

$$f(\theta) = \sum_m \int_{-\infty}^{\infty} \hat{f}(\eta) \delta(\eta - \theta - 2\pi m) d\eta \quad (5.4)$$

where  $\delta$  is the Dirac delta function<sup>3</sup> and  $\hat{f}(\eta)$  provides the weight for the contribution of each delta function to the periodic function. This representation samples the infinite function at intervals of  $2\pi$  and sums these to give the value of a periodic function at  $\theta$ , which is illustrated pictorially in figure 5.2.

The integral in eqn. 5.4 must converge in order for this representation to be applicable; this implies the boundary condition  $\hat{f}(\eta) \rightarrow 0$  for  $\eta \rightarrow \pm\infty$ . Making use of the relation<sup>4</sup>:

$$2\pi \sum_n \delta(r - 2\pi n) = \sum_m e^{imr} \quad (5.5)$$

allows eqn. 5.4 to be written as

$$f(\theta) = (2\pi)^{-1} \sum_m \int_{-\infty}^{\infty} \hat{f}(\eta) e^{im(\eta-\theta)} d\eta \quad (5.6)$$

This representation is equivalent to that introduced in Ref [132], known as the bal-

<sup>3</sup>It can be noted that the summation of delta functions represented here is often referred to as the Dirac comb,  $\delta_N$ . The resulting integral can be seen to be sampling the function  $\hat{f}(\eta)$  with a sampling period of  $2\pi$ .

<sup>4</sup>This is an example of the Poisson summation formula.

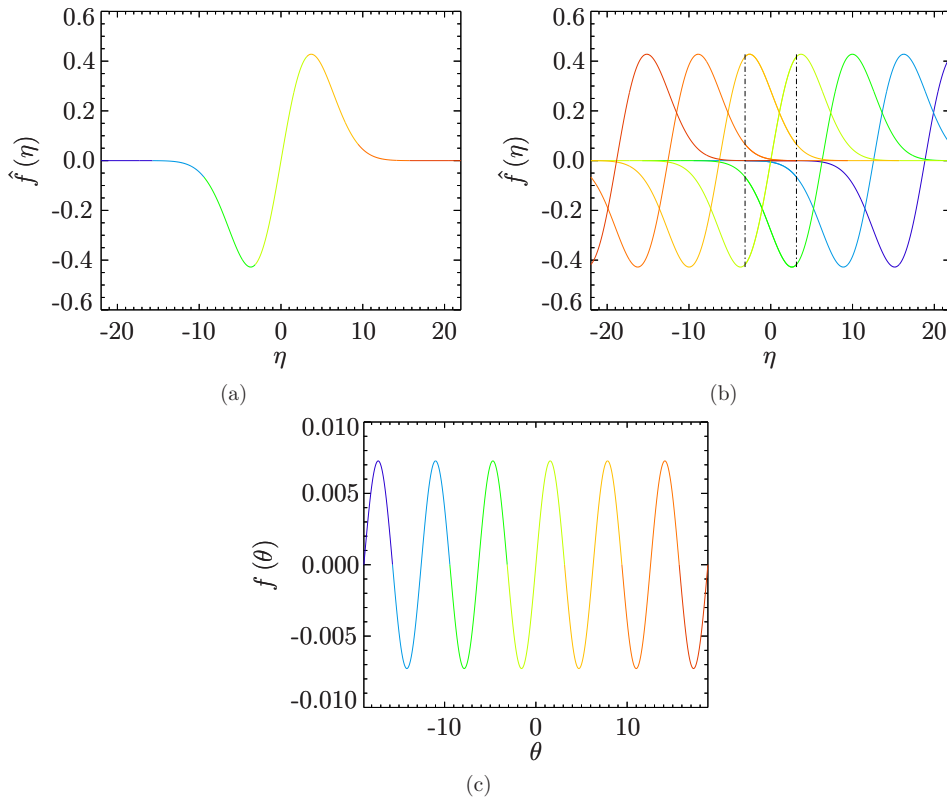


**Figure 5.2:** The procedure to map a function on the infinite domain,  $\hat{f}(\eta)$ , to a function on the periodic domain,  $f(\theta)$ , is illustrated schematically by figure 5.2(a), figure 5.2(b) and figure 5.2(c). The initial function on the infinite domain is shown in figure 5.2(a), by summing over the function sampled at  $2\pi$  intervals (or equivalently summing over an infinite number of copies of the function each shifted by integer multiple of  $2\pi$  as illustrated by figure 5.2(b)) a periodic function will be constructed provided  $\hat{f}(\eta) \rightarrow 0$  as  $\eta \rightarrow \pm\infty$ .

looning transform, where a Fourier representation for  $\phi$  was adopted

$$\phi(r, \theta) = \sum_m A_m e^{-im\theta} \quad (5.7)$$

and the amplitude coefficients,  $A_m$ , are represented according to eqn. 5.6 as integrals over the infinite ballooning domain:

$$\phi(r, \theta) = \sum_m e^{-im\theta} \int_{-\infty}^{\infty} e^{im\eta} \hat{\phi}(r, \eta) d\eta \quad (5.8)$$

It is important to highlight that the representation given in eqn. 5.8 ensures periodicity in  $\theta$  for any  $\hat{\phi}$ , which vanishes for  $\eta \rightarrow \pm\infty$ .

Following Ref [132] the ballooning transformation allows the original system, which is described by the generic 2D eigenvalue equation in  $r$ - $\theta$ :

$$(\mathcal{L}(r, \theta) - \lambda) \phi(r, \theta) = 0 \quad (5.9)$$

to be mapped to one in  $r$ - $\eta$ :

$$(\mathcal{L}(r, \eta) - \lambda) \hat{\phi}(r, \eta) = 0 \quad (5.10)$$

where the eigenvalue,  $\lambda$ , is the same in both cases<sup>5</sup>. This means the true, periodic, problem has been replaced with one in the  $r$ - $\eta$  domain with the same eigenvalue. The advantage of this is that the periodic boundary conditions in  $\theta$ , which prevent an eikonal approach, have been replaced with conditions on  $\eta \rightarrow \pm\infty$ , specifically that  $\hat{\phi} \rightarrow 0$  for  $\eta \rightarrow \pm\infty$  such that the integration in eqn. 5.8 converges. This allows an eikonal representation for  $\hat{\phi}$ :

$$\hat{\phi}(x, \eta) = A(x, \eta) e^{-inq'[x\eta - S(x)]} \quad (5.11)$$

where  $x$  is the radial variable,  $x = r - r_s$  with  $r_s$  some reference rational surface position, and the amplitude function  $A(x, \eta)$  is slowly varying. The function  $S(x)$  is constant on a field line and varies slowly with  $x$  such that the phase factor  $\exp(inq'S(x))$  describes rapid variation in the perpendicular direction but is constant along the field line describing  $k_{\parallel} \ll k_{\perp}$  as in eqn. 5.1. Taking the radial derivative of eqn. 5.11 and taking the leading order terms gives

$$\frac{\partial}{\partial x} \rightarrow inq' \left( \frac{dS(x)}{dx} - \eta \right) \quad (5.12)$$

Comparing with the Fourier derivative representation  $d/dx \rightarrow ik_x$  it is seen that  $dS/dx$  can be related to the radial wavenumber  $k_x$  (evaluated at  $\eta = 0$ ) and hence the shorthand

$$\frac{dS(x)}{dx} = k \quad (5.13)$$

will be used throughout the remainder of the chapter.

By expanding the operator,  $\mathcal{L}$ , in orders of  $1/nq'$  it is possible to obtain the lowest order equation, which describes the behaviour of  $\hat{\phi}(x, \eta)$  in the absence of profile variations (which only enter at the next order in  $1/nq'$ ). This lowest order equation is the ‘‘local’’ representation of the problem, and it will be shown in section 5.2.2 that this takes the form of an ordinary differential equation in  $\eta$ . The solution of the local equation determines  $\hat{u}(\eta)$  for specified  $x$  and  $k$ . The local frequency,  $\Omega_0(x, k)$ , emerges as an eigenvalue of the local equation and it is important to note that its value depends on both  $x$  and  $k$ . At this stage both  $x$  and  $k$  are free parameters with no conditions placed upon their selection; it is only with consideration of terms at higher order in  $1/nq'$  that these free parameters are determined. To be able to relate  $\Omega_0$  to the true, global frequency,  $\Omega$ , it is crucial to select  $x$  and  $k$  carefully. These

---

<sup>5</sup>An illustration of this will be given later for specific operators corresponding to a simplified gyrokinetic ITG model.

higher order considerations are not typically accounted for in local gyrokinetic codes despite their potential importance.

In order to investigate the importance of these higher order profile effects, and to numerically validate the theoretical findings implicit in the earlier literature, a reduced gyrokinetic ITG model has been studied. The reduced model takes the form of a 2D eigenvalue equation for the perturbed potential,  $\phi_1(x, \theta)$ , and retains the effects of profile variations. This global model, discussed in section 5.2.1, describes the electrostatic ITG mode in a simple toroidal geometry and was first introduced in the form used here in Ref [134]. Taking the limit of large  $n$  it is possible to obtain the local limit of the global model, and this is discussed in section 5.2.2.

The simplifications applied in deriving the global model make numerical solution feasible over a large range of toroidal mode numbers, and here the global ITG mode is studied for  $n$  in the range  $\sim 20 < n < 2000$ . Hence by comparing the global model in the limit of large  $n$  with the local model, we will investigate how best to treat  $x$  and  $k$  in applications of the local representation, such as in local gyrokinetic codes.

## 5.2 A gyrokinetic toroidal ITG model

Whilst the two fluid ITG model introduced in section 3.2.2 provided some insight into the underlying physical mechanisms behind the ITG mode it neglects many important effects which can significantly modify its behaviour. This neglect is due in part to the simplified geometry and the fluid species treatment adopted in order to make the analytic study tractable. The toroidal ITG model derived here improves on this simple two fluid picture, treating a large aspect ratio concentric circular cross-section toroidal system. A consequence of the large aspect ratio assumption is that the magnetic drift frequency,  $\omega_D$ , is much smaller than the real mode frequency<sup>6</sup> such that:

$$\omega_D = 2\epsilon_n \omega_{*i}^n \ll \omega \quad (5.14)$$

where  $\epsilon_n = L_n/R$  and  $\omega_{*i}^n = -\omega_{*e}^n/\tau$ . The electrons are once again taken to be adiabatic, and specifically the ordering

$$k_{\parallel} v_{the} \gg \omega \gg k_{\parallel} v_{thi} \quad (5.15)$$

is assumed. The ion species is treated using a gyrokinetic description, which retains finite larmor radius (FLR) effects, which can modify the ion dynamics.

---

<sup>6</sup>This can be seen to be as a consequence of the two separate orderings  $\omega_{*i}^n \approx \omega$  and  $L_n \approx a$  in combination with the large aspect ratio ordering,  $a/R \ll 1$ .

### 5.2.1 The global model

The global model derivation relies upon applying quasineutrality in conjunction with expressions for the ion and electron perturbed densities in order to obtain an equation for the perturbed potential,  $\phi_1$ . The adiabatic electron approximation sets the electron perturbed density to be

$$n_{1e} = n_0 \frac{e\phi_1}{T_e} \quad (5.16)$$

where  $n_0$  is the equilibrium ion and electron density. The perturbed ion density,  $n_{1i}$ , is simply

$$n_{1i} = \int f_1^1 \underline{dv}^3 \quad (5.17)$$

with  $f_1^1$  (the perturbed distribution function to leading order in  $\rho_*$ ) given by the leading order gyrokinetic equation, eqn. 3.56. Assuming  $f_0^1$  (the equilibrium distribution function) is given by the isotropic Maxwellian distribution,  $f_M$ ,

$$f_M = n(r) \left( \frac{m}{2\pi T(r)} \right)^{3/2} \exp\left(-\frac{m\kappa}{T(r)}\right) \quad (5.18)$$

with  $\kappa = v^2/2$ , eqn. 3.56 then reduces to

$$f_1^1 = -\frac{e\phi_1}{T} f_M + g \exp(-i\mathbf{k} \cdot \boldsymbol{\rho}_i) \quad (5.19)$$

Substituting this into eqn. 5.17 yields

$$n_{1i} = -n_0 \frac{e\phi_1}{T_i} + \int g \exp(-i\mathbf{k} \cdot \boldsymbol{\rho}_i) \underline{dv}^3 \quad (5.20)$$

Applying quasineutrality then expresses  $\phi_1$  as a velocity integral of the non-adiabatic component of the perturbed distribution function,  $g$ :

$$n_0 \frac{e\phi_1}{T_e} (1 + \tau) = \int g \exp(-i\mathbf{k} \cdot \boldsymbol{\rho}_i) \underline{dv}^3 \quad (5.21)$$

with  $\tau = T_e/T_i$ . Expanding  $\underline{dv}^3$  as  $v_\perp dv_\perp dv_\parallel d\alpha$  and noting  $\mathbf{k} \cdot \boldsymbol{\rho}_i = k_\perp v_\perp \sin(\alpha) / \omega_c$ , eqn. 5.21 becomes

$$n_0 \frac{e\phi_1}{T_e} (1 + \tau) = 2\pi \int_{-\infty}^{\infty} \int_0^{\infty} g J_0(z) v_\perp dv_\perp dv_\parallel \quad (5.22)$$

where the relation

$$\int_0^{2\pi} \exp(-i\mathbf{k} \cdot \boldsymbol{\rho}_i) d\alpha = \int_0^{2\pi} \exp(-ik_\perp \rho_i \cos \alpha) d\alpha = 2\pi J_0(z) \quad (5.23)$$

with  $z = k_\perp v_\perp / \omega_c$  has been used to represent the integral over the gyrophase,  $\alpha$ .

The non-adiabatic component,  $g$ , is described by the GKE, eqn. 3.61, which after making the substitution  $\partial/\partial t \rightarrow -i\omega$  and neglecting magnetic perturbations becomes:

$$\left[-i\omega + (v_{\parallel}\underline{b} + \underline{v}_D) \cdot \underline{\nabla}\right] g = -\frac{\underline{\nabla}f_M}{B} \cdot \underline{b} \times \underline{\nabla}_{\perp}\phi_1 J_0(z) + i\omega\phi_1 J_0(z) \frac{q}{m} \frac{\partial f_M}{\partial \kappa} \quad (5.24)$$

where the ion species subscript has been neglected. Using eqn. 5.18 to evaluate the derivatives of  $f_M$  on the RHS of eqn. 5.24 gives

$$\frac{\partial f_M}{\partial \kappa} = -\frac{m}{T_i} f_M \quad (5.25)$$

$$\underline{\nabla}f_M = \left[1 + \eta_i \left(\frac{v^2}{v_{thi}^2} - \frac{3}{2}\right)\right] \frac{f_M}{L_n} \hat{e}_r = \alpha \frac{f_M}{L_n} \hat{e}_r \quad (5.26)$$

where  $\eta_i = L_{ni}/L_{Ti}$  and  $\alpha$  is given by

$$\alpha = \left[1 + \eta_i \left(\frac{v^2}{v_{thi}^2} - \frac{3}{2}\right)\right] \quad (5.27)$$

Substituting eqn. 5.25 and eqn. 5.26 into eqn. 5.24 and letting  $\underline{\nabla} \rightarrow i\underline{k}$  this becomes

$$\left[v_{\parallel} \frac{\partial}{\partial \hat{e}_{\parallel}} + i(\underline{k} \cdot \underline{v}_D - \omega)\right] g = i \frac{q}{T_i} \left[\frac{\omega_{*e}^n \alpha}{\tau} - \omega\right] f_M \phi_1 J_0(z) \quad (5.28)$$

where  $\omega_{*e}^n$  is given by

$$\omega_{*e}^n = -\frac{k_y T_e}{q B L_n} \quad (5.29)$$

and  $\partial/\partial \hat{e}_{\parallel}$  is the parallel derivative term,  $\underline{b} \cdot \underline{\nabla}$ , given by

$$\frac{\partial}{\partial \hat{e}_{\parallel}} = \underline{b} \cdot \left(\frac{\hat{e}_{\theta}}{r} \frac{\partial}{\partial \theta} + \frac{\hat{e}_{\varphi}}{R_0 + r \cos(\theta)} \frac{\partial}{\partial \varphi}\right) \approx \frac{b_{\theta}}{r} \frac{\partial}{\partial \theta} + \frac{inb_{\varphi}}{R} = \frac{b_{\varphi}}{Rq} \left(\frac{\partial}{\partial \theta} + inq\right) \quad (5.30)$$

Here, the known toroidal variation,  $\exp(in\varphi)$  has been used to replace the toroidal angle derivative with  $in$ . The drift velocity due to the magnetic geometry,  $\underline{v}_D$ , is given by

$$\underline{v}_D = \frac{\underline{b} \times \underline{\nabla}B}{\omega_c} \left[\frac{\mu}{m} + \frac{v_{\parallel}^2}{B}\right] \quad (5.31)$$

Noting that  $B \approx R_0 B_0/R$ , with  $B_0$  the magnetic field strength on the magnetic axis, and for a circular cross-section  $R = R_0(1 + (r/R_0)\cos\theta)$ , applying the large aspect ratio approximation,  $r/R_0 \ll 1$  [135] gives the magnetic field strength as

$$B = B_0 \left(1 - \frac{r}{R} \cos(\theta)\right) \quad (5.32)$$

This allows  $\underline{k}_\perp \cdot (\underline{b} \times \nabla B)$  to be written as

$$\begin{aligned} \underline{k}_\perp \cdot (\underline{b} \times \nabla B) &= -\frac{1}{R_0} [\sin(\theta) \hat{e}_r + \cos(\theta) \hat{e}_\theta] \cdot [k_r \hat{e}_r + k_\theta \hat{e}_\theta] \\ &= -\frac{k_\theta}{R_0} \left[ \cos(\theta) + \frac{k_r}{k_\theta} \sin(\theta) \right] \end{aligned} \quad (5.33)$$

The magnetic drift frequency can then be written as

$$\underline{k}_\perp \cdot \underline{v}_D = \frac{\omega_D}{2} \left( \frac{2v_\parallel^2}{v_{thi}^2} + \frac{v_\perp^2}{v_{thi}^2} \right) \left[ \cos(\theta) + \frac{k_r}{k_\theta} \sin(\theta) \right] = \bar{\omega}_D \quad (5.34)$$

with  $\omega_D$  defined in eqn. 5.14. Rearranging eqn. 5.28 and treating the parallel derivative as small,  $v_\parallel \partial / \partial \hat{e}_\parallel \ll (\bar{\omega}_D - \omega)$ , allows an expression for  $g$  to be found to  $\mathcal{O}(\delta^2)$ <sup>7</sup>:

$$g = \frac{q}{T_i} \frac{f_M J_0(z)}{\omega - \bar{\omega}_D} \left[ \omega - \frac{\omega_{*e}^n \alpha}{\tau} \right] \left( 1 - i \frac{\delta}{(\omega - \bar{\omega}_D)} - \frac{\delta^2}{(\omega - \bar{\omega}_D)^2} \right) \phi_1 \quad (5.35)$$

where  $\delta$  is given by

$$\delta = v_\parallel \frac{\partial}{\partial \hat{e}_\parallel} \quad (5.36)$$

Taking advantage of the small magnetic drift frequency ordering,  $\omega_D \ll \omega$ , a secondary expansion of eqn. 5.35 in  $\Delta = \bar{\omega}_D / \omega$  can be performed to give:

$$g = \frac{q}{T_i} f_M J_0(z) \left[ 1 - \frac{\omega_{*e}^n \alpha}{\omega \tau} \right] \left( 1 + \Delta - i \frac{\delta}{\omega} - i \frac{2\delta\Delta}{\omega} - \frac{\delta^2}{\omega^2} \right) \phi_1 \quad (5.37)$$

Substituting eqn. 5.37 into eqn. 5.22 yields

$$\begin{aligned} \phi_1 \frac{(1 + \tau)}{\tau} &= \frac{2}{v_{thi}^3 \sqrt{\pi}} \\ \int_{-\infty}^{\infty} \int_0^{\infty} e^{\frac{-v_\parallel^2 - v_\perp^2}{v_{thi}^2}} \left( 1 - \frac{k_\perp^2 v_\perp^2}{2\omega_c^2} \right) \left[ 1 - \frac{\omega_{*e}^n \alpha}{\omega \tau} \right] \left( 1 + \Delta - \frac{\delta^2}{\omega^2} \right) \phi_1 v_\perp dv_\perp dv_\parallel & \quad (5.38) \end{aligned}$$

where terms even in  $v_\parallel$  have been dropped as they integrate to zero and the Bessel function has been expanded for  $k_\perp v_\perp \ll \omega_c$  using  $J_0^2(z) \approx 1 - z^2/2$  for small  $z$ . Expanding the brackets on the RHS of eqn. 5.38, neglecting products of small para-

<sup>7</sup>It is necessary to keep terms of order  $\delta^2$  in order to retain parallel dynamics in the final result as in the upcoming velocity integral terms linear in  $\delta$  will integrate to zero.

meters, leads to

$$\phi_1 \frac{(1+\tau)}{\tau} = \frac{2}{v_{thi}^3 \sqrt{\pi}} \int_{-\infty}^{\infty} \int_0^{\infty} e^{-\frac{v_{\parallel}^2 - v_{\perp}^2}{v_{thi}^2}} \left[ -\frac{\eta_i (v_{\parallel}^2 + v_{\perp}^2)}{v_{thi}^2 \Omega \tau} + \left(1 + \frac{3\eta_i}{2\Omega\tau} - \frac{1}{\Omega\tau}\right) \right. \quad (5.39)$$

$$\left. \left(1 - \frac{\epsilon_n}{\tau\Omega} \left[ \cos(\theta) + \frac{k_r}{k_{\theta}} \sin(\theta) \right] \left[ \frac{2v_{\parallel}^2}{v_{thi}^2} + \frac{v_{\perp}^2}{v_{thi}^2} \right] - \frac{k_{\perp}^2 v_{\perp}^2}{2\omega_c^2} - \frac{v_{\parallel}^2}{\Omega^2 \omega_{*e}^n} \frac{\partial^2}{\partial l^2} \right) \right] \phi_1 v_{\perp} dv_{\perp} dv_{\parallel}$$

where  $\Omega = \omega/\omega_{*e}^n$  is the normalised mode frequency. The integral in eqn. 5.39 can be evaluated by noting that the integration over velocity space only involves terms of the general form

$$I_{p,q} = \int_{-\infty}^{\infty} \exp\left(-\frac{v_{\parallel}^2}{v_{thi}^2}\right) v_{\parallel}^p \int_0^{\infty} \exp\left(-\frac{v_{\perp}^2}{v_{thi}^2}\right) v_{\perp}^{(q+1)} dv_{\perp} dv_{\parallel} \quad (5.40)$$

and that such integrals have the standard solution [136] of

$$I_{p,q} = \frac{v_{thi}^3 v_{thi}^{p+q}}{2} \Gamma\left(\frac{p+1}{2}\right) \Gamma\left(\frac{q+2}{2}\right) \quad (5.41)$$

where  $\Gamma(x)$  is the gamma function (or generalised factorial). The values of the gamma functions for  $p, q = 0, 2, 4$  are shown in table 5.1.

$x$	$\Gamma\left(\frac{x+1}{2}\right)$	$\Gamma\left(\frac{x+2}{2}\right)$
0	$\sqrt{\pi}$	1
2	$\frac{\sqrt{\pi}}{2}$	1
4	$\frac{3\sqrt{\pi}}{5}$	2

**Table 5.1:** Values of the gamma function for selected arguments, including those required to evaluate the velocity integrals in eqn. 5.40.

Expressing eqn. 5.39 in terms of the generic integral form, eqn. 5.40 leads to

$$\phi_1 \frac{(1+\tau)}{\tau} = \frac{2}{v_{thi}^3 \sqrt{\pi}} \left[ -\frac{\eta_i}{v_{thi}^2 \Omega \tau} (I_{2,0} + I_{0,2}) + \left(1 + \frac{3\eta_i}{2\Omega\tau} - \frac{1}{\Omega\tau}\right) \right. \quad (5.42)$$

$$\left. \left( I_{0,0} - \frac{\epsilon_n}{\tau\Omega} \left[ \cos(\theta) + \frac{k_r}{k_{\theta}} \sin(\theta) \right] \left[ \frac{2I_{2,0}}{v_{thi}^2} + \frac{I_{0,2}}{v_{thi}^2} \right] - \frac{k_{\perp}^2 I_{0,2}}{2\omega_c^2} - \frac{I_{2,0}}{\Omega^2 \omega_{*e}^n} \frac{\partial^2}{\partial l^2} \right) \right] \phi_1$$

Substituting for  $I_{p,q}$  using eqn. 5.41 provides

$$\phi_1 \frac{(1+\tau)}{\tau} = \left[ -\frac{3\eta_i}{2\Omega\tau} + \left(1 + \frac{3\eta_i}{2\Omega\tau} - \frac{1}{\Omega\tau}\right) \right. \quad (5.43)$$

$$\left. \left(1 - \frac{2\epsilon_n}{\tau\Omega} \left[ \cos(\theta) + \frac{k_r}{k_{\theta}} \sin(\theta) \right] - \frac{k_{\perp}^2 v_{th}^2}{2\omega_c^2} - \frac{v_{th}^2}{\Omega^2 \omega_{*e}^n} \frac{\partial^2}{\partial l^2} \right) \right] \phi_1$$

Noting that  $\rho_i^2 = v_{th}^2/2\omega_c$  and

$$\frac{v_{th}^2}{\omega_{*e}^2} = \frac{2L_n^2}{k_y^2 \rho_i^2 \tau^2} \quad (5.44)$$

eqn. 5.43 can be simplified to

$$\left[ -\frac{2\epsilon_n}{\tau\Omega} \left[ \cos(\theta) + \frac{k_r}{k_\theta} \sin(\theta) \right] - \left( \frac{\Omega - 1}{\Omega\tau + 1.5\eta_i + 1} \right) - k_\perp^2 \rho_i^2 - \left( \frac{L_n}{k_\theta \rho_i \tau \Omega} \right)^2 \frac{\partial^2}{\partial l^2} \right] \phi_1 = 0 \quad (5.45)$$

Manipulating eqn. 5.45 and substituting for the parallel derivative from eqn. 5.30 leads to the eigenvalue equation for the perturbed potential,  $\phi_1$ :

$$\left[ \rho_s^2 \frac{\partial^2}{\partial x^2} - c - \frac{2\epsilon_n}{\Omega} \left( \cos(\theta) + \frac{i \sin(\theta)}{k_\theta} \frac{\partial}{\partial x} \right) - \left( \frac{\sigma}{\Omega} \right)^2 \left[ \frac{\partial}{\partial \theta} + inq'x \right]^2 - \frac{\Omega - 1}{\Omega + \eta_s} \right] \phi_1(x, \theta) = 0 \quad (5.46)$$

where  $x = r - r_s$  with  $r_s$  some reference rational surface,  $\rho_s^2 = \rho_i^2 \tau$ ,  $c = k_\theta^2 \rho_i^2 \tau$ ,  $\eta_s = (1 + 1.5\eta_i)/\tau$ , the substitution  $k_r \rightarrow i\partial/\partial x$  has been made and  $\sigma$  is defined as

$$\sigma = \frac{\epsilon_n}{\sqrt{cq}} \quad (5.47)$$

The first two terms in eqn. 5.46 are due to the FLR effects, the third term is due to the magnetic drifts and is known as the coupling term, the fourth term represents the parallel dynamics<sup>8</sup> whilst the fifth is the eigenvalue. The coefficients in eqn. 5.46, such as  $\epsilon_n$  and  $q$ , are free to vary with radial position,  $x$ .

### 5.2.1.1 Poloidal Fourier decomposition

Following eqn. 5.7 it is possible to introduce a poloidal Fourier decomposition of  $\phi_1$ :

$$\phi_1 = \sum_m u_m(x) e^{-im\theta} \quad (5.48)$$

---

<sup>8</sup>The expression in eqn. 5.30 has been used to give the parallel derivative. The transformation  $inq \rightarrow inq'x$  has been made by Taylor expanding  $q$  as  $q_{x_0} + q'x$  and then factoring out the constant variation at  $x_0$  given by  $im_0$ .

This allows eqn. 5.46 to be replaced with:

$$\sum_m \left[ \rho_s^2 \frac{\partial^2}{\partial x^2} - c - \frac{\epsilon_n}{\Omega} \left( \left[ 1 - \frac{1}{k_\theta} \frac{\partial}{\partial x} \right] e^{i\theta} + \left[ 1 + \frac{1}{k_\theta} \frac{\partial}{\partial x} \right] e^{-i\theta} \right) + \left( \frac{\sigma}{\Omega} \right)^2 [m - k_\theta \hat{s}x]^2 - \frac{\Omega - 1}{\Omega + \eta_s} \right] u_m(x) e^{-im\theta} = 0 \quad (5.49)$$

where  $u_m(x)$  is the  $m^{\text{th}}$  Fourier mode and  $nq'$  has been replaced by  $k_\theta \hat{s}$ . Recalling that  $ik_\theta = \nabla_\theta$  it is clear that  $k_\theta = m/r$  should vary as  $m$  varies<sup>9</sup>. As  $m = nq \gg 1$  and the change in  $m$  across the width of the mode  $\delta m \approx nq' \delta x$  the relative change in  $k_\theta$  across the mode is  $\sim q'x/q$ . Assuming  $q' \sim q/L$  then for  $\delta x \ll L$  this variation is negligible. All the coefficients in eqn. 5.49 are assumed independent of  $\theta$  (except where explicitly indicated), multiplying by  $\exp(ij\theta)$  and integrating from  $-\pi$  to  $\pi$  allows the summation over  $m$  to be eliminated to leave

$$\rho_s^2 \frac{\partial^2 u_m(x)}{\partial x^2} - c u_m(x) - \frac{\epsilon_n}{\Omega} \left( \left[ 1 + \frac{1}{k_\theta} \frac{\partial}{\partial x} \right] u_{m+1}(x) + \left[ 1 - \frac{1}{k_\theta} \frac{\partial}{\partial x} \right] u_{m-1}(x) \right) + \left( \frac{\sigma}{\Omega} \right)^2 [m - k_\theta \hat{s}x]^2 u_m(x) - \frac{\Omega - 1}{\Omega + \eta_s} u_m(x) = 0 \quad (5.50)$$

This form explicitly highlights the coupling of the  $m \pm 1$  modes into the equation for  $u_m(x)$  due to the third term (the drift term). The original 2D eigenmode equation for  $\phi_1(x, \theta)$  given in eqn. 5.46 is now represented by the set of coupled equations for  $\{u_m(x)\}$  given in eqn. 5.50. Truncating the set of equations to a given range of  $m$  provides a system which is suitable for numerical solution using a “shooting” algorithm [138], discussed in section 5.4.1.

## 5.2.2 The local model

As the toroidal mode number increases the rational surface spacing decreases and a growing separation of scales develops between the rational surface spacing and the equilibrium length scales. This leads to a situation whereby the equilibrium properties on two adjacent rational surfaces are approximately constant. In this limit the equation for  $u_{m+1}(x)$  is nearly identical to that for  $u_m(x)$  and it is possible to represent  $u_{m+1}(x)$  as simply a shifted and scaled form of  $u_m(x)$ , a property referred to as translational invariance. Specifically, under the transformation  $x \rightarrow x + 1/nq'$  and  $m \rightarrow m + 1$  eqn. 5.50 is essentially unchanged, provided the radially varying coefficients do not change noticeably (i.e.  $1/nq' \ll L_{eq}$  with  $L_{eq}$  an equilibrium length

<sup>9</sup>This was noted in Ref [137] which retains the full variation of  $k_\theta$  across the mode.

scale). It is therefore appropriate to seek solutions of the form

$$u_m(x) = u_0 \left( x - \frac{\delta m}{nq'} \right) e^{iF_m} \quad (5.51)$$

where  $\delta m = m - m_0$  with  $m_0$  the poloidal mode number corresponding to the rational surface at which  $x = 0$  and  $F_m$  is a complex number which introduces an amplitude and phase factor. It is useful to split the contribution of  $F_m$  into two components to yield

$$e^{iF_m} = A(x) e^{im\theta_0} \quad (5.52)$$

where  $A(x)$  encapsulates the slow, equilibrium length scale amplitude variation<sup>10</sup> and  $\theta_0$  is a slowly varying function of  $x$  such that  $\exp(im\theta_0)$  varies rapidly relative to  $A(x)$ .

Writing the generic radial function,  $u_0(x)$ , as a Fourier transform:

$$u_0(x) = \int_{-\infty}^{\infty} e^{im_0\eta} e^{-inq'x\eta} \hat{u}(\eta) d\eta \quad (5.53)$$

allows the perturbation to be written as

$$\phi_1(x, \theta) = \sum_m e^{im(\theta_0 - \theta)} \int_{-\infty}^{\infty} e^{i(m - nq'x)\eta} A(x) \hat{u}(\eta) d\eta \quad (5.54)$$

where the integral represents a Fourier transform between the shifted, normalised radial coordinate<sup>11</sup>,  $m - nq'x$ , and the field line coordinate,  $\eta$ . It can be seen here that  $\theta_0$  is acting as an offset to the poloidal coordinate,  $\theta$ , and as such it sets the poloidal angle where the different Fourier harmonics constructively interfere. This leads to  $\theta_0$  being referred to as the ballooning angle as the perturbation will peak, or “balloon”, at this given poloidal angle.

Comparison of eqn. 5.54 with eqn. 5.8 using eqn. 5.11 shows that this Fourier transform representation is equivalent to the ballooning transform introduced in section 5.1 provided

$$\hat{u}(\eta) A(x) e^{im\theta_0} = A(x, \eta) e^{inq'S(x)} \quad (5.55)$$

Assuming  $A(x, \eta) \approx \hat{u}(\eta) A(x)$  (strictly  $\hat{u}(\eta)$  is  $\hat{u}(\eta, x)$ ) then eqn. 5.55 is satisfied by

$$m\theta_0 = nq'S(x) \quad (5.56)$$

Noting that  $\theta_0$  is slowly varying in  $x$  and near a rational surface  $\delta m \approx nq'x$  it can be seen that

$$\theta_0 \approx \frac{dS(x)}{dx} = k \quad (5.57)$$

<sup>10</sup>Here the  $m$  dependence of  $F_m$  has been extended to a radial dependence.

<sup>11</sup>This radial coordinate is  $m_0$  on the rational surface where  $q = m/n$

and  $\theta_0$  can be related to the radial wavenumber<sup>12</sup> introduced in eqn. 5.12. It should be noted that here  $S(x)$  is complex and as such  $\theta_0$  is also complex. In order to be able to treat  $\theta_0$  as a real number it is possible to absorb the exponential term resulting from the imaginary component into the amplitude function,  $A(x) \rightarrow A^*(x) = A(x) \exp[-m\mathcal{I}(\theta_0)]$ .

Thus the ballooning representation for the radial Fourier modes is obtained:

$$u_m(x) = \int_{-\infty}^{\infty} A(x) e^{inq'S(x)} e^{i(m-nq'x)\eta} \hat{u}(\eta) d\eta \quad (5.58)$$

From eqn. 5.58 it can be seen that:

$$\begin{aligned} \frac{\partial u_m(x)}{\partial x} = \int_{-\infty}^{\infty} \left[ inq' \left( \frac{dS}{dx} - \eta \right) + in \frac{dq'}{dx} (S - x\eta) \right. \\ \left. + \frac{1}{A(x)} \frac{dA}{dx} \right] A(x) e^{inq'S} e^{i(m-nq'x)\eta} \hat{u}(\eta) d\eta \end{aligned} \quad (5.59)$$

and

$$i(m - nq'x) u_m(x) = \int_{-\infty}^{\infty} \left[ \frac{\partial}{\partial \eta} - \frac{1}{\hat{u}(\eta)} \frac{\partial \hat{u}(\eta)}{\partial \eta} \right] A(x) e^{inq'S} e^{i(m-nq'x)\eta} \hat{u}(\eta) d\eta \quad (5.60)$$

Noting that the derivatives of  $\hat{u}(\eta)$  w.r.t.  $\eta$  and  $A(x)$  w.r.t.  $x$  are small in  $nq'$  relative to the other terms (as required by the eikonal representation), and assuming  $q'$  is also slowly varying, the 0<sup>th</sup> order transformations are found<sup>13</sup>:

$$\frac{\partial}{\partial x} \rightarrow -inq' [\eta - k] \quad (5.61)$$

$$(m - nq'x) \rightarrow -i \frac{\partial}{\partial \eta} \quad (5.62)$$

Using these transformations the system of coupled equations, represented by

$$\mathcal{L}(\partial/\partial x, m - nq'x, \Omega) \{u_m(x)\} = 0 \quad (5.63)$$

becomes, to lowest order in  $1/nq'$ :

$$\mathcal{L}(\eta, k, \Omega) \hat{u}(\eta) = 0 \quad (5.64)$$

<sup>12</sup>In the literature  $\theta_0$  is sometimes referred to as the ballooning angle and sometimes as the radial wavenumber. There is little difference in these two terminologies, however recalling eqn. 5.12 it is clear that the true radial wavenumber also incorporates  $\eta$  and as such the term ballooning angle will be used throughout this work.

<sup>13</sup>These transformations are equivalent to the relation between functions of the two Fourier conjugate coordinates  $m - nq'x$  and  $\eta - k$ . For example, suppose  $F(k)$  is the Fourier transform of  $f(x)$  then  $df/dx$  transforms to  $ikF(k)$  and  $xf(x)$  transforms to  $idF/dk$ .

Substituting eqn. 5.61, eqn. 5.62 and eqn. 5.58 into eqn. 5.50 yields:

$$\left[ (\rho_s n q')^2 (\eta - k)^2 + c + \frac{2\epsilon_n}{\Omega} [\cos(\eta) + \hat{s}(\eta - k) \sin(\eta)] + \left(\frac{\sigma}{\Omega}\right)^2 \frac{\partial^2}{\partial \eta^2} + \frac{\Omega - 1}{\Omega + \eta_s} \right] \hat{u}(\eta) = 0 \quad (5.65)$$

which is the lowest order ballooning (or local) equation representing the global model in the limit  $n \rightarrow \infty$ . This is a one dimensional ordinary differential equation which can be solved numerically for  $\hat{u}(\eta)$  given  $k$  and  $x$  (which are free parameters at this order). The boundary condition  $\hat{u}(\eta) \rightarrow 0$  for  $\eta \rightarrow \pm\infty$ , required for the integrability of eqn. 5.58, can only be satisfied for the correct value of  $\Omega$ , which may be considered as an eigenvalue of the equation, for specified values of  $x$  and  $k$ . The substitution  $\Omega \rightarrow \Omega_0(x, k)$ , with  $\Omega_0$  the local frequency, can be used to highlight two important points:

1. The eigenvalue of the local equation,  $\Omega_0$ , depends upon the values of  $x$  and  $k$  used.
2. For a specified  $x$  and  $k$  the eigenvalue of the local equation, eqn. 5.65,  $\Omega_0$ , is not necessarily the same as the eigenvalue of the global equation, eqn. 5.50,  $\Omega$ .

This makes it clear that proper treatment of the free parameters  $x$  and  $k$  is crucial for the ability of the local representation to represent the global solution, and this is discussed in section 5.3.

### 5.3 Choosing the local model's free parameters to fit the global model

Whilst the parameters of the local equation,  $x$  and  $k$ , are free at the lowest order in  $1/nq'$ , at the next order conditions are imposed upon their treatment. It is only when these conditions are satisfied that  $\Omega_0$  and the local solution,  $\hat{u}(\eta)$ , can be used to describe the solution to the global problem. For the correct values of  $x$  and  $k$ , and only then, it is possible to write  $\Omega = \Omega_0(x, k) + \mathcal{O}(1/nq')$ .

For the system considered here the local frequency can be represented with the model

$$\Omega_0(x, k) = \Lambda + g(x) + h(k) \quad (5.66)$$

where  $\Lambda$  is a model parameter to be determined<sup>14</sup>. Once suitable forms for  $g(x)$  and  $h(k)$  are selected, it is possible to determine any free coefficients in these forms by fitting to the  $\Omega_0(x, k)$  obtained from solution of the local equation for the range of  $x$  and  $k$  of interest.

The radial variation,  $g(x)$ , will be dependent upon the equilibrium profiles used, but as the radial extent of interest is small relative to the equilibrium scale length it is possible to Taylor expand about  $x = 0$ :

$$g(x) \approx \lambda_1 x + \lambda_2 x^2 \quad (5.67)$$

where  $g(x = 0) = 0$  is assumed and  $\lambda_n$ , which can be determined by fitting to  $\Omega_0(x, k)$ , represents the  $n^{\text{th}}$  Taylor expansion coefficient and is proportional to the  $n^{\text{th}}$  radial derivative of  $g(x)$ . This leads to two different situations; either the linear term will dominate and  $g(x) \approx \lambda_1 x$  or  $dg/dx = 0$  and  $g(x) \approx \lambda_2 x^2$ .

To help select a suitable form for  $h(k)$  it is useful to consider the properties of the local equation and  $u_m(x)$ . Under the joint transformations  $\eta \rightarrow \eta + 2\pi$  and  $k \rightarrow k + 2\pi$  the expression for  $u_m(x)$ , eqn. 5.58, is unchanged provided the local eigenfunction  $\hat{u}(\eta)$  is unchanged. The local equation, eqn. 5.65 and hence the eigenfunction  $\hat{u}(\eta)$ , will only be unchanged if the eigenvalue,  $\Omega_0$ , is also invariant under these transformations and hence  $\Omega_0$  must be periodic in  $k$ . Using the periodicity of  $\Omega_0$ , it is clear that  $h(k)$  must be a periodic function. By defining  $\Lambda$  to be the average of  $\Omega_0$  over one period in  $k$ , evaluated at  $x = 0$ :

$$\Lambda \equiv \frac{1}{2\pi} \int_0^{2\pi} \Omega_0(x = 0, k) dk = \langle \Omega_0 \rangle_k \quad (5.68)$$

it is clear that the average of  $h(k)$  must be zero. For the circular cross-section equilibrium studied in this chapter a suitable choice for  $h(k)$  which satisfies these criteria is simply  $\beta \cos(k)$ . The resulting model is then:

$$\Omega_0(x, k) = \Lambda + \lambda_l x^l + \beta \cos(k) \quad (5.69)$$

with  $l$  either 1 or 2. Considering the contour in  $\{x, k\}$  where  $\Omega_0 = \Omega$  (which is as yet unknown) eqn. 5.69 represents a relation between the unknown global frequency,  $\Omega$ ,

---

<sup>14</sup>For this system the separation of the  $x$  and  $k$  variation into independent terms should be reasonable provided the radial variation of the coefficients in the local equation, eqn. 5.65, all vary on the equilibrium length scale (as required for the local equation to be valid). If this is not satisfied then it is clear that at different radial locations across the global mode's width different terms may dominate the local equation, and hence the dependence of  $\Omega_0$  on  $k$  could vary between radial locations. In general systems the  $x$  and  $k$  dependence cannot be separated simply and a more complex model for  $\Omega_0$  is required.

and the free parameters  $k(x)$  and  $x$ , which can be written as

$$x^l = \alpha [d - \cos(k)] \quad (5.70)$$

where  $\alpha = \beta/\lambda_l$  and

$$d = \frac{\Omega - \Lambda}{\beta} \quad (5.71)$$

In order to solve for  $k(x)$  it is necessary to provide extra information; specifically the value of  $d$  is required.

### 5.3.1 The Fourier-Ballooning representation

Whilst the ballooning representation used earlier to derive the local equation is a relatively intuitive decomposition of the perturbed potential,  $\phi_1$ , it is in fact more convenient to adopt an alternative, equivalent, form when considering the relation between  $\Omega$  and the free parameters. Combining the ballooning representation for the radial mode function, eqn. 5.58, with the poloidal Fourier decomposition of the perturbed potential, eqn. 5.48, leads to:

$$\phi_1(x, \theta) = A(x) e^{inq'S(x)} \sum_m \int_{-\infty}^{\infty} e^{im(\eta-\theta)} e^{-inq'x\eta} \hat{u}(\eta) d\eta \quad (5.72)$$

It is possible to represent the radial variation given by the terms outside of the summation as a Fourier transform:

$$A(x) e^{inq'S} = \int_{-\infty}^{\infty} \chi(p) F(p) e^{inq'xp} dp \quad (5.73)$$

where  $p$  represents the conjugate variable to  $inq'x$ , with  $\chi(p)$  and  $F(p)$  representing the slow and fast variations in  $p$  respectively. The fast variation in  $p$  is often written in the eikonal form:

$$F(p) = e^{inq'\hat{S}(p)} \quad (5.74)$$

Noting that the integral in eqn. 5.72 is of the form of eqn. 5.6 allows it to be written as

$$\sum_m e^{-im\theta} \int_{-\infty}^{\infty} \hat{u}(\eta) e^{i(m-inq'x)\eta} d\eta = f(\theta, x) = \xi(\theta) e^{-inq'x\theta} \quad (5.75)$$

Using eqn. 5.73 and eqn. 5.75 the perturbed potential is given by:

$$\phi_1(x, \theta) = \int_{-\infty}^{\infty} \xi(\theta) \chi(p) F(p) e^{inq'x(\theta-p)} dp \quad (5.76)$$

which is known as the Fourier-ballooning representation [137, 139]. Under this representation the local equation is unchanged provided the transformations:

$$p \rightarrow k \quad (5.77)$$

$$x \rightarrow \frac{i}{nq'} \frac{d}{dp} \quad (5.78)$$

are made [126]. It can be noted that eqn. 5.78 leads to

$$x \rightarrow -\frac{d\hat{S}(p)}{dp} \quad (5.79)$$

when applied to  $F(p)$ . For simplicity eqn. 5.77 will be used in to connect  $p$  with  $k$  and all future instances of  $p$  will be replaced with  $k$ . Noting that  $\xi(\theta)\chi(k)$  is unchanged under the transformation  $k \rightarrow k + 2\pi$  and  $\theta \rightarrow \theta + 2\pi$ , then to ensure periodicity in  $\theta$  it is necessary that:

$$F(k) = F(k + 2\pi) \quad (5.80)$$

and hence using eqn. 5.79

$$\hat{S}(k + 2\pi) - \hat{S}(k) = \frac{2\pi j}{nq'} \quad (5.81)$$

with  $j \in \mathbb{Z}$ . The change in  $\hat{S}(k)$  given in eqn. 5.81 is related to the change in  $x$ , such that  $j \sim nq'x$  and hence  $2\pi j/nq' \ll 1$ . This additional information regarding the free parameter  $d\hat{S}/dk$  can be used in the model for  $\Omega_0$  in order to relate  $\Omega$  to  $\Lambda$ .

### 5.3.2 Relating the local and global mode frequencies

Returning to eqn. 5.70 and applying eqn. 5.78, this can now be written as a differential equation for  $F(k)$

$$\left(\frac{-i}{nq'} \frac{d}{dk}\right)^l F(k) = \alpha [d - \cos(k)] F(k) \quad (5.82)$$

Solving the differential equation given by eqn. 5.82 provides  $d$  as an eigenvalue. The solution,  $F(k)$ , can be used directly with the Fourier-Ballooning representation, eqn. 5.76, to give the global mode structure. Alternatively as the value of  $d$  is now known eqn. 5.70 can be used to provide an expression for  $k(x)$

$$k(x) = \cos^{-1}\left(d - \frac{x^l}{\alpha}\right) \quad (5.83)$$

in terms of  $d$ ,  $x$  and  $\alpha$  which can be used directly with eqn. 5.54 to give the global mode structure.

The procedure shown here provides both a relation between the global frequency and the averaged local frequency and an expression for  $k(x)$  which allows the global mode structure to be determined. This shows that all of the information required to fully describe the global solution can be determined from information provided by solving the local equation over a range of  $x$  and  $k$  values. The procedure for determining  $d$  will now be demonstrated for the two different types of radial variation which can be encountered and this information will then be used in section 5.3.3 to predict the expected properties of the global mode in these two scenarios.

### 5.3.2.1 Quadratic radial variation: Isolated modes

Considering a situation where the equilibrium profiles provide the local frequency with an extremum at  $x = 0$ , i.e. when the radial variation is best described by choosing  $l = 2$ , then eqn. 5.82 can be written as

$$-\frac{1}{(nq')^2} \frac{d^2}{dk^2} F(k) = \alpha [d - \cos(k)] F(k) \quad (5.84)$$

Anticipating that the solution will be peaked around the stationary point at  $k = 0$  it is possible to expand  $\cos(k)$  as  $1 - k^2/2$ . Substituting this, along with eqn. 5.74, into eqn. 5.84 and proposing<sup>15</sup>

$$\hat{S} = bk^2 \quad (5.85)$$

yields

$$-\frac{i2b}{nq'} + (2bk)^2 = \alpha \left[ d - 1 + \frac{k^2}{2} \right] \quad (5.86)$$

Balancing the  $k^2$  terms leads to

$$b = \frac{1}{2} \sqrt{\frac{\alpha}{2}} \quad (5.87)$$

Substituting this back into eqn. 5.86 gives an expression for  $d$ :

$$d = 1 - \frac{i}{nq' \sqrt{2\alpha}} \quad (5.88)$$

Assuming  $nq' \sqrt{2\alpha} \gg 1$  eqn. 5.88 simply becomes  $d = 1$ . Recalling eqn. 5.71 this suggests that  $\Omega$  is related to the averaged local frequency through:

$$\Omega = \Lambda + \beta \quad (5.89)$$

---

<sup>15</sup>Clearly this definition does not satisfy the periodicity constraint eqn. 5.81, however due to the expansion about  $k = 0$  the solution is only valid in this region and eqn. 5.85 may be considered as some function which satisfies eqn. 5.81 expanded about  $k = 0$ .

Noting eqn. 5.69 it is clear that eqn. 5.89 suggests that the global frequency  $\Omega$  is approximately given by the local frequency evaluated at  $x = 0, k = 0$ , as posited. Modes which arise in situations where there is a stationary point in  $\Omega_0$  were the first class of drift mode studied in the literature using the ballooning transform [134]. The higher-order treatment given in the literature for these modes follows that of the original MHD based ballooning work [132]. Rather than transforming to the Fourier-Ballooning representation as done here, the findings of the earlier MHD study were used to show that the mode was expected to be localised about the stationary point, in agreement with the results found here. These modes are known as “isolated modes” due to the localisation about the stationary point.

Strictly, eqn. 5.89 is only valid within an  $\mathcal{O}(1/nq')$  correction, and hence it is expected that the difference between  $\Omega_0(x = 0, k = 0)$  and the true mode frequency found by solving the global equation will be given by a term inversely proportional to  $nq'$ . This “correction factor” is a consequence of the finite radial width of the mode<sup>16</sup>, which will be calculated in section 5.3.3.1, may be a more accurate estimate of the true mode frequency.

### 5.3.2.2 Linear radial variation: General modes

The existence of a stationary point in  $\Omega_0$  is a special situation and hence the isolated modes just introduced will only be found at certain radial locations<sup>17</sup>. As the observed drift wave driven transport does not just occur in a few small radial regions, corresponding to a stationary point and the associated isolated mode’s radial width, it is clear that modes must also exist which do not require stationary points in  $\Omega_0$ . Taking the more common case whereby the radial dependence of the local frequency is approximately linear yields “general modes”. Whilst these modes can be treated using the ballooning representation as done in the literature for isolated modes, it is more complicated than the isolated case and the Fourier-ballooning approach is more straightforward.

Setting  $l = 1$  eqn. 5.82 becomes

$$-\frac{i}{nq'} \frac{d}{dk} F(k) = \alpha [d - \cos(k)] F(k) \quad (5.90)$$

<sup>16</sup>It can be noted that for the quadratic variation considered here such an average will always be less than the value at  $x = 0$  and as such the  $1/nq'$  correction is expected to always be negative in this case.

<sup>17</sup>Indeed as both the real and imaginary components of  $\Omega_0$  must be stationary at the same position, suitable locations for isolated modes are a rare occurrence.

Substituting eqn. 5.74 into eqn. 5.82 yields

$$\frac{d\hat{S}}{dk} = \alpha [d - \cos(k)] \quad (5.91)$$

Integrating this over one period in  $k$  and applying the periodicity constraint eqn. 5.81 leads to

$$d = \frac{2\pi j}{nq'} \quad (5.92)$$

and as such  $d \approx 0$ . This implies  $\Omega = \Lambda$  and recalling eqn. 5.68 this shows that the global frequency in such a scenario is given to  $\mathcal{O}(1/nq')$  by the average of the local frequency over one period in  $k$ , evaluated at  $x = 0$ . The growth rate of general modes can therefore be significantly reduced from that for the isolated modes. To account for the  $\mathcal{O}(1/nq')$  correction it is again necessary to compare with the average taken over the radial width of the mode, which will be calculated in section 5.3.3.2.

### 5.3.3 Predicting the global mode structure

Through the ballooning representation of the radial Fourier modes, eqn. 5.58, it can be seen that the radial variation is primarily given by  $A(x) \exp(inq'S(x))$ . Using eqn. 5.83 along with the values of  $d$  obtained in the previous section it is possible to estimate the radial width of the global mode determined by the imaginary component of  $S(x)$ , i.e. assuming  $A(x)$  can be treated as constant over the width of the global mode<sup>18</sup>. Further to this the approximate relation between  $\theta_0$  and  $k$  given in eqn. 5.57 can be used along with eqn. 5.54 such that the poloidal angle at which constructive interference is expected between adjacent radial Fourier modes,  $u_m(x)$ , is given by the real component of  $k$ .

This ability to predict the radial width and poloidal angle at which the mode peaks will be illustrated for the isolated and general modes considered in section 5.3.2 and the resulting predictions will be tested against direct solutions of the global model in section 5.6.1.

#### 5.3.3.1 Isolated modes: Radial width and poloidal angle

To determine the properties of the isolated global mode it will be necessary to use the expression for  $k(x)$  given by eqn. 5.83 with  $d = 1$ :

$$k(x) = \cos^{-1} \left( 1 - \frac{x^2}{\alpha} \right) \quad (5.93)$$

---

<sup>18</sup>This is valid provided the global mode width is sufficiently less than the equilibrium scale length.

Taking the real component of  $k(x)$  and expanding for  $x \approx 0$  allows the poloidal angle at which the mode is expected to peak to be written as:

$$k(x) \approx 0 + x\sqrt{\frac{2}{\alpha}} \quad (5.94)$$

which indicates the mode is expected to peak at the outboard midplane, where  $\theta = 0$ .

To obtain the radial width information recall from eqn. 5.54 that the radial amplitude envelope is contained within the imaginary component of  $S(x)$ . Integrating eqn. 5.93 provides:

$$S(x) = x \cos^{-1} \left( 1 - \frac{x^2}{\alpha} \right) + 2\sqrt{2\alpha - x^2} \quad (5.95)$$

Expanding eqn. 5.95 about  $x = 0$  to second order gives:

$$S(x) \approx 2\sqrt{2\alpha} + \frac{x^2}{\sqrt{2\alpha}} \quad (5.96)$$

and hence the radial full width half maximum,  $\Delta w$ , of the amplitude envelope  $\exp[-nq'\mathcal{I}(S)]$  is described by

$$\Delta w = \frac{2\sqrt{2 \log(2)} |\sqrt{2\alpha}|}{\sqrt{2nq'\mathcal{I}(\sqrt{2\alpha})}} \quad (5.97)$$

where  $\mathcal{I}(\sqrt{2\alpha})$  is the imaginary component of  $\sqrt{2\alpha}$ . This shows that the mode's radial width is expected to scale as  $1/\sqrt{nq'}$  for fixed equilibrium parameters and will allow a quantitative prediction of the global mode's radial width. This could also be used to set the radial range over which to average  $\Omega_0$  when trying to improve the comparison with  $\Omega$ .

### 5.3.3.2 General modes: Radial width and poloidal angle

In the case of general global modes,  $d = 0$  and eqn. 5.83 gives  $k(x)$  as:

$$k(x) = \cos^{-1} \left( -\frac{x}{\alpha} \right) \quad (5.98)$$

Expanding eqn. 5.98 about  $x = 0$  provides

$$k(x) \approx \pm \left( \frac{\pi}{2} + \frac{x}{\alpha} \right) \quad (5.99)$$

so that the global mode structure will be centred poloidally about  $\theta = \pm\pi/2$ . The sign must be selected such that the resulting amplitude variation produces a confined

mode (i.e. the amplitude must decay as  $x$  increases), this is determined by the sign of  $\mathcal{I}(\alpha)$ . Assuming  $\mathcal{I}(\alpha)$  is *+*ve it is appropriate to select the *+*ve form of eqn. 5.99. Integrating eqn. 5.98 yields

$$S(x) = \alpha \sqrt{1 - \frac{x^2}{\alpha^2}} + x \cos^{-1} \left( -\frac{x}{\alpha} \right) \quad (5.100)$$

Expanding this about  $x = 0$  gives

$$S(x) \approx \alpha + \frac{\pi x}{2} + \frac{x^2}{2\alpha} \quad (5.101)$$

which suggests the radial width due to  $\exp[-nq'\mathcal{I}(S)]$  will be given by

$$\Delta w = \frac{2\sqrt{2 \log(2)} |\alpha|}{\sqrt{nq'\mathcal{I}(\alpha)}} \quad (5.102)$$

This width takes a similar form to that for the isolated modes, eqn. 5.97, except that the dependence is now on  $\alpha$  rather than  $\sqrt{2\alpha}$ . It is important to note that  $\alpha$  will vary between the two cases as the value of  $\lambda_l$  will depend upon the specific equilibrium profiles in each case and as such a direct comparison between eqn. 5.102 and eqn. 5.97 is not appropriate.

## 5.4 Numerical solutions

In order to test and validate the procedures outlined in section 5.3, which should allow the global mode properties to be determined entirely from solutions to the local equation, it is useful to be able to obtain solutions to both the global model, eqn. 5.50, and the local model, eqn. 5.65. A numerical approach to the solution of these equations is essential as an analytic result is not possible with non-zero coupling (i.e. in toroidal geometry). A code has been developed which will solve both equations for a given set of equilibrium profiles, providing  $\Omega$ ,  $\{u_m(x)\}$ ,  $\Omega_0$  and  $\hat{u}(\eta)$ . This code can be used to compare the true global frequency with that from the local model using the procedure outlined in section 5.3. The approaches adopted in the global and local sections of the code will now be outlined.

### 5.4.1 Numerical approach: Global model

Considering a mode with a finite radial width it is clear that only a finite number of rational surfaces must be coupled together in the global mode. It is possible to truncate the infinite set of coupled equations in eqn. 5.50 to retain only  $M = 2\delta m + 1$

equations for the range of poloidal mode numbers  $m_0 - \delta m \leq m_0 \leq m_0 + \delta m$ , where the global mode is centred on the rational surface with  $q = m_0/n$ . To represent these equations numerically it is helpful to discretise in the radial direction, which is achieved by introducing a finite difference representation for the radial derivatives. Using central differences the derivatives can be written as

$$\left. \frac{\partial f(x)}{\partial x} \right|_{x=x_i} = \frac{f_{i+1} - f_{i-1}}{2h} \quad (5.103)$$

$$\left. \frac{\partial^2 f(x)}{\partial x^2} \right|_{x=x_i} = \frac{f_{i+1} - 2f_i + f_{i-1}}{h^2} \quad (5.104)$$

where the subscript refers to the radial grid point and  $h$  is the (uniform) spacing between grid points. This allows the system of equations, eqn. 5.50, to be written as

$$\underline{\underline{P}}^i \cdot \underline{U}^{i-1} + \underline{\underline{Q}}^i \cdot \underline{U}^i + \underline{\underline{S}}^i \cdot \underline{U}^{i+1} = 0 \quad (5.105)$$

where  $\underline{U}^i$  is a vector of length  $M$  representing the values of  $\{u_m(x_i)\}$  and the square  $M \times M$  matrices  $\underline{\underline{P}}^i$ ,  $\underline{\underline{Q}}^i$  and  $\underline{\underline{S}}^i$  represent the coefficients of the equation acting at the  $i-1$ ,  $i$  and  $i+1$  grid points respectively and are defined in table 5.2. Due to the coupling of the  $m \pm 1$  modes the matrices  $\underline{\underline{P}}$ ,  $\underline{\underline{Q}}$  and  $\underline{\underline{S}}$  are tridiagonal and the system can be solved using a tridiagonal shooting method which will now be outlined.

Array \ Index	$j = k - 1$	$j = k$	$j = k + 1$
$P_{j,k}$	$\frac{\chi \epsilon_n^i}{2\Omega h k q}$	$\frac{\rho_i^2}{h^2}$	$-P_{k-1,k}$
$Q_{j,k}$	$-\frac{\chi \epsilon_n^i}{\Omega}$	$\left([m_j - nq'x^i] \frac{\sigma^i}{\Omega}\right)^2 - 2P_{j,k} - \frac{\Omega-1}{\Omega+\eta_s^i} - c$	$Q_{k-1,k}$

**Table 5.2:** The three non-zero elements of the tridiagonal matrices  $\underline{\underline{P}}_{j,k}^i$  and  $\underline{\underline{Q}}_{j,k}^i$ . The matrices, along with  $\underline{\underline{S}}_{j,k}^i = \underline{\underline{P}}_{k,j}^i$ , represent the global dispersion relation, eqn. 5.50.

The solution begins with the ansatz

$$\underline{U}^{i-1} = \underline{\underline{\alpha}}^{i-1} \cdot \underline{U}^i + \underline{\underline{\beta}}^{i-1} \quad (5.106)$$

where the matrix  $\underline{\underline{\alpha}}^i$  and vector  $\underline{\underline{\beta}}^i$  are to be found at each meshpoint. Using eqn. 5.106 then given  $\underline{U}$  at a single mesh point it is possible to find  $\underline{U}$  everywhere provided  $\underline{\underline{\alpha}}$  and  $\underline{\underline{\beta}}$  can be determined. Substituting eqn. 5.106 into eqn. 5.105 yields

$$\left[ \underline{\underline{P}}^i \cdot \underline{\underline{\alpha}}^{i-1} + \underline{\underline{Q}}^i \right] \cdot \underline{U}^i = -\underline{\underline{S}}^i \cdot \underline{U}^{i+1} - \underline{\underline{P}}^i \cdot \underline{\underline{\beta}}^{i-1} \quad (5.107)$$

Multiplying both sides of eqn. 5.107 from the left with the inverse of  $\left[ \underline{\underline{P}}^i \cdot \underline{\underline{\alpha}}^{i-1} + \underline{\underline{Q}}^i \right]$  provides an expression for  $\underline{U}^i$ :

$$\underline{U}^i = - \left[ \underline{\underline{P}}^i \cdot \underline{\underline{\alpha}}^{i-1} + \underline{\underline{Q}}^i \right]^{-1} \cdot \underline{\underline{S}}^i \cdot \underline{U}^{i+1} - \left[ \underline{\underline{P}}^i \cdot \underline{\underline{\alpha}}^{i-1} + \underline{\underline{Q}}^i \right]^{-1} \cdot \left( \underline{\underline{P}}^i \cdot \underline{\underline{\beta}}^{i-1} \right) \quad (5.108)$$

where the  $[\underline{L}]^{-1}$  notation refers to the inverse of the matrix  $\underline{L}$ . Incrementing  $i$  by 1 in eqn. 5.106 and comparing with eqn. 5.108 leads to expressions for  $\underline{\alpha}^i$  and  $\underline{\beta}^i$  to be found in terms of  $\underline{P}$ ,  $\underline{Q}$ ,  $\underline{S}$ ,  $\underline{\alpha}^{i-1}$  and  $\underline{\beta}^{i-1}$ :

$$\underline{\alpha}^i = - [\underline{P}^i \cdot \underline{\alpha}^{i-1} + \underline{Q}^i]^{-1} \cdot \underline{S}^i \quad (5.109)$$

$$\underline{\beta}^i = - [\underline{P}^i \cdot \underline{\alpha}^{i-1} + \underline{Q}^i]^{-1} \cdot (\underline{P}^i \cdot \underline{\beta}^{i-1}) \quad (5.110)$$

These relations allow  $\underline{\alpha}$  and  $\underline{\beta}$  to be found at all points given the values at a single grid point.

In practice  $\underline{\beta}$  is treated as an  $M \times M$  matrix,  $\underline{\underline{\beta}}$ , rather than a vector of length  $M$ , with each column representing a linearly independent solution<sup>19</sup>. The state vector,  $\underline{U}^i$ , must also be expanded to matrix form,  $\underline{\underline{U}}^i$ , in this case. The algorithm to solve eqn. 5.105 can then be summarised as:

1. Provide boundary value of  $\underline{\alpha}$  and  $\underline{\beta}$  at the central mesh point,  $x = x_c$ ,  $i = i_c$ . These are taken to be  $\underline{\alpha}^{i_c} = 0$  and  $\underline{\underline{\beta}}_{j=l}^{i_c} = 1$ ,  $\underline{\underline{\beta}}_{j \neq l}^{i_c} = 0$  where  $1 \leq l \leq M$  labels the  $M$  linearly independent solutions<sup>20</sup>.
2. Apply eqn. 5.109 and eqn. 5.110 to determine  $\underline{\alpha}$  and  $\underline{\beta}$  at all other mesh points.
3. Use eqn. 5.106 with the determined values of  $\underline{\alpha}$  and  $\underline{\beta}$  and vanishing boundary conditions for  $\underline{U}$  at the lower boundary,  $i = 1$ , (i.e.  $\underline{\underline{U}}^{i=1} = 0$ ) to determine  $\underline{U}$  at the next mesh point,  $i = 2$ .
4. Continue to use eqn. 5.106 to generate  $\underline{\underline{U}}^{i+1}$  until  $i = i_c - 1$  is reached.
5. Use eqn. 5.106 with the determined values of  $\underline{\alpha}$  and  $\underline{\beta}$  and vanishing boundary conditions for  $\underline{U}$  at the upper boundary,  $i = n_x$ , to determine  $\underline{U}$  at the next mesh point,  $i = n_x - 1$ .
6. Repeat until  $i = i_c + 1$  is reached.
7. Now that  $\underline{\underline{U}}^i$  has been found for  $i < i_c$  and  $i > i_c$  it is necessary to check that the solution across the central region satisfies the eigenvalue condition:

$$\underline{L} \cdot \underline{f} = \lambda \mu_l \underline{f} = 0 \quad (5.111)$$

with

$$\underline{P}^i \cdot \underline{\underline{U}}^{i_c-1} + \underline{Q}^i \cdot \underline{\underline{U}}^{i_c} + \underline{S}^i \cdot \underline{\underline{U}}^{i_c+1} = \underline{L} \quad (5.112)$$

<sup>19</sup>This is equivalent to performing  $M$  independent solutions, each with an independent initialisation of  $\underline{\beta}$ . The advantage of the matrix formulation is that the entire set of solutions can be found within a single pass through the algorithm. A vector representation of  $\beta$  and  $U$  can provide a small reduction in memory requirements so may be of use in situations where the storage of several  $M \times M \times n_x$  arrays (where  $n_x$  is the number of radial mesh points) is a limiting factor in the performance of the algorithm.

<sup>20</sup>These boundary conditions imply  $\underline{\underline{U}}^{i_c} = \underline{\underline{\beta}}^{i_c}$ .

8. The  $M$  eigenvalues,  $\mu_l$ , and eigenvectors,  $\underline{f}_l$ , of  $\underline{L}$  are determined and the smallest value of  $\mu_l$  is selected as the desired value. If this is not sufficiently small (less than  $10^{-6}$  say) then  $\Omega$  must be updated (described in section 5.4.1.1) and the algorithm returns to step 1. Otherwise a valid solution has been found. The eigenvector  $\underline{f}_l = \underline{F}$  corresponding to the smallest eigenvalue then describes how the  $M$  independent solutions must be combined to form the radial wavefunctions,  $\{u_m(x)\}$ :

$$u_m(x_i) = \underline{U}^i \cdot \underline{F} \quad (5.113)$$

### 5.4.1.1 Updating the frequency

As the matrices  $\underline{P}$ ,  $\underline{Q}$  and  $\underline{S}$  depend upon the global frequency,  $\Omega$ , the eigenvalue condition, eqn. 5.111, will only be satisfied for certain values of  $\Omega$ . These values are unknown and it is necessary to try to converge to values which satisfy this equation. By starting with an initial guess for  $\Omega$ , it is possible to cast the determination of the correct value as a root finding problem where the desired root is the value of  $\Omega$  required to provide  $\mu_l \approx 0$ . This has been implemented using two similar methods; the first is the secant method and the second is the Muller method [138]. Taking  $\mu_l = \mu_l(\Omega)$  the secant method defines a straight line through two pairs of  $\{\mu_l, \Omega\}$  values (provided by the current and previous iteration through the solution algorithm) and solves to estimate the root. The Muller method is very similar except it fits a quadratic through three sets of points (provided by the current and two previous iterations). Typically the Muller method is used as experience has indicated that it tends to be more robust than the secant method and generally leads to faster convergence. The computational requirements of the root finding algorithms can depend strongly upon how close the initial guess for  $\Omega$  is to the actual solution and hence this is an important consideration, which will be discussed in section 5.4.3.

### 5.4.2 Numerical approach: Local model

The solution of the local equation, eqn. 5.65, is significantly less demanding than the global problem, eqn. 5.50, as it is a single ordinary differential equation rather than a coupled set of equations. Provided the initial conditions  $\hat{u}(\eta = \eta_0)$  and  $\hat{u}'(\eta = \eta_0)$  (with  $\hat{u}' = d\hat{u}/d\eta$ ), the common 4<sup>th</sup> order Runge-Kutta method (RK4) [138] can be used to numerically integrate eqn. 5.65 from  $\eta = \eta_0$  to  $\eta = \pm\eta_m$ , with  $\pm\eta_m$  the upper and lower boundaries. Whilst boundary conditions on  $\hat{u}(\eta)$  for  $\eta \rightarrow \pm\infty$  are known<sup>21</sup>, the local model does not provide suitable initial conditions to use in

the RK4 scheme. The algorithm developed to solve eqn. 5.65 using the RK4 method overcomes this lack of initial conditions by combining solutions obtained from even and odd trial solutions such that the boundary conditions are satisfied at one boundary and then iterating on  $\Omega_0$  until the conditions are satisfied at the second boundary. This algorithm can be summarised as:

1. Assume initial conditions representing an even function (zero gradient, non-zero amplitude) at the central mesh point,  $\eta = \eta_0$ , and apply the RK4 method to integrate to the upper boundary, yielding  $\hat{u}(\eta)_1$ .
2. Assume initial conditions representing an odd function (non-zero gradient, zero amplitude) at the central mesh point,  $\eta = \eta_0$ , and apply the RK4 method to integrate to the upper boundary, yielding  $\hat{u}(\eta)_2$ .
3. Find  $c$  such that  $\hat{u}(\eta)_1 + c\hat{u}(\eta)_2 = 0$  at the upper boundary.
4. The correct boundary conditions at  $\eta = \eta_0$  are then the amplitude used in step one and the gradient used in step 2 scaled by  $c$ .
5. Use these initial values and the RK4 method to integrate from  $\eta = \eta_0$  to the lower boundary.
6. If the boundary conditions are not satisfied at the lower boundary then  $\Omega_0$  must be updated and the algorithm repeated, else a valid solution has been found.

The techniques used for updating  $\Omega_0$  are the same as in the global algorithm (either the secant or Muller methods are used) but here the role of the fictitious eigenvalue,  $\mu_l$ , is played by the value of  $\hat{u}(\eta)$  at the lower boundary. As with the algorithm to solve the global model, the computational demands of this algorithm depend somewhat upon the initial guess for the local frequency,  $\Omega_0$ , and a scheme for optimising this will be introduced in section 5.4.3.

It should be noted that whilst the boundary conditions that have been implemented here are of Dirichlet type (i.e. they specify the value of the function at the boundary) this is only a necessary condition for  $\hat{u}(\eta) \rightarrow 0$  for  $\eta \rightarrow \pm\infty$  and is not sufficient to guarantee this. For example a solution of the form  $\hat{u}(\eta) = \sin(c\eta)$  would satisfy the imposed boundary conditions but does not provide the required convergence properties. Ideally Cauchy type boundary conditions would be implemented where both the value and gradient of  $\hat{u}(\eta)$  are fixed to specified values, which in this case would be zero. These have not been implemented in this case in order to minimise the code's complexity and as a result it is necessary to perform an additional check to ensure that solutions returned by this algorithm do indeed have the required

---

<sup>21</sup>These boundary conditions are that  $\hat{u}(\eta)$  must decay to zero for  $\eta \rightarrow \pm\infty$  such that the integral in eqn. 5.58 converges.

behaviour.

### 5.4.3 The cylindrical limit

In the limit of negligible coupling, which arises due to the magnetic drifts, the system can be considered to represent the cylindrical limit<sup>22</sup>. In this limit both the global and local equations can be solved analytically, moreover because there is no coupling the global solution will only depend upon local equilibrium properties and the global and local cylindrical mode frequencies should agree. Dropping the drift term in eqn. 5.50 leads to a set of uncoupled equations, where the equation for each  $u_m(x)$  is:

$$\left[ \rho_s^2 \frac{\partial^2}{\partial x^2} - c + \left( \frac{\sigma k_\theta \hat{s} x_*}{\Omega} \right)^2 - \frac{\Omega - 1}{\Omega + \eta_s} \right] u_m(x) = 0 \quad (5.114)$$

where the substitution  $x = x_* + x_0$  has been made with  $x_0 = m/k_\theta \hat{s}$ . Assuming a solution of the form  $u_m(x) = \exp(-i\delta x_*^2)$  and substituting into eqn. 5.114 gives

$$\left[ 2\rho_s^2 (-2\delta^2 x_*^2 - i\delta) - c + \left( \frac{\sigma k_\theta \hat{s} x_*}{\Omega} \right)^2 - \frac{\Omega - 1}{\Omega + \eta_s} \right] u_m(x) = 0 \quad (5.115)$$

where it has been assumed that  $\delta$  is independent of  $x_*$ . It is necessary to choose  $\delta$  such that  $x_*$  is removed from the equation and hence:

$$\delta = \frac{\sigma k_\theta \hat{s}}{2\rho_s \Omega} \quad (5.116)$$

This leaves an equation for  $\Omega$  in terms of the equilibrium parameters and the poloidal wave number only:

$$i \left( \frac{\sigma \hat{s} \sqrt{c}}{\Omega} \right) + c + \frac{\Omega - 1}{\Omega + \eta_s} = 0 \quad (5.117)$$

with  $c = (k_\theta \rho_s)^2$ . Rearranging eqn. 5.117 leads to the quadratic equation

$$\Omega^2 (1 + c) + \Omega (c\eta_s - 1 + i\sigma \hat{s} \sqrt{c}) + (i\sigma \eta_s \hat{s} \sqrt{c}) = 0 \quad (5.118)$$

which can be solved to yield the mode frequency in the limit of no coupling:

$$\Omega = \frac{-c\eta_s + 1 - i\sigma \hat{s} \sqrt{c} \pm \sqrt{(c\eta_s - 1 + i\sigma \hat{s} \sqrt{c})^2 - 4i(1 + c)\sigma \eta_s \hat{s} \sqrt{c}}}{2(1 + c)} \quad (5.119)$$

Introducing a fictitious parameter,  $\chi$ , which multiplies the coupling term in the global equation it is possible to control the strength of the magnetic drifts in the local and

<sup>22</sup>In the true cylindrical limit  $\epsilon_n \rightarrow 0$  as  $R \rightarrow \infty$  and both the coupling term and the parallel term become zero. The solution for  $u_m(x)$  is then of the form of an outgoing wave.

global equations. By setting  $\chi = 0$  in the numerical codes it is expected that the root finding algorithm should converge to the analytic  $\Omega$ . By providing this value as an initial guess and then slowly increasing  $\chi$  in steps, the solution can be tracked from the known analytic limit to the situation of interest, such as  $\chi = 1$ . Using the converged solution of the previous step as the initial guess for the current step means that the root finding algorithm should rapidly converge to a solution, vastly reducing the time taken to find the final answer.

#### 5.4.4 Benchmarking: Global code

The algorithm discussed in section 5.4.1 for solving the coupled equations given by eqn. 5.50 has been implemented in a Fortran code. This code outputs both the complex mode frequency,  $\Omega$ , and the radial Fourier modes,  $\{u_m(x)\}$ , as a function of coupling strength,  $\chi$ . To provide some confidence in the algorithm's implementation it is possible to compare the analytical value of  $\Omega$ , calculated from eqn. 5.118, with that obtained from the numerical code in the case of no coupling. Using "standard quadratic" equilibrium parameters at  $x = 0$  (introduced in section 5.5) the analytical mode frequency is found to be  $\Omega_a = -0.106 + i0.229$ , which is in exact agreement with the converged numerical value found using  $n = 50$ . Whilst this tests the algorithm in the case of no coupling, these coupling effects are important to the full global mode and further tests with non-zero coupling are useful.

As was shown in section 5.3.3.1 the isolated mode's radial width is expected to scale as  $1/\sqrt{nq'}$  and additionally the mode frequency will be given by a constant plus  $\mathcal{O}(1/nq')$  terms. By setting up the equilibrium profiles such that there is a stationary point in the diamagnetic frequency (see section 5.5.1 for details) it is expected that an isolated mode will be found. The  $n$  dependence of the full width half maximum of the radial amplitude envelope,  $\Delta w$ , and the mode's complex frequency,  $\Omega$ , has been determined using the global code and compared to the predicted scalings. The results of this scan in  $n$  are shown in figure 5.3.

The gradient of a straight line fit to  $\ln(n)$  vs  $\ln(\Delta w)$  is  $-0.51$ , showing excellent agreement with the higher order prediction. Similarly a fit of the form:

$$\gamma = A_0 n^{A_1} + A_2 \tag{5.120}$$

to the data shown in figure 5.3(b) yields  $A_1 = -1.066$  which again shows good agreement with the higher order prediction. It is interesting to note that the coefficient  $A_2$ , which is found to be 0.3842, represents the expected value of the global mode frequency in the limit  $n \rightarrow \infty$ , i.e. in the local limit. As such this provides a benchmark test for the numerical implementation of the local solution.

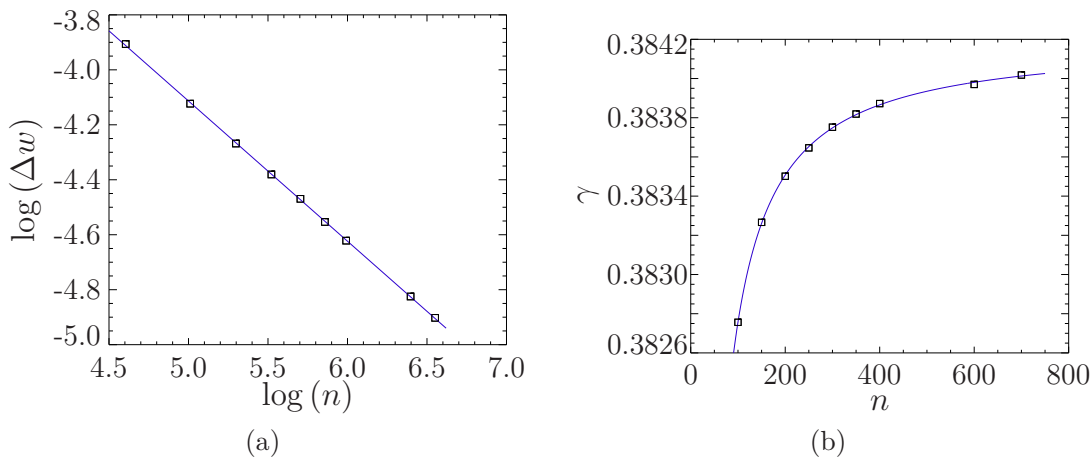


**Figure 5.3:** The behaviour of an isolated mode's radial width,  $\Delta w$ , as the toroidal mode number is increased (points) and a fit to  $\log(w) = B_0 + B_1 \log(n)$  (line), is shown in figure 5.3(a) with  $B_0 = -1.56$  and  $B_1 = -0.51$ . The behaviour of the growth rate,  $\gamma$ , as the toroidal mode number is increased (points) and a fit to  $\gamma = A_0 n^{A_1} + A_2$  (line), is shown in figure 5.3(b) with  $A_0 = -0.1950$ ,  $A_1 = -1.066$  and  $A_2 = 0.3842$ .

### 5.4.5 Benchmarking: Local code

The numerical algorithm for solving the local equation has also been implemented within the code used for solving the global problem. It provides the local mode frequency,  $\Omega_0$ , and eigenfunction,  $\hat{u}(\eta)$ , for specified  $x$  and  $k$  values as a function of the coupling strength,  $\chi$ . In the analytic limit ( $\chi = 0$ ) the local mode frequency for  $x = 0$  (and any  $k$ ) is found to be  $-0.106 + i0.229$ , which is in perfect agreement with the analytic prediction.

For  $\chi \neq 0$  the local equation should be equivalent to the global model in the limit  $n = \infty$ . It is therefore possible to compare the local growth rate with that found by extrapolating the global fit, eqn. 5.120, to the limit of  $n = \infty$ . To perform the comparison with the local value it is necessary to specify the correct  $x$  and  $k$  values to use. The equilibrium profiles used for these benchmark cases lead to a quadratic radial variation in  $\Omega_0$  and hence using the results of section 5.3.3.1 it is clear that the comparison should be made with  $\Omega_0(x = 0, k = 0)$ . This growth rate is found to be 0.3843, which is in very good agreement with the value found by extrapolating the results of the toroidal mode number scaling study performed in the global benchmark and shown in figure 5.3(b).

### 5.4.6 Convergence testing

It is important to verify that the results obtained from both the global and local codes are independent of the details of the numerical implementation. In particular

it is important to verify that a sufficient number of grid points have been used in discretising the equations to accurately resolve the structures present in the solution and the associated gradients and that the grids cover a sufficient range that the boundary conditions can be satisfied. For the simulations presented here convergence testing has been performed to identify a suitable grid resolution and extent to be used which minimises the computational expense whilst still providing a sufficiently accurate result. In practice the global simulations presented here use 2000 grid points covering the radial domain  $-0.1 \leq x \leq 0.1$  and 61 poloidal modes whilst the local simulations use 2000 grid points<sup>23</sup> covering the ballooning domain  $-2 \leq \eta \leq 2$ . Results from simulations using both 1000 and 4000 grid points in  $x$  and  $\eta$  do not vary significantly from those presented here.

## 5.5 Global modes: The effect of profiles

Now that the code to solve the global and local models has been benchmarked it is possible to use this to probe the theoretical work discussed in section 5.3. This theory suggests that solutions of the global model can yield either isolated or general type modes dependent upon the spatial variation of the local frequency,  $\Omega_0$ , and that these modes should have significantly different properties. To test this the global code discussed in section 5.4 can be exploited to investigate the global solutions for two different classes of equilibrium profiles.

Assuming the radial variation of the local frequency has the same form as that of the analytical (cylindrical) frequency, given by eqn. 5.119, then it is clear that the class of solution expected depends solely upon the equilibrium profiles used. The drive for the ITG mode is contained within the parameter  $\eta_s$  and, assuming all other parameters are approximately constant, the existence of a stationary point in  $\Omega_0$  requires a stationary point in  $\eta_s$ . By setting the  $\eta_s$  profile it should be possible to select either isolated or general modes. In practice, however, the variation of the other equilibrium parameters will also influence the radial profile of  $\Omega_0$ . To remove this complication in the global code it has been assumed that all other equilibrium parameters used are constant<sup>24</sup>, which allows the expected mode type to be controlled by the  $\eta_s$  profile alone. It should be noted that this introduces a slight inconsistency into the problem as it is necessary to retain a non-zero value for  $\hat{s}$  such that the resonance at rational surfaces, given by integer values of  $m - nq'x$ , is included in the system. This resonant behaviour at rational surfaces is of importance to the global

<sup>23</sup>It is important to note that error accumulation can be an issue for the RK4 algorithm used in obtaining the local solution and as such it is also important that not too many grid points are used here.

<sup>24</sup>This assumption is not essential to the solution of the global model and indeed the developed code is capable of treating arbitrary variation in all equilibrium parameters.

mode's behaviour and hence to include this correctly a  $q$  profile of the form:

$$q(r) = (q_a - q_0) \left(\frac{r}{a}\right)^{q_p} \quad (5.121)$$

has been selected with  $q_a$  and  $q_0$  the value of  $q$  at the edge and centre of the plasma respectively,  $a$  is the minor radius and  $q_p$  is a constant. Such a  $q$  profile leads to a naturally constant shear profile with  $\hat{s} = q_p$ . The equilibrium and system parameters used throughout the simulations presented here are given in table 5.3, with  $q_m = m_0/n$  the value of  $q$  at  $x = 0$ .

Parameter	Value
$q_0$	0.75
$q_a$	4.2
$q_m$	1.8
$n$	50
$m_0$	90
$\hat{s}$ (or $q_p$ )	2
$nq'$	498.6
$a$	0.5 m
$R_0$	5.0 m
$\epsilon_n$	0.03088
$k_\theta \rho_s$	0.33

**Table 5.3:** A summary of the equilibrium profile parameters used throughout the numerical ITG simulations.

### 5.5.1 Isolated modes

In order to investigate isolated modes an  $\eta_s$  profile of the form

$$\eta_s(x) = \eta_m (1 - \eta_g x^2) \quad (5.122)$$

is used, which introduces a stationary point in the analytical frequency at  $x = 0$ . For the studies presented here the values  $\eta_m = 5.0$  and  $\eta_g = 62.5$  have been used.

Running the global code with the equilibrium parameters given in table 5.3 and retaining 30 poloidal modes either side of the central value yields the complex mode frequency as a function of coupling strength, as shown in figure 5.4. At the coupling strength considered here,  $\chi = 0.5$ , the complex mode frequency is given by  $\Omega = 0.0062 + i0.3812$ . It is useful to note that the difference between this and the local frequency at  $x = 0$ ,  $k = 0$ , found in section 5.4.2, is indeed  $\mathcal{O}(1/nq')$  and that the global value is less than the local value, as anticipated in section 5.3.2.1.

The set of 61 radial functions,  $\{u_m(x)\}$ , produced by the code are shown in figure 5.5(a). As expected, each  $u_m(x)$  is found to peak at the rational surface where

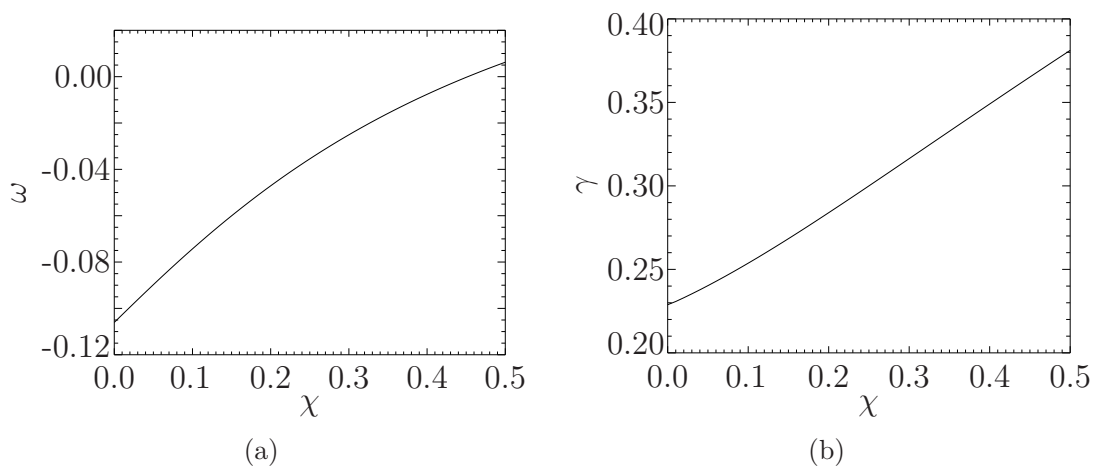


**Figure 5.4:** The mode frequency and growth rate as a function of coupling strength,  $\chi$ , for the global problem with isolated profiles.

$q = m/n$ . The phase relationship between adjacent Fourier modes can be found by

$$k_{2D} = \theta_0 = \log \left( \frac{u_m(x_m)}{u_{m+1}(x_{m+1})} \right) \quad (5.123)$$

where  $x_m$  is the location of the  $m^{\text{th}}$  rational surface. Analysing this phase relationship it can be seen that the relative phase,  $\theta_0$  (or equivalently the wavenumber  $k$ ), is around zero for this mode, as shown in figure 5.6. Using  $\{u_m(x)\}$  with eqn. 5.48 it is possible to reconstruct the 2D potential  $\phi_1(x, \theta)$  and the result of this is shown in figure 5.5(b). The mode is centred on the outboard midplane, which is a consequence of the specific relative phase found between the Fourier modes. This is also consistent with the mode being centred about the stationary point in the local growth rate as the net drive for the mode peaks at the outboard midplane,  $\theta = 0$ , due to unfavourable curvature.

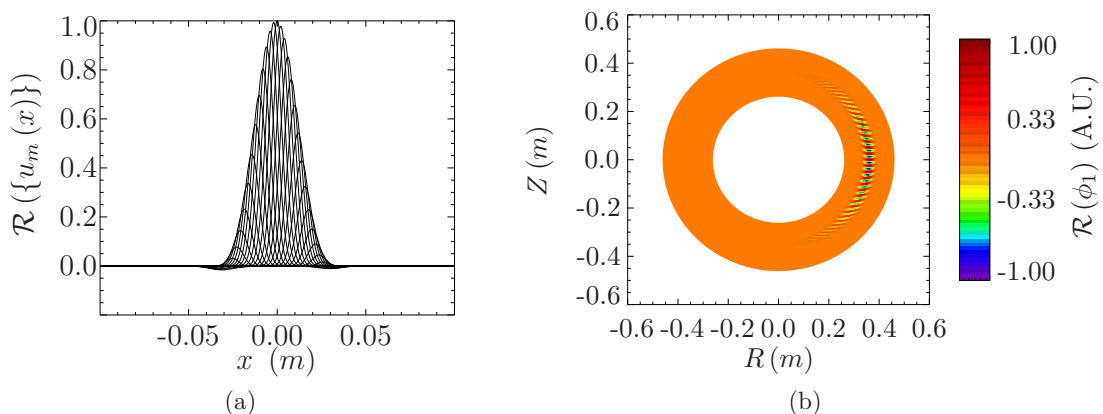


**Figure 5.5:** The real component of the radial Fourier modes,  $\mathcal{R}(\{u_m(x)\})$ , as found by the global code [figure 5.5(a)] and the reconstructed global mode structure,  $\mathcal{R}(\phi_1(x, \theta))$ , [figure 5.5(b)]. Each radial Fourier mode  $u_m(x)$  peaks at the rational surface where  $m = nq'x$  and has approximately zero phase relative to its neighbours, resulting in the 2D structure peaking at the outboard midplane,  $\theta = 0$ .

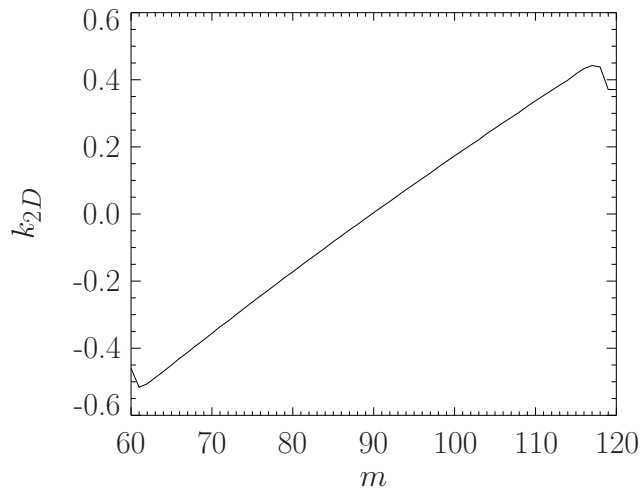


**Figure 5.6:** The relative phase between adjacent radial Fourier modes,  $k_{2D}$  (or  $\theta_0$ ), as a function of poloidal mode number,  $m$ , for isolated profiles calculated using eqn. 5.123. The phase is centred on 0, suggesting the Fourier modes will constructively interfere at the outboard midplane,  $\theta = 0$ , as seen in figure 5.5(b).

### 5.5.2 General modes

The investigation of general modes uses an  $\eta_s$  profile of the form

$$\eta_s(x) = \eta_m - \eta_g x \quad (5.124)$$

which provides a linear variation in the analytic frequency<sup>25</sup>. For the studies presented here the values  $\eta_m = 5.0$  and  $\eta_g = 40.0$  have been used.

Using the standard equilibrium parameters described earlier and again retaining 30 poloidal modes either side of the central value provides the complex mode frequency as a function of coupling strength, shown in figure 5.7. In this case the complex mode frequency is given by  $\Omega = -0.1068 + i0.2317$  at the coupling strength of interest,  $\chi = 0.5$ , which shows a reduced growth rate,  $\gamma$ , relative to the isolated case. It can be noted that as the coupling is increased to 0.5 the complex mode frequency varies from the cylindrical value by less than 1.5%.

The radial Fourier modes found in this case are shown in figure 5.8(a). This radial mode structure is somewhat different to that seen in figure 5.5(a), which is due to a change in the phase relationship between adjacent Fourier modes. It can be seen from figure 5.9 that the relative phase,  $\theta_0$ , in the general mode case is around  $\pi/2$ , which is consistent with the value of  $k$  predicted by eqn. 5.99. The reconstructed 2D potential  $\phi_1(x, \theta)$ , given in figure 5.8(b), shows that the 2D mode structure is indeed centred at  $\pi/2$ , as expected from this calculated relative phase.

<sup>25</sup>Provided the same value of  $\eta_m$  is used then  $\eta_s(x=0)$  will be the same for both isolated and general cases and as such the local solution at  $x=0$  will be identical in the two cases.

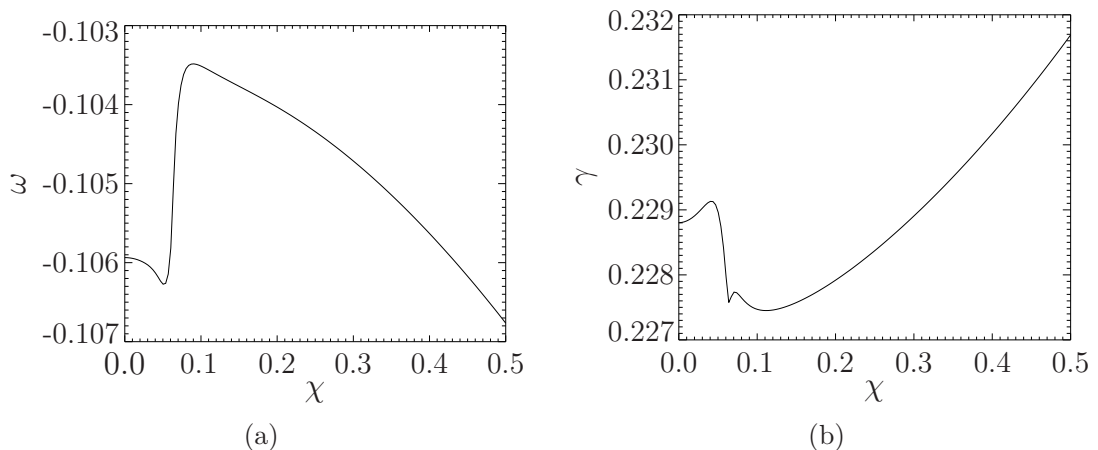


**Figure 5.7:** The mode frequency and growth rate as a function of coupling strength,  $\chi$ , for the global problem with general profiles.

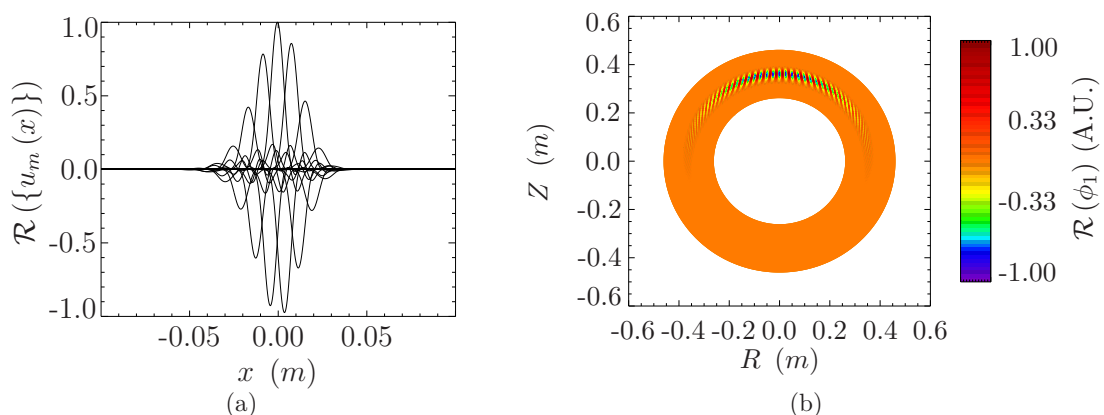


**Figure 5.8:** The real component of the radial Fourier modes,  $\mathcal{R}(\{u_m(x)\})$ , as found by the global code [figure 5.8(a)] and the reconstructed global mode structure,  $\mathcal{R}(\phi_1(x, \theta))$ , [figure 5.8(b)]. Each radial Fourier mode  $u_m(x)$  peaks at the rational surface where  $m = nq'x$  and has approximately  $\pi/2$  phase relative to its neighbours, resulting in the 2D structure peaking at the top of the plasma,  $\theta = \pi/2$ .

## 5.6 From local to global

The solutions of the global model introduced in the previous section show good qualitative agreement with the predictions of the higher order ballooning theory introduced in section 5.3. The power of the higher order theory is not limited to qualitative predictions however, and using the expressions derived in section 5.3 it is possible to provide quantitative calculations of the properties of global modes entirely from solutions of the local equation. To achieve this it is necessary to determine the model parameters,  $\Lambda$ ,  $\lambda$  and  $\beta$  used in the model equation for  $\Omega_0(x, k)$ . This involves performing many local calculations scanning over the range of  $x$  and  $k$  of interest<sup>26</sup> to obtain the necessary  $\Omega_0(x, k)$  data. Whilst the local equation does not contain any explicit radial variation, as the value of  $x$  is scanned it is necessary to vary the

<sup>26</sup>It is important to note that the solution at each  $x$  and  $k$  value is entirely independent and hence this scan is perfectly parallelisable.

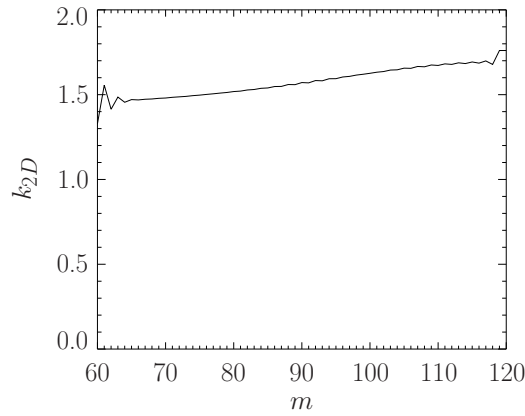


**Figure 5.9:** The relative phase between adjacent radial Fourier modes,  $k_{2D}$  (or equivalently  $\theta_0$ ), as a function of poloidal mode number,  $m$ , for general profiles. The phase is centred on  $\pi/2$ , suggesting the Fourier modes will interfere constructively at the top of the plasma,  $\theta = \pi/2$ , as seen in figure 5.8(b).

equilibrium parameters such that they remain consistent with the values used in the global solutions. Separate studies have been made for the quadratic and linear profile cases described in the previous section.

### 5.6.1 Quadratic profiles

Adopting the quadratic profiles used to study the isolated global modes in section 5.5.1 it is possible to find the local frequency,  $\Omega_0(x, k)$ , and this is shown in figure 5.10. It can be seen that selecting a quadratic  $\eta_s$  profile has indeed led to a radial variation of  $\Omega_0$  which has a stationary point at  $x = 0$ . The local frequency at this stationary point is  $\Omega_0(x = 0, k = 0) = 0.0058 + i0.3843$ .

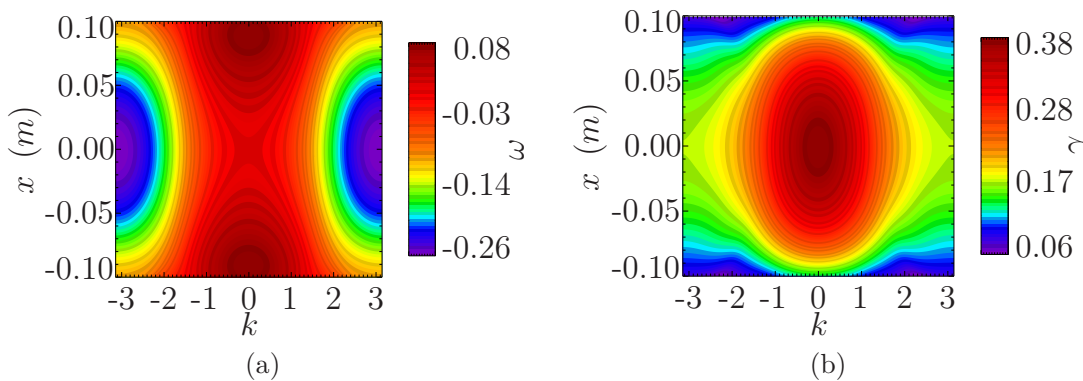


**Figure 5.10:** The real local mode frequency, figure 5.10(a), and local growth rate, figure 5.10(b), as a function of  $x$  and  $k$  determined from solution of the local equation using isolated profiles.

Fitting the model for  $\Omega_0(x, k)$ , eqn. 5.69 with  $l = 2$ , to this data yields the following

model parameters:

$$\Lambda = -0.1183 + i0.2571 \quad (5.125)$$

$$\lambda = 12.61 - i15.90 \quad (5.126)$$

$$\beta = 0.1257 + i0.0831 \quad (5.127)$$

which leads to  $\beta/\lambda = \alpha = 0.0006 + i0.0074$ . It should be noted that the value of  $\Lambda$  has been constrained to be exactly the average of  $\Omega_0$  over  $k$  at  $x = 0$ . The fit of the model to the data has discrepancies of up to 1%, translating to an error on the model parameters of between 0.1% and 1%.

The model parameter values can be used in conjunction with the expressions derived in section 5.3.2.1, eqn. 5.93 and eqn. 5.95, to give  $k(x)$  and  $S(x)$ . These functions, evaluated at the rational surfaces, are shown in figure 5.11. The  $k$  profile can be compared with that shown in figure 5.6 from analysing the relative phase of the neighbouring radial Fourier modes. The value derived from the global mode structure appears to be slightly smaller than that from the local model. Importantly, agreement is found between the local and global values for  $k$  at  $m = m_0 = 90$  which sets the poloidal angle of constructive interference and has the largest influence on the 2D mode structure.

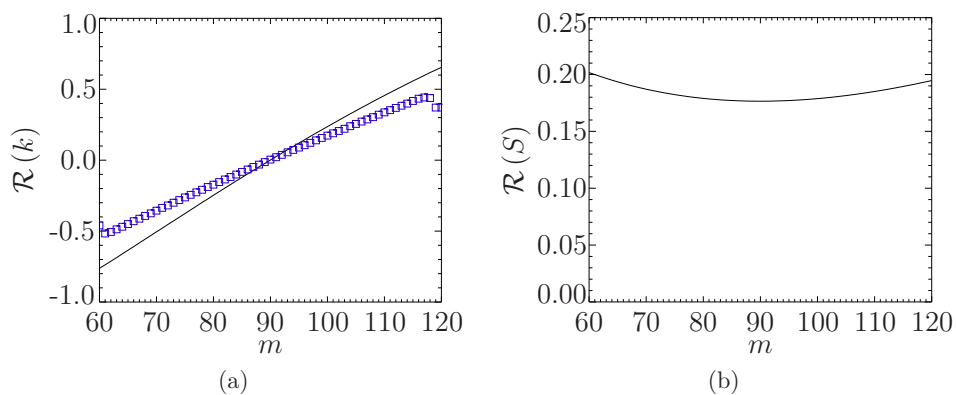


**Figure 5.11:** The real components of the functions  $k(x)$  [figure 5.11(a)] and  $S(x)$  [figure 5.11(b)] calculated from the local model parameters (black lines). The value of  $k(x)$  determined directly from the global mode structure is shown by blue points.

The radial half width of the global mode is predicted using eqn. 5.97 to be  $\Delta w = 0.0317$ , which agrees within  $\sim 9\%$  with the width calculated directly from the global mode structure,  $\Delta w = 0.0292$ . Using the expression for  $k(x)$  along with this radial width allows the local frequency to be averaged along the curve defined by  $\{x, k(x)\}$  over this width. This averaging provides  $\langle \Omega_0 \rangle = 0.0065 + i0.3821$  which compares well with the global frequency,  $\Omega = 0.0062 + i0.3812$ , and is an improvement on the lowest order local value found by taking  $x = 0$  and  $k = 0$  given above. Whilst the correction between the lowest order local frequency and this averaged value is relatively small

in this case, the ability to calculate this correction using data available from the lowest order equation shows the potential to describe the global mode properties to a high degree of accuracy even at modest  $nq'$ .

Finally the expression for  $S(x)$ , eqn. 5.95, can be determined solely in terms of  $x$  by substituting for  $\alpha$ . Substituting this and the solutions of the local equation<sup>27</sup>  $\hat{u}(\eta)$  into the ballooning representation, eqn. 5.58, it is possible to calculate  $\phi_1(x, \theta) = \sum_m u_m(x) \exp(-im\theta)$ . The result of this calculation is shown in figure 5.12, and good qualitative agreement can be seen with the mode structure obtained by direct solution of the global equation shown in figure 5.5(b). This agreement is a consequence of the good quantitative comparison between the global and predicted mode widths and the value of  $k$  evaluated at the rational surface  $x = 0$  using both the global and local methods.

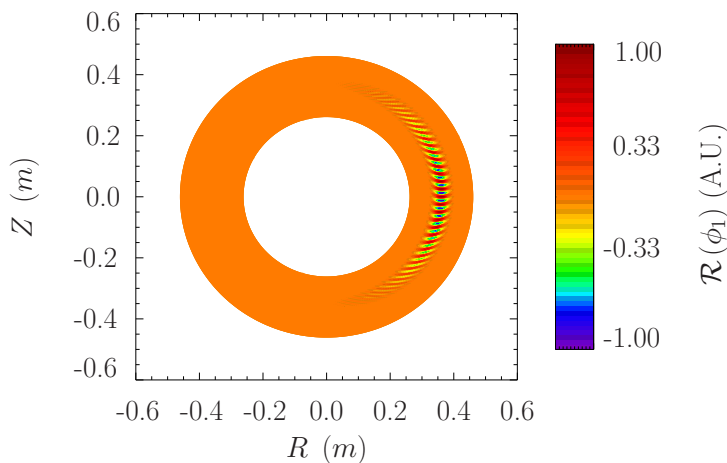


**Figure 5.12:** The real component of the global mode structure,  $\mathcal{R}(\phi_1(x, \theta))$ , for the case of a quadratic  $\eta_s$  profile calculated using the solution of the local equation along with the relevant higher order theory. Good agreement is seen between this and the mode structure found by direct solution of the global equation, shown in figure 5.5(b).

### 5.6.2 Linear profiles

Changing to the linear  $\eta_s$  profile used to study the general modes in section 5.5.2 yields  $\Omega_0(x, k)$  shown in figure 5.13. It can be seen that with this linear  $\eta_s$  profile  $\Omega_0$  does not have a stationary point at  $x = 0$  and is approximately linear. Following eqn. 5.99 and evaluating the local complex mode frequency at  $k = \pi/2$  yields  $\Omega_0(x = 0, k = \pi/2) = -0.1091 + i0.2306$ .

Fitting the model for  $\Omega_0(x, k)$ , eqn. 5.69 with  $l = 1$ , to this data yields the following

<sup>27</sup>The  $\hat{u}(\eta)$  function used at each point here is that calculated at  $x = 0, k = 0$  however it is possible to use the function calculated using the appropriate value of  $k$  at each value of  $x$  as calculated from eqn. 5.93 but this does not significantly alter the global structure.

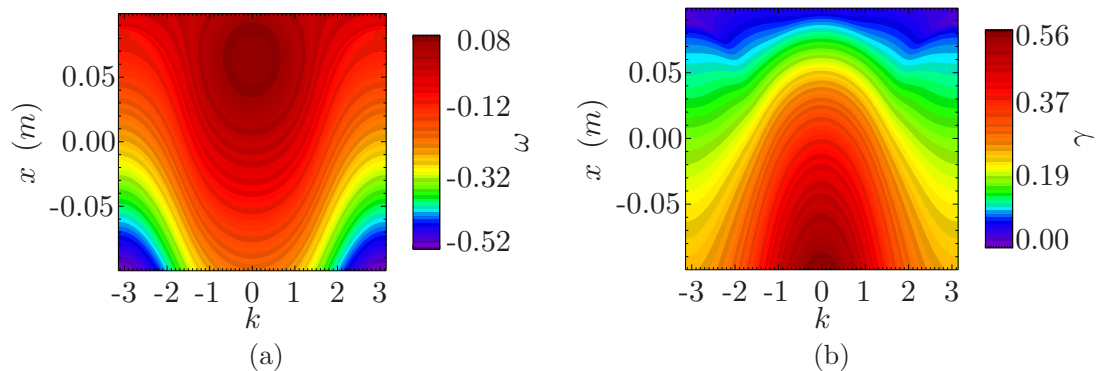


**Figure 5.13:** The real local mode frequency, figure 5.13(a), and local growth rate, figure 5.13(b), as a function of  $x$  and  $k$  determined from solution of the local equation using general profiles.

model parameters:

$$\Lambda = -0.1163 + i0.2553 \quad (5.128)$$

$$\lambda = 2.2543 - i1.4035 \quad (5.129)$$

$$\beta = 0.1459 + i0.1309 \quad (5.130)$$

which leads to  $\beta/\lambda = \alpha = 0.0206 + i0.0709$ . As in the quadratic profile case the fit of the model to the data is not perfect<sup>28</sup> and discrepancies of up to 1% are again observed, translating to an error on the model parameters of between 0.1% and 1%.

These model parameters can be used with the expressions derived in section 5.3.2.2, eqn. 5.98 and eqn. 5.100, to give  $k(x)$  and  $S(x)$ , and these are shown in figure 5.14 evaluated at the rational surfaces. Comparing the  $k$  profile shown here with that derived from the global mode structure, shown in figure 5.9, fairly good agreement is seen between the local and global values of  $k$  for the range of poloidal mode numbers of interest.

Using the expression for the expected mode radial width, eqn. 5.102, the predicted half width of the global mode is  $\Delta w = 0.0292$ , which agrees to within around 5% with the observed global mode width,  $\Delta w = 0.0309$ . Using the expression for  $k(x)$  along with this radial width allows the local frequency to be averaged along the curve defined by  $\{x, k(x)\}$  over this width. This averaging provides  $\langle \Omega_0 \rangle = -0.1102 + i0.2300$  which compares very well with the global frequency,  $\Omega$ , and is very similar to the lowest order value found by taking  $x = 0$  and  $k = \pi/2$  given above. The averaged local frequency is not a significant improvement in this case, unlike the quadratic profile case. This is because the local frequency in this case is approximately linear

<sup>28</sup>Indeed the local solution becomes more difficult as the growth rate drops making  $\Omega_0$  for  $x > 0.05$  untrustworthy in this case. As such the fitting in this case has been performed over the reduced  $x$  range  $-0.1 \leq x \leq 0.05$ .

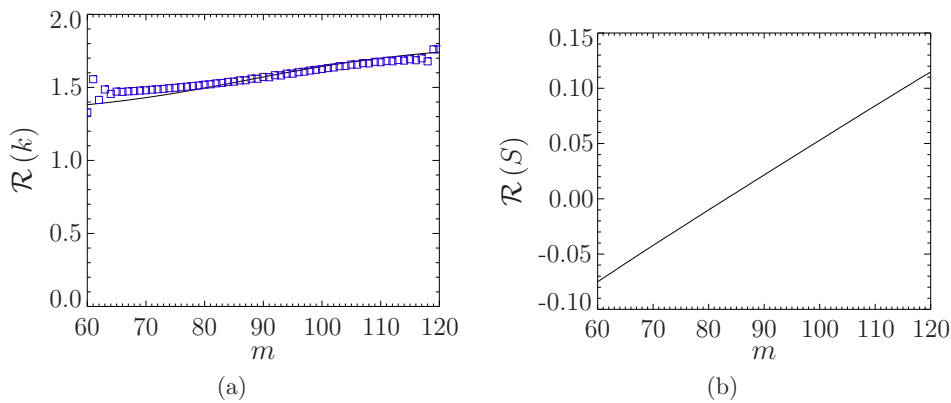


**Figure 5.14:** The real components of the functions  $k(x)$  [figure 5.14(a)] and  $S(x)$  [figure 5.14(b)] calculated from the local model parameters. The value of  $k(x)$  determined directly from the global mode structure is shown by blue points.

in both the  $x$  and  $k$  directions about  $x = 0$ ,  $k = \pi/2$ . The average over a small range in  $x$  centred about  $x = 0$  is therefore very close to the value at  $x = 0$ ,  $k = \pi/2$ .

As in the case with quadratic profiles, using  $\alpha$  with the expression for  $S(x)$ , eqn. 5.95, it is possible to calculate  $\phi_1(x, \theta) = \sum_m u_m(x) \exp(-im\theta)$  by substituting this and the solutions of the local equation,  $\hat{u}(\eta)$ , into the ballooning representation, eqn. 5.58, and numerically evaluating the integral over  $\eta$ .

The result of this calculation is shown in figure 5.15, and good qualitative agreement can be seen with the mode structure obtained by direct solution of the global equation shown in figure 5.8(b). The quantitative agreement shown by the comparison between the radial widths, the poloidal angle of constructive interference and the complex mode frequency is very good.

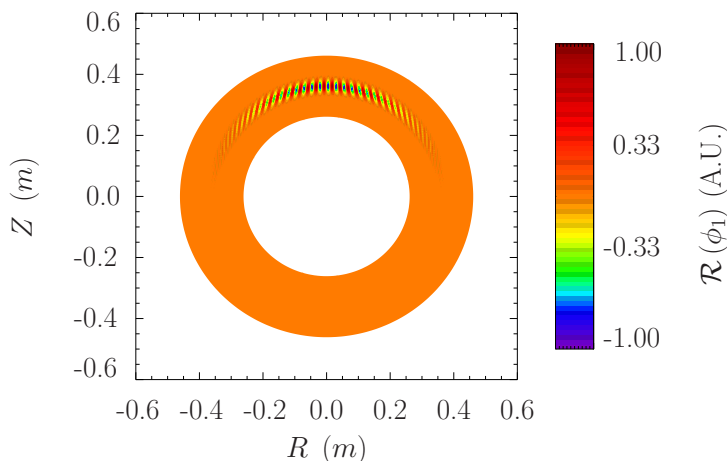


**Figure 5.15:** The real component of the global mode structure,  $\mathcal{R}(\phi_1(x, \theta))$ , for the case of a quadratic  $\eta_s$  profile calculated using the solution of the local equation along with the relevant higher order theory. Good agreement is seen between this and the mode structure found by direct solution of the global equation, shown in figure 5.8(b).

## 5.7 Discussion

The results presented in this chapter have shown that the properties of global eigenmodes depend strongly on the equilibrium profiles. This remains true even in the limit of  $1/nq'L_{eq} \rightarrow 0$ , where the equilibrium length scale,  $L_{eq}$ , is much larger than the mode's radial width. In this limit there exists a separation of scales, which results in an approximate degeneracy of radial locations. This degeneracy, which allows the radial direction to be treated as quasi-periodic, was exploited to replace the 2D global eigenvalue equation with a 1D eigenvalue equation in the extended ballooning coordinate,  $\eta$ , by application of the well known ballooning representation. Whilst the resulting local equation is much simpler to solve than the full global equation, it requires both the radial position,  $x$ , and the wavenumber (or ballooning angle),  $k$  (or  $\theta_0$ ), to be specified. A common practice in the exploitation of linear local gyrokinetic codes is either to select  $k$  to maximise the growth rate, or to use a range of values for  $k$ , treating each as independent. Linear results are therefore often presented only for  $k = 0$ , which positions the mode at the outboard midplane ( $\theta = 0$ ). This is where the pressure and magnetic fields gradients align (the so called region of bad curvature) and local growth rates are expected to be maximum. Such an approach is consistent with the original literature introducing the ballooning transformation, assuming the local frequency has a stationary point at the radial location of interest. However, the results presented in Ref [132] are strictly only applicable to Hermitian systems (such as the ideal MHD system that was the focus of Ref [132]) where the eigenvalue is real whilst the gyrokinetic system is non-Hermitian as the eigenvalue is complex. This brings additional complexities into determining the conditions imposed upon  $k$  and also in properties such as the amplitude envelope. Returning to the higher order terms neglected in the standard local approach the restrictions that are placed upon the choice of  $k$  for a specified  $x$  were discussed. Theoretical treatment of this system suggests that in the case where both components of the local frequency have a stationary point at the same  $x$  and  $k$  then the global mode will indeed be localised about this point in  $\{x, k\}$ . Whilst there will always be at least two  $k$  values for which  $\Omega_0$  is stationary in  $k$  (due to the periodicity in  $k$ ), generally the frequency and growth rate of an instability will have different parametric dependencies on the equilibrium parameters. Only in very special circumstances will both components of  $\Omega_0$  be stationary in  $x$  at the same radial location leading to the existence of isolated modes. These modes are expected to be an uncommon occurrence in experiments. At positions where there is not a stationary point in both components of  $\Omega_0$ , one expects to find general modes which have a global complex frequency equivalent to the local value averaged over  $k$  and a mode structure that is centred on some non-zero poloidal angle.

By solving both the global and local equations for situations with and without a

stationary point in  $\Omega_0$  it has been verified numerically for the first time that the global modes do indeed behave as predicted by the higher order local theory. Whilst the isolated modes sit at the outboard midplane with the maximum growth rate, the general modes do not, and their growth rate is significantly reduced from the maximum value. The results presented here have important consequences for local linear gyrokinetic calculations which usually implicitly assume the existence of a stationary point in  $\Omega_0$  at the radial position being studied. The local growth rate will typically overestimate the true global growth rate. In situations where local linear gyrokinetic studies are being used to probe the basic qualitative characteristics of microinstabilities this may have limited impact, but where quantitative calculations are required this overestimate is likely to be important. For example quasi-linear predictions of heat and particle fluxes which depend upon the linear growth rate, will commonly be an overestimate of what might be expected from the global eigenmode.

Utilising the expressions derived from the higher order local theory along with the solutions of the local equation it was demonstrated that by treating  $x$  and  $k$  appropriately it is possible to recover the properties of the global mode to a reasonable accuracy. This is important as it shows that whilst the standard operation of local gyrokinetic codes will generally overestimate the instability of the system, existing local codes can be used to predict the properties of the true global mode. The appropriate procedure to obtain this information involves entirely independent calculations and is therefore perfectly parallelisable. This motivates the use of local codes as a complementary tool to global simulations for studies of global instabilities. Indeed the use of local codes along with the procedures outlined here may in fact be preferable in some scenarios due to the parallelisable nature of this procedure and to take advantage of features available in a given local code.

### 5.7.1 Sheared flows

As introduced earlier, sheared flows are believed to play an important role in the formation of transport barriers through the suppression of turbulence and the underlying microinstabilities. This has motivated the inclusion of linearly sheared flows in local gyrokinetic codes in order to explore this behaviour, and to study experimental scenarios of relevance to transport barrier formation. It is important to note that equilibrium flows will be close to toroidal in direction due to collisional damping of poloidal flows<sup>29</sup> [140, 141]. The decomposition of these equilibrium flows into components parallel and perpendicular to the magnetic field therefore depends upon  $q$ . It is only the shear in the perpendicular flow,  $dU_{\perp}/dr$ , which provides a stabil-

---

<sup>29</sup>As it is only the passing particles which may contribute to the net flow, collisions between these and trapped particles results in an effective drag on the passing particles leading to flow damping.

ising influence, whilst the parallel velocity gradient,  $dU_{\parallel}/dr$ , provides an instability drive analogous to that provided by the temperature gradient [142, 143]. Only the stabilising effect, due to the perpendicular flow shear, will be considered here.

The effect of including these flows is to add a time dependence to the eikonal phase,  $S$ , [144, 145] which translates to a time dependent ballooning angle. This leads to the picture that a linearly sheared flow causes the mode to convect along the field line [142], which clearly translates to poloidal motion when considering an axisymmetric system<sup>30</sup>. As the mode moves through the good and bad curvature regions the instantaneous growth rate will oscillate in time as shown in figure 5.16.

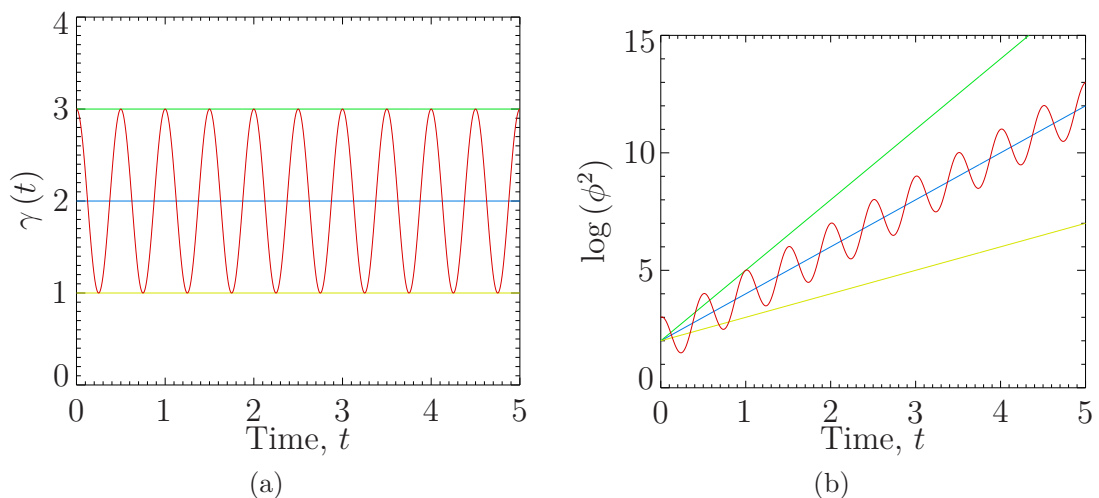


**Figure 5.16:** The time dependent instantaneous growth rate (red) along with the minimum, maximum and average values (orange, green and blue) due to a sheared poloidal flow [figure 5.16(a)]. The logarithm of the linear perturbation amplitude,  $\phi^2$ , is shown in figure 5.16(b) for the different growth rates. The average growth rate (blue) is reduced from the maximum value (green) corresponding to times when the perturbation is at the outboard midplane (i.e.  $\theta_0 = 0$ ).

By averaging the instantaneous growth rate over some period suitably longer than the oscillation period,  $\tau_F$ , (known as the Floquet period) the effective growth rate of the mode will be found. This time averaged growth rate is equivalent to the local growth rate (in the absence of a sheared flow) averaged over a  $2\pi$  period in  $k$ . This Floquet averaged  $\gamma$  is consistent with the treatment of general modes outlined in this chapter. The local codes in essence assume that introducing a linearly sheared flow into the system forces the original mode (which is implicitly assumed to be of isolated type) to become a general type mode. Whilst this treatment is correct in the case where there is indeed an isolated mode in the absence of flow, it has already been discussed above that in general such situations are rare. Even in the absence of a sheared flow, when taking into account other global effects the general

<sup>30</sup>An alternative picture is simply that radially extended structures, such as those seen in the global mode structure plots figure 5.5(b) and figure 5.8(b), will be tilted (or sheared) poloidally by the sheared flow such that the radial correlation length is decreased.

mode will already have a growth rate equivalent to the  $k$  (or time) averaged value and introducing a linearly sheared flow is unlikely to significantly alter the modes behaviour; i.e. whilst the linearly sheared flow converts an isolated mode to a general mode, it will rarely convert the general mode to an isolated mode<sup>31</sup>. To investigate this in the global and local models the transformation  $\Omega \rightarrow \Omega - \Gamma_E$  can be made, where  $\Gamma_E = \Gamma_E(x)$  represents the Doppler shift to the real frequency due to the linearly sheared flow and following Ref [146] has been defined as<sup>32</sup>

$$\Gamma_E(x) = \gamma_e \frac{x}{r_0} \frac{nq_0}{\sqrt{2}} \quad (5.131)$$

where  $\gamma_e$  is known as the shearing rate and sets the relative strength of the flow shear. Such a representation makes it clear that if the equilibrium profiles initially provide a stationary point in both components of  $\Omega_0$  then the introduction of the linearly sheared flow will lead to a radial shift of the stationary point in the real frequency whilst the local growth rate's radial dependence will remain unchanged. In the case of equilibrium profiles where  $\Omega_0$  is already linear in radius it can be seen that linearly sheared flows will only act to alter the gradient of  $\Omega_0$  (either increasing or decreasing it depending upon the direction of flow). This modifies the model parameter  $\lambda$  and for this reason it is anticipated that whilst the growth rate of the general mode will not be significantly affected by the sheared flow, the mode's radial width will change.

### 5.7.1.1 Isolated modes

The inclusion of a linearly sheared Doppler shift to the real component of the global frequency alters the evolution of the global frequency and growth rate as the coupling strength is increased. Using the same equilibrium profiles as used to study the isolated modes in section 5.5.1 the growth rate and radial width have been found as a function of shearing rate,  $\gamma_e$ , and this is shown in figure 5.17.

It can be seen that the growth rate of the mode for small shearing rates is close to that found for the general mode (which is itself close to the analytical value found in the limit of no coupling). This is much reduced from the value found in the absence of a sheared Doppler shift ( $\gamma_e = 0 \rightarrow \gamma = 0.3812$ ), which highlights the significant impact a small amount of sheared flow has on isolated modes. This dramatic effect is consistent with the picture introduced above that the linearly sheared Doppler shift removes the stationary point in the local real frequency<sup>33</sup> which means an isolated

<sup>31</sup>Although the special situations where this can occur may well be of interest.

<sup>32</sup>Representing the perpendicular flow as  $v_{E \times B} \sim E/B$  then the characteristic frequency associated with this motion in the binormal ( $y$ ) direction is  $k_y E/B$ . Taylor expanding  $E$  about the radial position where  $E = 0$  then yields the radial variation in the shearing rate,  $(k_y x/B)E'$ , which noting that  $k_y \approx nq_0/r_0$  yields eqn. 5.131 where  $\gamma_e = \sqrt{2}E'/B$ .

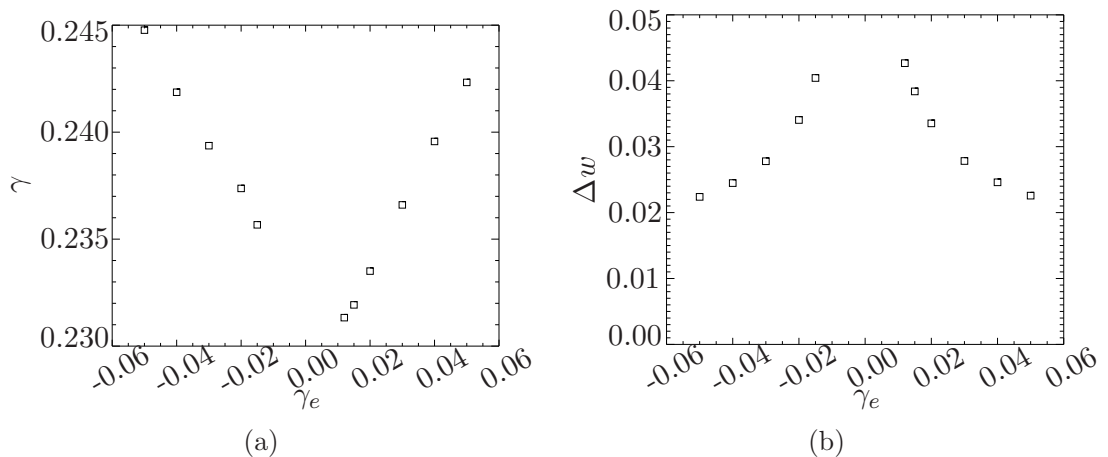


**Figure 5.17:** The global growth rate [figure 5.17(a)] and radial full width half maximum [figure 5.17(b)] as a function of shearing rate,  $\gamma_e$ , using isolated type equilibrium profiles and a linearly sheared Doppler shift. The growth rate is much reduced from the value in the absence of shear flow,  $\gamma = 0.3812$ , and is in fact close to that found for the general mode,  $\gamma = 0.2317$ . The radial width in the absence of sheared flow was found to be 0.0292 which is somewhat below the widths found here for the lowest shearing rates studied.

mode can no longer exist and it is in fact a general mode which exists in this case.

This is further supported by the radial mode structure which is found to have a relative phase of  $\pi/2$  between adjacent Fourier modes, as previously observed for the general modes.

As the shearing rate is reduced the mode's radial width does not tend towards that found in the absence of a sheared flow, found to be 0.0292, and it can be seen that the radial width in fact increases rapidly as the shearing rate is reduced towards zero. This actually limits the lowest shearing rate which can be studied using the code due to memory restrictions which impose limits on the total number of rational surfaces which can be treated. The explanation for this trend can again be provided by considering the global mode found in the presence of the sheared flow to be of the general type. In the cases with  $\gamma_e \neq 0$  the lowest order radial variation in  $\Omega_0$  is set by the sheared Doppler shift, and as such as the shearing rate is decreased this radial variation is reduced. The extrapolation of this behaviour to the case with  $\gamma_e = 0$  would suggest that there is no radial variation in  $\Omega_0$  and as such the modes radial envelope is not bounded in  $x$ . Of course this is not the true behaviour in this unique case and the isolated mode structure would indeed be recovered for  $\gamma_e = 0$ . This highlights an interesting point which can impact the interpretation of local linear gyrokinetic simulations including sheared flows. In such simulations the time averaged growth rate will be independent of the shearing rate provided the

<sup>33</sup>The stationary point is not actually destroyed however, it is simply shifted, and as such it may be possible that this change can allow isolated modes to exist elsewhere provided suitable conditions exist at the shifted location.

time range over which it is averaged is much larger than a Floquet period,  $\tau_F$ . As a result of this the growth rate for  $\gamma_e = 0$  does not agree with that found in the limit  $\gamma_e \rightarrow 0$ . The reason for this apparent inconsistency is that in the limit  $\gamma_e \rightarrow 0$  the Floquet period becomes larger,  $\tau_F \rightarrow \infty$ , and as such the initial perturbation will have grown in amplitude by many orders of magnitude in this time. This means that in fact the perturbation will likely have exceeded the threshold for nonlinear effects to be important well before it has sampled one full period. If the time averaging is restricted to only cover the time range between the initial perturbation and the time the nonlinear threshold is crossed then the growth rate in the limit  $\gamma_e \rightarrow 0$  should smoothly match onto that at  $\gamma_e = 0$ .

### 5.7.1.2 General modes

Following from the results observed in the previous section, where the introduction of a linearly sheared flow caused the isolated mode to become a general type mode, it may be expected that there will be little effect on the case where the mode is already of general type. Using the same equilibrium profiles as used to study general modes in section 5.5.2 the growth rate and radial width have been found as a function of shearing rate,  $\gamma_e$ , and are shown in figure 5.18.

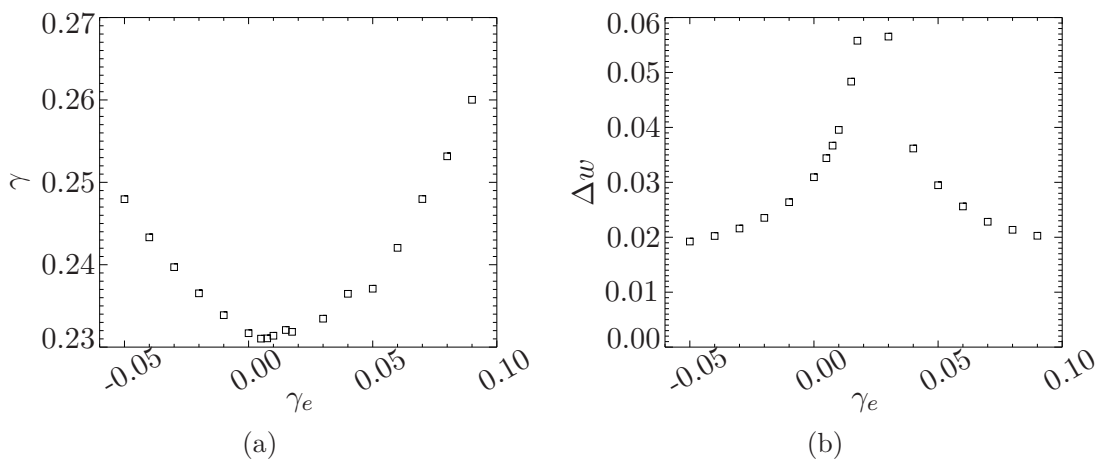


**Figure 5.18:** The global growth rate [figure 5.18(a)] and radial full width half maximum [figure 5.18(b)] as a function of shearing rate,  $\gamma_e$  using general type equilibrium profiles and a linearly sheared Doppler shift.

It can be seen that in this case the growth rate for  $\gamma_e = 0$  fits with the behaviour for  $\gamma_e \neq 0$  suggesting the mode seen here with sheared flow is not drastically different to the case in the absence of sheared flows. Similar asymmetry seen in the  $\gamma$  vs.  $\gamma_e$  data has been observed in global gyrokinetic simulations [147]. The mode's width varies with  $\gamma_e$ , and like in the isolated case the width appears to peak for a particular value of  $\gamma_e$ . Whilst the width peaked as  $\gamma_e \rightarrow 0$  for the isolated case, in the general case shown here it can be seen that the width peaks for  $\gamma_e \neq 0$ . This relates to

the fact that there is already a linear variation in  $\Omega_0$  before the sheared flow is introduced and hence the radial variation will be removed for a specific, non-zero, value of  $\gamma_e$ , at which point the radial width will peak. The linear Doppler shift can oppose the radial variation due to the  $\eta_s$  variation, which is given by the local model parameter  $\lambda$ . Using eqn. 5.131 with the equilibrium parameters used here, it can be seen that to achieve  $d\Gamma_E/dx = 2.2543$  (which is the real component of  $\lambda$ , given by eqn. 5.129) requires  $\gamma_e = 0.0128$  which is slightly below the shearing rate where the peak actually occurs. The discrepancy is due to the fact that the radial variation in the local growth rate is not altered by the introduction of sheared flow, and hence whilst there is no radial variation in  $\mathcal{R}(\Omega_0)$  it is necessary to counter the effect of the variation in  $\mathcal{I}(\Omega_0)$  by “over-compensating” the variation in real frequency. A simple illustration of this can be made by considering the expression for the mode radial width, eqn. 5.102, in terms of the real and imaginary components of both  $\beta = \beta_r + i\beta_i$  and  $\lambda = \lambda_r + i\lambda_i$ :

$$\Delta w = \frac{2\sqrt{2\log(2)}|\beta|}{\sqrt{nq'(\beta_i\lambda_r - \beta_r\lambda_i)}} \quad (5.132)$$

It is clear from eqn. 5.132 that  $\Delta w \rightarrow \infty$  for  $\beta_i\lambda_r \rightarrow \beta_r\lambda_i$  rather than simply for  $\lambda_r = 0$ . This suggests that a shearing rate which gives an effective radial variation in  $\mathcal{R}(\Omega_0)$  of  $\lambda_r \approx \lambda_i\beta_r/\beta_i$  will correspond to a mode with a very large radial width. Substituting in the values for the real and imaginary components of  $\lambda$  and  $\beta$  leads to the prediction that for  $d\Gamma_E/dx = 3.81863$  the mode’s radial width will be very large. This corresponds to  $\gamma_e = 0.0217$  which agrees well with the data shown in figure 5.18(b).

## 5.7.2 Future work

Whilst the results presented here have illustrated how it is possible to use the solutions of the local model to describe the properties of the global mode, there remain several important areas of interest that have not been explored. Perhaps the most obvious next step is to demonstrate the extension of the procedure highlighted here to general magnetic geometry and more complex physical systems than the simple model discussed. This can be achieved using existing local gyrokinetic codes, such as GS2, to map out  $\Omega_0(x, k)$ . This can then be used with the general procedure outlined here to calculate the global mode’s properties. These results can be benchmarked against global gyrokinetic codes in order to provide confidence in the extension to the general gyrokinetic system. This would allow experimentally relevant scenarios to be investigated. In particular 2D observations of fluctuations from electron cyclotron emission diagnostics provides an interesting opportunity to compare the predicted

poloidal position of the mode with that of the observations.

It has been shown that to fully describe the global mode it is strictly necessary to consider a range of  $x$  and  $k$ . Despite this a reasonable approximation can be made selecting  $x = 0$  and  $k = k_{\text{eff}}$ , where  $k_{\text{eff}}$  is an effective ballooning angle which, provided  $k(x)$  is slowly varying, is approximately  $k_{\text{eff}} = k(x = 0)$ . By parameterising the dependence of  $k(x = 0)$  on geometrical factors, such as triangularity and elongation, it should be possible to provide a reasonable prediction of  $k_{\text{eff}}$  provided the radial variation of  $\Omega_0$  is known<sup>34</sup>. This would be useful for any quasi-linear transport calculations where the saturated turbulent amplitudes are assumed to be related to the linear growth rate. By using  $k = 0$  in the quasi-linear calculations the linear growth rate will typically be significantly overestimated compared to the value found using  $k = k_{\text{eff}}$ , resulting in an overestimate of the quasi-linear transport. Furthermore, the radial size of the mode can be determined using this information which can help set the appropriate lengthscales in the problem. In addition, a non-zero ballooning angle is of large importance to the study of momentum transport, where terms which break the symmetry of the system are crucial [148, 149] (e.g. by providing a Reynolds stress that introduces plasma rotation [150]). By providing an effective ballooning angle it is possible to estimate the contribution to symmetry breaking due to the radial profile variation, allowing this to be included in simple transport models without the need for global simulations.

Only linear systems, where each toroidal mode number can be treated independently, have been discussed here. The applicability and impact of these results for nonlinear systems has not been considered. The global eigenmodes treated here essentially represent the final linear state of a time evolving instability. If in the time taken to form these eigenmode structures background fluctuations have had enough time to grow in amplitude to reach the nonlinear phase then it may be expected that these eigenmode structures will never form. In this scenario it is the peak growth rate, i.e. that for  $k = 0$ , that is of interest and the effective linear  $k$  will have little impact. It should be noted that until the eigenmode has formed the individual rational surfaces remain essentially uncoupled and shear damping may be expected to play a significant role. Moreover, if the rational surfaces are uncoupled then the ballooning nature of the instability will be somewhat destroyed and the poloidal amplitude will be set purely by the instabilities dependence on  $k$ . To answer the question as to how the time scale to reach the nonlinear phase and for eigenmode formation compare it will be necessary to recast the global model as an initial value problem<sup>35</sup> such that it is possible to investigate the time scale for eigenmode formation. This can then

<sup>34</sup>This could either be provided by a parameterisation of  $\Omega_0$  on the equilibrium profiles or through direct calculation by a local gyrokinetic or gyrofluid code for example.

<sup>35</sup>This can be achieved by retaining the  $d/dt$  terms in the original gyrokinetic equation rather than making the substitution  $d/dt \rightarrow -i\omega$ .

be compared with the growth rate of the local mode found for  $k = 0$ .



# Chapter 6

## Gyrokinetic stability of the MAST H-mode pedestal

### 6.1 Predicting the pedestal’s properties

The plasma performance (i.e. density and temperature) in the core is strongly coupled to that of the edge due to a feature known as “profile stiffness”. This stiffness refers to experimental observations that in the central region between the core and edge there is typically a minimum profile length scale that can be achieved [151–153], i.e. that the density and temperature gradients cannot exceed a given level. This behaviour is thought to be due to the onset of microinstability driven turbulent transport when exceeding the critical gradient for the onset of the mode. Assuming the transport increases rapidly with increasing drive<sup>1</sup> this will clamp the gradient driving the mode to this marginal point. This idea is exploited by numerous transport calculations (such as those discussed in section 2.7) as the expected gradients can be determined simply by searching for the linear instability threshold and it becomes possible to develop relatively simple transport models [154, 155]. By suppressing these microinstabilities and the resulting transport in a region, for example through sheared flows near the plasma edge, the driving gradients may be increased above their usual limits, leading to a region of improved confinement. Outside of this region the profile stiffness remains which highlights the importance of the edge region in setting the core performance. The prediction of the pedestal height and width is therefore extremely important in predicting the plasma performance of tokamaks operating in H-mode. Transport calculations based on 1D gyrofluid models indicate that a temperature pedestal height of 4 keV is required for ITER to be able to meet its performance targets [156].

---

<sup>1</sup>Whilst no clear definition is generally used to rigorously quantify the stiffness the rate at which transport increases with increasing drive is often used to characterise a mode’s stiffness.

Without external intervention the H-mode pedestal will typically evolve until an explosive edge localised mode (ELM) is triggered, causing the pedestal to collapse in a cyclical process known as the ELM cycle. Understanding what processes determine the pedestal evolution and what triggers the ELM is crucial to being able to predict the state of the pedestal just prior to the ELM and in the times leading up to the crash. Unlike in current machines, ELMs are a serious concern for the lifetime of plasma facing components (PFCs) in ITER [66, 157, 158] and it is necessary to consider the stability of the ITER pedestal to ELMs<sup>2</sup>. Techniques for triggering ELMs early (ELM mitigation) or preventing them entirely (ELM suppression) are being investigated on current generation tokamaks [111, 112, 159] and typically involve the application of a magnetic perturbation to the edge of the plasma<sup>3</sup>. These studies suggest that it should be possible to increase the ELM frequency, thereby reducing the peak power transferred to the PFCs<sup>4</sup>. As these techniques prevent the pedestal from achieving its natural final state it is important for ITER that the dynamics of the pedestal are understood. It is insufficient simply to describe the limiting case just prior to a natural ELM crash.

### 6.1.1 The peeling-ballooning ELM model

Signatures of an ELM can be observed with a number of different diagnostics, providing useful information in the development of an ELM model. These signatures can vary somewhat depending on the operational regime leading to the classification of ELMs into numerous different categories. The definition of these ELM types will not be discussed here<sup>5</sup> other than to say that type I ELMs, associated with operating at powers well above that required to enter H-mode, tend to provide the largest transient heat loads ( $\sim 5 - 15\%$  of stored energy in  $10^2 - 10^3 \mu\text{s}$  [161]) and are the most concerning for ITER. The following discussion will focus on these type I ELMs.

Perhaps some of the most useful observations arise from optical imaging of the plasma during the ELM crash. The spherical tokamak MAST is especially well suited to capture such images and an example is shown in figure 6.1. These images show filamentary, field aligned structures associated with the ELM and the associated toroidal mode number, typically found to be  $10 < n < 20$  [162], can be estimated

<sup>2</sup>Calculations, assuming that ELMs in ITER have similar characteristics to current observations, suggest that for ITER to survive its proposed 3000 shots the typical ELM energy loss must be less than  $\sim 4$  MJ and ELMs exceeding this limit must be rare [157].

<sup>3</sup>Techniques for directly triggering ELMs are also being investigated, often known as ELM pacing. These include methods such as injecting pellets or providing a rapid vertical plasma displacement [160].

<sup>4</sup>The energy deposited by an ELM is typically proportional to the time since the previous ELM, i.e.  $W_{\text{ELM}}f_{\text{ELM}} \approx \text{const.}$  with  $W_{\text{ELM}}$  the energy lost per ELM and  $f_{\text{ELM}}$  the ELM frequency [64].

<sup>5</sup>A good outline of the various ELM types is provided in Ref [63].

by analysing the filaments [163]. The filaments are seen to erupt radially out of the plasma on the low field side of the tokamak (i.e. in the direction of increasing major radius) with a radial velocity on the order of  $0.1 - 1 \text{ km s}^{-1}$  [161].

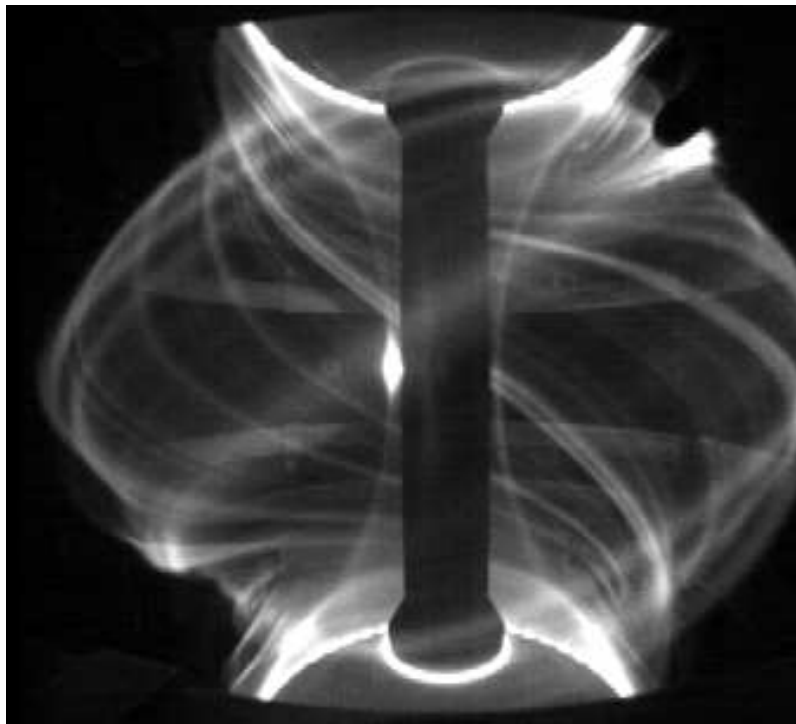


**Figure 6.1:** Visible image during ELM crash taken from MAST. Reprinted with permission from Ref [163].

Magnetic fluctuations with frequency similar to the Alfvén frequency,  $\mathcal{O}(10^5 \text{ Hz})$ , are often observed leading up to (and during) the ELM crash [65]. This, in conjunction with the timescales associated with the ELM crash,  $\mathcal{O}(10 \mu\text{s})$ , suggests that ELMs have an origin in MHD instability [164]. This is further corroborated by the observation that the normalised pressure gradient

$$\alpha = -\frac{2\mu_0 R q^2}{B^2} \frac{dp}{dr} = -\frac{\beta R q^2}{L_p} \quad (6.1)$$

with  $p$  the plasma pressure,  $\beta = 2\mu_0 p/B^2$  the normalised plasma pressure and  $L_p = p/p'$ , is typically close to the critical value for onset of the ideal MHD ballooning instability [165],  $\alpha_c$ , in the pedestal [64, 166]. Whilst this suggests that the ideal MHD ballooning instability may be playing an important role in the ELM cycle, observations of pedestals with pressure gradients around  $\alpha_c$  which don't display type I ELMs [167] and observations showing the pressure gradient may reach this value well before the ELM crash [168] suggest that these ballooning modes do not lead directly to the ELMs but an additional trigger is required.

The large pressure gradient associated with the pedestal region results in a large current density peak through the “bootstrap current” [169]. The origins of this parallel current can be elucidated by considering the trapped particle orbits in the

presence of a density gradient. As the sense of the banana orbit is set by the trapped particle's charge it is clear that two like trapped particles centred on the flux surfaces at  $r$  and  $r + \delta_b$ , where  $\delta_b$  is the banana orbit width, will both pass through  $r + \delta_b/2$  (assuming  $\delta_b$  doesn't vary significantly over this scale) but will have the opposite sign of  $v_{\parallel}$  at this point. If there is a density gradient, such that there are more trapped particles at  $r$  than  $r + \delta_b$ , then there will be more trapped particles travelling in one direction than the other at a given radial position, leading to an apparent net parallel momentum in the trapped particles<sup>6</sup>. This gives rise to a friction on passing electrons, whilst the same process occurs for the ions but with a reversed parallel velocity (due to the reversed banana orbit direction) leading to a parallel current. The current is limited by passing electron-ion collisions. The calculation of this bootstrap current for arbitrary geometry and collisionality is complicated and a numerically derived formulation, often referred to as the Sauter formula, is often used [170, 171]. There can be additional contributions to the current (such as the diamagnetic current) which can be taken into account, though are often negligible relative to the bootstrap term.

MHD instabilities can be driven by both the pressure and current gradients [172] and the induced bootstrap current due to the pedestal pressure gradient can lead to the destabilisation of additional MHD modes. The role of low- $n$  “kink” modes (driven mainly by radial current gradients) in setting operational limits<sup>7</sup> [172] has led to these being well studied and it has been suggested that a related instability may play a significant role in the ELM [173]. Ideal external kink modes<sup>8</sup> require a resonant rational surface outside of the plasma, with the growth rate increasing as the rational surface moves towards the plasma surface. When the rational surface is very close to the plasma surface the instability is strongly localised to the edge region [173, 174], suggesting higher  $n$ , and the instability is dependent upon the parallel current flowing at the plasma edge,  $J_{\parallel}$ . Simulations of these modes, referred to as peeling modes [175], can be used to derive stability boundaries in terms of normalised pressure gradient,  $\alpha$ , and shear<sup>9</sup>,  $\hat{s}$ , [174, 176]. Importantly studies, in a simple circular cross section geometry (similar to that used in chapter 5), also calculated the stability of the ballooning modes and it was found that for appropriate edge parameters these could couple to the peeling modes resulting in peeling-ballooning (PB) modes [174, 176, 177], though the precise behaviour is sensitive to many factors

---

<sup>6</sup>This is similar to the mechanism behind the diamagnetic current, though here it is the difference in the number of particles with the two senses of the Larmor orbit rather than the banana orbit and hence this is in the binormal (in flux surface perpendicular) direction.

<sup>7</sup>The low- $n$  ( $n \sim 3$ ) nature of these modes means the resulting instability has a global effect on the plasma, leading to a distortion or “kinking” of the entire plasma.

<sup>8</sup>The qualifier “external” is occasionally used to distinguish it from the internal,  $n = m = 1$ , kink mode associated with the sawtooth crash [29, 172].

<sup>9</sup>Here the shear is used to represent the normalised edge current density in a more accessible term.

including the magnetic geometry [178, 179]. These PB modes can extend further into the plasma than the localised peeling modes and have been proposed as a model for the ELM [174]. In the following text we use PB to refer to pure peeling and ballooning modes as well as the coupled peeling-ballooning modes unless otherwise stated.

The stability of PB modes will depend upon both the edge current and pressure gradient. A simple cartoon given in Ref [174] to describe the ELM cycle based on the evolving stability of these MHD modes is as follows:

1. Immediately following a large ELM (or after the L-H transition) the edge current density and pressure gradient is low but increases rapidly (due to suppressed turbulence) until the ballooning boundary is reached.
2. The edge current evolves (possibly on a similar timescale to that of the pressure [180]) increasing until the peeling ballooning boundary is reached.
3. Further increases lead to PB instability which reduces the pressure gradient, further enhancing the instability leading to a large drop in pressure gradient and current density and the plasma returns to near its initial state.

An example stability boundary is shown in figure 6.2 with the three phases labelled.

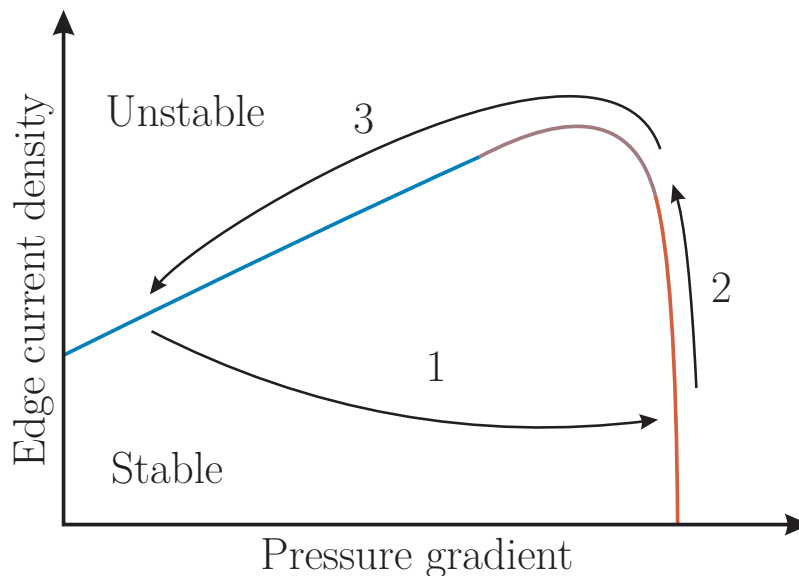


**Figure 6.2:** A cartoon based on the peeling-ballooning model for the plasma evolution during an ELM cycle proposed in Ref [174]. The red, blue and purple lines represent the ballooning, peeling and peeling-ballooning stability boundaries, respectively, as a function of pressure gradient and edge current density. The proposed evolution during the ELM cycle is described in the main text.

In practice quantitative calculations of these stability boundaries are complicated by the dual role of the pressure gradient and associated bootstrap current:

- Whilst the ballooning modes are pressure gradient driven this pressure gradient can in fact stabilise the peeling modes.
- The bootstrap current associated with the pressure gradient provides a driving term for the peeling mode whilst reducing the edge shear which can stabilise the ballooning modes.

The interplay between these effects will depend upon many factors such as the flux surface shaping and the impurity content. Detailed numerical calculations are required in order to calculate the stability boundary determined by the PB modes for a given equilibrium as a function of edge current and pressure gradient.

The linear ideal MHD stability code, ELITE [181, 182], was developed in order to calculate the growth rate and mode structure of PB instabilities for arbitrary geometry. This uses ballooning theory modified to include surface terms important for peeling modes, which were neglected in Ref [132]. Importantly finite  $n$  corrections are included, allowing the treatment of the intermediate  $n$  modes associated with ELMs<sup>10</sup>. This allows stability calculations to be performed for experimentally consistent equilibria, providing a means to test the PB model of the ELM crash. Early calculations using ELITE of the stability of PB modes for several times leading up to an ELM crash, based upon DIII-D data, showed the  $n = 10$  PB growth rate increasing rapidly just prior to the ELM crash [182]. Furthermore, the profile of observed electron temperature loss due to the ELM matches the amplitude of the calculated radial PB mode structure<sup>11</sup>. Further studies of DIII-D data [183, 184] and other tokamaks, such as Alcator C-Mod [182], have shown good qualitative and quantitative comparisons between the observed pedestal properties and the PB stability<sup>12</sup>. Such studies using real experimental equilibria and profiles provide compelling evidence for the PB ELM model.

### 6.1.2 The EPED model

Given magnetic equilibrium data, including the pressure profile, it is possible to use ELITE to determine if the PB mode is unstable. Without information about the expected form of the pressure profile an equilibrium cannot be constructed and it is not possible to provide predictions of the actual pedestal pressure profiles likely to be obtained prior to an ELM in future experiments. However, by assuming a functional form for the pressure profile it is possible to study the limits imposed on the pedestal height as a function of the model parameters. An example functional

<sup>10</sup>The lower limit in  $n$  is given in Ref [182] to be  $\sim 5$ .

<sup>11</sup>In other words the relative electron temperature loss is largest where the PB eigenfunction is largest.

<sup>12</sup>These comparisons typically either illustrate the PB mode being just above marginal immediately prior to the ELM crash or stable in ELM free H-mode.

form is:

$$F(\psi) = F_s + F_c \left[ 1 - \left( \frac{\psi}{\psi_p} \right)^{\alpha_1} \right]^{\alpha_2} + F_p \left[ \tanh \left( \frac{2 - 2\psi_m}{\Delta} \right) - \tanh \left( \frac{2\psi - 2\psi_m}{\Delta} \right) \right] \quad (6.2)$$

where  $\psi$  is the poloidal flux normalised to the value at the separatrix,  $\Delta$  is the pedestal width,  $\psi_m$  and  $\psi_p$  set the location of the pedestal midpoint and top,  $F_s$ ,  $F_p$ ,  $F_c$  control the separatrix, pedestal and core values respectively and  $\alpha_1$  and  $\alpha_2$  are model parameters used to control the core profile. Functions of the form given in eqn. 6.2 were used to represent the density and temperature profiles in a study of ITER using ELITE [177]. Here  $\alpha_1$  and  $\alpha_2$  were picked to be in rough agreement with core transport modelling. Multiple ELITE runs with varying temperature pedestal height,  $T_{ped}$ , and fixed density pedestal height,  $n_{e,ped}$ , were used to find the limiting pedestal temperature (and hence pressure) for a given pedestal width and with toroidal mode numbers in the range  $8 \leq n \leq 30$ . This limit was taken to be set when the calculated growth rate exceeded a small threshold level. These calculations indicate that in order for ITER to achieve the required temperature pedestal of 4 keV [156] (introduced in section 6.1) the pedestal width must be greater than about 2.5% of the minor radius. This study highlights three unknowns preventing the prediction of the temperature pedestal height in current and future tokamaks:

1. The toroidal mode number,  $n$ .
2. The pedestal width,  $\Delta$ .
3. The relative density and temperature contributions to the pressure profile.

The toroidal mode number can be restricted to a modest range based on the observations made on existing tokamaks, such as  $5 < n < 30$ . Whilst this may give a reasonable estimate as to the stability limits in a given device, in cases such as ITER, which must operate near these stability limits without crossing them, the variations in the prediction can be important. For example, for a pedestal width of 2.5% of the minor radius the stable ITER temperature pedestal height found in Ref [177] covers a range  $\sim 3.5 \text{ keV} < T_{ped} < 4.5 \text{ keV}$  for  $15 < n < 30$  which translates to a fusion gain of  $7 < Q < 13$  [156]. Physically it is expected that the toroidal mode number with the largest growth rate will correspond to the ELM. Whilst ELITE provides the growth rate for a given mode number it does not include all the relevant physics which may determine which toroidal mode number has the largest growth rate. For example the effect of sheared flows (not included in ELITE) on the stability of a mode is likely to depend upon its radial extent, which is something that will change with toroidal mode number. ELITE therefore may not correctly identify the most

unstable toroidal mode number<sup>13</sup>. It is possible to incorporate additional effects, such as sheared toroidal flows, diamagnetic effects and others discussed in Ref [185], into existing codes such as ELITE, allowing a more accurate calculation of the most unstable mode number and improved treatment of threshold effects.

To determine the pedestal width,  $\Delta$ , it is useful to consider the state of the edge region immediately after the L-H transition. It is widely thought that this transition is related to the suppression of edge turbulence due to sheared flows. The associated reduction in transport allows the temperature and density gradients to increase in this region until some stability limit is reached<sup>14</sup>. The pedestal width may then evolve due to other processes (such as current diffusion and the evolution of the flow). As the pedestal width evolves the height will also evolve to maintain the critical gradient. This will continue until the PB mode stability boundary is crossed and an ELM is triggered<sup>15</sup>. By characterising the instability responsible for setting the pressure gradient limit it is possible to calculate the limiting pedestal height for a given width, using the same procedure as described earlier for calculating the peeling ballooning limit. This provides a constraint on the pedestal height as a function of the pedestal width. Should this constraint lie above that set by the PB stability boundary then the plasma will enter the PB unstable region, leading to an ELM crash. This idea is illustrated in figure 6.3 which shows a cartoon of the PB stability curve (black line) as a function of pedestal height and width along with three other example potential stability limits. The location where these stability limits cross the PB limit, highlighted by the square points, sets the prediction of the pedestal height and width immediately prior to the ELM. If they do not cross then it is anticipated a typical ELM crash will not occur and the pedestal will continue to evolve until another mechanism causes this to halt.

A model known as EPED has been developed to make predictions of the pedestal height and width based on such a two constraint procedure [110]. The stability of kinetic ballooning modes (KBMs) are employed to provide a secondary constraint in addition to the PB stability limit. These are electromagnetic kinetic microinstabilities which are the kinetic analogue of the ideal ballooning modes discussed earlier. Indeed KBMs can be described by similar equations to the ideal ballooning mode [186], though the kinetic effects provide a destabilising influence for low  $k_{\perp}\rho_i$  and a stabilising influence for higher  $k_{\perp}\rho_i$  [187]. Importantly, the critical  $\beta = \beta_k$  (or  $\alpha = \alpha_k$ ) associated with these instabilities is expected to be around that of the ideal MHD mode and therefore the observations of the pedestal gradient remaining around

<sup>13</sup>Indeed such missing effects are also likely to introduce a small error into the calculated stability limits for a given toroidal mode number.

<sup>14</sup>In the PB model, introduced in the previous section, this limit is set by the onset of ideal MHD ballooning modes.

<sup>15</sup>Alternatively others factors, such as externally applied perturbations, could act to halt the pedestal width evolution, preventing the ELM being triggered.

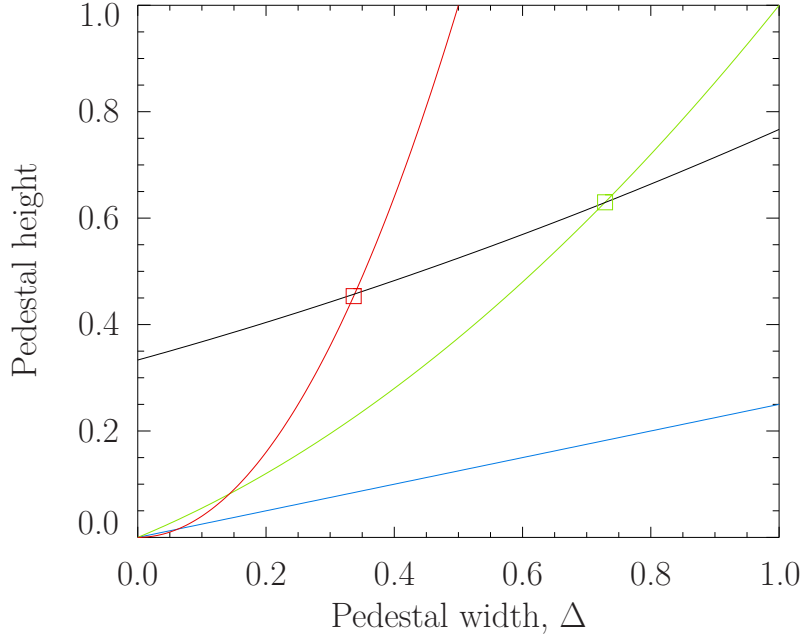


**Figure 6.3:** A cartoon of the pedestal height limits at a given width for the peeling-ballooning mode (black) and three example models for the critical gradient limit (red, green and blue). Immediately after the ELM crash the pedestal height is low but quickly increases until it reaches the first boundary, e.g. the red, green or blue curves; the pedestal then evolves along this curve until the peeling-ballooning limit is crossed (black) at which point an ELM is triggered and the process repeats. This two constraint model for the pedestal provides a prediction of the limiting pedestal height and width immediately prior to an ELM crash based on where the two stability limits intersect.

the critical ballooning value is consistent with a KBM limit. These KBMs may be thought of as setting a local constraint on the pressure gradient (although non-local effects are likely to have some influence in the pedestal) whilst the PB mode imposes a global constraint. Whilst the KBM stability may be considered, to first approximation, to be local, i.e. it only depends on the parameters on a given flux surface, factors like the bootstrap current (and hence the shear) depend upon the gradients away from this surface<sup>16</sup>. To achieve a pressure profile which is precisely at the critical gradient across the entire pedestal is therefore a complicated minimisation problem, requiring iteration. Hence when determining the pedestal height limit set by KBMs for an assumed profile shape it is unlikely that the entire pedestal will be at the marginal gradient. This raises the question as to how to define the limit; does the entire pedestal need to be at marginal or beyond or is it sufficient that a certain proportion of the pedestal is marginal? Depending upon how this limit is defined the precise stability limit may move, thereby altering the prediction and hence this definition must be made as part of the two constraint predictive model.

<sup>16</sup>For example should the pressure gradient increase outboard of a given surface then on that surface the value of  $\beta$  will rise, thereby altering the critical  $L_p$  (c.f. eqn. 6.1).

There have been several iterations of the EPED model, with the current version known as EPED1.6. These iterations introduce various refinements as new techniques are developed and understanding improves. Here only the differences in the model used to represent the KBM stability limit will be discussed. When the EPED model was first developed the computational requirements and numerical difficulties associated with electromagnetic linear gyrokinetic simulations in the outer regions of shaped plasmas made it prohibitive to perform direct calculations of the KBM stability for the large number of cases required to accurately determine the stability limit as a function of pedestal height and width. A parameterisation for the pedestal width based on arguments relating  $\alpha_k$  and its average across the pedestal,  $\langle\alpha_k\rangle$ , to the poloidal beta at the top of the pedestal,  $\beta_{\theta,ped} = \beta_{ped}B^2/B_\theta^2$ , for large aspect ratio tokamaks was introduced [110]:

$$\Delta = 0.076\sqrt{\beta_{\theta,ped}} \quad (6.3)$$

This scaling is consistent with observations from a number of tokamaks [188]. The parameter 0.076 in eqn. 6.3, is taken to be fixed for all standard aspect ratio tokamaks and was determined by fitting  $c_1\sqrt{\beta_{\theta,ped}}$  to data from a large number (>4000) of DIII-D timeslices [110]. The predicted pedestal width and height using this stability constraint along with the PB constraint was tested against data from a number of standard aspect ratio tokamaks and was found to show quite good agreement [188]. An example of the predicted and the measured pedestal width and height immediately prior to an ELM crash on DIII-D is shown in figure 6.4.

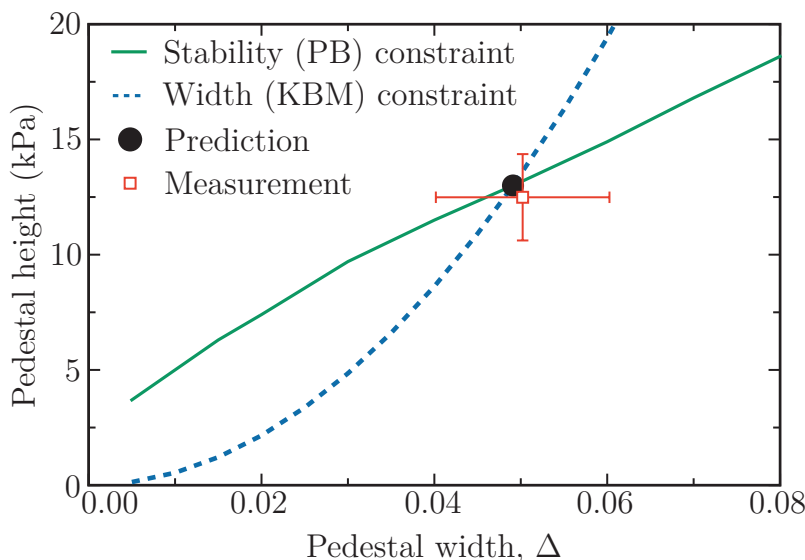


**Figure 6.4:** The calculated PB (green) and  $0.076\sqrt{\beta_{\theta,ped}}$  (blue) stability limits for DIII-D shot 132010. The predicted pedestal height and width (dot) agree within errors with the observed values immediately prior to and ELM (red square). This figure is based on figure 5 of Ref [110]. Reprinted with permission from [110]. Copyright 2009, American Institute of Physics.

Version 1.5 of EPED exploits the similarity of ideal local (i.e.  $n = \infty$ ) ballooning modes (referred to as  $n_\infty$  modes) with KBMs observed in the core [189, 190] to replace the  $0.076\sqrt{\beta_{\theta,ped}}$  constraint with one based upon the stability of ideal ballooning modes [191]. These calculations are relatively computationally inexpensive, but allow for important effects such as plasma shaping to be included unlike in EPED1. This provides the possibility of using EPED1.5 to predict the pedestal properties of spherical tokamaks. The application of an EPED1.5 type model to predicting the pedestal properties of the spherical tokamak MAST [192] forms part of the work discussed in section 6.2. As the ideal ballooning stability is a local quantity it is necessary to consider the precise definition of when the ballooning modes set a limit on the pedestal height. In Ref [191] the procedure used to determine the limiting pedestal height is when a region of the pedestal greater than 1% (measured in  $\psi_N$ ) is ideal ballooning unstable. Recently version 1.6 of EPED has been introduced which uses a technique referred to as the “ballooning critical pedestal” (BCP) technique to characterise the KBM limit [127]. Once again the onset of the KBM is taken to be set by the onset of the ideal ballooning modes. Importantly, the BCP technique defines the pedestal height to be limited when 50% of the pedestal is marginal or unstable<sup>17</sup> to the ideal ballooning modes. The value of 50% has been selected in order to represent the entire pedestal region being near marginal on average. The various versions of EPED have been extensively tested against data from numerous standard aspect ratio tokamaks. These tests, discussed in some detail in Ref [127], typically show very good agreement between the model and experiment, with the ratio of experimental to predicted pedestal heights often found to be around  $1 \pm 0.2$  (i.e. the predictions are within 20% of observations).

The remaining missing component in predicting the core performance, that of the relative contribution of the temperature and density to the pressure, is perhaps the most challenging. The separate evolution of the density and temperature pedestal profiles from the initial state following the ELM crash will depend upon both the heat and particle sources and the transport mechanisms (i.e. the microinstabilities) in the edge region. It will be shown later that the KBM growth rate responds equally to changes in the density and temperature gradients (i.e. it is the pressure gradient that drives the instability) and therefore the KBM constraint on its own doesn't help isolate the separate effects of density and temperature. In this case it may be expected that the final density and temperature profiles will be set by the relative size of the particle and heat sources. However, in the picture of the ELM cycle proposed by the EPED model it is typically assumed that the pedestal width will increase throughout the ELM cycle. Considering a flux surface which is initially just in from the pedestal (i.e. towards the core) it is clear that for the pedestal to expand through

---

<sup>17</sup>In fact as the ballooning modes can enter a “second stable” region for sufficiently large  $\alpha$  the criterion is in fact simply at or beyond the lower stability boundary.

this surface the shallow gradients initially present here must be allowed to steepen. The evolution of the pedestal as it expands inwards is determined by the transport processes occurring in the shallow gradient region at the top of the pedestal. For example if a temperature gradient driven instability is unstable at the pedestal top then attempts to increase the temperature gradient here are likely to be met by large increases in the heat flux. This is again a manifestation of the stiff nature of the core transport resulting in the gradients being pinned to critical values. In such a scenario it may be expected that whilst the density gradients are free to evolve the temperature pedestal will remain roughly constant throughout the ELM cycle due to the temperature gradient driven turbulence<sup>18</sup>. As the many instabilities which can exist in plasmas respond in different ways to the density and temperature gradients, the precise relation between density and temperature is complicated. To fully determine this relationship it is necessary to perform a transport analysis that includes turbulence and the full heat and particles sources<sup>19</sup> which is an extremely challenging task.

## 6.2 Testing an EPED-type model for the MAST pedestal

The EPED model has been tested on a range of standard aspect ratio tokamaks but not on spherical tokamaks (STs) and it is unknown whether it is possible to accurately predict the pedestal properties in such devices using this model. To test such a model for STs a type-I ELMy H-mode discharge from MAST will be investigated and the PB and  $n_\infty$  stability constraints calculated to determine if the pedestal immediately prior to the ELM crash is consistent with the intersection of the PB and  $n_\infty$  constraints. Further to this by studying the stability constraints as a function of time it is possible to determine if the pedestal gradients are indeed limited by the  $n_\infty$  stability limit throughout the ELM cycle, as implied by the EPED model.

The remainder of this chapter introduces a study of the pedestal evolution for a MAST H-mode discharge. The experimental measurements of electron density and temperature profiles are discussed in section 6.2.1 and an EPED1.5 type stability analysis based on the equilibria obtained is made in order to test if such a model is applicable to spherical tokamaks, and this will be discussed in section 6.2.2. Fol-

---

<sup>18</sup>However, as the density gradient evolves the turbulence is likely to be affected and it may then become possible to achieve higher temperature gradients at the same time as higher density gradients. The precise behaviour observed is likely to be strongly dependent on the specific equilibrium conditions and the particle and heat sources.

<sup>19</sup>Including neutral penetration from the edge for example.

lowing this a linear gyrokinetic analysis of the microstability of both the steep and shallow gradient regions is presented in section 6.3 allowing the dominant instabilities to be identified. This provides an opportunity to test the validity of the KBM constraint used by the EPED model as well as offering insight into the role that microinstabilities at the top of the pedestal play in its evolution.

### 6.2.1 Experimental observations

To study the inter-ELM pedestal evolution it is necessary to obtain accurate measurements of both the density and temperature profiles throughout an ELM cycle. The electron density and temperature can be obtained through a Thomson scattering diagnostic. This diagnostic technique involves firing a laser through the plasma and analysing the properties of the scattered light<sup>20</sup>. The Thomson scattering system on MAST has high spatial resolution [193, 194] resulting in 130 measurement points across the plasma, with several ( $\sim 6$ ) in the pedestal, providing a good determination of the pedestal width (and gradient). In addition to this, whilst each Thomson laser has a firing rate of approximately 33 ms, the temporal resolution is improved due to the use of 8 separate lasers. This provides an average temporal resolution of 4.2 ms with the additional possibility of firing the lasers in a rapid burst, with resolutions of up to 5  $\mu$ s being used in experiment [195]. In MAST, typical type-I ELM cycles are around 6 – 12 ms in duration meaning that there are typically 1 or 2 laser pulses per cycle. Using just these single laser pulses to diagnose the ELM cycle will provide poor temporal resolution and may not well represent any different phases of the ELM cycle that may exist. Whilst the burst mode offers a way to get higher resolution data this can be somewhat challenging to use to diagnose a particular ELM cycle. To improve the statistics of the measurements used in the study presented here a H-mode discharge with periodic ELMs was repeated three times<sup>21</sup> with the Thomson lasers firing at evenly spaced intervals. Extracting the Thomson measurements during the type-I ELMing phase provides 50 profiles which can be arranged by the time since the previous ELM,  $\delta t$ , normalised to the period between two ELMs,  $\tau_{\text{ELM}}$ , thus representing a series of measurements as a function of normalised time,  $0 \leq t = \delta t / \tau_{\text{ELM}} \leq 1$ . Modified hyperbolic tangent, or mtanh, models:

$$F(r) = \frac{a_{\text{ped}} - a_{\text{sol}}}{2} \left[ \text{mtanh} \left( \frac{a_{\text{etb}} - r}{2a_{\Delta}}, a_{\text{slope}} \right) + 1 \right] + a_{\text{sol}} \quad (6.4)$$

with

$$\text{mtanh}(r, b) = \left( \frac{(1 + br)e^r - e^{-r}}{e^r + e^{-r}} \right) \quad (6.5)$$

<sup>20</sup>See [25] for a brief summary.

<sup>21</sup>The shot numbers of these discharges are #24452, #24459 and #24763.

can be used to parameterise the density and temperature profiles in terms of the four model parameters,  $\{a\}$ . By binning the model parameters corresponding to the different time points into five time ranges it is possible to obtain mtanh profiles characteristic of the experimental pedestal evolution, described by the average model parameters in each of the time bins.

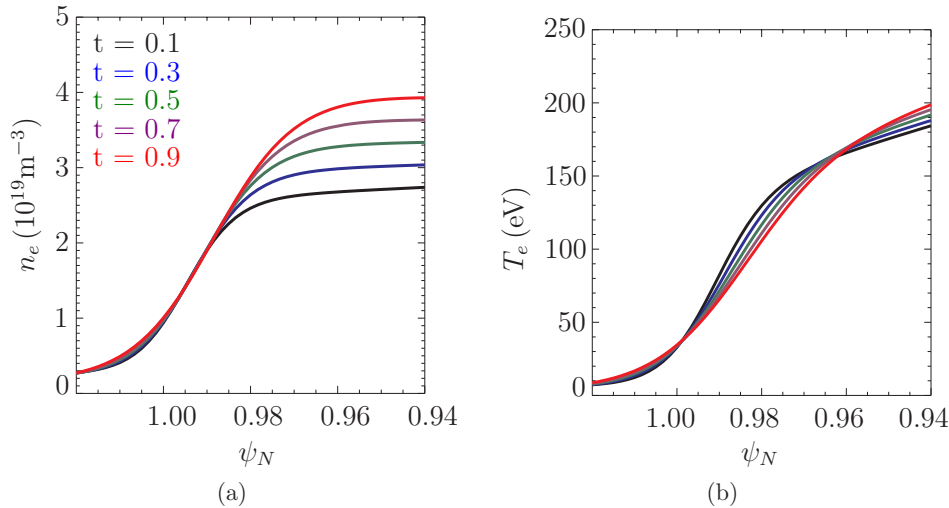


**Figure 6.5:** The density [figure 6.5(a)] and temperature [figure 6.5(b)] profiles generated by the composite-binning technique for five equally sized temporal bins representing the entire inter-ELM period corresponding to the times (normalised to the ELM period) 0.1, 0.3, 0.5, 0.7 and 0.9 (i.e. the temporal bins correspond to 0-20%, 20-40%, 40-60%, 60-80% and 80-100% of the ELM cycle).

The five electron temperature and density profiles are shown in figure 6.5. It can be seen that whilst there is little difference in the temperature profile throughout the ELM cycle<sup>22</sup> the density continues to evolve up until the ELM crash. In both cases it appears that the peak gradient is fixed to some value, though the region over which this peak gradient exists increases with time for the density. It is useful to look at the net pressure evolution, as it is this which is important for the instabilities underlying the EPED model. The pressure profile evolution is given in figure 6.6 along with the corresponding pressure gradient profiles. It can be seen that whilst the peak pressure gradient increases by around 10% throughout the ELM cycle the region of steep normalised pressure gradient ( $> 10$  kPa for example) increases by a factor  $\sim 2-3$ , agreeing with the behaviour shown by the density evolution. It should be noted that the use of fixed functional forms (such as the mtanh form used here) can emphasise or obscure certain features of the profile measurements. For example the mtanh form can overestimate the peak gradient whilst underestimating that near the top and foot of the pedestal<sup>23</sup> on DIII-D measurements [197]. Whilst the use

<sup>22</sup>As the profiles are generated from binned data the collapse and recovery of the profiles are not observed here. High temporal resolution data from JET shows that the crash and subsequent pedestal recovery can occur rapidly compared to the inter-ELM time scale [196].

<sup>23</sup>Indeed this is (at least part of) the motivation for the BCP constraint introduced by EPED1.6.

of such functional forms is still desirable<sup>24</sup> it is important to retain these issues in mind whilst drawing conclusions based upon results using these profiles.

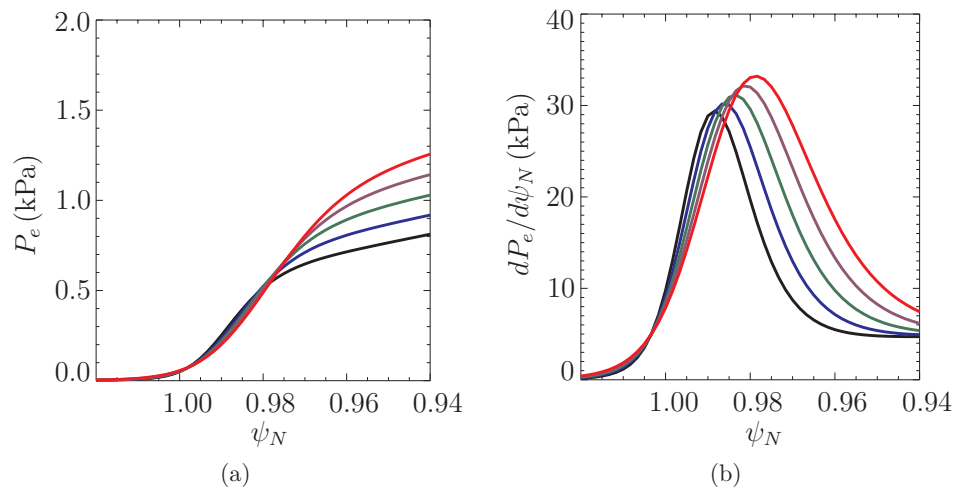


**Figure 6.6:** The pressure [figure 6.6(a)] and corresponding gradient [figure 6.6(b)] profiles for the five times through the ELM cycle considered here, calculated using the density and temperature profiles given in figure 6.5.

## 6.2.2 MHD stability analysis

Now that the pressure profile has been obtained at the five times (normalised to the ELM period)  $t = 0.1, 0.3, 0.5, 0.7$  and  $0.9$ , it is possible to perform MHD (PB and  $n_\infty$ ) stability analysis for the evolving pedestal. In order to achieve this it is necessary to reconstruct MHD equilibria at each of the five time points, with particular focus given to the edge region. In addition to the electron density and temperature measurements provided by the Thomson scattering system this equilibrium reconstruction requires information about the main species ion profiles as well as impurity ion concentrations. This extra information can alter the equilibrium reconstruction and the bootstrap current, which is known to play a key role in the PB stability. The MHD stability may be sensitive to the assumptions made regarding these ion quantities and it is useful to check how the stability varies as these assumptions change. In particular two models for the ion temperature have been tested; the first of these is the equal temperature assumption  $T_i = T_e$  whilst the second is known as the “flat” model where  $T_i = T_e$  is assumed in the core but in the pedestal  $T_i$  is found by extrapolating from the pedestal top using the  $T_e$  gradient from the core such as to avoid a steep ion temperature gradient<sup>25</sup>. Carbon is assumed to be the main impurity species (as

<sup>24</sup>These functional forms help to work around the limitations of low diagnostic resolution. In addition they provide a useful way to generate the profiles required as input to predictive PB calculations, which can also be compared easily to experiment through the model parameters.

<sup>25</sup>Edge ion temperature measurements on MAST indicate that in low collisionality discharges the flat model is appropriate whilst in high collisionality cases the equal temperature model is suitable [198].

the divertor targets are made from carbon fibre composites) and the effective charge,  $z_{\text{eff}}$ , is taken to be 2 everywhere, consistent with experimental measurements from MAST [199], leading to the main species ion density being given by  $n_i = 5n_e/6$ . Using the boundary shape, total plasma current and vacuum magnetic field calculated in equilibrium reconstructions made using EFIT [200] along with calculations of the bootstrap current using the Sauter formula [170, 171], the HELENA code [201] can be used to reconstruct high precision equilibria.

The HELENA code also provides a calculation of the  $n_\infty$  stability as a function of flux surface so that the region unstable to  $n_\infty$  modes is known immediately once the equilibrium has been found. The  $n_\infty$  unstable region for the five experimental time points is shown in figure 6.7 for both ion temperature models. It can be seen that the unstable region expands throughout the ELM cycle as the pedestal expands. The choice of the ion temperature gradient model has little impact on the  $n_\infty$  stability. This insensitivity to the ion temperature model has been found for all the stability calculations considered here and hence following results will all be for the  $T_i = T_e$  model.

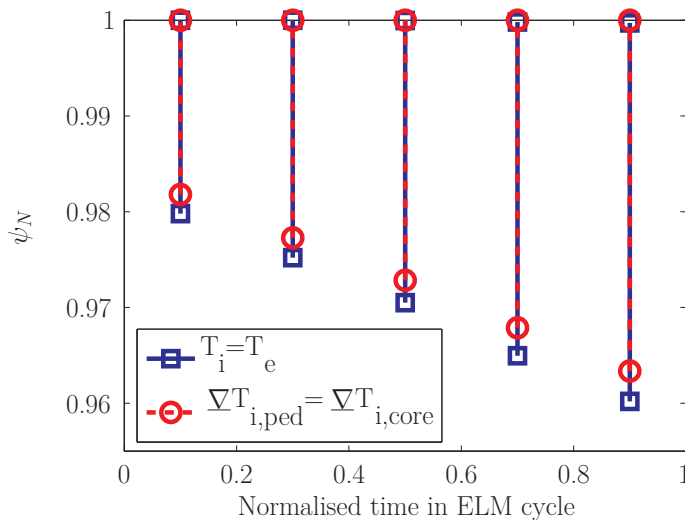


**Figure 6.7:** The region in normalised poloidal flux,  $\psi_N$ , unstable to  $n_\infty$  ballooning modes throughout the ELM cycle for equal (blue solid, square) and flat (red dashed, circle) ion temperature models.

Whilst this procedure allows the MHD stability of the experiment to be tested at each of the five time points, it provides no information about how far from the stability boundary the experiment is. In order to map out the stability constraints used by the EPED model it is necessary to scale the pressure pedestal height at fixed width. This can be achieved by scaling the density and temperature profiles by some factor and the resulting profiles are characterised by the peak normalised pressure gradient,  $\alpha_{\text{max}}$ . The procedure used here is to scale the density profile for fixed temperature as

this is closest to the experimental behaviour<sup>26</sup>. For each new set of profiles the full equilibrium reconstruction procedure can be performed, including a self-consistent calculation of the bootstrap current.

As the pressure profile is scaled the  $n_\infty$  ballooning stability provided by HELENA can be used to find the limiting gradient (i.e. the KBM constraint), following either an EPED1.5 or EPED1.6 (BCP) approach. To calculate the PB stability the HELENA generated equilibrium can be used with the finite- $n$  stability code ELITE introduced earlier. In these calculations the toroidal mode number has been limited to the range  $5 \leq n \leq 25$  consistent with the range observed for ELM filaments in MAST [202]. The growth rate of the finite- $n$  PB modes (for  $n = 25$ ) is shown as a function of the maximum normalised local pressure gradient,  $\alpha_{\max}$ , in figure 6.8 based on scaling the pressure profile for the case just after the ELM crash (i.e. for a narrow pedestal) and just before the ELM crash (i.e. for a wide pedestal). It can be seen that the experimental case just before the ELM crash is PB unstable and that the growth rate increases rapidly for small increases in the normalised pressure gradient above the experimental value. The case just after the ELM crash is stable to PB modes and  $\alpha_{\max}$  must be increased by a large amount (almost a factor 2) in order to become unstable.

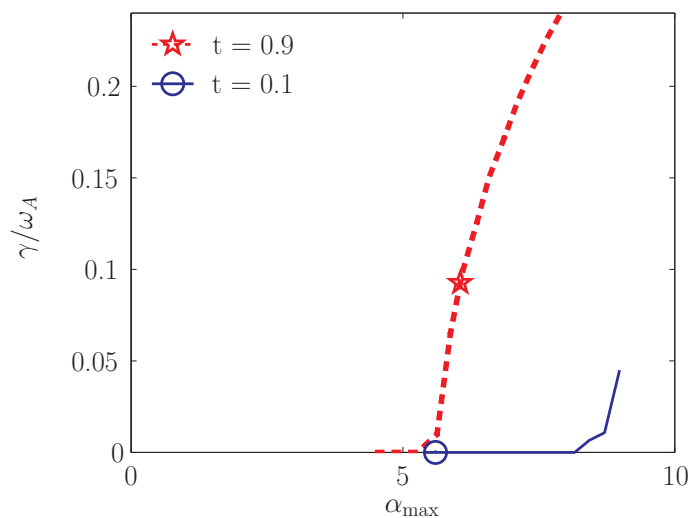


**Figure 6.8:** The growth rate,  $\gamma$ , of  $n = 25$  PB modes normalised to the Alfvén frequency,  $\omega_A = B / (\sqrt{\mu_0 n_i m_i} q R)$  (for the core plasma) calculated by ELITE as a function of maximum normalised pressure gradient,  $\alpha_{\max}$ , for the cases immediately after (blue solid) and just before (red dashed) the ELM crash. The experimental values of  $\alpha_{\max}$  are indicated by the circle and star symbols.

The PB stability constraint can be represented by the  $\alpha_{\max}$  for which the growth rate found by ELITE increases above zero (or some small threshold value). This has been calculated for each of the five time points during the ELM cycle and is

<sup>26</sup>Repeated studies scaling the temperature profile for fixed density have also been performed but yield very similar results despite the different dependence of the bootstrap current on density and temperature gradients.

shown in figure 6.9 along with the experimental values of  $\alpha_{\max}$ . It can be seen that the experimental curve crosses the stability boundary just prior to the ELM crash, which is consistent with the EPED model. The experimental value of  $\alpha_{\max}$  remains roughly constant (consistent with the local gradients being limited to a critical value) but the stability boundary moves to lower gradients as the pedestal widens. This highlights the global nature of the PB modes whereby both the pedestal gradient and width influence the stability.

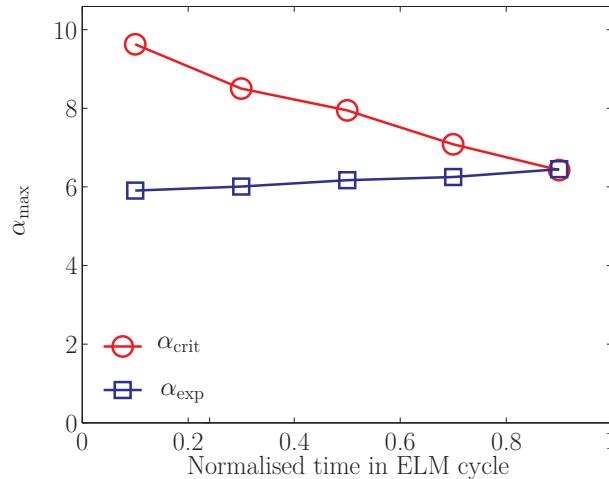


**Figure 6.9:** The critical  $\alpha_{\max}$  representing the  $n = 25$  PB stability boundary,  $\alpha_{\text{crit}}$ , (red circles) above which PB modes are unstable, calculated by ELITE for each of the five time points during the ELM cycle. The experimental value of  $\alpha_{\max}$  (blue squares) is given for each time point. The experiment enters the unstable region just before the ELM crash.

It is possible to represent the data shown in figure 6.9 in terms of the pedestal height rather than  $\alpha_{\max}$  and this is given in figure 6.10. In addition the limiting pedestal height determined by various  $n_{\infty}$  stability constraints (corresponding to 1% in  $\psi_N$  (EPED1.5), 50% of the pedestal (EPED1.6) and 100% of the pedestal being  $n_{\infty}$  unstable) are shown along with the experimental pedestal height. This shows that whilst the experiment crosses the  $n = 25$  PB stability boundary immediately prior to the ELM crash none of the  $n_{\infty}$  stability constraints cross the PB stability boundary at any point. Indeed the experimental pedestal height lies well above both the EPED constraints tested, though reasonable agreement can be obtained using the constraint that 100% of the pedestal is  $n_{\infty}$  unstable. Extrapolating this stability boundary to later times suggests that it would cross the PB stability boundary for  $t \sim 1$ . These results suggest that an EPED type model could be successful for describing the evolution and final state of the MAST H-mode pedestal (in the type-I regime studied here) but highlights the problems with using the local stability of  $n_{\infty}$  ballooning modes to provide a second global stability constraint on the pedestal. Indeed the precise definition of this constraint strongly effects the results obtained here whilst

a truly global calculation could provide a constraint without this ambiguity.

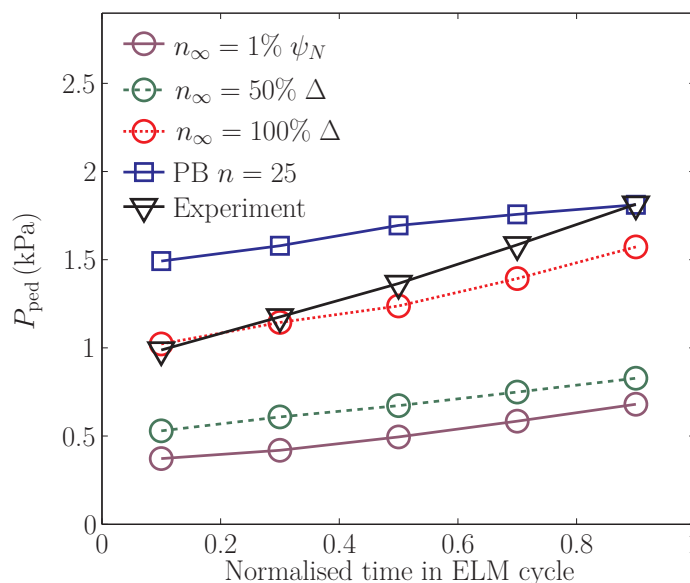


**Figure 6.10:** The limiting pedestal height,  $P_{\text{ped}}$ , based on  $n = 25$  PB (blue) and various  $n_\infty$  ballooning stability criteria as a function of normalised time. The  $n_\infty$  constraints are such that the pedestal height is limited for an unstable region equal to 1% in  $\psi_N$  (purple, EPED1.5 like), 50% of the pedestal width,  $\Delta$ , (green, EPED1.6 like) and 100% of  $\Delta$  (red). The experimental pedestal height is also shown (black).

As the ELM cycle progresses the pedestal is widening and as such the results shown in figure 6.10 can be interpreted as representing the typical EPED predictive plot, such as that shown in figure 6.4. It is useful however to apply a procedure identical to that used by EPED, in order to clearly indicate the prediction that would be made by such a model. This involves taking the equilibrium corresponding to  $t = 0.9$  and scanning in both the pedestal height and width in order to calculate the stability boundaries and to find their intersection. The results of such a study are shown in figure 6.11 along with the experimental value immediately prior to the ELM crash. This clearly shows that the two  $n_\infty$  constraints often employed in the EPED model would not provide a good prediction of the pedestal properties. The new constraint tested here which requires the entire pedestal to be  $n_\infty$  unstable provides a prediction which is much closer to that observed by experiment, with a predicted pedestal height approximately 10% larger than that observed at  $t = 0.9$ . Whilst the predicted pedestal height is reasonably close to the experimental value, the predicted pedestal width is about 50% larger than the experimental observation.

The results presented here all suggest that an EPED type model for the limiting pedestal properties (and the implied inter-ELM evolution) is applicable to the type-I ELMing H-mode on MAST studied here but that the definition of the  $n_\infty$  (i.e. KBM) constraint used in recent EPED revisions is not suitable here. Indeed a new constraint requiring 100% of the pedestal to be  $n_\infty$  unstable has been tested and shows

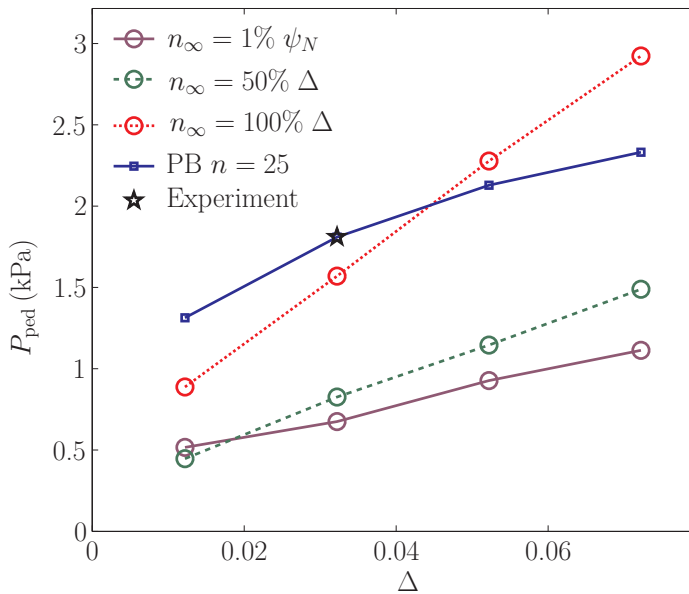


**Figure 6.11:** The limiting pedestal height,  $P_{\text{ped}}$ , based on  $n = 25$  PB (blue) and various  $n_\infty$  ballooning stability criteria as a function of pedestal width based on scans around the equilibrium for  $t = 0.9$ . The  $n_\infty$  constraints are as in figure 6.10. The experimental pedestal height and width measured at  $t = 0.9$  is shown by the star.

reasonable agreement with experiment. These  $n_\infty$  constraints are somewhat arbitrary, with no physics justification for their selection. Within the limits of the current procedure, which enforces a fixed functional form for the density and temperature profiles, it is unlikely that a well justified constraint can be obtained<sup>27</sup> and the best approach may be to calibrate the  $n_\infty$  criteria for a given machine. This provides uncertainties to the prediction of the pedestal properties on future devices. Improvements in the profile descriptions and the resulting equilibria, combined with better stability calculations (such as global gyrokinetics), may offer a means to minimise this problem.

### 6.3 A gyrokinetic study of the MAST pedestal region

Whilst there is much evidence to suggest that the type-I ELM crash is associated with crossing the PB stability boundary, the actual pedestal evolution up to this point is controlled by the balance of particle and heat sources and the corresponding transport. As in the core, edge transport is likely dominated by microinstability driven turbulence. The gyrokinetic description of these instabilities is more complete (through the inclusion of kinetic effects etc.) than that provided by MHD models,

<sup>27</sup>This is due to the fact that in experiment the limiting gradient on a given surface will depend upon the limiting gradients found further out, resulting in a complex dependence likely to lead to profiles not well described by a simple functional form.

motivating a gyrokinetic study of the pedestal region. Further motivation for the use of gyrokinetics in this region arises as the  $n_\infty$  ballooning stability calculations used by the EPED model are in fact acting as a proxy for the KBM stability. The correspondence between  $n_\infty$  MHD modes and KBMs has not previously been tested in the edge region. By performing a linear gyrokinetic study of the pedestal region it is possible to compare the region unstable to  $n_\infty$  MHD modes and KBMs.

The use of gyrokinetics in the edge region of a tokamak plasma is challenging and the validity of the gyrokinetic model can be strained in this region. Recalling that the derivation of the GKE introduced in section 3.4 involves the ordering  $\rho_* = \rho_s/L_{eq} \ll 1$  (and a subsequent expansion), it is clear that in the pedestal, where the equilibrium length scales are short, this ordering can be violated<sup>28</sup> and the GKE is no longer strictly applicable. The profile of  $\rho_*$  in the edge region<sup>29</sup> for the H-mode case at  $t = 0.5$  discussed in section 6.2 is shown in figure 6.12, highlighting the violation of the small  $\rho_*$  ordering for large  $\psi_N$ . Whilst formulations of gyrokinetics applicable to the conditions<sup>30</sup> found in internal transport barriers and the edge region are being developed [203] the implementation and verification of this system into numerical simulations is still some way off.

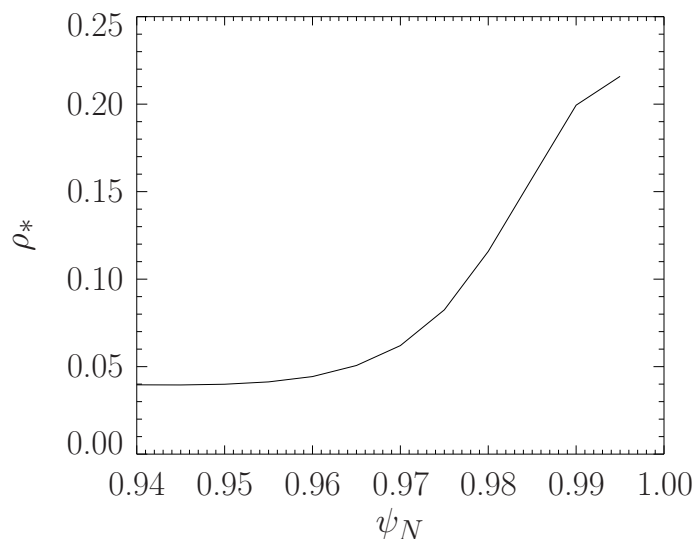


**Figure 6.12:** The ratio of ion gyroradius,  $\rho_i$ , to the temperature length scale,  $L_T$  as a function of normalised poloidal flux,  $\psi_N$ , calculated for the  $t = 0.5$  profiles given in figure 6.5(b).

<sup>28</sup>The assumption that the fluctuations associated with the microinstabilities are much smaller than the equilibrium values can also be questionable near the edge where the profiles tend towards zero and  $\delta n/n \sim \mathcal{O}(1)$  (e.g. see figure 2.3).

<sup>29</sup>The profile shown is for ions and uses  $L_{eq} = L_T$  as  $L_T < L_n$ .

<sup>30</sup>In particular allowing relatively large normalised fluctuation amplitudes, e.g.  $q\phi_1/T \sim \mathcal{O}(1)$ .

### 6.3.1 Microstability during the ELM cycle

As a first step towards a complete gyrokinetic study of the pedestal region it is desirable to exploit existing gyrokinetic codes to investigate the microstability of the H-mode edge region. The data presented in figure 6.12 indicates that the validity of the standard formulation of gyrokinetics is indeed being pushed in the steep gradient region of the pedestal and as such the results obtained in this region should be treated with caution, though are likely to be indicative of the full kinetic behaviour (and are an improvement on MHD/fluid treatments in terms of including FLR and kinetic effects). In particular  $\rho_*$  drops quite quickly (and smoothly) as  $\psi_N$  is reduced and gyrokinetics in the transition and shallow gradient regions should be reasonable. Further to this the electron physics will remain well described by the GKE throughout the region studied due to the smaller Larmor radius.

GS2 is a local electromagnetic gyrokinetic initial value code [128] which, in the linear mode used here, returns the eigenfunction and complex mode frequency of the dominant instabilities as a function of the binormal wavenumber,  $k_y$ , on a specified flux surface of a given equilibrium. Using the five equilibria generated for the MHD study, discussed in section 6.2.2, as input to GS2 it is possible to map out the microstability evolution on a given flux surface through the ELM cycle. By repeating this for a number of flux surfaces in the edge region, the stability of the pedestal and shallow gradient regions throughout the ELM cycle can be resolved in order to give some insight into the dynamics of the microstability evolution. This allows the identification of the dominant instabilities and provides the opportunity to seek KBMs in the region found to be unstable to  $n_\infty$  MHD modes.

To probe the edge region 12 evenly spaced flux surfaces have been studied for  $0.94 \leq \psi_N \leq 0.995$  at each of the five time points during the ELM cycle. These simulations retain collisions and electromagnetic perturbations, which are important towards the edge, but neglect sheared plasma flows. The sheared plasma flows may be significant in the pedestal but are likely to be small in the shallow gradient region [204]. Each simulation includes three gyrokinetic species (deuterium, electrons and carbon) which are assumed to have the same density and temperature length scales<sup>31</sup> as electrons, consistent with the composite profiles discussed in section 6.2.1.

Whilst a non-adiabatic electron response is included in solving the gyrokinetic system, the binormal wavenumber range, which consists of 80 points, is restricted to near ion scales,  $0.07 \leq k_y \rho_i \leq 5.5$ , such that electron scale instabilities (such as the electron temperature gradient mode) are excluded, allowing focus to be given to KBMs (which are ion scale instabilities).

---

<sup>31</sup>Simulations using the flat ion temperature model yield very similar results to those with the equal model.

The combined output of these simulations consists of a large amount of data<sup>32</sup> and it is useful to define a simple metric to describe the character of the instabilities allowing a summary of the results to be made before a more detailed study is presented. In electromagnetic simulations the parallel perturbed magnetic vector potential,  $A_{\parallel}$ , can lead to a net radial perturbation to the magnetic field line such that the perturbed magnetic field line does not return to the equilibrium flux surface. Such instabilities are referred to as tearing, whilst instabilities in which the perturbed magnetic field line returns to the equilibrium flux surface are known as twisting<sup>33</sup>. It is possible to characterise this behaviour through the “parity factor”,  $C_{\text{par}}$ , defined as:

$$C_{\text{par}} = 1 - \frac{\left| \int A_{\parallel} d\theta \right|}{\int |A_{\parallel}| d\theta} \quad (6.6)$$

such that  $C_{\text{par}} = 0$  and  $C_{\text{par}} = 1$  correspond to pure tearing and twisting parity instabilities respectively. By considering only the most unstable instability at each  $\psi_N$  and  $t$  the amount of data can be reduced substantially.

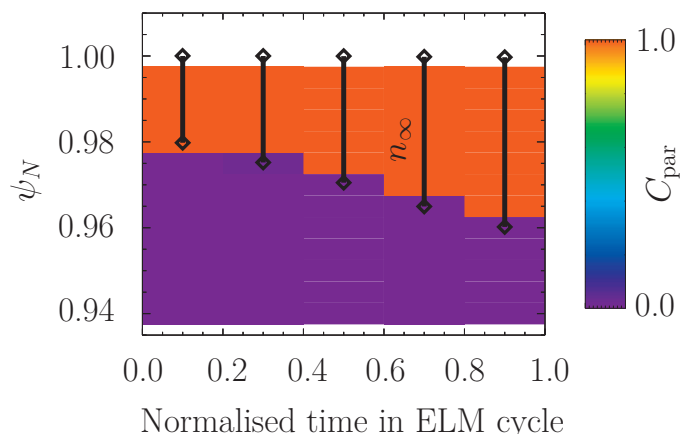


**Figure 6.13:** The parity factor,  $C_{\text{par}}$ , of the dominant instability in the edge region during the ELM cycle. The region unstable to  $n_{\infty}$  ballooning modes (lines with points) agrees quite well with the twisting parity region (red).

The parity factor for the dominant instabilities is shown in figure 6.13 as a function of  $\psi_N$  and  $t$ . There are two distinct regions in the parity data, and these correspond well to the shallow and steep gradient regions. The dominant instabilities in the shallow gradient region have tearing parity whilst those in the steep gradient are twisting in nature. Example  $\phi$  and  $A_{\parallel}$  eigenfunctions for these twisting and tearing modes are given in figure 6.14 for  $\psi_N = 0.95$  and  $\psi_N = 0.98$  at  $t = 0.5$ , highlighting the distinction between tearing and twisting parity. The region found unstable to  $n_{\infty}$

<sup>32</sup>In total there are 5 times, 12 surfaces and 80  $k_y \rho_i$  values resulting in 4800 data points, each with a frequency, growth rate and 3 eigenfunctions ( $\phi$ ,  $A_{\parallel}$  and  $B_{\parallel}$ ).

<sup>33</sup>Most commonly studied microinstabilities, such as the ITG mode, are twisting in nature. Indeed electrostatic instabilities can have no tearing component (although finite  $\beta$  modifications allow a tearing component to develop [205]).

ballooning modes is overlaid on the parity data. It can be seen that the  $n_\infty$  unstable region is similar to (though slightly larger than) the twisting parity region.

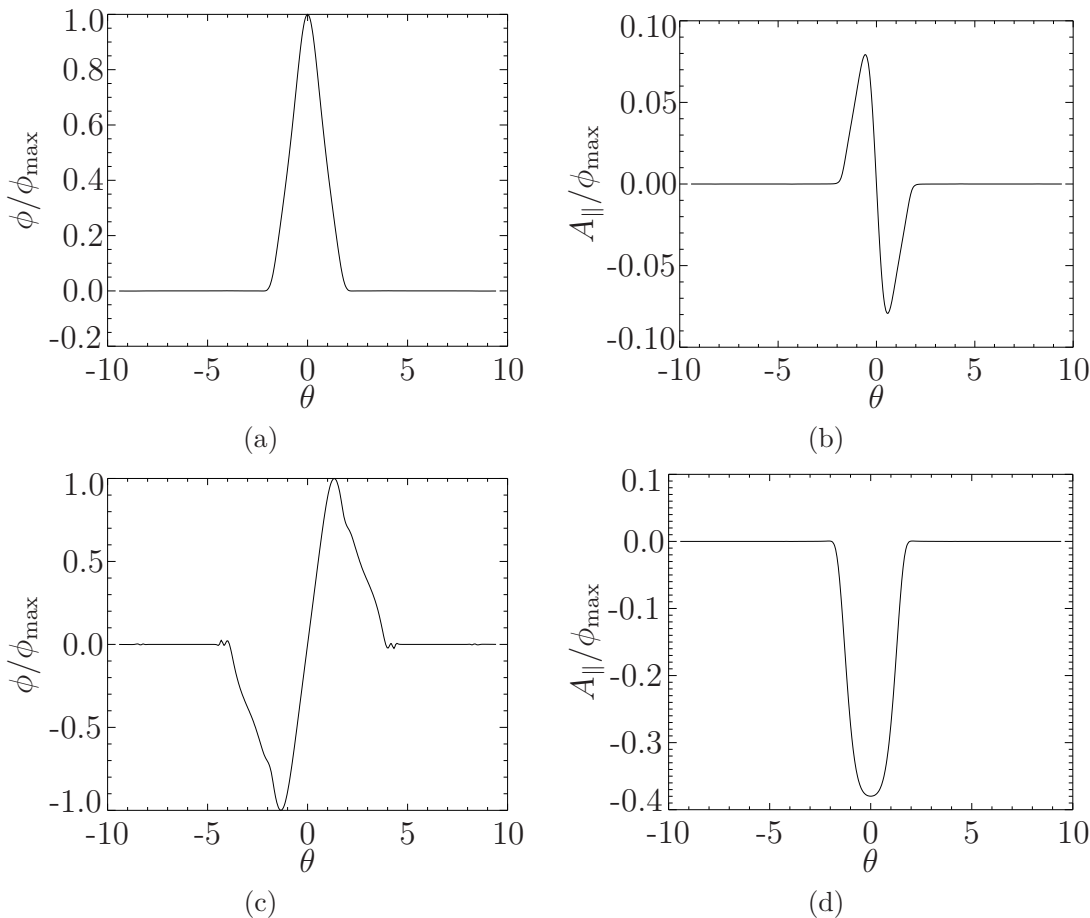


**Figure 6.14:** The  $\phi$  and  $A_{\parallel}$  eigenfunctions (normalised to the maximum value of  $\phi$ ,  $\phi_{\max}$ ) for the dominant instabilities at  $t = 0.5$  on surfaces  $\psi_N = 0.98$  [figure 6.14(a), figure 6.14(b)] and  $\psi_N = 0.95$  [figure 6.14(c), figure 6.14(d)] with  $k_y \rho_i = 0.149$  and  $k_y \rho_i = 3.276$  respectively. These correspond to twisting and tearing parity modes respectively.

To identify the specific type of instabilities found in these simulations it is necessary to investigate the dependencies that the growth rate,  $\gamma$ , has on the various equilibrium gradients and other plasma parameters. It is possible to identify the twisting parity modes found in the steep gradient region as KBMs due to the rapid increase in  $\gamma$  with increasing  $\beta$ , shown in figure 6.15(a), which is expected for KBMs<sup>34</sup> (and opposite to that typically observed for other ion scale twisting parity instabilities [206]). The good agreement seen between the twisting parity and  $n_\infty$  regions therefore implies that the KBM stability is indeed well described by the  $n_\infty$  stability calculations. The tearing parity modes are also found to respond strongly to  $\beta$  as shown in figure 6.15(b). Further to this the electron temperature gradient is found to be destabilising for the tearing parity modes, which is consistent with the behaviour expected for microtearing modes (MTMs) [101, 207–213]. It can be noted that

<sup>34</sup>In addition the growth rate is also found to increase with both density and temperature gradients, which is again characteristic of KBMs.

MTMs have been observed in simulations near the edge of ASDEX-Upgrade [214] and JET [215].

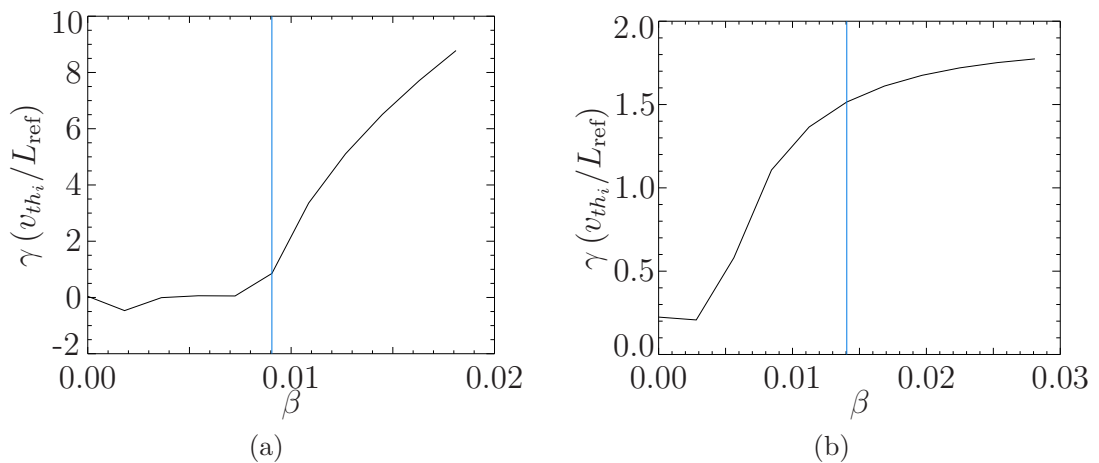


**Figure 6.15:** The growth rate,  $\gamma$ , of the dominant twisting [figure 6.15(a)] and tearing [figure 6.15(b)] parity instabilities as a function of  $\beta$  based on a scan about the equilibrium corresponding to  $t = 0.5$  and  $\psi_N = 0.98$  and  $\psi_N = 0.95$  respectively. The experimental value of  $\beta$  is indicated by the vertical blue line. The effect of varying  $\beta$  is simply to scale the strength of the magnetic perturbations ( $A_{\parallel}$  and  $B_{\parallel}$ ) in the gyrokinetic Maxwell’s equations.

Whilst it has been found that the dominant instabilities in the steep gradient region are KBMs and in the shallow gradient region they are MTMs, the instabilities vigour (i.e. the growth rate) is not revealed through the parity plots generated so far. This is crucial to develop a deeper understanding of the pedestal behaviour. For example, whilst the dominant modes in the steep gradient region are KBMs it is possible that the MTMs are simply slightly less unstable than the KBMs here and could therefore also be playing an important role in setting the critical pedestal gradient observed experimentally. This could be seen by looking at plots of  $\gamma(k_y \rho_i)$  as the MTMs and KBMs are well separated in  $k_y \rho_i$ . To investigate the behaviour of these instabilities in more detail it is useful to look at the behaviour of the growth rate as a function of  $k_y \rho_i$ ,  $\psi_N$  and  $t$ .

The growth rate as a function of  $k_y \rho_i$  and  $\psi_N$  is shown for  $t = 0.1$  and  $t = 0.9$  in figure 6.16. The separation in  $k_y \rho_i$  of the MTMs and KBMs is clearly apparent, with  $k_y \rho_i > 1$  indicating MTMs whilst KBMs are at lower  $k_y \rho_i$  values. It can be seen that at all radial locations there is only a single type of instability unstable: MTMs are stable in the steep gradient region whilst KBMs are stable in the shallow gradient region. The growth rate of the KBMs for  $t = 0.9$  shows an interesting behaviour. There are two peaks in the growth rate as a function of  $\psi_N$  and these occur at the foot and “knee” of the pedestal<sup>35</sup> where the gradients are below the

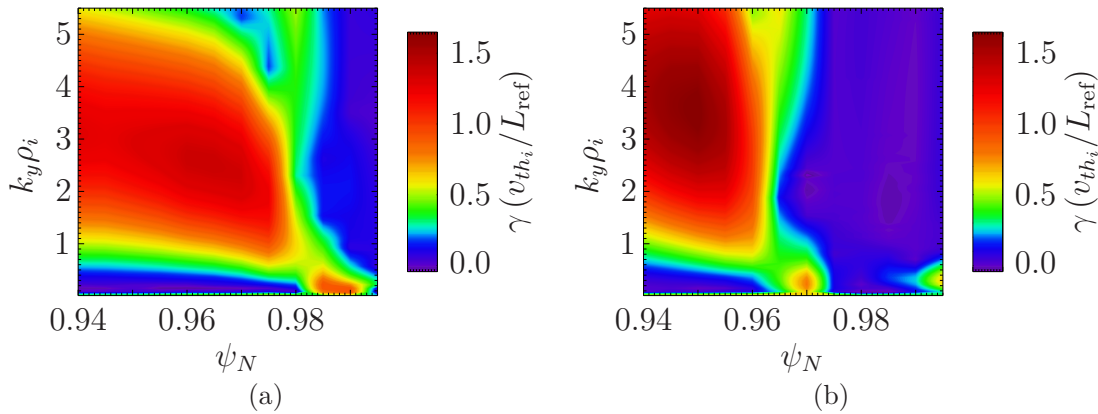


**Figure 6.16:** The growth rate spectra,  $\gamma(k_y \rho_i)$ , as a function of  $\psi_N$  for  $t = 0.1$  [figure 6.16(a)] and  $t = 0.9$  [figure 6.16(b)]. The unstable modes with  $k_y \rho_i > 1$  are MTMs whilst those at low  $k_y \rho_i$  are KBMs.

maximum value. In the steep gradient region the KBMs are in fact only marginally unstable. The KBMs found here are strongly sensitive to the shear (with the growth rate dropping for reductions in the shear) and become significantly more unstable for small increases in the shear. In this steep gradient region the magnetic shear is reduced due to the bootstrap current. Recalling that the mtanh profiles, used to represent the density and temperature, can overestimate the peak gradient then it is clear that the magnetic shear in this steep gradient region may be slightly too low, which will modify the KBMs stability. As the gradients increase at a given location in the shallow gradient region (as part of the pedestal expansion) the MTMs that exist there are stabilised. However, by comparing the MTM stability at  $\psi_N = 0.95$  for the two times shown it is clear that as the pedestal expands (at higher  $\psi_N$ ) the MTM growth rate increases despite the fact that the gradients at this location are unaltered. As  $n_e$  is increasing here, the length scales are also increasing, and this is what provides the destabilising influence. This suggests the MTMs may become more difficult to stabilise as the pedestal expands, therefore making it more difficult for the pedestal to expand further inwards. To see this more clearly it is useful to look at  $\gamma(k_y \rho_i, t)$  for  $\psi_N = 0.95$  as shown in figure 6.17(a) which clearly shows the increase in MTM growth rate as the ELM cycle progresses.

### 6.3.2 Exploring the pedestal expansion

The contour plot of  $\gamma(k_y \rho_i, t)$  for  $\psi_N = 0.97$  shown in figure 6.17(b) shows that as the gradients steepen on a surface in the shallow gradient region the MTMs become less unstable until the KBM threshold is reached and KBMs become the dominant instability. Better understanding the nature of this transition may help shed light upon the following questions:

<sup>35</sup>The knee of the pedestal is the location where the shallow and steep gradient regions connect. This is also often known as the transition region or the pedestal shoulder.

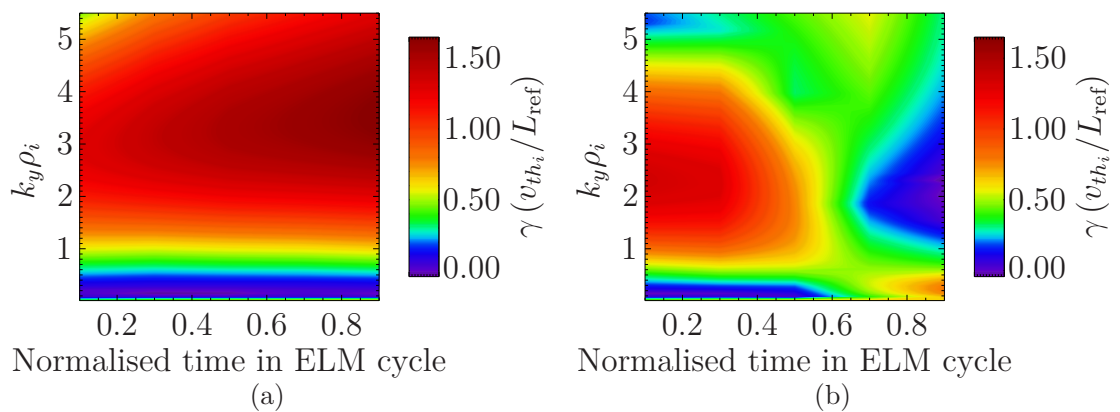


**Figure 6.17:** The growth rate spectra,  $\gamma(k_y \rho_i)$ , as a function of  $t$  for  $\psi_N = 0.95$  [figure 6.17(a)] and  $\psi_N = 0.97$  [figure 6.17(b)].

- Why does the density pedestal expand whilst the temperature pedestal is fixed<sup>36</sup>?
- Does anything stop the pedestal expansion<sup>37</sup>?

To probe the transition between MTMs and KBMS in more detail and to try to answer these questions it is useful to perform artificial parameter scans around the experimental equilibria. This allows the response to changes in various parameters, such as the density and temperature length scales, to be probed.

In investigating these questions there are three scenarios of interest:

- A surface initially in the shallow gradient region which enters the pedestal.
- A surface which remains in the shallow gradient region throughout the ELM cycle.
- A surface which is in the transition region at the end of the ELM cycle (i.e. it doesn't quite enter the pedestal before the ELM crash).

These surfaces are illustrated in figure 6.18 and here we specifically take  $\psi_N = 0.97$  and  $t = 0.5$  for surface *a*,  $\psi_N = 0.95$  and  $t = 0.9$  for surface *b* and  $\psi_N = 0.96$  and  $t = 0.9$  for surface *c*.

### 6.3.2.1 Surface *a*

In the experimental evolution on surface *a* the density gradient increases whilst the temperature gradient remains roughly fixed. To probe this behaviour the normalised inverse density length scale,  $L_{\text{ref}}/L_{n_e}$ , has been scanned around its nominal value (whilst scaling the gradient of  $\beta$ ,  $\beta'$ , consistently<sup>38</sup>) and the resulting effect on the

<sup>36</sup>This will depend upon the particle and heat sources as well as the instabilities present and as such can't be answered fully by the linear gyrokinetic study presented here.

<sup>37</sup>Aside from entering the PB unstable region.

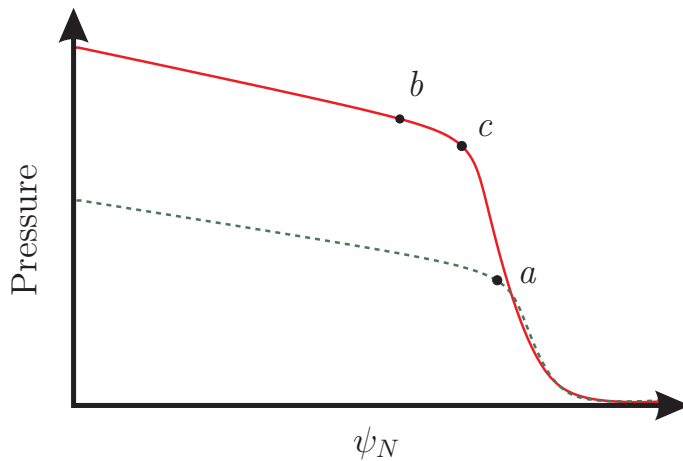


**Figure 6.18:** Cartoon representing the pressure profile at  $t = 0.5$  (dashed green) and  $t = 0.9$  (solid red). The three surfaces about which artificial scans are performed are indicated schematically by the points which represent  $a$   $\psi_N = 0.97$  at  $t = 0.5$ ,  $b$   $\psi_N = 0.95$  at  $t = 0.9$  and  $c$   $\psi_N = 0.96$  at  $t = 0.9$ .

growth rate spectra is shown in figure 6.19(a). It can be seen that for the lowest density gradient investigated the MTMs are strongly unstable, but that increasing this gradient up to the experimental value provides a stabilising influence (both in the peak  $\gamma$  and in the range of  $k_y \rho_i$  which is unstable). Further increases in the gradient above this point remain stabilising to the MTMs, however increasing  $L_{\text{ref}}/L_{n_e}$  above 4 results in KBMs becoming strongly unstable<sup>39</sup>. If the temperature gradient is scaled at fixed density gradient (again scaling  $\beta'$  consistently) somewhat different behaviour is seen, as shown in figure 6.19(b). Here it can be seen that as the temperature gradient is increased from the experimental value there is a small stabilising impact on the MTMs but these modes remain unstable throughout the range studied<sup>40</sup>. At  $L_{\text{ref}}/L_{T_e} = 8$  the KBMs also become unstable such that both MTMs and KBMs are unstable at the same time. It can be noted that in both the temperature and density gradient scans the KBM onset occurs at the same  $\beta'$  value<sup>41</sup> highlighting that it is the pressure gradient that is the key source of free energy for the KBM.

The behaviour observed in figure 6.19 provides a simple picture for why the density pedestal can expand inwards whilst the temperature pedestal remains fixed. As the density gradient increases on a surface in the transition region the MTM is stabil-

<sup>38</sup>This parameter is related to  $\alpha$  (recall eqn. 6.1) and increases as the density and temperature gradients increase.

<sup>39</sup>In addition to the change in  $k_y \rho_i$  at which the growth rate peaks, there is a clear switch in parity (highlighted by the black line in figure 6.19(a)) indicating a switch in mode from MTM to KBM.

<sup>40</sup>There is however an upshift in the  $k_y \rho_i$  associated with the MTMs which may be expected to lead to a slight reduction in the transport associated with these modes.

<sup>41</sup>Indeed the  $\gamma$  vs.  $\beta'$  data agrees very well between the density and temperature gradient scans for the low  $k_y \rho_i$  modes.

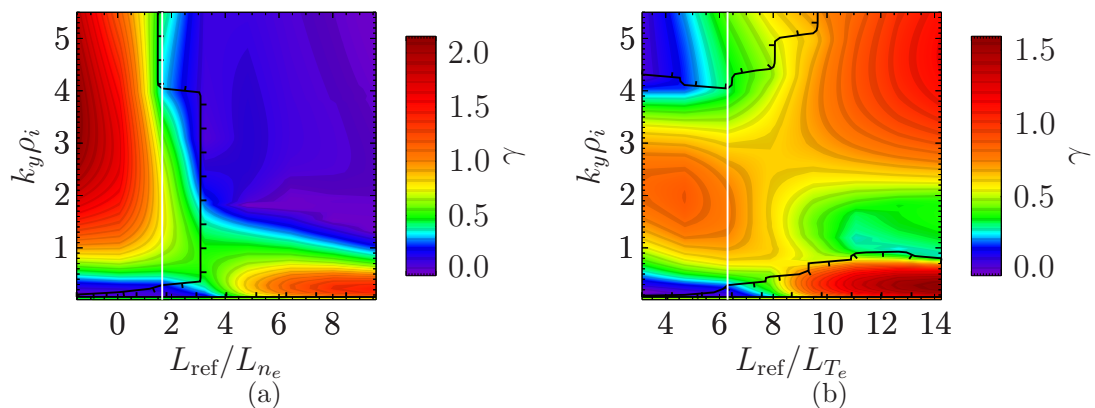


**Figure 6.19:** The variation in  $\gamma(k_y \rho_i)$  as the inverse density [figure 6.19(a)] and temperature [figure 6.19(b)] length scales are varied from the equilibrium values on surface *a*. The experimental value is indicated by the vertical white line whilst the black line is the contour where  $C_{\text{par}} = 0.9$  (the tics point towards higher values).

ised, removing a transport mechanism and allowing the pressure gradient to increase further. This can continue until the KBM limit is reached. Due to the strongly stiff nature of the KBM and the fact that it responds equally to density and temperature gradients any further attempts to steepen the pressure gradient through an increase in heat or particles arriving at the surface will be balanced by an increase in turbulent transport here. The fact that increasing the temperature gradient does not lead to a strong stabilisation of the MTM may prevent the temperature gradient from increasing significantly as any increases may lead to an increased heat flux. Whilst this simple picture seems to explain the different density and temperature evolution observed for this specific MAST scenario it is necessary to perform nonlinear simulations to probe the behaviour of the particle and heat fluxes through scans such as those presented here. This is beyond the scope of the work presented here. Importantly the available heat and particle sources may also impact on the evolution observed.

The variation in  $\beta'$  which occurs as the density and temperature gradients are varied has an influence on the growth rate, as shown in figure 6.20. It can be noted that the small stabilising effect seen for increases in  $L_{\text{ref}}/L_{T_e}$  around the experimental value is in fact due to the increase in  $\beta'$  and scans keeping this fixed show the MTMs becoming more unstable for increasing temperature gradient. It is useful to recall that surface *a* is initially in the transition region and the density gradient has already started to steepen up so that  $\beta'$  is larger than in the shallow gradient region. It might be anticipated that the destabilising influence of increasing the temperature gradient is weakened in this case. By performing a similar investigation on surface *b*, which is in the shallow gradient region, this effect can be probed.

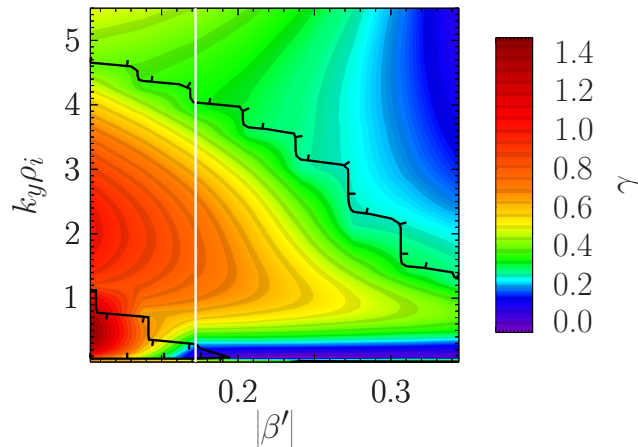


**Figure 6.20:** The variation in  $\gamma(k_y\rho_i)$  as the gradient in  $\beta$ ,  $\beta'$  is varied for surface  $a$ . The experimental value is indicated by the vertical white line whilst the black line is the contour where  $C_{\text{par}} = 0.9$  (the tics point towards higher values).

### 6.3.2.2 Surface $b$

Scans in the density and temperature gradients identical to those presented in figure 6.19 have been performed using surface  $b$ , which is in the shallow gradient region, as a starting point and are shown in figure 6.21. The behaviour of the growth rate as the density gradient is changed is very similar to that shown in figure 6.19(a), though the experimental point is much further from the KBM threshold. The temperature gradient scan shown in figure 6.21(b) shows significantly different behaviour from that seen in figure 6.19(b) however. Here the increase in temperature gradient is seen to be destabilising throughout the range from the experimental position to the KBM threshold. This strengthens the picture developed previously for why the density pedestal expands whilst the temperature pedestal remains fixed. Comparing figure 6.19(b) with figure 6.21(b) it can be seen that as the density gradient increases it becomes possible for the temperature gradient to increase without the MTM growth rate increasing significantly. This may provide a window in which the temperature gradient is able to increase, however due to the proximity of the experiment to the KBM onset seen in figure 6.19(b) this opportunity is likely to be limited<sup>42</sup>.

During the experimental pedestal evolution the gradients do not increase significantly on surface  $b$ , the main change in the equilibrium is an increase in  $\beta$  due to the gradients increasing at larger  $\psi_N$ . To probe this behaviour an artificial scan varying only  $\beta$  has been performed<sup>43</sup> using surface  $b$  as a starting point, and the results are

<sup>42</sup>In other discharges and tokamaks the separation of the KBM onset and the point at which increases in the temperature gradient are possible could be separated by a large distance, allowing more significant variation in the temperature gradient.

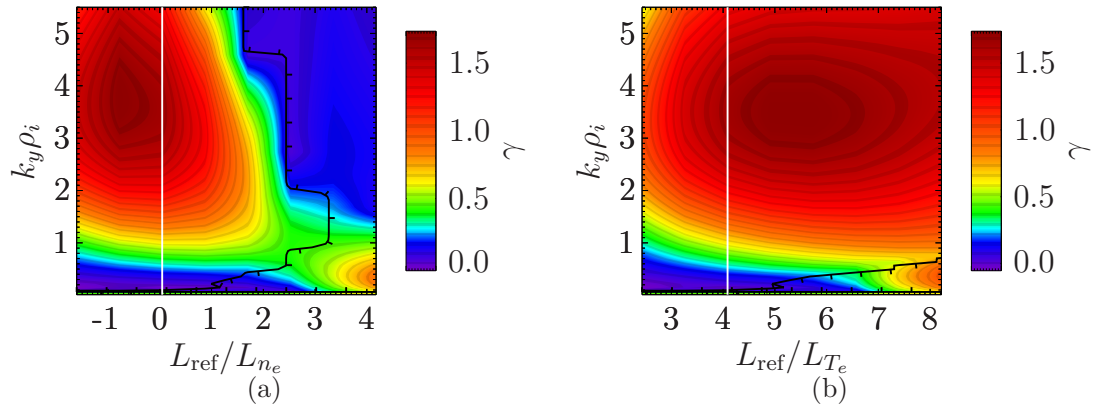


**Figure 6.21:** The variation in  $\gamma(k_y \rho_i)$  as the inverse density [figure 6.21(a)] and temperature [figure 6.21(b)] length scales are varied from the equilibrium values on surface  $b$ . The experimental value is indicated by the vertical white line whilst the black line is the contour where  $C_{\text{par}} = 0.9$  (the tics point towards higher values).

shown in figure 6.22. It can be seen that as  $\beta$  is increased the MTMs become more unstable and for sufficiently high  $\beta$  the KBMs can also be driven unstable. It can be noted that the  $\beta$  at which KBMs are destabilised is significantly above the experimental value. Noting that the experimental conditions are those at the end of the ELM cycle it is clear that the onset of KBMs seen here will not be experienced in experiment. Despite this the general trend seen here, where both the MTMs and KBMs become more unstable on surfaces in the shallow gradient region as the pedestal expands, suggests that there may be a natural width for which further pedestal expansion leads to a significant degradation of the confinement further towards the core.

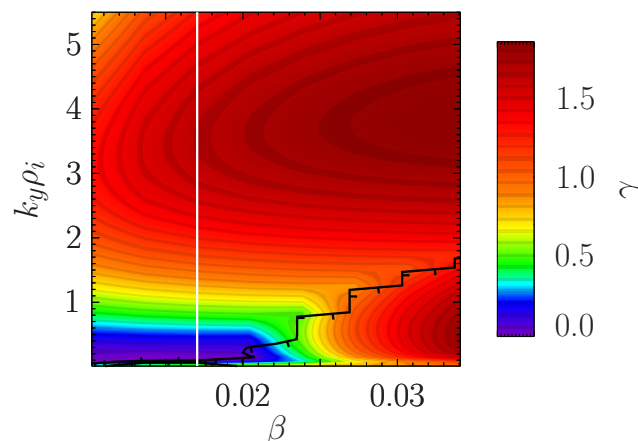


**Figure 6.22:** The variation in  $\gamma(k_y \rho_i)$  as  $\beta$  is varied for surface  $b$ . The experimental value is indicated by the vertical white line whilst the black line is the contour where  $C_{\text{par}} = 0.9$  (the tics point towards higher values).

<sup>43</sup>A similar scan also varying  $\beta'$  in order to keep the  $\beta$  length scale fixed shows similar behaviour to the scan in  $\beta$  only.

### 6.3.2.3 Surface $c$

The final region of interest is surface  $c$ , which is just entering the transition region at the end of the ELM cycle. As the pedestal evolves the gradients further into the transition region (larger  $\psi_N$ ) steepen, leading to an increase in  $\beta$  on surface  $c$ . To study this the  $\beta$  has been scaled consistently with the density, such that  $L_{\text{ref}}/L_{n_e}$  increases for increasing  $\beta$ , and  $\beta'$ , which is consistent with the experimentally observed evolution. The results of this scan are shown in figure 6.23. It can be seen that for relatively small increases in  $\beta$  above the experimental value that there is an onset of KBM modes. This is similar to the behaviour shown in figure 6.22 but the KBM onset here is much closer to the experimental value than on surface  $b$ , due to the increased gradients in the transition region. This shows that the transition region shortly prior to the ELM crash is very close to a position in  $\beta$  and  $\beta'$  for which both MTMs and KBMs are strongly unstable over a large range of  $k_y \rho_i$ . The transport due to KBMs can be large [189] and it is has also recently been shown that MTMs can drive significant levels of heat flux [216, 217]. It might be expected that the situation above  $\beta = 0.02$  shown in figure 6.23 will be associated with a strong increase in the transport levels. This is likely to make it difficult for the pedestal to expand beyond this point in operating space. Nonlinear simulations investigating the transport due to the MTMs and KBMs and the coupling between these modes are extremely challenging though may yield useful insights into the processes occurring at the top of the pedestal.

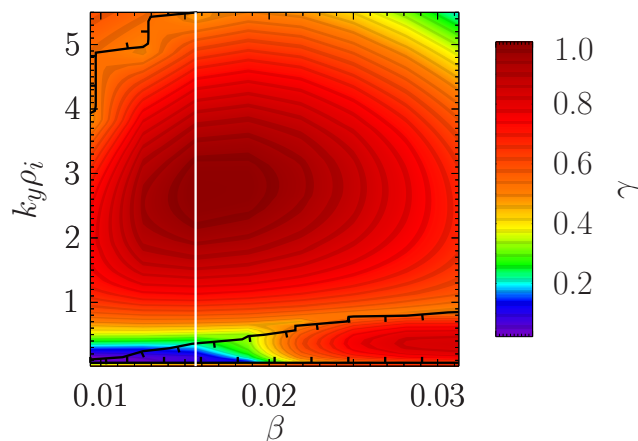


**Figure 6.23:** The variation in  $\gamma(k_y \rho_i)$  as  $\beta$  is varied for surface  $c$ . The experimental value is indicated by the vertical white line whilst the black line is the contour where  $C_{\text{par}} = 0.9$  (the tics point towards higher values).

## 6.4 Discussion

In this chapter the evolution of the MAST H-mode pedestal in the type-I ELMing regime has been studied. Experimental measurements of the density and temperature profiles during the ELM cycle show that the density pedestal width increases throughout the ELM cycle whilst the temperature pedestal width remains roughly constant. The peak pressure gradient varies by less than 10% over the ELM cycle, consistent with being limited to some critical value.

MHD analysis of five equilibria representing the entire ELM cycle have been used to probe the PB and ideal  $n_\infty$  MHD ballooning stability. This shows that the region unstable to  $n_\infty$  modes occupies the steep gradient region and expands as the pedestal expands. Throughout the ELM cycle the region unstable to  $n_\infty$  modes is wider than 1% in  $\psi_N$  and 50% of the pedestal width, which are the two constraints invoked by versions 1.5 and 1.6 of the EPED model. It was found that a constraint based on 100% of the pedestal being  $n_\infty$  unstable gave much better agreement with experiment. The PB mode with  $n = 25$  becomes unstable just prior to the ELM crash, consistent with the PB model for the ELM cycle.

The equilibrium immediately prior to the ELM crash was used as a basis for scans in the pedestal width and height, with the resulting data used to calculate the PB and  $n_\infty$  stability constraints, following an EPED type approach. The intersection of the PB and  $n_\infty$  stability curves provides a prediction of the pedestal height and width immediately prior to the ELM crash. Three different  $n_\infty$  pedestal height constraints were tested, based on the EPED1.5 and EPED1.6 constraints and a constraint requiring 100% of the pedestal to be  $n_\infty$  unstable. It was found that the EPED constraints did not cross the PB boundary for the entire range of data studied, suggesting there would be no ELM crash. The prediction using the 100% criterion yields a pedestal height approximately 10% larger than that observed at a normalised time  $t = 0.9$  whilst the pedestal width is about 50% larger<sup>44</sup>. Tests of the EPED model on a number of discharges from many standard aspect ratio tokamaks typically show predictions of the pedestal height which vary by up to 20% from the observations [110], suggesting the prediction for MAST found here is within the usual model accuracy. Overall it appears that the approach used in the EPED predictive model is applicable to MAST (and other STs), suggesting that the physics of the type-I ELM cycle is relatively unchanged between large and tight aspect ratio tokamaks.

It is clear however, that there is some freedom within the approach used here which can lead to large variations in the predictions achieved. The PB stability constraint

<sup>44</sup>Due to the relatively low gradient of the PB stability curve, shown in figure 6.11, it is clear that the predicted pedestal height is fairly insensitive to the predicted width.

depends upon the toroidal mode number,  $n$ , used. Whilst it may be expected that it is the most unstable  $n$  which is the most relevant, the ELITE code used to calculate the PB stability does not contain all the physics which may be relevant in setting the peak  $n$ . Perhaps the clearest issue with the procedure used here is in selecting the constraint to use in setting the  $n_\infty$  limit. Whilst the EPED1.5 and EPED1.6 constraints have been used successfully for a substantial range of large aspect ratio cases, here they yielded very poor predictions<sup>45</sup>. The 100% constraint introduced here was found to provide much better predictions of the pedestal height and width. Importantly none of these  $n_\infty$  constraints have a clear physical justification. Whilst it's possible to calibrate this constraint for each existing tokamak for which predictions are to be made, this approach is not possible for future devices such as ITER. The EPED model states that the pedestal pressure gradient is limited to the critical value for the  $n_\infty$  ballooning mode (or KBM) onset. In theory it is possible to construct a pedestal pressure profile which is precisely critical across the entire pedestal, though due to the dependence of the bootstrap current on the pressure gradient this becomes a complicated non-local problem. The BCP approach used in EPED1.6 attempts to approximate this by using a simple mtanh form for the profiles and then requiring 50% of the pedestal to be at or beyond the critical value. The quality of the fit of the functional form used to the experimental data<sup>46</sup> will alter the precise size of the unstable region obtained for the functional profiles required to match the experimental data. The mtanh profiles used here are a very good fit to the MAST data [3] which may help explain why the constraint of 100% of the pedestal being unstable gave good agreement here. In the case of DIII-D the mtanh fits seems to give slightly worse agreement with the data [197] suggesting that the BCP approach is more applicable here. By calculating a critical pedestal profile for future machines such as ITER it should be possible to select a functional form which closely matches this. This could then be used as a basis for the typical EPED type studies that are used to make predictions of the pedestal height and width, but using the 100%  $n_\infty$  unstable constraint. Variations in the calculated bootstrap current (either through a change in parameters, such as impurity concentration, or through the use of an alternative model) are likely to effect the shape of the critical profile. If the optimised pedestal profile significantly changes shape then this approach will no longer be valid and either a new functional form must be selected or a BCP type approach (possibly with a different width selection) will be required, i.e. the region required to be  $n_\infty$  unstable must be changed.

Whilst the  $n_\infty$  stability is used as part of the EPED model, it is actually KBMs which are thought to set the pedestal pressure gradient limit. The use of  $n_\infty$  stability

<sup>45</sup>In fact the results shown in figure 6.11 suggest that the EPED based  $n_\infty$  constraints will cross the PB curve only for  $\Delta$  much larger than that seen in experiment.

<sup>46</sup>In other words how close the “non-locally optimised” profile is to the functional form.

as a proxy to KBM stability is based upon both instabilities being described by similar equations. Whilst this relation has been tested in the core through reasonable agreement in the critical gradient [189] it has not been previously verified for edge conditions. A linear gyrokinetic study of the equilibria used in the MHD investigation indicates that KBMs are unstable in the steep gradient region. The region unstable to KBMs agrees very well with that found for  $n_\infty$  modes. It should be noted that the accuracy of the gyrokinetic model in the steep gradient region is limited due to the large  $\rho_*$ . A global treatment using a formulation of gyrokinetics suitable for  $\rho_* \sim 0.1$  is required to capture the full physics important for the KBM, and the unstable region may vary from that found here. Such simulations are not currently feasible, though it can be noted that the relative success of the EPED model suggests any modification should be relatively small.

These gyrokinetic simulations also show that in the shallow gradient region towards the core, where  $\rho_*$  is much smaller, MTMs are the dominant instability. These modes are suppressed by the increasing density gradient and are stable in the steep gradient region. On the surfaces which don't enter the steep gradient region the MTMs survive and become more unstable through the ELM cycle (due to increasing local  $\beta$ ). The expansion of the pedestal will depend upon the behaviour of the instabilities in this shallow gradient region at the top of the pedestal. In order to probe this artificial scans were performed around three different equilibria in the shallow gradient and transition regions. This provides a simple plausible picture for the pedestal evolution observed on MAST in terms of the microstability behaviour:

1. The steep pedestal pressure gradient is limited to near the KBM threshold.
2. MTMs dominate the shallow gradient region and limit the electron temperature gradient achievable here.
3. The density pedestal can expand inwards as MTMs are stabilised by increasing the density gradient, allowing the pressure gradient to increase further until the KBM limit is reached.
4. As the pedestal expands the local  $\beta$  on surfaces further towards the core increases, making the MTMs more unstable and therefore making it harder for the pedestal to expand further through suppression of the MTMs.
5. Towards the end of the ELM cycle the pressure gradient transition region is close to a position in  $\beta, \beta'$  operating space where both KBMs and MTMs are simultaneously unstable over a large range of  $k_y \rho_i$ . Entering this region may trigger a large change in the transport properties and is likely to limit the pedestal expansion.

As the evolution of the pedestal depends upon the behaviour of instabilities found in

the shallow gradient region<sup>47</sup> it may be expected that this picture will vary between discharges and tokamaks. There have, however, been observations of unstable MTMs at the top of the JET pedestal [215] and towards the edge of ASDEX-Upgrade [214] suggesting the behaviour seen here for MAST may have relevance for other devices.

### 6.4.1 Future work

The study presented here has provided some insight into the processes underlying the pedestal evolution and tested an EPED type model for predicting the pedestal properties seen on MAST. In addition to the improvements of the EPED approach discussed earlier<sup>48</sup> there are several areas of further work relating to the gyrokinetic study which can help improve understanding further.

The simple picture developed for the pedestal evolution involving the evolution of the MTM and KBM stability is based upon the results of linear simulations of the experimental equilibria. These simulations did not include the effects of sheared  $\underline{E} \times \underline{B}$  flows, which are thought to be significant, especially in the pedestal. Sheared  $\underline{E} \times \underline{B}$  flows are likely to result in an up-shift in the KBM threshold gradient, though this is likely to be a relatively small effect due to the stiffness of the KBM transport. To build upon this study it is useful to try to better understand the instabilities involved. This can be achieved by studies of the MTM and KBM in simplified systems based on edge conditions. In relation to this it is important to note that electron scale instabilities have been excluded from the results presented here. Preliminary studies looking at  $10 \leq k_y \rho_i \leq 100$  have indicated the existence of electron temperature gradient (ETG) modes in the shallow gradient region and these modes may also be important in the pedestal evolution. Similar analyses of different types of discharge and other tokamaks will provide some indication as to how generic this process is and may indicate other instabilities which can play a role. In reality non-linear simulations, which provide calculations of the heat and particle fluxes, are required in order to verify the change in transport with increasing density gradients in the transition region assumed in this simple picture. These simulations will be challenging but could provide valuable insight.

The experimental gradients, and their evolution, occur due to a balance between heat and particle sources and the resulting turbulent fluxes. To fully describe this process a transport analysis is required including a range of effects such as neutral penetration. This is likely to be very challenging and rely upon accurate calculation of the

<sup>47</sup>The sources of heat and particles will also effect the pedestal evolution.

<sup>48</sup>These include the incorporation of more relevant effects into the PB stability calculation and a change to the definition of the  $n_\infty$  stability constraint.

nonlinear fluxes. The implementation and use of a formulation of global gyrokinetics valid in the pedestal region is required in order to improve the confidence of the gyrokinetic results obtained in this region. Whilst such formulations are starting to be developed the implementation and testing of these in numerical simulations is still not likely for a significant period of time.



# Chapter 7

## Summary and discussion

The effective confinement of heat and particles is crucial for the economic viability of future fusion reactors. The turbulent transport of these quantities, driven by small scale instabilities, greatly increases the rate at which they are lost from tokamaks, leading to the need to build larger, more expensive, machines. By understanding this turbulence and optimising operational scenarios to minimise its impact, confinement can be improved for a fixed size device, greatly improving the cost per unit energy produced.

The field of gyrokinetics has been developed in order to study theoretically this plasma turbulence and the underlying linear instabilities. Numerous codes exist to solve the gyrokinetic system and many exploit the separation of scales often observed between the characteristic radial size of the instability and the length scale of equilibrium variations to further simplify to a local system.

In this thesis two key questions for the gyrokinetic study of confinement have been addressed:

1. How important is the effect of radial equilibrium profile variations, neglected in the local system, for linear instabilities?
2. What role do microinstabilities play in the dynamics of the edge transport barrier evolution observed during the favourable H-mode operation?

These two topics are at the forefront of current research and are among a number of questions which must be addressed in order to improve understanding of transport barriers near the edge. The main findings, limitations and remaining questions for these two areas will now be discussed.

## 7.1 The effect of equilibrium variations

A global electrostatic gyrokinetic ITG model for a simple large aspect ratio geometry was developed in chapter 5. The application of the ballooning transformation and an expansion in  $1/nq'$  was used to reduce this model to a local system. It was shown that by considering the dependence of the local complex mode frequency,  $\Omega_0$ , on radius,  $x$ , and wavenumber (or ballooning angle),  $k$ , it was possible to obtain an expression for the global complex mode frequency,  $\Omega$ , only in terms of parameters obtained from solution of the local model. Furthermore, this procedure yields analytic expressions for  $k(x)$  which can be used to reconstruct the global mode structure again based purely on solution of the local model, predicting both the radial width and poloidal orientation of the perturbation. Two classes of instability were identified, dependent upon the equilibrium profiles present:

- *Isolated* modes which peak at the outboard midplane,  $\theta = 0$  where the growth rate is maximised and are captured by existing local codes.
- *General* modes which peak at  $\theta = \pm\pi/2$  with a reduced growth rate and are not captured within the standard operation of local codes.

A code was developed to solve both local and global models, allowing the predictions implicit in the analytic expressions for  $k(x)$  and  $\Omega$  to be tested. Very good agreement was found between the global mode's properties and those predicted using this procedure with the local solutions, for both classes of instability.

These results illustrate the significant finding that the solution of the global model can be entirely reconstructed using multiple local solutions. This offers a novel means to study the effect of radial equilibrium variations utilising existing local gyrokinetic codes through application of the trivially parallelisable procedure developed here. This allows general geometry to be treated as well as including multiple effects of relevance to experiment which have been neglected in the models used here. Moreover, it provides an additional means to benchmark global codes against the results of well benchmarked local simulations.

The ability to calculate an effective ballooning angle,  $k(x=0)$ , is appealing for quasi-linear transport models. Not only does this provide an estimate for the growth rate of the instability and its associated radial scale, both of which are crucial in such models, but it also yields an estimate of the symmetry breaking due to the profile shearing effects, which are important for momentum transport.

It is important to note that the analysis presented here is only applicable to linear systems and the implications of these results for the nonlinear case remains an open question. If the time taken for an initial perturbation to reach the nonlinear threshold is much shorter than the time taken to form a radially coupled eigenmode then the

nonlinear physics will dominate and the effects discussed here may be less important. However, if this is indeed the case then the formation of ballooning structures, which requires radial coupling, is no longer possible and one may expect shear damping to suppress the instability [131]. A study of the relevant time scales is required in order to make progress with this outstanding question and necessitates the use of a global initial value code.

## 7.2 Stability of the pedestal

The spontaneous transition to a regime of high confinement, or H-mode, is observed on many tokamaks. This is associated with the formation of an edge transport barrier, known as the pedestal, in which a steep pressure gradient is achieved. The periodic collapse of the pedestal, associated with the onset of ELMs, limits the achievable performance improvement and is concerning for ITER due to the ejection of large amounts of energy in a very short time, leading to large power loads which can cause significant damage.

A linear local gyrokinetic study of the pedestal and the neighbouring shallow gradient region has been presented in chapter 6 for a H-mode case from the spherical tokamak MAST at five times between two ELMs. These simulations show that kinetic ballooning modes (KBMs) are the dominant instability in the pedestal whilst microtearing modes (MTMs) are dominant in the shallow gradient region. Artificial parameter scans around the experimental equilibria have been used to probe the behaviour of both the MTMs and KBMs as the density and temperature gradient length scales evolve. This provides a simple picture for the observed pedestal evolution in terms of the microstability behaviour:

1. The pressure gradient in the pedestal is limited to near the KBM threshold.
2. MTMs dominate in the shallow gradient region and limit the electron temperature gradient.
3. The density pedestal can expand inwards, provided there is a particle source, as MTMs are stabilised by increasing density gradient, allowing the pressure gradient to increase further until the KBM limit is reached.
4. As the pedestal expands, the local  $\beta$  on surfaces further towards the core increases, making the MTMs more unstable. This may make it harder for the pedestal to expand further through suppression of the MTMs.
5. Towards the end of the ELM cycle the pressure gradient transition region is close to a position in  $\{\beta, \beta'\}$  operating space where both KBMs and MTMs are simultaneously unstable over a large range of  $k_y \rho_i$ . Entering this region could

trigger a large change in the transport properties and may limit the pedestal expansion.

These results highlight the importance of the microinstabilities in the shallow gradient region in influencing the evolution of the density and temperature profiles.

The picture developed here is based on the results of linear simulations whilst the experimental profile evolution will be determined by a balance of the heat and particle sources with the nonlinear turbulent fluxes. Therefore an important next step in this study is to develop nonlinear simulations in the shallow gradient region in order to probe the behaviour of these fluxes through similar artificial scans to those performed here. These are likely to be extremely challenging<sup>1</sup> though will be an important test of the picture developed here.

It is important to acknowledge that the short equilibrium length scales and large normalised fluctuations near the edge and in the pedestal stretch the validity of the standard formulation of gyrokinetics used in this study in the steep gradient region. The development and implementation of gyrokinetics suitable for such regimes is extremely challenging but very important in improving the accuracy of gyrokinetic studies of the pedestal. Despite this, it is useful to extend the study performed here to investigate the shallow gradient region, where the gyrokinetic model used here is more valid, to other tokamaks to probe the similarities and differences across machines and scenarios. Employing a global approach to study the mode transition at the interface between the shallow and steep gradient regions is desirable to help better understand the behaviour in this region.

---

<sup>1</sup>Indeed the first converged nonlinear simulations of MTMs in the core have only recently been achieved [216, 217].

# Appendix A

## Fluid equations from the kinetic equation

Taking velocity moments of the ensemble averaged distribution function,  $f_s$ , leads to expressions for the fluid variables. For example the species density,  $n_s$ , and flow,  $\underline{V}_s$ , are given by the 0<sup>th</sup> and 1<sup>st</sup> order moments respectively:

$$n_s = \int f_s d\underline{v} \quad (\text{A.1})$$

$$n_s \underline{V}_s = \int f_s \underline{v} d\underline{v} \quad (\text{A.2})$$

The fluid equations used in section 3.2 can also be rigorously derived from the kinetic equation, achieved by taking velocity moments of eqn. 3.35. This will be illustrated for the continuity equation using the Vlasov equation<sup>1</sup> (i.e. eqn. 3.35 in the absence of collisions). Multiplying eqn. 3.35 by  $\underline{v}^0$  and integrating leads to

$$\frac{\partial}{\partial t} \left( \int f_s d\underline{v} \right) + \int \underline{v} \cdot \frac{\partial f_s}{\partial \underline{x}} d\underline{v} + \frac{1}{m_s} \int \underline{F} \frac{\partial f_s}{\partial \underline{v}} d\underline{v} = 0 \quad (\text{A.3})$$

where  $\underline{F}$  is the Lorentz force. Progress can be made by considering each term individually, for example the first term in eqn. A.3 is given by

$$\frac{\partial}{\partial t} \left( \int f_s d\underline{v} \right) = \frac{\partial n_s}{\partial t} \quad (\text{A.4})$$

Noting that  $\partial/\partial \underline{x}$  is performed at fixed  $\underline{v}$  the second term can be rewritten as

$$\int \underline{v} \cdot \frac{\partial f_s}{\partial \underline{x}} d\underline{v} = \frac{\partial}{\partial \underline{x}} \int \underline{v} f_s d\underline{v} = \frac{\partial}{\partial \underline{x}} (n_s \underline{V}_s) \quad (\text{A.5})$$

---

<sup>1</sup>Provided the collision operator does not alter the number of particles, integration of the collision term over velocity space should yield 0.

The third term can be simplified using integration by parts to give

$$\int \underline{F} \frac{\partial f_s}{\partial \underline{v}} d\underline{v} = [\underline{F} f_s]_{\underline{v}} - \int f_s \frac{\partial \underline{F}}{\partial \underline{v}} d\underline{v} \quad (\text{A.6})$$

Noting that  $f_s \rightarrow 0$  for  $\underline{v} \rightarrow \pm\infty$  the first term of eqn. A.6 must be zero. As each component of the Lorentz force,  $\underline{F}$ , is independent of the corresponding velocity component the second term in eqn. A.6 is also 0 and eqn. A.3 can be written as

$$\frac{\partial n_s}{\partial t} + \frac{\partial}{\partial \underline{x}} (n_s \underline{V}_s) = 0 \quad (\text{A.7})$$

which is the continuity equation introduced previously, eqn. 3.1.

# Bibliography

- [1] D. Dickinson, C. M. Roach, and H. R. Wilson, Probing the linear structure of toroidal drift modes., in 38th EPS Conference on Plasma Physics, edited by A. Becoulet, T. Hoang, and U. Stroth, pages 1–4, Strasbourg, 2011, European Physical Society, [\[Online\]](#).
- [2] H. R. Wilson, D. Dickinson, and C. M. Roach, Toroidal drift mode structure revisited : A model for small ELM regimes, in 39th EPS Conference on Plasma Physics, edited by S. Ratynskaya, L. Blomberg, and A. Fasoli, pages 1–4, Stockholm, 2012, European Physical Society, [\[Online\]](#).
- [3] D. Dickinson et al., Plasma Physics and Controlled Fusion **53**, 115010 (2011).
- [4] D. Dickinson et al., Physical Review Letters **108**, 135002 (2012).
- [5] The World Bank, World Development Indicators, 2011, [\[Online\]](#).
- [6] British Petroleum, Statistical Review of World Energy 2011, 2011, [\[Online\]](#).
- [7] S. Shafiee and E. Topal, Energy Policy **37**, 181 (2009).
- [8] Electricity generated from renewable sources: Social Trends 34, 2004, [\[Online\]](#).
- [9] Environmental Accounts: Energy consumption, 2011, [\[Online\]](#).
- [10] J. Freidberg, Plasma physics and fusion energy, Cambridge University Press, 2007, [\[Online\]](#).
- [11] H. Lightfoot et al., 2006 IEEE EIC Climate Change Conference , 1 (2006).
- [12] J. Huba, U. S. O. of Naval Research, and N. R. L. (U.S.), NRL plasma formulary, NRL publication, Naval Research Laboratory, 2009, [\[Online\]](#).
- [13] A. Hasegawa, L. Chen, and M. E. Mauel, Nuclear Fusion **30**, 2405 (1990).
- [14] D. Moreau, Nuclear Fusion **17**, 13 (1977).
- [15] J. R. de Laeter et al., Pure and Applied Chemistry **75**, 683 (2003).
- [16] L. L. Lucas and M. P. Unterweger, Journal Of Research Of The National Institute Of Standards And Technology **105**, 541 (2000).
- [17] T. K. Park, Nuclear Engineering and Design **163**, 405 (1996).
- [18] D. Fasel and M. Tran, Fusion Engineering and Design **75-79**, 1163 (2005).
- [19] J. D. Lawson, Proceedings of the Physical Society. Section B **70**, 6 (1957).
- [20] F. F. Chen, Introduction to Plasma Physics and Controlled Fusion, Springer, 2010, [\[Online\]](#).

- [21] Y. Kosmann-Schwarzbach, The Noether Theorems: Invariance & Conservation Laws in the 20<sup>th</sup> Century, Sources and Studies in the History of Mathematics and Physical Sciences, Springer, 2010, [Online].
- [22] R. D. Hazeltine and J. D. Meiss, Plasma confinement, Dover Publications, 2003, [Online].
- [23] M. Kikuchi, Nuclear Fusion **30**, 265 (1990).
- [24] European Fusion Development Agreement, [EFDA.org](http://EFDA.org).
- [25] J. Wesson, Tokamaks, Clarendon Press, 3rd edition, 2004, [Online].
- [26] EFDA-JET, [Figure database](#).
- [27] M. Greenwald et al., Nuclear Fusion **28**, 2199 (1988).
- [28] M. Greenwald, Plasma Physics and Controlled Fusion **44**, R27 (2002).
- [29] ITER Physics Expert Group on Disruptions Plasma Control and MHD and ITER Physics Basis Editors, Nuclear Fusion **39**, 2251 (1999).
- [30] F. C. Schuller, Plasma Physics and Controlled Fusion **37**, A135 (1995).
- [31] A. Fick, Philosophical Magazine Series 4 **10**, 30 (1855).
- [32] A. Einstein translated by Cowper, A D (1926), Annalen der Physik **322**, 549 (1905).
- [33] G. Thomson and M. Blackman, Improvements in or relating to gas discharge apparatus for producing thermonuclear reactions, Patent, British Patent Office, 1959, [Online].
- [34] R. S. Pease, Plasma Physics and Controlled Fusion **29**, 1439 (1987).
- [35] M. F. Hoyaux, American Journal of Physics **35**, 232 (1967).
- [36] F. L. Hinton and R. D. Hazeltine, Reviews of Modern Physics **48**, 239 (1976).
- [37] J. W. Connor and H. R. Wilson, Plasma Physics and Controlled Fusion **36**, 719 (1994).
- [38] S. A. Cohen, Journal of Nuclear Materials **76-77**, 68 (1978).
- [39] R. A. Pitts and P. C. Stangeby, Plasma Physics and Controlled Fusion **32**, 1237 (1990).
- [40] E. Mazzucato, Physical Review Letters **36**, 792 (1976).
- [41] W. Mandl et al., Plasma Physics and Controlled Fusion **35**, 1373 (1993).
- [42] A. R. Field et al., The Review of scientific instruments **80**, 073503 (2009).
- [43] R. P. Hsia et al., Review of Scientific Instruments **66**, 834 (1995).
- [44] H. Park et al., Review of Scientific Instruments **75**, 3787 (2004).
- [45] A. J. Wootton et al., Physics of Fluids B: Plasma Physics **2**, 2879 (1990).
- [46] P. Liewer, Nuclear Fusion **25**, 543 (1985).
- [47] D. Froula et al., Plasma Scattering of Electromagnetic Radiation: Theory and Measurement Techniques, Academic Press/Elsevier, 2010, [Online].

- [48] S. Zweben, P. Liewer, and R. Gould, *Journal of Nuclear Materials* **111-112**, 39 (1982).
- [49] S. J. Levinson et al., *Nuclear Fusion* **24**, 527 (1984).
- [50] C. P. Ritz et al., *Physics of Fluids* **27**, 2956 (1984).
- [51] C. P. Ritz et al., *Physical Review Letters* **62**, 1844 (1989).
- [52] K. W. Gentle et al., *Plasma Physics and Controlled Fusion* **26**, 1407 (1984).
- [53] E. Mazzucato, *Physical Review Letters* **48**, 1828 (1982).
- [54] C. M. Surko and R. E. Slusher, *Physical Review Letters* **37**, 1747 (1976).
- [55] M. Keilhacker, *Nuclear Fusion* **25**, 1045 (1985).
- [56] F. Wagner et al., *Physical Review Letters* **49**, 1408 (1982).
- [57] M. Cox, *Fusion Engineering and Design* **46**, 397 (1999).
- [58] A. R. Field et al., *Nuclear Fusion* **51**, 063006 (2011).
- [59] E. J. Doyle et al., *Physics of Fluids B: Plasma Physics* **3**, 2300 (1991).
- [60] D. Borba et al., *Plasma Physics and Controlled Fusion* **48**, 757 (2006).
- [61] U. Stroth et al., *Plasma Physics and Controlled Fusion* **40**, 1551 (1998).
- [62] J. W. Connor and H. R. Wilson, *Plasma Physics and Controlled Fusion* **42**, R1 (2000).
- [63] H. Zohm, *Plasma Physics and Controlled Fusion* **38**, 105 (1996).
- [64] J. W. Connor, *Plasma Physics and Controlled Fusion* **40**, 531 (1998).
- [65] A. Kirk et al., *Physical Review Letters* **96**, 1 (2006).
- [66] A. Loarte et al., *Plasma Physics and Controlled Fusion* **45**, 1549 (2003).
- [67] Y. Koide et al., *Physical Review Letters* **72**, 3662 (1994).
- [68] G. T. Hoang et al., *Nuclear Fusion* **34**, 75 (1994).
- [69] J. W. Connor et al., *Nuclear Fusion* **44**, R1 (2004).
- [70] Y. Koide et al., *Plasma Physics and Controlled Fusion* **38**, 1011 (1996).
- [71] JET Team (prepared by A.C.C Sips), *Nuclear Fusion* **41**, 1559 (2001).
- [72] F. Söldner et al., *Nuclear Fusion* **39**, 407 (1999).
- [73] X. Litaudon et al., *Plasma Physics and Controlled Fusion* **44**, 1057 (2002).
- [74] C. M. Greenfield et al., *Physical Review Letters* **86**, 4544 (2001).
- [75] C. M. Roach et al., *Nuclear Fusion* **48**, 125001 (2008).
- [76] A. Sips, *Plasma Physics and Controlled Fusion* **47**, A19 (2005).
- [77] E. Joffrin et al., *Nuclear Fusion* **45**, 626 (2005).
- [78] L. A. Artsimovich et al., *Soviet Atomic Energy* **22**, 325 (1967).
- [79] V. D. Shafranov, *Plasma Physics* **13**, 757 (1971).

- [80] ITER Physics Expert Group on Confinement and Transport: ITER Physics Expert Group on Confinement Modelling and Database and ITER Physics Basis Editors, Nuclear Fusion **39**, 2175 (1999).
- [81] S. M. Kaye and I. C. D. W. Group, Nuclear Fusion **37**, 1657 (1997).
- [82] F. W. Perkins et al., Physics of Fluids B: Plasma Physics **5**, 477 (1993).
- [83] R. E. Waltz et al., Physics of Plasmas **4**, 2482 (1997).
- [84] G. M. Staebler, J. E. Kinsey, and R. E. Waltz, Physics of Plasmas **14**, 055909 (2007).
- [85] J. E. Kinsey, G. M. Staebler, and R. E. Waltz, Physics of Plasmas **15**, 055908 (2008).
- [86] M. Barnes et al., Physics of Plasmas **17**, 056109 (2010).
- [87] J. Candy et al., Physics of Plasmas **16**, 060704 (2009).
- [88] M. Keilhacker et al., Nuclear Fusion **39**, 209 (1999).
- [89] R. Aymar et al., Nuclear Fusion **41**, 1301 (2001).
- [90] ITER Physics Expert Group on Confinement and Transport: ITER Physics Expert Group on Confinement Modelling and Database and ITER Physics Basis Editors, Nuclear Fusion **39**, 2137 (1999).
- [91] R. Budny et al., Nuclear Fusion **48**, 075005 (2008).
- [92] V. Mukhovatov et al., Nuclear Fusion **43**, 942 (2003).
- [93] L. Chen et al., Nuclear Fusion **19**, 373 (1979).
- [94] D. L. Brower et al., Physical Review Letters **59**, 48 (1987).
- [95] S. C. Cowley, R. M. Kulsrud, and R. Sudan, Physics of Fluids B: Plasma Physics **3**, 2767 (1991).
- [96] J. J. Ramos, Physics of Plasmas **12**, 112301 (2005).
- [97] L. Pearlstein and H. Berk, Physical Review Letters **23**, 220 (1969).
- [98] J. B. Taylor and R. J. Hastie, Plasma Physics **10**, 479 (1968).
- [99] P. H. Rutherford and E. A. Frieman, Physics of Fluids **11**, 569 (1968).
- [100] P. J. Catto, W. M. Tang, and D. E. Baldwin, Plasma Physics **23**, 639 (1981).
- [101] D. J. Applegate, Gyrokinetic Studies of a Spherical Tokamak H-mode Plasma, PhD thesis, Imperial College London, 2005.
- [102] C. M. Roach, Gyrokinetics, Private communication, 2012.
- [103] M. Artun and W. M. Tang, Physics of Plasmas **1**, 2682 (1994).
- [104] X. Garbet et al., Nuclear Fusion **50**, 043002 (2010).
- [105] V. Grandgirard et al., Plasma Physics and Controlled Fusion **49**, B173 (2007).
- [106] L. Villard et al., Plasma Physics and Controlled Fusion **52**, 124038 (2010).
- [107] T. Görler et al., Physics of Plasmas **18**, 056103 (2011).

- [108] J. Candy and R. E. Waltz, *Physical Review Letters* **91**, 4 (2003).
- [109] C. Holland et al., *Journal of Physics: Conference Series* **125**, 012043 (2008).
- [110] P. B. Snyder et al., *Physics of Plasmas* **16**, 056118 (2009).
- [111] T. E. Evans et al., *Nuclear Fusion* **48**, 024002 (2008).
- [112] A. Kirk et al., *Nuclear Fusion* **50**, 034008 (2010).
- [113] X. Xu et al., *Nuclear Fusion* **47**, 809 (2007).
- [114] T. S. Hahm, L. Wang, and J. Madsen, *Physics of Plasmas* **16**, 022305 (2009).
- [115] G. Kawamura and A. Fukuyama, *Physics of Plasmas* **15**, 042304 (2008).
- [116] Y. Idomura et al., *Nuclear Fusion* **49**, 065029 (2009).
- [117] J. A. Heikkinen et al., *Journal of Computational Physics* **227**, 5582 (2008).
- [118] R. H. Cohen and X. Xu, *Contributions to Plasma Physics* **48**, 212 (2008).
- [119] F. Halpern et al., *Physics of Plasmas* **15**, 062505 (2008).
- [120] P. H. Diamond et al., *Nuclear Fusion* **49**, 045002 (2009).
- [121] R. E. Waltz et al., *Physics of Plasmas* **14**, 122507 (2007).
- [122] A. G. Peeters et al., *Computer Physics Communications* **180**, 2650 (2009).
- [123] F. J. Casson et al., *Physics of Plasmas* **16**, 092303 (2009).
- [124] Y. Camenen et al., *Physical Review Letters* **102**, 1 (2009).
- [125] J. W. Connor, J. B. Taylor, and H. R. Wilson, *Physical Review Letters* **70**, 1803 (1993).
- [126] J. B. Taylor, H. R. Wilson, and J. W. Connor, *Plasma physics and controlled fusion* **38**, 243 (1996).
- [127] P. B. Snyder et al., *Nuclear Fusion* **51**, 103016 (2011).
- [128] M. Kotschenreuther, G. Rewoldt, and W. M. Tang, *Computer Physics Communications* **88**, 128 (1995).
- [129] E. G. Highcock, *The Zero Turbulence Manifold in Fusion Plasmas*, PhD thesis, University of Oxford, 2012, [[Online](#)].
- [130] N. A. Krall and M. N. Rosenbluth, *Physics of Fluids* **8**, 1488 (1965).
- [131] J. B. Taylor, Does magnetic shear stabilize drift waves?, in *Proceedings Of The Sixth International Conference On Plasma Physics And Controlled Nuclear Fusion Research*, volume 6, pages 323–329, Vienna, 1977, [[Online](#)].
- [132] J. W. Connor, R. J. Hastie, and J. B. Taylor, *Proceedings of the Royal Society A: Mathematical, Physical and Engineering Sciences* **365**, 1 (1979).
- [133] J. W. Connor and R. J. Hastie, *Plasma Physics* **17**, 97 (1975).
- [134] R. J. Hastie, K. W. Hesketh, and J. B. Taylor, *Nuclear Fusion* **19**, 1223 (1979).

- [135] V. D. Shafranov, Plasma equilibrium in a magnetic field, in Reviews of Modern Physics, edited by M. A. Leontovich, pages 103–151, Consultants Bureau, New York, 1966, [\[Online\]](#).
- [136] I. S. Gradshteyn and I. M. Ryzhik, Table of integrals, series and products, Academic press, 4th edition, 1965, [\[Online\]](#).
- [137] Y. Zhang and S. M. Mahajan, Physics Letters A **157**, 133 (1991).
- [138] W. H. Press et al., Numerical recipes in FORTRAN, Cambridge University Press, 2nd edition, 1992, [\[Online\]](#).
- [139] J. B. Taylor and H. R. Wilson, Plasma physics and controlled fusion **38**, 1999 (1996).
- [140] S. P. Hirshman, Nuclear Fusion **18**, 917 (1978).
- [141] R. C. Morris, M. G. Haines, and R. J. Hastie, Physics of Plasmas **3**, 4513 (1996).
- [142] S. L. Newton, S. C. Cowley, and N. F. Loureiro, Plasma Physics and Controlled Fusion **52**, 125001 (2010).
- [143] P. J. Catto, Physics of Fluids **16**, 1719 (1973).
- [144] C. M. Roach et al., Plasma Physics and Controlled Fusion **51**, 124020 (2009).
- [145] M. Reshko, Gyrokinetic Simulations of the Effects of Equilibrium ExB Flow Shear on Microinstabilities and Transport in Tokamaks, PhD thesis, Univeristy of York, 2009.
- [146] G. M. Staebler and R. R. Dominguez, Nuclear Fusion **31**, 1891 (1991).
- [147] P. Hill et al., Plasma Physics and Controlled Fusion **54**, 065011 (2012).
- [148] Y. Camenen et al., Nuclear Fusion **51**, 073039 (2011).
- [149] R. E. Waltz, G. M. Staebler, and W. M. Solomon, Physics of Plasmas **18**, 042504 (2011).
- [150] H. R. Wilson et al., Nuclear Fusion **40**, 713 (2000).
- [151] W. Suttrop et al., Plasma Physics and Controlled Fusion **39**, 2051 (1997).
- [152] F. Ryter et al., Plasma Physics and Controlled Fusion **43**, A323 (2001).
- [153] F. Ryter et al., Nuclear Fusion **41**, 537 (2001).
- [154] X. Garbet et al., Plasma Physics and Controlled Fusion **46**, B557 (2004).
- [155] X. Garbet et al., Plasma Physics and Controlled Fusion **46**, 1351 (2004).
- [156] J. E. Kinsey et al., Nuclear Fusion **43**, 1845 (2003).
- [157] G. Federici, a. Loarte, and G. Strohmayer, Plasma Physics and Controlled Fusion **45**, 1523 (2003).
- [158] G. Federici et al., Journal of Nuclear Materials **313-316**, 11 (2003).
- [159] W. Suttrop et al., Physical Review Letters **106**, 1 (2011).
- [160] A. W. Degeling et al., Plasma Physics and Controlled Fusion **45**, 1637 (2003).

- [161] A. Kirk et al., *Plasma Physics and Controlled Fusion* **47**, 995 (2005).
- [162] A. Kirk et al., *Journal of Physics: Conference Series* **123**, 012011 (2008).
- [163] A. Kirk et al., *Plasma Physics and Controlled Fusion* **49**, 1259 (2007).
- [164] J. W. Connor, *Plasma Physics and Controlled Fusion* **40**, 191 (1998).
- [165] J. W. Connor, R. J. Hastie, and J. B. Taylor, *Physical Review Letters* **40**, 396 (1978).
- [166] P. Gohil et al., *Physical Review Letters* **61**, 1603 (1988).
- [167] H. Zohm et al., *Nuclear Fusion* **35**, 543 (1995).
- [168] T. Kass et al., *Nuclear Fusion* **38**, 111 (1998).
- [169] R. J. Bickerton, J. W. Connor, and J. B. Taylor, *Nature physical science* **229**, 110 (1971).
- [170] O. Sauter, C. Angioni, and Y. R. Lin-Liu, *Physics of Plasmas* **6**, 2834 (1999).
- [171] O. Sauter, C. Angioni, and Y. R. Lin-Liu, *Physics of Plasmas* **9**, 5140 (2002).
- [172] J. Wesson, *Nuclear Fusion* **18**, 87 (1978).
- [173] J. Manickam, *Physics of Fluids B: Plasma Physics* **4**, 1901 (1992).
- [174] J. W. Connor et al., *Physics of Plasmas* **5**, 2687 (1998).
- [175] D. Lortz, *Nuclear Fusion* **15**, 49 (1975).
- [176] H. R. Wilson et al., *Physics of Plasmas* **6**, 1925 (1999).
- [177] P. B. Snyder and H. R. Wilson, *Plasma Physics and Controlled Fusion* **45**, 1671 (2003).
- [178] S. Y. Medvedev et al., *Plasma Physics and Controlled Fusion* **48**, 927 (2006).
- [179] A. J. Webster and C. G. Gimblett, *Physics of Plasmas* **16**, 082502 (2009).
- [180] A. Burckhart et al., *Plasma Physics and Controlled Fusion* **52**, 105010 (2010).
- [181] H. R. Wilson et al., *Physics of Plasmas* **9**, 1277 (2002).
- [182] P. B. Snyder et al., *Physics of Plasmas* **9**, 2037 (2002).
- [183] P. B. Snyder et al., *Nuclear Fusion* **44**, 320 (2004).
- [184] P. B. Snyder et al., *Plasma Physics and Controlled Fusion* **46**, A131 (2004).
- [185] G. T. A. Huysmans, *Plasma Physics and Controlled Fusion* **47**, B165 (2005).
- [186] W. M. Tang, J. W. Connor, and R. J. Hastie, *Nuclear Fusion* **20**, 1439 (1980).
- [187] R. J. Hastie and K. W. Hesketh, *Nuclear Fusion* **21**, 651 (1981).
- [188] P. B. Snyder et al., *Nuclear Fusion* **49**, 085035 (2009).
- [189] P. B. Snyder and G. W. Hammett, *Physics of Plasmas* **8**, 744 (2001).
- [190] J. Candy, *Physics of Plasmas* **12**, 072307 (2005).
- [191] R. J. Groebner et al., *Nuclear Fusion* **50**, 064002 (2010).

- [192] A. Sykes et al., *Nuclear Fusion* **41**, 1423 (2001).
- [193] R. Scannell et al., *The Review of scientific instruments* **79**, 10E730 (2008).
- [194] R. Scannell et al., *The Review of scientific instruments* **81**, 10D520 (2010).
- [195] R. Scannell et al., *Plasma Physics and Controlled Fusion* **49**, 1431 (2007).
- [196] T. W. Versloot et al., *Plasma Physics and Controlled Fusion* **52**, 045014 (2010).
- [197] R. J. Groebner et al., *Nuclear Fusion* **49**, 045013 (2009).
- [198] T. W. Morgan et al., A new diagnostic to measure edge ion temperatures on MAST, in *37th EPS Conference on Plasma Physics*, edited by C. McKenna, Dublin, 2010, European Physical Society, [[Online](#)].
- [199] A. Patel et al., *Review of Scientific Instruments* **75**, 4944 (2004).
- [200] L. L. Lao et al., *Nuclear Fusion* **25**, 1611 (1985).
- [201] G. T. A. Huysmans, J. P. Goedbloed, and W. Kerner, *International Journal of Modern Physics C* **02**, 371 (1991).
- [202] A. Kirk et al., *Plasma Physics and Controlled Fusion* **47**, 315 (2005).
- [203] A. M. Dimits, *Physics of Plasmas* **19**, 022504 (2012).
- [204] H. Meyer et al., *Journal of Physics: Conference Series* **123**, 012005 (2008).
- [205] W. M. Nevins, E. Wang, and J. Candy, *Physical Review Letters* **106**, 1 (2011).
- [206] E. A. Belli and J. Candy, *Physics of Plasmas* **17**, 112314 (2010).
- [207] R. D. Hazeltine, D. Dobrott, and T. S. Wang, *Physics of Fluids* **18**, 1778 (1975).
- [208] M. Kotschenreuther et al., *Nuclear Fusion* **40**, 677 (2000).
- [209] H. R. Wilson et al., *Nuclear Fusion* **44**, 917 (2004).
- [210] D. J. Applegate et al., *Physics of Plasmas* **11**, 5085 (2004).
- [211] D. J. Applegate et al., *Plasma Physics and Controlled Fusion* **49**, 1113 (2007).
- [212] W. Guttenfelder et al., *Physics of Plasmas* **19**, 022506 (2012).
- [213] H. Doerk et al., *Physics of Plasmas* **19**, 055907 (2012).
- [214] D. Told et al., *Physics of Plasmas* **15**, 102306 (2008).
- [215] S. Saarelma et al., Pedestal Modelling Based MHD Analyses on MAST and JET Plasmas, in *39th EPS Conference on Plasma Physics*, edited by S. Ratynskaya, L. Blomberg, and A. Fasoli, pages 1–4, Stockholm, 2012, European Physical Society, [[Online](#)].
- [216] H. Doerk et al., *Physical Review Letters* **106**, 1 (2011).
- [217] W. Guttenfelder et al., *Physical Review Letters* **106**, 1 (2011).